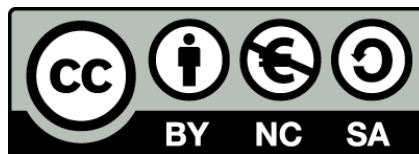




UNIVERSITAT_{DE}
BARCELONA

Leptonic CP Violation and its Origin

Iván Esteban Muñoz



Aquesta tesi doctoral està subjecta a la llicència **Reconeixement- NoComercial – Compartir Igual 4.0. Espanya de Creative Commons.**

Esta tesis doctoral está sujeta a la licencia **Reconocimiento - NoComercial – Compartir Igual 4.0. España de Creative Commons.**

This doctoral thesis is licensed under the **Creative Commons Attribution-NonCommercial-ShareAlike 4.0. Spain License.**

LEPTONIC CP VIOLATION AND ITS ORIGIN

IVÁN ESTEBAN MUÑOZ

PHD ADVISOR:

PROF. DR. MARÍA CONCEPCIÓN GONZÁLEZ GARCÍA



UNIVERSITAT DE
BARCELONA

Leptonic CP Violation and its Origin

Memoria presentada para optar al grado de doctor por la Universidad de
Barcelona

(Programa de Doctorado en Física)

Autor: Iván Esteban Muñoz

Directora: Prof. Dr. María Concepción González García

Tutor: Prof. Dr. Domènec Espriu Climent

Departament de Física Quàntica i Astrofísica
Institut de Ciències del Cosmos
Universitat de Barcelona



UNIVERSITAT DE
BARCELONA

Resumen

Esta tesis se centra en la cuantificación y caracterización de los resultados experimentales que apuntan hacia la existencia de violación de la simetría CP en el sector leptónico. Se hace especial énfasis en el origen físico de esta señal, para cuya interpretación se emplean datos recogidos por diversos experimentos de neutrinos. Los resultados presentados en esta tesis se basan en trabajos publicados en revistas internacionales de física de altas energías (Refs. [1–6]).

El Modelo Estándar es el paradigma actual para describir los componentes más fundamentales de la naturaleza y sus interacciones. Para su construcción tanto teórica como experimental, los neutrinos desempeñaron un papel importante. Pese a ello, los neutrinos son las partículas elementales más elusivas que se han logrado detectar. Cuando fueron inicialmente propuestos por Wolfgang Pauli, para explicar la conservación de la energía en decaimientos nucleares beta [7], se pensó que su detección era imposible. El motivo es su minúscula sección eficaz de interacción: el poder penetrante en materia sólida de neutrinos emitidos en decaimientos beta es del orden de 10^4 años luz [8]. Por ello, no fue hasta 26 años después de que fueran propuestos teóricamente que se pudieron detectar en un experimento subterráneo llevado a cabo por C.L. Cowan y F. Reines [9].

Las primeras características de los neutrinos medidas experimentalmente estaban de acuerdo con las predicciones del Modelo Estándar. Por una parte, los neutrinos se introdujeron en el modelo mínimamente, solo para explicar sus interacciones. Tal y como se detallará en el Capítulo 2, no existe ninguna manera de dar masa a los neutrinos consistentemente con las simetrías del modelo sin introducir nuevos grados de libertad. Por tanto, el Modelo Estándar predecía que los neutrinos tienen una masa exactamente cero, tal y como confirmaban cotas obtenidas mediante medidas cinemáticas [10].

Por otra parte, la misma estructura matemática que prohíbe que los neutrinos tengan masa también predice que su sabor (definido como el tipo de leptón cargado generado junto con la producción o detección del neutrino) debe conservarse. Los primeros experimentos con neutrinos confirmaron asimismo esta predicción [11].

Pero los paradigmas en física fundamental parecen incapaces de sobrevivir más de cinco décadas. A finales del siglo XX, una serie de experimentos que estudiaban neutrinos provenientes del Sol o de rayos cósmicos que colisionaban contra la atmósfera terrestre mostraron que estas partículas pueden cambiar su sabor [12–18], comportándose de una manera que el Modelo Estándar prohíbe explícitamente. El camino hacia la comprensión de las propiedades de los neutrinos, que podría revelar la siguiente estructura subyacente de la naturaleza, ha guiado desde entonces a miles de científicos. El escenario al inicio del trabajo de esta tesis estaba impulsado por la última sorpresa experimental de los neutrinos: los primeros indicios que apuntan hacia su fuerte violación de la simetría materia-antimateria.

En este sentido, uno de los misterios más profundos de la ciencia moderna, que podría guiarnos hacia una descripción más precisa de la naturaleza, es la asimetría materia-antimateria del Universo [19, 20]. La antimateria aparece de forma natural de la siguiente manera: las interacciones en el Modelo Estándar están mediadas por partículas de espín 1 con una simetría *gauge*

asociada a ellas. Las partículas cargadas bajo estas interacciones han venido descritas por campos de números complejos, ya que las transformaciones *gauge* modifican su fase. Por tanto, la cantidad de grados de libertad se duplica. Una consecuencia inmediata es la existencia de antimateria, es decir, partículas con propiedades cinemáticas idénticas pero con toda «carga» (asociada tanto a simetrías globales como *gauge*) opuesta. Como consecuencia, las partículas y antipartículas se pueden aniquilar eficientemente dando lugar a los mediadores de la interacción.

De acuerdo con el modelo del *Big Bang*, toda la materia en el Universo estuvo en algún momento en equilibrio térmico, es decir, su abundancia solamente dependía de su masa. Por consiguiente, en el Universo primitivo debería haber iguales cantidades de materia que de antimateria, que se habrían aniquilado dejando un Universo que contendría solamente radiación. Nuestra propia existencia, por tanto, exige una interacción que distinga entre materia y antimateria, creando más de la primera fuera del equilibrio térmico [21].

Ingenuamente distinguir entre materia y antimateria simplemente requeriría que dicha interacción violara la simetría de conjugación de carga C . Pero esto no es suficiente, porque las partículas también tienen un grado de libertad interno adicional: la helicidad. Por lo que si una interacción viola C pero conserva CP , la acción combinada de C y la inversión espacial (o paridad) P , creará la misma cantidad de partículas con una helicidad que de antipartículas con la helicidad opuesta. Como, por lo que sabemos, las partículas elementales no tienen más grados de libertad internos, distinguir entre materia y antimateria solamente requiere una interacción que viole C y CP [21]. Si bien es relativamente sencillo construir una teoría que viole C (la interacción débil, por ejemplo, lo hace de manera máxima), es algo más elaborado formular una interacción que viole también CP .

En el Modelo Estándar, dicha interacción existe para los quarks siempre que haya tres generaciones de partículas. No obstante, su intensidad no es suficientemente fuerte como para generar la asimetría materia-antimateria del Universo [22]. Sin embargo, la nueva física que induce las transiciones de sabor de los neutrinos está mostrando indicios de violar fuertemente CP . Caracterizar su significación estadística, robustez y origen físico es el principal objetivo que persigue esta tesis.

Para poner este problema en contexto, en el Capítulo 2 se resumen las propiedades básicas del Modelo Estándar relevantes para las interacciones de neutrinos y para la violación de CP . Además, se explora cómo el modelo se puede extender para incluir masas de neutrinos y mezcla leptónica, y cómo esto explica de forma natural las transiciones de sabor observadas en los neutrinos. Lo que es más, la mezcla leptónica entre tres generaciones abre la posibilidad de que exista violación de CP . Por tanto, las masas de los neutrinos serían no solo nuestra primera prueba en el laboratorio de que existe física más allá del Modelo Estándar, sino también una fuente potencialmente grande de asimetría materia-antimateria.

Pero la física, como toda ciencia, ha de estar fundamentada en datos experimentales. Para establecer y parametrizar empíricamente el mecanismo responsable de las transiciones de sabor de los neutrinos, durante las últimas tres décadas se viene llevando a cabo un vasto programa experimental (resumido en el Capítulo 3). Este comenzó detectando con precisión las transiciones de sabor en neutrinos solares [23–31] y atmosféricos [18, 32, 33]. Estas medidas fueron posteriormente confirmadas con haces de neutrinos artificiales provenientes de reactores nucleares [34] y aceleradores de partículas [35, 36]. Después de que una serie de experimentos de neutrinos provenientes de reactores nucleares midieran el último ángulo de mezcla leptónico [37–39], había aún tres preguntas sin respuesta experimental: el octante del ángulo de mezcla responsable de las transiciones de sabor de neutrinos atmosféricos, el orden de los autoestados de masa de los neutrinos, y la existencia y magnitud de la violación de CP leptónica.

Para desentrañar estas incógnitas, particularmente la violación de CP , hay un amplio programa de experimentos de neutrinos con aceleradores a largas distancias, tanto presentes [40, 41]

como futuros [42, 43]. En estos experimentos, un haz de protones acelerado choca contra un blanco fijo, produciendo piones que, tras decaer, dan lugar a un haz de neutrinos. Este haz de neutrinos, originalmente de sabor principalmente muónico, se detecta en sabores muónico y electrónico después de viajar centenares de kilómetros. En particular, el canal de aparición de neutrinos electrónicos aborda las tres cuestiones abiertas arriba mencionadas.

Al principio del desarrollo de esta tesis, el experimento de neutrinos con acelerador a larga distancia $\text{NO}\nu\text{A}$ publicó sus primeros resultados. Para obtener una visión global, el Capítulo 4 los combina con los resultados de otros experimentos de neutrinos relevantes. Con ello, se puede evaluar cuantitativamente el estatus de la mezcla leptónica y de la violación de CP. Asimismo, se comprueba que el límite gaussiano, que normalmente se da por sentado en análisis estadísticos, es una buena aproximación para evaluar la significación de la violación de CP leptónica. Posteriormente, se resume la evolución de dicha significación conforme los experimentos de neutrinos con aceleradores han publicado resultados. El capítulo finaliza resumiendo el estatus global de la mezcla leptónica al finalizar esta tesis. En general, los resultados de este capítulo están basados en los trabajos publicados [1] y [3], así como en las actualizaciones en las Refs. [44–46].

Según las incógnitas empezaban a clarificarse, los datos apuntaban hacia una violación de CP máxima. Este indicio, en ligera tensión con los datos de $\text{NO}\nu\text{A}$, está dominado por un exceso de neutrinos electrónicos en el experimento de neutrinos con acelerador a larga distancia T2K. Dentro del paradigma de tres neutrinos masivos, y con el resto de parámetros de mezcla leptónica medidos con precisión en varios experimentos, el exceso solamente se puede acomodar mediante una violación de CP grande.

A pesar de esto, tres neutrinos masivos es solamente una extensión mínima del Modelo Estándar: podría haber otra nueva física enmascarando los resultados, ya que la violación de CP leptónica aún no se ha medido de manera directa y concluyente. Por ello, el Capítulo 5, basado parcialmente en la publicación [4], reseña la nueva física que podría afectar a los experimentos de transiciones de sabor de neutrinos. El escenario menos acotado por otros experimentos, las interacciones no estándar de corriente neutra entre neutrinos y materia (NSI , de sus siglas en inglés), afecta a las transiciones de sabor de los neutrinos modificando la dispersión coherente con el medio atravesado. Las NSI podrían introducir nuevas degeneraciones y fuentes de violación de CP, cuyo formalismo se resume en ese capítulo. Físicamente, su origen son nuevas interacciones entre neutrinos y materia mediadas por partículas potencialmente ligeras. En cualquier caso, este trabajo adopta un punto de vista agnóstico y estudia las consecuencias fenomenológicas de los modelos de NSI independientemente de su origen.

En el Capítulo 6, basado en las publicaciones [2] y [4], estos modelos se confrontan con datos experimentales. Debido a la gran dimensión del espacio de parámetros, primero se exploran NSI que conservan CP (es decir, sus módulos). Se evalúan las cotas actuales, así como las sinergias y complementariedad entre diferentes experimentos. Gracias a que estos detectan neutrinos con diferentes energías y que han recorrido diferentes distancias, la determinación de los parámetros de mezcla leptónica resulta ser bastante robusta. Por ello, es posible avanzar un paso más y evaluar la sensibilidad actual a la violación de CP leptónica suponiendo que existen las NSI más genéricas que violan CP. La violación de CP inducida por las masas de los neutrinos y por la mezcla leptónica resulta ser bastante robusta, debido a la gran cantidad de datos de transiciones de sabor de neutrinos recopilados a lo largo de tres décadas.

En cualquier caso, las NSI introducen una degeneración exacta a nivel de probabilidad de transición de sabor. Esta degeneración reduce la sensibilidad a violación de CP leptónica. Aunque hoy en día el efecto no es muy drástico debido a la limitada sensibilidad experimental, la siguiente generación de experimentos con aceleradores a largas distancias [42, 43] pretende llevar a cabo medidas de precisión que podrían verse severamente afectadas. Debido a ello, sería altamente beneficioso constreñir independientemente las NSI .

En principio, se podrían obtener restricciones fuertes con experimentos de dispersión de corriente neutra o con medidas de precisión electrodébiles con leptones cargados. Sin embargo, las *NSI* afectan a la propagación de los neutrinos modificando la dispersión coherente con el medio atravesado, un proceso con transferencia de momento nula que ha de ser comparada con las típicas transferencias de momento en otros experimentos, $\mathcal{O}(\text{GeV})$. Si la partícula mediadora de las *NSI* es suficientemente ligera, sus efectos estarían suprimidos para transferencias de momento altas, y se evadirían cotas de otros experimentos.

Afortunadamente, durante los últimos años el experimento COHERENT [47] ha proporcionado cotas independientes sobre las *NSI*. Este experimento emplea el flujo de neutrinos producido mediante decaimiento de piones en reposo en las fuentes de espalación de neutrones, abundante y que se comprende bien. COHERENT mide la dispersión coherente de corriente neutra entre neutrinos y núcleos, un proceso en el que un neutrino interactúa coherentemente con todo un núcleo atómico. Esto ocurre cuando el momento intercambiado es del orden del inverso del tamaño nuclear, $\mathcal{O}(\text{MeV})$. Debido a las bajas transferencias de momento, este proceso es bastante sensible a *NSI* inducidas por mediadores ligeros. En el Capítulo 7, basado en las publicaciones [4] y [5], los datos del experimento COHERENT se analizan e integran en los análisis globales del Capítulo 6. Esto requiere comprender rigurosamente el procedimiento para analizar los datos de COHERENT. Se presta particular atención a cómo los resultados dependen de las suposiciones sobre la señal de fondo en el experimento, la estructura nuclear, y la respuesta del detector. La combinación de los datos de COHERENT con los de experimentos de transición de sabor desvela su papel incipiente en aumentar la robustez de la interpretación global de los datos.

Estos primeros resultados podrían mejorar ampliamente si se incrementase la estadística de la señal y/o si las medidas se llevasen a cabo con diferentes núcleos, sensibles a diferentes modelos de *NSI*. Para ello, una instalación futura idónea es la Fuente Europea de Espalación de Neutrones. Producirá un haz de neutrinos cuya intensidad será un orden de magnitud mayor que la de COHERENT, y como aún se encuentra en construcción se podría habilitar espacio para diversos detectores modernos. Sus perspectivas para acotar *NSI*, basadas en el trabajo publicado [6], también se exploran en el Capítulo 6.

En resumen, esta tesis estudia el indicio en los datos actuales de una violación sustancial de CP en el sector leptónico. Primero cuantifica su significación global, y después procede a verificar su robustez respecto del marco teórico en el que se interpretan los datos experimentales. Para ello, los experimentos complementarios de interacción coherente entre neutrinos y núcleos juegan, y continuarán jugando en el futuro, un papel importante. Por ello, se aborda el problema desde una perspectiva global para evaluar rigurosamente si las medidas punteras de física de sabor leptónico están apuntando hacia una nueva violación fuerte de una simetría de la naturaleza.

Contents

Resumen	i
List of publications	1
List of abbreviations	3
1 Introduction	5
2 The Standard Model and the neutrino path beyond it	9
2.1 The Standard Model of Particle Physics: formalism	9
2.1.1 Spontaneous symmetry breaking: fermion masses and mixing	11
2.1.2 CP violation and global symmetries	13
2.2 Neutrino phenomenology	16
2.2.1 Massive neutrinos	17
2.2.2 Charged current interaction Lagrangian	18
2.2.3 Neutrino flavour oscillations	19
2.2.4 Flavour transitions in matter	22
2.2.5 Leptonic CP violation as a consequence of neutrino masses	26
2.3 Summary	26
3 Three-neutrino fit to oscillation experiments: framework	28
3.1 Solar neutrinos	29
3.1.1 Analysis and interpretation of solar neutrino data	32
3.2 Atmospheric neutrinos	34
3.3 Reactor neutrinos	36
3.4 Accelerator neutrinos	40
3.4.1 Simulation of long baseline accelerator experiments	44
3.5 Summary	49
4 Three-neutrino fit to oscillation data: results	50
4.1 Global fit as of November 2016	50
4.1.1 Global analysis: determination of oscillation parameters	50
4.1.2 Issues in the analysis	55
4.1.3 Monte Carlo evaluation of confidence levels for θ_{23} , δ_{CP} and ordering	65
4.1.4 Conclusions	72
4.2 Results on δ_{CP} : from 2016 to present	73
4.2.1 November 2017 update	73
4.2.2 January 2018 update	75

4.2.3	November 2018 update	75
4.2.4	July 2019 update	78
4.3	Summary and conclusions	78
5	Beyond the three-neutrino paradigm: framework	84
5.1	Formalism	84
5.1.1	Neutrino oscillations in the presence of NSI	86
5.2	Leptonic CP violation beyond the three-neutrino paradigm	87
5.3	The generalised mass ordering degeneracy	90
5.4	Summary	91
6	Beyond the three-neutrino paradigm: fit to oscillation data	93
6.1	CP-conserving analysis: bounds on NSI moduli	94
6.1.1	Formalism	94
6.1.2	Analysis of solar and KamLAND data	97
6.1.3	Results of the global oscillation analysis	102
6.1.4	Summary	110
6.2	General analysis: robustness of LBL accelerator experiments under NSI	111
6.2.1	Analysis framework	112
6.2.2	Results	114
6.2.3	Summary	119
6.3	Summary and conclusions	120
7	COHERENT constraint of beyond three-neutrino scenarios	122
7.1	Analysis of COHERENT data	123
7.1.1	Coherent elastic neutrino-nucleus scattering	123
7.1.2	Implementation of the COHERENT experiment	126
7.1.3	Results: Fit to COHERENT data	135
7.1.4	Summary	138
7.2	Combining COHERENT and oscillation data	139
7.2.1	Including COHERENT in the CP-conserving analysis of Section 6.1	139
7.2.2	Including COHERENT in the CP violation and mass ordering analysis of Section 6.2	144
7.3	Future prospects: coherent elastic neutrino-nucleus scattering at the European Spallation Source	148
7.4	Summary and conclusions	152
8	Conclusions	154
	List of Figures	163
	List of Tables	173
	References	175

List of publications

The original contents of this thesis are based on the following publications:

1. I. Esteban, M. C. Gonzalez-Garcia, M. Maltoni, I. Martinez-Soler, and T. Schwetz, “Updated fit to three neutrino mixing: exploring the accelerator-reactor complementarity”, *JHEP* **01** (2017) 087, [arXiv:1611.01514 \[hep-ph\]](#).
2. I. Esteban, M. C. Gonzalez-Garcia, M. Maltoni, I. Martinez-Soler, and J. Salvado, “Updated Constraints on Non-Standard Interactions from Global Analysis of Oscillation Data”, *JHEP* **08** (2018) 180, [arXiv:1805.04530 \[hep-ph\]](#).
3. I. Esteban, M. C. Gonzalez-Garcia, A. Hernandez-Cabezudo, M. Maltoni, and T. Schwetz, “Global analysis of three-flavour neutrino oscillations: synergies and tensions in the determination of θ_{23} , δ_{CP} , and the mass ordering”, *JHEP* **01** (2019) 106, [arXiv:1811.05487 \[hep-ph\]](#).
4. I. Esteban, M. C. Gonzalez-Garcia, and M. Maltoni, “On the Determination of Leptonic CP Violation and Neutrino Mass Ordering in Presence of Non-Standard Interactions: Present Status”, *JHEP* **06** (2019) 055, [arXiv:1905.05203 \[hep-ph\]](#).
5. D. Baxter *et al.*, “Coherent Elastic Neutrino-Nucleus Scattering at the European Spallation Source”, *JHEP* **02** (2020) 123, [arXiv:1911.00762 \[physics.ins-det\]](#).
6. P. Coloma, I. Esteban, M. C. Gonzalez-Garcia, and M. Maltoni, “Improved global fit to Non-Standard neutrino Interactions using COHERENT energy and timing data”, *JHEP* **02** (2020) 023, [arXiv:1911.09109 \[hep-ph\]](#).
7. I. Esteban, M. Gonzalez-Garcia and M. Maltoni, “On the effect of NSI in the present determination of the mass ordering”, [arXiv:2004.04745 \[hep-ph\]](#).

The following publications have been developed in parallel to the content of this thesis, although they have not been included in this dissertation:

1. I. Esteban, J. Lopez-Pavon, I. Martinez-Soler and J. Salvado, “Looking at the axionic dark sector with ANITA”, *Eur. Phys. J.* **C80** no. 3, (2020) 259, [arXiv:1905.10372 \[hep-ph\]](#).
2. M. Dentler, I. Esteban, J. Kopp and P. Machado, “Decaying Sterile Neutrinos and the Short Baseline Oscillation Anomalies”, [arXiv:1911.01427 \[hep-ph\]](#).

List of abbreviations

BSM	Beyond the Standard Model
CEνNS	Coherent elastic neutrino-nucleus scattering
CP	Charge Parity
ESS	European Spallation Source
IO	Inverted ordering
LBL	Long baseline
NO	Normal ordering
NSI	Non-Standard Interactions
NSI-CC	Charged Current Non-Standard Interactions
NSI-NC	Neutral Current Non-Standard Interactions
QF	Quenching Factor
SM	Standard Model
SNS	Spallation Neutron Source

Chapter 1

Introduction

I wish to establish some sort of system, not guided by chance but by some sort of definite and exact principle.

— Dmitri Ivanovich Mendeleev

*El microcosmos de la física moderna
—después de muerto me basta ser electrón—*

— Blas de Otero

Throughout the centuries, the most ambitious quest of fundamental physics, and thus of fundamental science, has been to understand Nature at its most basic level. The crusade began in the 19th century, interpreting the mass ratios in chemical reactions as indicatives of an underlying structure — atoms [48]. The early atomic theory was then complemented by scattering experiments that explored the electromagnetic properties of atoms in the early 20th century [49–51]. Startlingly, these experiments showed the existence of even more fundamental particles: electrons and a nucleus that, eventually, was observed to be composed of protons and neutrons.

And thus the picture seemed complete, but the exploration of cosmic rays led to discovering an unexpected zoo of new particles and interactions. Once again, their properties were understood in terms of various underlying structures that were further explored and eventually checked at particle colliders. And so a consistent picture emerged during the second half of the 20th century: the Standard Model of Particle Physics (SM) [52–57].

Neutrinos play a special role in the construction of the SM. As a start, they are the most elusive elementary particles we have detected. First proposed by Wolfgang Pauli to account for energy conservation in nuclear beta decays [7], they were back then deemed as impossible to detect. The reason was their low interaction cross section: the penetrating power in solid matter of neutrinos emitted in beta decay is around 10^4 light years [8]. Therefore, it was 26 years after their existence was proposed that neutrinos were first directly observed in an underground experiment carried out by C.L. Cowan and F. Reines [9].

The observed properties of neutrinos were in accordance with the predictions of the SM. On the one hand, neutrinos were introduced in the model minimally, just to explain their interactions. As will be discussed in Chapter 2, there is no way to provide neutrinos with a mass consistent with the symmetries of the model without introducing new degrees of freedom. Thus, the SM predicted neutrinos to be exactly massless, as confirmed by bounds from direct kinematic measurements [10].

On the other hand, the same mathematical structure forbidding neutrino masses also predicts that their flavour (identified with the charged lepton generated along with neutrino production or detection) must be conserved. Early neutrino experiments confirmed this picture, too [11].

But paradigms in fundamental physics seem to hardly survive more than five decades. At the end of the 20th century, experiments studying neutrinos coming from the Sun and cosmic rays hitting the atmosphere revealed that these particles can change their flavour [12–18], behaving in a way that the SM explicitly forbids. The quest for understanding the properties of neutrinos, which may reveal the next underlying structure of Nature, has since then led thousands of scientists. The scenario when this thesis was initiated was driven by the latest experimental surprise that neutrinos provided: the initial hints towards their strong violation of the particle-antiparticle symmetry.

CP violation

One of the deepest mysteries of current science, which may lead us to a more precise theory of Nature, is the matter-antimatter asymmetry of the Universe [19,20]. Antimatter arises naturally as follows: interactions in the SM are mediated by spin-1 particles with an associated gauge symmetry. Describing particles charged under these interactions requires complex-valued fields, because gauge transformations modify their phase. Thus, the amount of degrees of freedom doubles. An immediate consequence is the existence of antimatter, that is, particles with identical kinematic properties, but with opposite charges under any gauge interaction. As a result, particles and antiparticles can efficiently annihilate into the interaction mediators.

Assuming the Hot Big Bang model, all the matter in the Universe was at some point in thermal equilibrium, i.e., its abundance only depended on its mass. Thus, equal amounts of matter and antimatter should have been present, which by today would have annihilated, leaving a Universe only filled with radiation. Our existence therefore calls for an interaction that distinguishes between matter and antimatter, creating more of the former out of thermal equilibrium [21].

Naively, distinguishing between matter and antimatter would just require that the interaction violates the charge conjugation symmetry C . But this is not enough, because particles also have one additional internal degree of freedom: helicity. And so if an interaction violates C but conserves CP , the combined action of C and space inversion — or parity — P , it will create the same amount of particles with a given helicity as of antiparticles with the opposite helicity. Since, as far as we know, elementary particles have no more internal degrees of freedom, distinguishing between matter and antimatter only requires that there must exist an interaction that violates C and CP [21]. The weak interaction maximally violates C , but an interaction violating CP as well is more involved.

In the SM, such an interaction exists in the quark sector as long as there are three particle generations. Unfortunately, its magnitude is not big enough to generate the particle-antiparticle asymmetry of the Universe [22]. However, the new physics inducing neutrino flavour transitions is currently showing a hint for rather large CP violation. Characterising the statistical significance, robustness and physical origin of that hint is the main goal that this thesis pursues.

Outline of this thesis

To put the aforementioned problem in context, Chapter 2 overviews the basic properties of the SM relevant for neutrino interactions and CP violation. In addition, it explores how the model can be extended to include neutrino masses and leptonic mixing, and how these naturally explain the observed neutrino flavour transitions. Interestingly, leptonic mixing among three generations opens the possibility for CP violation. Thus, neutrino masses would not only be our

first laboratory evidence for physics beyond the SM (BSM), but also a potentially large source of particle-antiparticle asymmetry.

But physics, as any science, is to be founded upon experimental data. In order to empirically pin down and parametrise the mechanism responsible for neutrino flavour transitions, a vast experimental programme (overviewed in Chapter 3) has been ongoing for the last three decades. It began with the precise detection of flavour transitions in solar [23–31] and atmospheric [18, 32, 33] neutrinos. These were later confirmed with artificial neutrino beams coming from nuclear reactors [34] and particle accelerators [35, 36]. After several nuclear reactor neutrino experiments measured the last leptonic mixing angle [37–39], three questions remained experimentally unanswered: the octant of the mixing angle driving atmospheric neutrino flavour transitions, the ordering of the neutrino mass eigenstates, and the existence and magnitude of leptonic CP violation.

To unveil these unknowns, particularly CP violation, there is a rich programme of present [40, 41] and future [42, 43] long baseline (LBL) accelerator neutrino experiments. In these experiments, a beam of accelerated protons hits a fixed target, generating pions that, after decaying, give rise to a neutrino beam. This neutrino beam, originally mostly of muon flavour, is detected in muon and electron flavours after travelling for several hundred kilometres. In particular, the electron neutrino appearance channels addresses the three open questions mentioned above.

At the beginning of the development of this thesis, the LBL accelerator neutrino experiment $\text{NO}\nu\text{A}$ released its first data. To obtain a global picture, Chapter 4 combines it with the results of other relevant neutrino experiments. The status of leptonic mixing and CP violation is quantitatively assessed. In addition, it is also checked that the Gaussian limit usually assumed in statistical analyses is a good approximation to evaluate the significance of leptonic CP violation. Then, the evolution of this significance as LBL accelerator neutrino experiments kept releasing data is summarised. The chapter finishes with the global status of leptonic mixing as of the completion of this thesis. Overall, the results in this chapter are based on the published works [1] and [3], as well as on the updates in Refs. [44–46].

As the unknowns start getting clarified, the data points towards maximal CP violation. This hint, though in slight tension with $\text{NO}\nu\text{A}$ data, is driven by an excess of electron neutrino appearance events in the LBL accelerator experiment T2K. In the three massive neutrino paradigm and with the other leptonic mixing parameters accurately measured by different experiments, the excess can only be accommodated by large CP violation.

Nevertheless, three massive neutrinos is just a minimal extension of the SM: other new physics could be present, masking the results as direct leptonic CP violation has not yet been conclusively observed. Because of that, Chapter 5, partly based on the published work [4], overviews the possible new physics entering neutrino flavour transition experiments. The scenario that is less bounded by other experiments, neutral current Non-Standard Interactions (NSI) among neutrinos and matter, affects neutrino flavour transitions by modifying neutrino coherent scattering with the traversed medium. NSI could introduce new degeneracies and sources of CP violation, whose formalism is overviewed in that chapter. Physically, they are generated by new interactions among neutrinos and matter mediated by potentially light particles. Nevertheless, in this work we adopt an agnostic point of view and study the phenomenological consequences of NSI models regardless of their origin.

In Chapter 6, based on the published works [2] and [4], these models are confronted with data. Due to the large parameter space involved, first just CP-conserving NSI (i.e., their moduli) are explored. Current bounds are evaluated, as well as the synergies and complementarity among different experiments. Thanks to the experiments working with various neutrino energies and travelled distances, the determination of leptonic mixing parameters is found to be quite robust. Thus, it is possible to move on and evaluate the current sensitivity to leptonic CP violation

assuming the most generic CP-violating NSI are present. CP violation induced by neutrino masses and leptonic mixing is found to be quite robust, due to the large amount of neutrino flavour transition data collected along three decades.

Nevertheless, NSI introduce a degeneracy that is exact at the flavour transition probability level. This degeneracy reduces the sensitivity to leptonic CP violation. Although currently the effect is not dramatic due to the rather limited experimental sensitivity, the next generation LBL accelerator experiments [42, 43] are aimed at precision measurements that could be severely affected. Because of that, it would be highly beneficial to independently constraint NSI.

In principle, tight constraints could come from neutral current scattering experiments or from precise electroweak measurements with charged leptons. However, NSI affect neutrino propagation by modifying coherent scattering with the traversed medium, a zero momentum transfer process to be compared with the typical $\mathcal{O}(\text{GeV})$ momentum transfers in other experiments. If the particle mediating NSI is quite light, its effects would be suppressed for high momentum transfers, and bounds from other experiments would be avoided.

Luckily, in the last years the COHERENT experiment [47] has provided independent constraints on NSI. This experiment makes use of the well-understood neutrino flux copiously produced by pion decay at rest in neutron spallation sources. COHERENT measures neutral current coherent neutrino-nucleus elastic scattering, a process in which a neutrino interacts coherently with an entire atomic nucleus. This happens when the exchanged momentum is of the order of the inverse nuclear size, $\mathcal{O}(\text{MeV})$. Due to the low momentum transfers, this process is quite sensitive to NSI induced by light mediators. In Chapter 7, based on the published works [4] and [5], the data from the COHERENT experiment is analysed and integrated into the global analyses from Chapter 6. This requires a rigorous understanding of the procedure for analysing COHERENT data. Particular attention is paid to how the results depend on the assumptions about the experiment background, nuclear structure, and detector response. Combining COHERENT data with flavour transition experiments unveils its incipient role in increasing the robustness of their interpretation.

These first results could be greatly improved by increasing the statistics of the signal and/or by performing the measurements with different nuclei sensitive to different NSI models. For that, the European Spallation Source is an ideal future facility. It will produce a neutrino beam one order of magnitude more intense than the one used at COHERENT, and as it is still under construction there is potential space for various modern detectors. Its prospects for bounding NSI, based on the published work [6], are also explored in Chapter 7.

In summary, this thesis deals with the current experimental hint for large CP violation in the leptonic sector. It first quantifies its global significance, and then moves on to checking its robustness against the framework in which the experimental data is interpreted. For that, complementary experiments on neutrino-nucleus coherent scattering play, and will keep on playing in the future, a significant role. Thus, a global approach is taken to rigorously assess whether cutting-edge leptonic flavour measurements are pointing towards a new strong violation of a symmetry of Nature.

Chapter 2

The Standard Model and the neutrino path beyond it

The current paradigm for understanding the basic constituents of Nature, and the laws through which they interact, is the SM of Particle Physics. In this chapter, we will overview the formalism of the SM, and how it implements CP violation, in order to set convention and unify notation. In addition, as mentioned in the introduction, neutrino flavour transitions constitute a laboratory evidence for BSM physics. We will explore why this is so, and how neutrino masses can explain the violation of leptonic flavour, that until the late XXth century was considered to be a good symmetry of Nature.

2.1 The Standard Model of Particle Physics: formalism

Just because things get a little dingy at the subatomic level doesn't mean all bets are off.

— Murray Gell-Mann

The mathematical formalism of the SM, Quantum Field Theory, can be considered an abstraction of the de Broglie hypothesis: all particles have an associated wave. This wave is represented by a field that, as any quantum observable, is actually an operator acting on a Hilbert space.

The matter content of the SM consists of 45 chiral fermions of spin- $\frac{1}{2}$. These fields represent all fermions that have ever been observed:

- The left-handed (L) and right-handed (R) electron, muon and tau: $e_{L/R}$, $\mu_{L/R}$ and $\tau_{L/R}$. These are the *charged leptons*.
- The left-handed electron, muon, and tau neutrinos: $\nu_{e,L}$, $\nu_{\mu,L}$ and $\nu_{\tau,L}$. These are the *neutral leptons*.
- The left-handed and right-handed quarks, each of them in three different colours i : the up quark, $u_{L/R}^i$; the down quark, $d_{L/R}^i$; the charm quark, $c_{L/R}^i$; the strange quark, $s_{L/R}^i$; the top quark, $t_{L/R}^i$; and the bottom quark, $b_{L/R}^i$.

The interactions among these particles can be constructed by first noticing that they can be arranged in 15 multiplets of the symmetry group $G_{\text{SM}} = SU(3)_C \times SU(2)_L \times U(1)_Y$ [52–57]

where the subindexes C, L, Y refer to colour, left-handedness, and hypercharge respectively. The particular multiplets and irreducible representations they fall in are summarised in Table 2.1.

$(SU(3), SU(2))_{U(1)}$					
$(\mathbf{1}, \mathbf{2})_{-\frac{1}{2}}$		$(\mathbf{3}, \mathbf{2})_{\frac{1}{6}}$		$(\mathbf{1}, \mathbf{1})_{-1} \quad (\mathbf{3}, \mathbf{1})_{\frac{2}{3}} \quad (\mathbf{3}, \mathbf{1})_{-\frac{1}{3}}$	
$L_L^e = \begin{pmatrix} \nu_e \\ e \end{pmatrix}_L$	$Q_L^{1,i} = \begin{pmatrix} u^i \\ d^i \end{pmatrix}_L$	e_R	u_R^i	d_R^i	
$L_L^\mu = \begin{pmatrix} \nu_\mu \\ \mu \end{pmatrix}_L$	$Q_L^{2,i} = \begin{pmatrix} c^i \\ s^i \end{pmatrix}_L$	μ_R	c_R^i	s_R^i	
$L_L^\tau = \begin{pmatrix} \nu_\tau \\ \tau \end{pmatrix}_L$	$Q_L^{3,i} = \begin{pmatrix} t^i \\ b^i \end{pmatrix}_L$	τ_R	t_R^i	b_R^i	

Table 2.1: Multiplets and irreducible representations in which SM fermions fall. For the $SU(3)$ and $SU(2)$ groups, 1, 2 and 3 denote the singlet, doublet and triplet representations. For $U(1)$, a subindex Y , known as the hypercharge, indicates that the fermion f transforms as $f \rightarrow e^{iY\theta} f$, where θ is a real number. The different fermions are also known as *flavours*.

When the symmetry transformations in G_{SM} are allowed to be position-dependent, additional Lorentz-vector fields (known as gauge fields) have to be introduced for each of the subgroups in G_{SM} . These fields will then mediate interactions among the fermions. Under the assumption of renormalisability, i.e. that the theory should be predictive at any energy scale, the most general Lagrangian — from which the Heisenberg equations of motion for the fields follow — one can write is

$$\mathcal{L}_{\text{fermion}} + \mathcal{L}_{\text{gauge}} = \sum_f \bar{f}(i\gamma^\mu D_\mu)f - \frac{1}{4} \sum_i (F_{\mu\nu}^i)^2, \quad (2.1)$$

where the sum runs over the 15 fermion multiplets f in Table 2.1 and γ^μ are the Dirac γ matrices. $D_\mu = \partial_\mu - ig_s \sum_i G_\mu^i t^i - ig \sum_i W_\mu^i \tau^i - ig' Y B_\mu$ is the so-called covariant derivative, where

- g_s, g and g' are the coupling constants of the interactions associated with the groups $SU(3)_C, SU(2)_L$ and $U(1)_Y$ respectively. The former corresponds to the strong interaction among quarks, whereas the others correspond to the electroweak interactions.
- G^i for $i = 1, 8, W^i$ for $i = 1, 3$ and B are, correspondingly, the $SU(3), SU(2)$, and $U(1)$ gauge fields that mediate the corresponding interactions.
- t^i for $i = 1, 8$ and τ^i for $i = 1, 3$ are the $SU(3)$ and $SU(2)$ generators in the representation to which f belongs, and Y is its hypercharge.

With these definitions the electric charge operator, Q is

$$Q = \tau_3 + Y. \quad (2.2)$$

Finally, the last term is the square of the gauge field tensor, which we have compactly denoted as $\sum_i (F_{\mu\nu}^i)^2$, with:

$$\begin{aligned} \sum_i (F_{\mu\nu}^i)^2 \equiv & \sum_{i=1}^8 (\partial_\mu G_\nu^i - \partial_\nu G_\mu^i + g_s f^{ijk} G_\mu^j G_\nu^k)^2 + \\ & \sum_{i=1}^3 (\partial_\mu W_\nu^i - \partial_\nu W_\mu^i + g \varepsilon^{ijk} W_\mu^j W_\nu^k)^2 + (\partial_\mu B_\nu - \partial_\nu B_\mu)^2. \end{aligned} \quad (2.3)$$

f^{ijk} are the structure constants of the $SU(3)$ group, and in each term the square of each tensor $T_{\mu\nu}$ has to be understood as the contraction $T_{\mu\nu}T^{\mu\nu}$.

The SM also contains a scalar field, the Higgs field Φ , a singlet under $SU(3)$ that transforms as a doublet under $SU(2)$ and has hypercharge $\frac{1}{2}$. Its gauge invariant Lagrangian reads:

$$\mathcal{L}_{\text{Higgs}} = D_\mu \Phi D^\mu \Phi - \mu^2 |\Phi|^2 - \lambda |\Phi|^4, \quad (2.4)$$

where λ and μ are constants.

Finally, the most general renormalisable Lagrangian also contains Yukawa interactions among the Higgs field and the fermions

$$\mathcal{L}_{\text{Yukawa}} = - \sum_{\alpha\beta} Y_{\alpha\beta}^u \overline{Q}_L^\alpha \Phi u_R^\beta - \sum_{\alpha\beta} Y_{\alpha\beta}^d \overline{Q}_L^\alpha \tilde{\Phi} d_R^\beta - \sum_{\alpha\beta} Y_{\alpha\beta}^e \overline{L}_L^\alpha \tilde{\Phi} e_R^\beta + \text{h.c.}, \quad (2.5)$$

where $\tilde{\Phi} = i\tau_2 \Phi^*$ and τ_2 is the second Pauli matrix, Q_L^α is a quark $SU(2)$ doublet ($\alpha \in \{1, 2, 3\}$), u_R^β is a right-handed up-type quark ($\beta \in \{1, 2, 3\} \equiv \{u, c, t\}$), d_R^β is a right-handed down-type quark ($\beta \in \{1, 2, 3\} \equiv \{d, s, b\}$), L_L^α is a lepton $SU(2)$ doublet ($\alpha \in \{e, \mu, \tau\}$), and e_R^β is a right-handed charged lepton ($\beta \in \{e, \mu, \tau\}$). Y^u , Y^d and Y^e are 3×3 matrices. h.c. refers to the Hermitian conjugate.

The model presented above, built throughout more than 50 years as a myriad of experimental data suggested and confirmed its different pieces, is currently able to explain almost all experimental results in the laboratory. As we shall see, though, data from neutrino experiments challenge it as the final description of Nature.

2.1.1 Spontaneous symmetry breaking: fermion masses and mixing

Before immersing in the experimental data that defies the validity of the SM, it is important to understand the consequences of its scalar sector [58–60]. The Lagrangian in Eq. (2.4) corresponds to a scalar potential energy density

$$V(\phi) = \mu^2 |\Phi|^2 + \lambda |\Phi|^4, \quad (2.6)$$

that, for $\mu^2 < 0$, does not have its minimum at $\Phi = 0$. On the contrary, there exist a continuous of degenerate minima fulfilling

$$|\Phi_{\text{min}}|^2 = -\frac{\mu^2}{2\lambda} \equiv \frac{v^2}{2}. \quad (2.7)$$

All these minima are related by a G_{SM} transformation, so when choosing a particular one above which the theory is quantised, the G_{SM} symmetry is *spontaneously* broken.

As seen in Eq. (2.2), the electromagnetic symmetry group, $U(1)_{em}$, is part of G_{SM} and, since electromagnetism is a good symmetry of Nature to all tested energies, the vacuum of the theory must leave that subgroup unbroken. With the chosen representation for Φ this is accomplished for $\Phi_{\text{min}} = \frac{1}{\sqrt{2}} \begin{pmatrix} 0 & v \end{pmatrix}^T$. So the quantum field for the scalar doublet can be written as

$$\Phi(x) = \frac{1}{\sqrt{2}} \begin{pmatrix} 0 \\ v + h(x) \end{pmatrix} \mathbf{e}^{-i \sum_{i=1}^3 \tau_i \xi_i(x)}. \quad (2.8)$$

where the three real fields ξ_i are the would-be Goldstone bosons associated with the generators of the broken subgroup. They can be gauged away by an $SU(2)$ gauge transformation, so the only quantum field operator whose excitations can be detected as particles is $h(x)$, the field of

the Higgs boson particle discovered in 2012 [61, 62]. In what follows we choose to work in the so-called unitary gauge [63], where the doublet scalar field contains only the physical particle degrees of freedom $\Phi(x) = \frac{1}{\sqrt{2}} \begin{pmatrix} 0 \\ v + h(x) \end{pmatrix}$.

Rewriting the entire Lagrangian in terms of v and h gives a very rich phenomenology. Regarding Eq. (2.4), the covariant derivative term generates masses for three of the four gauge bosons in the $SU(2) \times U(1)$ part of G_{SM} : the W bosons, $W_\mu^\pm = \frac{1}{\sqrt{2}}(W_\mu^1 \mp iW_\mu^2)$, that acquires a mass $m_W = \frac{1}{2}gv$; and the Z boson, $Z_\mu = \cos\theta_W W_\mu^3 - \sin\theta_W B_\mu$, whose mass is $m_Z = \frac{1}{2}\frac{gv}{\cos\theta_W}$. Here, $\theta_W = \arctan \frac{g'}{g}$ is the so-called Weinberg angle. A fourth linear combination, $A_\mu = \sin\theta_W W_\mu^3 + \cos\theta_W B_\mu$, remains massless and corresponds to the photon of electrodynamics.

Once the gauge bosons are written in the mass basis, Eq. (2.1) gives their interactions with fermions. The interactions involving W and Z bosons, the only mediators that interact with neutrinos, are given by

$$\begin{aligned} \mathcal{L}_{\text{int}}^{\text{weak}} = & -\frac{g}{\sqrt{2}}W_\mu^+ (\bar{\nu}_{e,L} \quad \bar{\nu}_{\mu,L} \quad \bar{\nu}_{\tau,L}) \gamma^\mu \begin{pmatrix} e_L \\ \mu_L \\ \tau_L \end{pmatrix} - \frac{g}{\sqrt{2}}W_\mu^- (\bar{u}_L \quad \bar{c}_L \quad \bar{t}_L) \gamma^\mu \begin{pmatrix} d_L \\ s_L \\ b_L \end{pmatrix} + \text{h.c.} \\ & - \frac{g}{\cos\theta_W} Z_\mu \sum_f [(T_3 - Q_f \sin^2\theta_W) \bar{f}_L \gamma^\mu f_L - Q_f \sin^2\theta_W \bar{f}_R \gamma^\mu f_R], \end{aligned} \quad (2.9)$$

where T_3 is the 3 component of the *weak isospin* of the fermion f (i.e., its eigenvalue for τ_3 of $SU(2)_L$) and $Q_f = T_3 + Y$ its electric charge. The first terms are the *charged current* interactions, and the second ones the *neutral current* interactions.

Finally, Eq. (2.5) generates, after spontaneous symmetry breaking, masses for all charged fermions. Defining the following matrices

$$M_u = \frac{v}{\sqrt{2}}Y^u, \quad (2.10) \quad M_d = \frac{v}{\sqrt{2}}Y^d, \quad (2.11) \quad M_e = \frac{v}{\sqrt{2}}Y^e, \quad (2.12)$$

the terms in Eq. (2.5) that do not involve the Higgs h read

$$\begin{aligned} \mathcal{L}_{\text{Yukawa}}^0 = & -(\bar{u}_L \quad \bar{c}_L \quad \bar{t}_L) M_u \begin{pmatrix} u_R \\ c_R \\ t_R \end{pmatrix} - (\bar{d}_L \quad \bar{s}_L \quad \bar{b}_L) M_d \begin{pmatrix} d_R \\ s_R \\ b_R \end{pmatrix} \\ & - (\bar{e}_L \quad \bar{\mu}_L \quad \bar{\tau}_L) M_e \begin{pmatrix} e_R \\ \mu_R \\ \tau_R \end{pmatrix} + \text{h.c.} \end{aligned} \quad (2.13)$$

After unitary diagonalisation, these terms lead to fermion masses. However, since M are not in general Hermitian matrices, two distinct unitary matrices V_L and V_R are needed to diagonalise them:

$$V_L^u M_u V_R^{u\dagger} = \begin{pmatrix} m_u & 0 & 0 \\ 0 & m_c & 0 \\ 0 & 0 & m_t \end{pmatrix}, \quad (2.14)$$

$$V_L^d M_d V_R^{d\dagger} = \begin{pmatrix} m_d & 0 & 0 \\ 0 & m_s & 0 \\ 0 & 0 & m_b \end{pmatrix}, \quad (2.15)$$

$$V_L^e M_e V_R^{e\dagger} = \begin{pmatrix} m_e & 0 & 0 \\ 0 & m_\mu & 0 \\ 0 & 0 & m_\tau \end{pmatrix}. \quad (2.16)$$

After this transformation, the mass eigenstates are given by ¹

$$(u \ c \ t)_{\text{mass}}^T = V_L^u (u_L \ c_L \ t_L)^T + V_R^u (u_R \ c_R \ t_R)^T, \quad (2.17)$$

$$(d \ s \ b)_{\text{mass}}^T = V_L^d (d_L \ s_L \ b_L)^T + V_R^d (d_R \ s_R \ b_R)^T, \quad (2.18)$$

$$(e \ \mu \ \tau)_{\text{mass}}^T = V_L^e (e_L \ \mu_L \ \tau_L)^T + V_R^e (e_R \ \mu_R \ \tau_R)^T. \quad (2.19)$$

Thus, in principle, the fermion interaction eigenstates, i.e., the fields that through the terms in Eq. (2.1) interact with the gauge bosons; and mass eigenstates, i.e., the fields that propagate; are different. However, for interactions that do not change the fermion flavour, the interaction term will only get a term $V_L V_L^\dagger$ or $V_R V_R^\dagger$, equal to $\mathbb{1}_{3 \times 3}$ because of unitarity. The only difference among interaction and mass eigenstates can thus appear in the only flavour-changing interactions in the SM, i.e., the charged current interactions with the W boson. Indeed, for the quark sector one gets, in the mass basis,

$$\mathcal{L}_{CC}^{\text{quark}} = -\frac{g}{\sqrt{2}} W_\mu^+ (\bar{u} \ \bar{c} \ \bar{t}) V^{\text{CKM}} \gamma^\mu P_L \begin{pmatrix} d \\ s \\ b \end{pmatrix} + \text{h.c.}, \quad (2.20)$$

where $V^{\text{CKM}} = V_L^u V_L^{d\dagger}$ is the CKM mixing matrix [64, 65], and $P_L = \frac{1-\gamma_5}{2}$ is a chiral projector.

In the lepton sector, however, there is nothing forbidding the unphysical rotation

$$\begin{pmatrix} \nu_{e,L} \\ \nu_{\mu,L} \\ \nu_{\tau,L} \end{pmatrix} \rightarrow V_L^{e\dagger} \begin{pmatrix} \nu_{e,L} \\ \nu_{\mu,L} \\ \nu_{\tau,L} \end{pmatrix}, \quad (2.21)$$

under which the entire interaction Lagrangian, Eq. (2.1), remains invariant when switching to the mass basis. Therefore, there is no mixing in the leptonic charged currents. Notice also that the symmetry above is incompatible with neutrino masses, as these mix left-handed and right-handed components of fermions. As we will see, the fact that the most general renormalisable Lagrangian compatible with the symmetry G_{SM} turns out to be invariant under the transformation (2.21) is intimately related not only with neutrino masses, but also with the sources of particle-antiparticle asymmetry in the leptonic sector.

2.1.2 CP violation and global symmetries

As discussed in the introduction, the matter-antimatter asymmetry of the universe calls for an interaction that violates CP, the combined action of charged conjugation C and parity P.

Mathematically, the CP conjugate of a Lagrangian changes all parameters into their complex conjugates. And so to have CP violation there must be complex parameters in the Lagrangian of the theory. In the SM, the only possible complex parameters are the matrices in Eq. (2.5).

¹In order to make the expressions more compact, we often write the vector containing three fields as a *transposed* 3-vector. Notice that the transpose operation acts on the 3-vector space but not on the field components, this is

we denote $(\psi_1 \ \psi_2 \ \psi_3)^T \equiv \begin{pmatrix} \psi_1 \\ \psi_2 \\ \psi_3 \end{pmatrix}$.

However, their observability is not immediate, because as has been noticed for the neutrinos, there exist global symmetry transformations that can remove these parameters from the theory.

This problem is better formulated as follows [66–69]: the SM Lagrangian, i.e., the most general renormalisable Lagrangian that can be built with the SM fermion content and gauge group, is accidentally invariant under a

$$SU(3)_{Q_L} \times SU(3)_{u_R} \times SU(3)_{d_R} \times SU(3)_{L_L} \times SU(3)_{e_R} \times U(1)_{B-L} \quad (2.22)$$

global symmetry [70, 71]. This symmetry, exact both at the classical and quantum levels, acts as follows over the fermion fields

$$SU(3)_{Q_L} : \quad (Q_L^1 \quad Q_L^2 \quad Q_L^3)^T \rightarrow P_{Q_L} (Q_L^1 \quad Q_L^2 \quad Q_L^3)^T \quad P_{Q_L} \in SU(3), \quad (2.23)$$

$$SU(3)_{u_R} : \quad (u_R \quad c_R \quad t_R)^T \rightarrow P_{u_R} (u_R \quad c_R \quad t_R)^T \quad P_{u_R} \in SU(3), \quad (2.24)$$

$$SU(3)_{d_R} : \quad (d_R \quad s_R \quad b_R)^T \rightarrow P_{d_R} (d_R \quad s_R \quad b_R)^T \quad P_{d_R} \in SU(3), \quad (2.25)$$

$$SU(3)_{L_L} : \quad (L_L^e \quad L_L^\mu \quad L_L^\tau)^T \rightarrow P_{L_L} (L_L^e \quad L_L^\mu \quad L_L^\tau)^T \quad P_{L_L} \in SU(3), \quad (2.26)$$

$$SU(3)_{e_R} : \quad (e_R \quad \mu_R \quad \tau_R)^T \rightarrow P_{e_R} (e_R \quad \mu_R \quad \tau_R)^T \quad P_{e_R} \in SU(3), \quad (2.27)$$

$$U(1)_{B-L} : \quad f \rightarrow e^{i\delta(B-L)} f \quad \delta \in \mathbb{R}, \quad (2.28)$$

where f is any fermion, B its baryon number ($\frac{1}{3}$ for quarks and 0 for leptons) and L its lepton number (1 for leptons and 0 for quarks). The symmetry also modifies the Yukawa matrices as

$$Y^u \rightarrow P_{Q_L}^\dagger Y^u P_{u_R}, \quad (2.29)$$

$$Y^d \rightarrow P_{Q_L}^\dagger Y^d P_{d_R}, \quad (2.30)$$

$$Y^e \rightarrow P_{L_L}^\dagger Y^e P_{e_R}. \quad (2.31)$$

Besides, CP acts on the Yukawa matrices as

$$Y \xrightarrow{\text{CP}} Y^*. \quad (2.32)$$

And so CP conjugation is physical if and only if the transformation above is not equivalent to a symmetry in Eq. (2.22). I.e., CP conjugation is physical if and only if there is no set of unitary matrices $\{P_{Q_L}, P_{u_R}, P_{d_R}, P_{L_L}, P_{e_R}\}$ satisfying

$$P_{Q_L}^\dagger Y^u P_{u_R} = Y^{u*}, \quad (2.33)$$

$$P_{Q_L}^\dagger Y^d P_{d_R} = Y^{d*}, \quad (2.34)$$

$$P_{L_L}^\dagger Y^e P_{e_R} = Y^{e*}. \quad (2.35)$$

Now, given a matrix A , its “square” AA^\dagger determines A up to unitary rotations $A \rightarrow AU$. Thus, one can work with the “squares” of the Yukawa matrices, and there is CP conservation if and

only if there exist unitary matrices $\{P_{Q_L}, P_{L_L}\}$ such that

$$P_{Q_L}^\dagger (Y^d Y^{d\dagger}) P_{Q_L} = (Y^d Y^{d\dagger})^* , \quad (2.36)$$

$$P_{Q_L}^\dagger (Y^u Y^{u\dagger}) P_{Q_L} = (Y^u Y^{u\dagger})^* , \quad (2.37)$$

$$P_{L_L}^\dagger (Y^e Y^{e\dagger}) P_{L_L} = (Y^e Y^{e\dagger})^* . \quad (2.38)$$

The condition Eq. (2.38) is trivially satisfied as any Hermitian matrix can be made real by a unitary rotation, simply choosing the unitary rotation that diagonalises it. Therefore, in the SM there is no CP violation in the leptonic sector. This happens because in the lepton sector there is a single flavour matrix, Y^e , whereas in the quark sector there are two, Y^u and Y^d . Indeed, the flavour transformation in Eq. (2.21) is unphysical because there is no “neutrino Yukawa matrix” Y^ν .

Regarding the other two conditions, they can be shown to be equivalent to [66–69]

$$\text{Im Tr} \left[(Y^d Y^{d\dagger})^2 (Y^u Y^{u\dagger})^2 (Y^d Y^{d\dagger}) (Y^u Y^{u\dagger}) \right] = 0 , \quad (2.39)$$

a condition independent of the symmetry transformation (2.22). For the particular case where the transformation is used to switch to the up quark mass basis, the condition reads

$$(m_b^2 - m_s^2)(m_b^2 - m_d^2)(m_s^2 - m_d^2)(m_t^2 - m_c^2)(m_t^2 - m_u^2)(m_c^2 - m_u^2)J = 0 \quad (2.40)$$

where J is the so-called Jarlskog invariant

$$J = \text{Im}[V_{us}^{\text{CKM}} V_{cb}^{\text{CKM}} V_{ub}^{\text{CKM}*} V_{cs}^{\text{CKM}*}] . \quad (2.41)$$

And so in the SM there is only CP violation in quark charged currents, and all CP-violating phenomena are proportional to Eq. (2.40). The experimentally measured value of this quantity ($J = (3.18 \pm 0.15) \times 10^{-5}$ [72]), though, is small enough to explain the matter-antimatter asymmetry of the Universe [22]. The SM is thus craving for an additional source of CP violation. As we shall see at the end of this chapter, neutrinos might provide it.

Particle number conservation laws

The symmetry group introduced in Eq. (2.22) should, because of Noether’s theorem, lead to conservation laws [73]. Notice though that some of the symmetry transformations require modifying the parameters in the Lagrangian as in Eqs. (2.29) to (2.31). Thus, some of the symmetry transformations do not leave the Lagrangian invariant, and therefore Noether’s theorem does not apply to them. Instead, they connect different physically equivalent theories.

To obtain the conservation laws stemming from the symmetry group (2.22), one has to disentangle the symmetry transformations that leave the Lagrangian invariant. An efficient way of doing so is first switching to the fermion mass basis with no leptonic mixing. In there, flavour-mixing symmetry transformations are forbidden because of the mass terms, and so the remaining symmetries are

$$q_\alpha \rightarrow e^{i\delta_\alpha^q} q_\alpha , \quad (2.42)$$

$$l_\alpha \rightarrow e^{i\delta_\alpha^l} l_\alpha , \quad (2.43)$$

$$\nu_\alpha \rightarrow e^{i\delta_\alpha^l} \nu_\alpha , \quad (2.44)$$

where l_α is a charged lepton. Now, the quark rephasings require modifying the CKM matrix

$$V_{\alpha\beta}^{\text{CKM}} \rightarrow e^{-i(\delta_\alpha^q - \delta_\beta^q)} , \quad (2.45)$$

and so the only symmetries that leave the Lagrangian invariant are

$$q_\alpha \rightarrow e^{i\delta^q} q_\alpha \forall \alpha, \quad (2.46)$$

$$l_\alpha \rightarrow e^{i\delta_\alpha^l} l_\alpha, \quad (2.47)$$

$$\nu_\alpha \rightarrow e^{i\delta_\alpha^l} \nu_\alpha. \quad (2.48)$$

Invariance at the quantum level requires $\delta^q + \sum_\alpha \delta_\alpha^l = 0$, and so we are left with 3 independent conservation laws

- The conservation of baryon minus lepton number, $B - L$.
- The conservation of the difference among any pair of lepton flavour numbers. E.g., the conservation of $L_\mu - L_\tau$ and $L_e - L_\mu$.

Nevertheless, as mentioned at the beginning, paradigms in fundamental physics seem to fail after about five decades. And, as we shall see, at the end of the 20th century, these conservation laws were explicitly violated in laboratory experiments.

2.2 Neutrino phenomenology

I have done a terrible thing, I have postulated a particle that cannot be detected.

— Wolfgang Pauli

In the old days, Pauli considered terrible a single undetectable particle. And now, we are not even ashamed by the entire supersymmetric spectrum!

— M. C. Gonzalez-García

As we have seen, the structure of the SM dictates several conservation laws that can be checked in experiments with leptons and, in particular, with neutrinos. The experimental study of these particles played a special role in constructing the SM, as briefly overviewed in the introduction.

Some years after their first detection, it was realised that the nuclear processes that fuel the Sun would emit copious amounts of electron neutrinos that could be detected at Earth [74–76]. When such neutrinos were detected, though, a deficit with respect to the theoretical predictions was systematically observed [12–15, 23–26, 77–80]. Particularly enlightening were the results from the SNO observatory [12–15]: when detecting *electron* neutrinos through charged current interactions a deficit was found. But if neutral current interactions were used to detect *any* neutrino flavour, there was no deficit. In other words, the electron neutrinos were undoubtedly changing their flavour as they propagated between their production point in the Sun and their detection point on the Earth. The leptonic flavours were seen to be violated: there is new physics.

Flavour change of neutrinos had also been observed in experiments detecting neutrinos generated when a cosmic ray hits the atmosphere [16–18]. The ratio among muon and electron neutrinos in these experiments significantly deviated from the expectations. Furthermore, the deviation was seen to be more important for neutrinos that travelled for longer distances.

Since the original discoveries, the effect has been independently confirmed with large statistical significance, both with natural and artificial neutrino sources [23, 28, 29, 31, 36, 38, 39, 81–97]. The relevant experiments will be described in Chapter 3.

2.2.1 Massive neutrinos

The experimental results described above are in direct contradiction with the SM. The reason for the conservation of lepton flavour numbers is the symmetry in Eqs. (2.47) and (2.48), that allows to independently rephase each leptonic flavour. This is not possible in the quark sector, because both up-type and down-type quarks have masses, and mass terms forbid independently rephasing each flavour, thus flavour mixing can be physical in the quark sector. Correspondingly, if neutrinos are massive leptonic flavours can also mix, each of the leptonic flavours will no longer be conserved, and the experiments above may be explained. The mass, however, must be very tiny ($\lesssim \mathcal{O}(\text{eV})$) to avoid entering in conflict with direct searches [10].

Intriguingly, though, the field content and gauge symmetry of the SM may also provide a mechanism for generating neutrino masses provided that we assume that some new physics must exist above a certain energy scale Λ . The Lagrangian introduced in the previous section is based on the assumption of renormalisability, i.e., the theory should give definite predictions up to arbitrarily large energy scales. If we relax this assumption, higher-dimensional operators made of the SM fields and respecting the SM gauge symmetry will enter the Lagrangian suppressed by the scale Λ at which the theory stops being predictive. Interestingly, the lowest order (least suppressed) effective operator that only contains SM fields and is consistent with gauge symmetry is [98]

$$\mathcal{O} = \frac{Z_{\alpha\beta}}{\Lambda} (\overline{L_L^\alpha} \tilde{\Phi}) (\tilde{\Phi}^T L_L^{\beta C}) + \text{h.c.}, \quad (2.49)$$

where $L_L^{\beta C} \equiv C L_L^{\beta C T} = -i\gamma^2 \gamma^0 \overline{L_L^{\beta C T}}$ is the charge conjugated field of the lepton doublet L_L^β (the transpose affects the Dirac indices of each spinor in the doublet). This operator violates total lepton number (and $B - L$) by two units but, being this an accidental symmetry of the SM, there is no reason why a more fundamental theory should conserve it.

After spontaneous symmetry breaking, Eq. (2.49) leads to

$$\mathcal{O} = \frac{Z_{\alpha\beta}^\nu v^2}{2\Lambda} \bar{\nu}_{L\alpha} \nu_{L\beta}^c + \text{h.c.}, \quad (2.50)$$

a term that induces neutrino masses and leptonic mixing. Furthermore, the mass eigenstates are Majorana fermions, i.e., $\nu_M^c = \nu_M$. Its mass is suppressed by Λ , i.e., the lightness of neutrinos is naturally explained by the large value of Λ .

Even though there are a variety of BSM theories that can generate the operator in Eq. (2.49), there is a particularly simple example. In principle, one can add to the theory any number of singlets under its gauge group G_{SM} : since they do not interact through the Lagrangian in Eq. (2.1), they may have easily evaded detection. These particles would be right-handed Weyl fermions with no weak hypercharge, commonly known as sterile neutrinos ν_s . The most general gauge invariant renormalisable Lagrangian one can add to the SM is then [99, 100]

$$-\mathcal{L}_{M_\nu} = \sum_{\substack{i=1, \dots, m \\ \alpha \in \{e, \mu, \tau\}}} Y_{i\alpha}^\nu \bar{\nu}_{si} \tilde{\Phi}^\dagger L_L^\alpha + \frac{1}{2} \sum_{i,j=1}^m M_{Nij} \bar{\nu}_{si} \nu_{sj}^c + \text{h.c.} \quad (2.51)$$

Y^ν and $M_N = M_N^T$ are complex $m \times 3$ and $m \times m$ matrices, respectively.

After electroweak spontaneous symmetry breaking, the first term in Eq. (2.51) generates at low energy a standard, or Dirac, mass term,

$$M_{Di\alpha} \bar{\nu}_{si} \nu_{\alpha,L}, \quad (2.52)$$

with $M_{Di\alpha} = Y_{i\alpha}^\nu \frac{v}{\sqrt{2}}$. This term is similar to the one present for the charged fermions, and with no additional operators gives neutrinos a mass $\sim M_D$.

The second term in Eq. (2.51), however, is more interesting. It has the structure of a Majorana mass term, violating any $U(1)$ charge carried by ν_s ; in particular it breaks lepton number L by two units if L is assigned to ν_s as to make the Dirac mass term L conserving.

The diagonalisation of the whole Lagrangian (2.51) leads to $3 + m$ mass eigenstates ν_M that are Majorana fermions, i.e., $\nu_M^c = \nu_M$. These eigenstates describe free neutrino propagation. In what refers to the eigenvalues, two interesting cases can be distinguished:

- $M_N = 0$: this option is equivalent to imposing *by hand* lepton number conservation in any theory embedding the SM (otherwise, even if $M_N = 0$ at tree level, loop corrections from new physics could induce $M_N \neq 0$ [101]). It allows to rearrange, for $m = 3$, the 6 Majorana eigenstates in 3 Dirac fermions. In this case, there is no natural explanation for the lightness of neutrinos, which would require $Y^\nu \lesssim 10^{-11}$.
- $M_N \gg M_D$: this is expected in SM extensions such as $SO(10)$ GUTs [102–104] or left-right symmetric models [105], where the new physics scale $\sim M_N$ is much larger than the electroweak scale. In this case, the diagonalisation leads to 3 light eigenstates of masses $\sim M_D^2/M_N$, which are mostly left-handed, and m heavy eigenstates of masses $\sim M_N$, which are mostly right-handed. This naturally explains the lightness of neutrinos through what is known as the *see-saw mechanism*: the heavier are the heavy states, the lighter are the light ones.

Indeed, if the Lagrangian (2.51) with $M_N \gg M_D$ is considered, integrating out the heavy eigenstates leads to a Lagrangian of the form (2.49) with $\Lambda \sim M_N$.

2.2.2 Charged current interaction Lagrangian

Besides the mass Lagrangian (2.51), the charged current Lagrangian gets also modified by introducing neutrino masses, leading to flavour mixing as in the quark sector. For $3 + m \equiv n$ neutrino mass eigenstates, in the mass basis this Lagrangian reads

$$-\mathcal{L}_{CC} = \frac{g}{\sqrt{2}} (\bar{e}_L \quad \bar{\mu}_L \quad \bar{\tau}_L) U^{\text{lep}} \begin{pmatrix} \nu_{M1} \\ \nu_{M2} \\ \nu_{M3} \\ \vdots \\ \nu_{Mn} \end{pmatrix} W_\mu^+ - \text{h.c.}, \quad (2.53)$$

where ν_i , $i \in \{1, \dots, n\}$ are the neutrino mass eigenstates and U^{lep} is a $3 \times n$ matrix verifying

$$U^{\text{lep}} U^{\text{lep}\dagger} = \mathbb{1}_{3 \times 3}. \quad (2.54)$$

If there is no new interactions for the charged leptons, U^{lep} can be identified as a $3 \times n$ submatrix of an $n \times n$ matrix V^ν relating neutrino flavour and mass eigenstates. In particular, for the Lagrangian (2.51):

$$\begin{pmatrix} \nu_{L1} \\ \nu_{L2} \\ \nu_{L3} \\ \nu_{s1}^c \\ \vdots \\ \nu_{sm}^c \end{pmatrix} = V^\nu P_L \begin{pmatrix} \nu_{M1} \\ \nu_{M2} \\ \nu_{M3} \\ \vdots \\ \nu_{Mn} \end{pmatrix}, \quad (2.55)$$

with P_L the left-handed projector.

If there is only three light Majorana neutrinos, U^{lep} is a 3×3 unitary matrix usually referred to as the PMNS matrix [65, 106, 107]. Using three angles $\theta_{12}, \theta_{13}, \theta_{23} \in [0, 90^\circ]$ and three phases $\delta_{\text{CP}}, \eta_1, \eta_2 \in [0, 2\pi]$, it can be conveniently parametrised as [108]²

$$\begin{aligned} U^{\text{lep}} &= \begin{pmatrix} 1 & 0 & 0 \\ 0 & c_{23} & s_{23} \\ 0 & -s_{23} & c_{23} \end{pmatrix} \begin{pmatrix} c_{13} & 0 & s_{13} \\ 0 & 1 & 0 \\ -s_{13} & 0 & c_{13} \end{pmatrix} \begin{pmatrix} c_{12} & s_{12}e^{-i\delta_{\text{CP}}} & 0 \\ -s_{12}e^{i\delta_{\text{CP}}} & c_{12} & 0 \\ 0 & 0 & 1 \end{pmatrix} \begin{pmatrix} e^{i\eta_1} & 0 & 0 \\ 0 & e^{i\eta_2} & 0 \\ 0 & 0 & 1 \end{pmatrix} \\ &= \begin{pmatrix} c_{12}c_{13} & s_{12}c_{13}e^{i\delta_{\text{CP}}} & s_{13} \\ -s_{12}c_{23}e^{-i\delta_{\text{CP}}} - c_{12}s_{13}s_{23} & c_{12}c_{23} - s_{12}s_{13}s_{23}e^{i\delta_{\text{CP}}} & c_{13}s_{23} \\ s_{12}s_{23}e^{-i\delta_{\text{CP}}} - c_{12}s_{13}c_{23} & -c_{12}s_{23} - s_{12}s_{13}c_{23}e^{i\delta_{\text{CP}}} & c_{13}c_{23} \end{pmatrix} \begin{pmatrix} e^{i\eta_1} & 0 & 0 \\ 0 & e^{i\eta_2} & 0 \\ 0 & 0 & 1 \end{pmatrix}, \end{aligned} \quad (2.56)$$

where $c_{ij} \equiv \cos \theta_{ij}$ and $s_{ij} \equiv \sin \theta_{ij}$. Note that, unlike in the parametrisation of the quark CKM mixing matrix, there is two new phases η_1 and η_2 . These phases appear due to the Majorana mass term (2.49) $\propto \bar{\nu}\nu^*$: because of it, global phases cannot be absorbed in the neutrino fields.

For three Dirac neutrinos, the parametrisation in Eq. (2.56) still holds with $\eta_1 = \eta_2 = 0$. Finally, for three light and m heavy neutrinos stemming from the Lagrangian (2.51), U^{lep} has the form

$$U^{\text{lep}} \simeq \left(\left(1 - \frac{1}{2} M_D^\dagger M_N^{*-1} M_N^{-1} M_D \right) V_l \quad M_D^\dagger M_N^{*-1} V_h \right), \quad (2.57)$$

where V_l and V_h are 3×3 and $m \times m$ unitary matrices, respectively. Therefore, if only light neutrinos are considered a 3×3 non-unitary mixing matrix is obtained. The unitarity violation, however, is suppressed by a factor $\sim (M_D/M_N)^2$ and can be safely ignored in what follows.

2.2.3 Neutrino flavour oscillations

An immediate phenomenological consequence of introducing neutrino masses, and consequently lepton flavour mixing, is that the flavour of neutrinos *oscillates* during their propagation. That is, since flavour eigenstates are not propagation eigenstates, a neutrino produced with a given flavour could, after travelling, be detected as a neutrino of a different flavour.

Getting into more detail, a flavour eigenstate neutrino produced in a weak interaction process, $|\nu_\alpha\rangle$, will in general be a superposition of mass eigenstates

$$|\nu_\alpha\rangle = \sum_{i=1}^n U_{\alpha i}^{\text{lep}*} |\nu_i\rangle, \quad (2.58)$$

where the sum runs over light neutrino mass eigenstates. The origin of the complex conjugation is that $|\nu_\alpha\rangle \propto \bar{\nu}_\alpha |0\rangle = \sum_i U_{\alpha i}^{\text{lep}*} \bar{\nu}_i |0\rangle \propto \sum_i U_{\alpha i}^{\text{lep}*} |\nu_i\rangle$, where ν_α is the neutrino field and $|0\rangle$ the vacuum.

After travelling for a time t , the state of the neutrino will be

$$e^{-i\hat{H}t} |\nu_\alpha\rangle, \quad (2.59)$$

where \hat{H} is the Hamiltonian operator. It is diagonal in the mass eigenstate basis, and for ultra-relativistic neutrinos,

$$e^{-i\hat{H}t} |\nu_\alpha\rangle = e^{iEL} \sum_{i=1}^n U_{\alpha i}^{\text{lep}*} e^{-i\frac{m_i^2 L}{2E}} |\nu_i\rangle, \quad (2.60)$$

²This expression differs from the usual one (see, e.g., Ref. [72]) by an overall unphysical rephasing. Its advantage is that vacuum CPT transformations, which will be relevant in Chapters 5 to 7, are more transparent to implement.

to lowest order in $\frac{m_i^2}{E}$. m_i is the mass of the i -th eigenstate, $L = ct$ is the travelled distance, and E is the average energy of the neutrino wave packet [109, 110].

Therefore, the probability $P_{\alpha\beta}$ that the neutrino will be detected in a charged-current process associated to a flavour $|\nu_\beta\rangle$ is given by

$$\begin{aligned} P_{\alpha\beta} &= \left| \langle \nu_\beta | e^{-i\hat{H}t} | \nu_\alpha \rangle \right|^2 = \left| \sum_{i=1}^n U_{\alpha i}^{\text{lep}*} U_{\beta i}^{\text{lep}} e^{-i\frac{m_i^2 L}{2E}} \right|^2 \\ &= \delta_{\alpha\beta} - 4 \sum_{i<j}^n \text{Re} \left[U_{\alpha i}^{\text{lep}*} U_{\beta i}^{\text{lep}} U_{\alpha j}^{\text{lep}} U_{\beta j}^{\text{lep}*} \right] \sin^2 \frac{\Delta m_{ij}^2 L}{4E} \\ &\quad + 2 \sum_{i<j}^n \text{Im} \left[U_{\alpha i}^{\text{lep}*} U_{\beta i}^{\text{lep}} U_{\alpha j}^{\text{lep}} U_{\beta j}^{\text{lep}*} \right] \sin \frac{\Delta m_{ij}^2 L}{2E}, \end{aligned} \quad (2.61)$$

where $\Delta m_{ij}^2 \equiv m_i^2 - m_j^2$. The transition probability for antineutrinos is obtained exchanging $U^{\text{lep}} \rightarrow U^{\text{lep}*}$, thus modifying the sign of the last term. Thus, the oscillation probability can be different for neutrinos and antineutrinos, and CP violation in the leptonic sector can be detected studying this phenomenon.

Several aspects of Eq. (2.61) are to be noticed. In general, to have mass-induced flavour transitions neutrinos must have different masses ($\Delta m_{ij}^2 \neq 0$) and must mix ($U_{\alpha i}^{\text{lep}} U_{\beta i}^{\text{lep}} \neq \delta_{\alpha\beta}$). Besides, the particular functional form makes the Majorana phases in Eq. (2.56) cancel out when multiplying $U_{\alpha i}^{\text{lep}} U_{\beta i}^{\text{lep}*}$, so they are not observable. This is expected: the transition does not depend on the Dirac or Majorana nature of the neutrinos. Lastly, expression (2.61) has an oscillatory behaviour with characteristic oscillation lengths

$$L_{ij}^{\text{osc}} = \frac{4\pi E}{|\Delta m_{ij}^2|} \simeq 2.48 \text{ km} \frac{E/\text{GeV}}{\Delta m_{ij}^2/\text{eV}^2}. \quad (2.62)$$

Since in real experiments neutrino beams are not monoenergetic but an incoherent superposition of different energy states and detectors have finite energy resolution, experiments do not measure $P_{\alpha\beta}$ but an average of it over some energy range. Thus, depending on the length L that neutrinos travel in an experiment, three different cases can be distinguished:

- $L \ll L_{ij}^{\text{osc}}$: in this case, oscillations do not have enough time to develop, the sines in Eq. (2.61) are small and neither Δm_{ij}^2 nor the leptonic mixing matrix elements $U_{\alpha i}^{\text{lep}}$ are measurable.
- $L \sim L_{ij}^{\text{osc}}$: in this case a well-designed experiment is sensitive to both Δm_{ij}^2 and the leptonic mixing matrix elements.
- $L \gg L_{ij}^{\text{osc}}$: in this case, the oscillation phase goes through many cycles when averaging over the energy and $\sin^2 \frac{\Delta m_{ij}^2 L}{4E}$ is averaged to $\frac{1}{2}$. The experiment can be sensitive to the leptonic mixing matrix elements but not to Δm_{ij}^2 .

This behaviour can also be understood graphically. Figure 2.1 represents the $\nu_e \rightarrow \nu_e$ (Fig. 2.1a) and $\nu_\mu \rightarrow \nu_\mu$ (Fig. 2.1b) oscillation probabilities as a function of the energy to distance ratio E/L for a three light neutrino paradigm with the oscillation parameters given in Ref. [111]. In this scenario, there are three non-independent oscillation lengths, $\frac{E}{L_{21}^{\text{osc}}} \simeq 2.98 \times 10^{-5} \text{ GeV/km}$, $\frac{E}{L_{32}^{\text{osc}}} \simeq 1.95 \times 10^{-4} \text{ GeV/km}$, and $\frac{E}{L_{31}^{\text{osc}}} = \frac{E}{L_{32}^{\text{osc}}} + \frac{E}{L_{21}^{\text{osc}}} \simeq 1.02 \times 10^{-3} \text{ GeV/km}$.

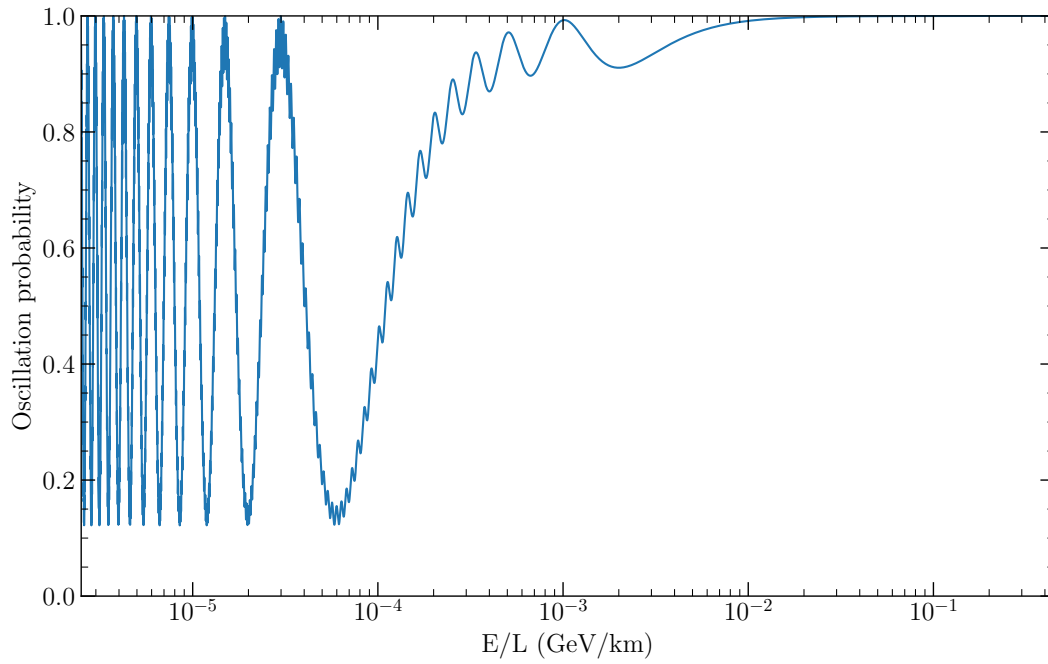
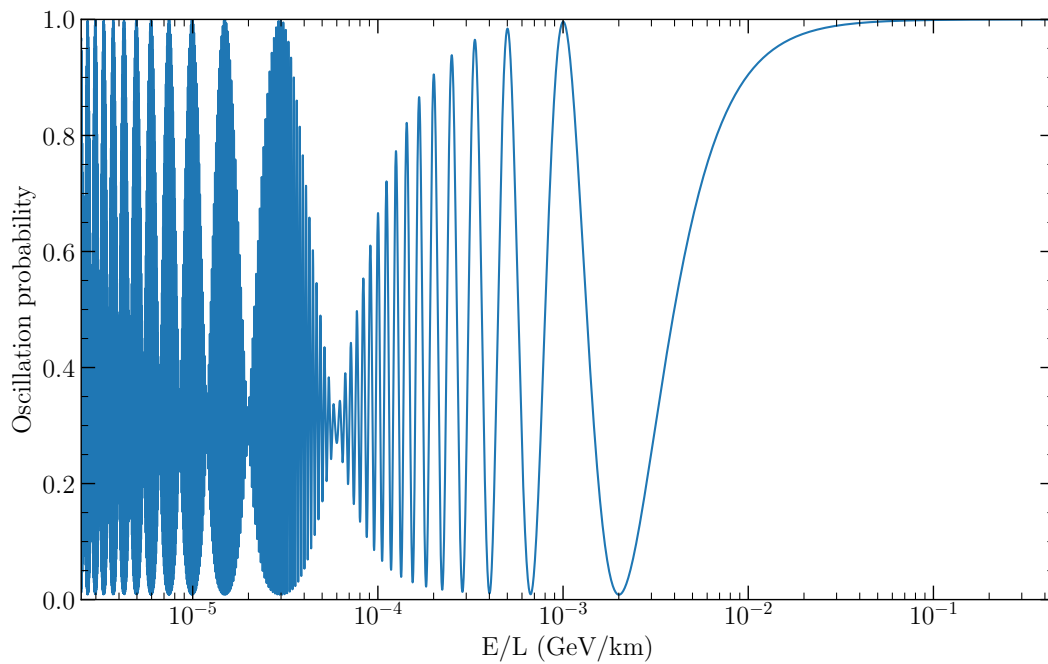
(a) $\nu_e \rightarrow \nu_e$ oscillation probability.(b) $\nu_\mu \rightarrow \nu_\mu$ oscillation probability.

Figure 2.1: Some neutrino flavour oscillation probabilities. The results have been obtained using Eq. (2.61) under the assumption of 3 light neutrinos and the values for the oscillation parameters in Ref. [111].

Figure 2.1a shows the transition between the regions where L_{21}^{osc} , L_{23}^{osc} , or none contribute: L_{13}^{osc} is suppressed with respect to L_{23}^{osc} because of their similar oscillation frequencies and the smallness of $U_{13}^{\text{lep}} < U_{12}^{\text{lep}}$. Nevertheless, since $U_{23}^{\text{lep}} \sim U_{22}^{\text{lep}}$, Fig. 2.1b shows the beats that typically appear when two oscillations of similar frequencies superpose.

Due to the three different oscillation regimes described above, some experimental results can be roughly understood in terms of an approximate two neutrino mixing. In that case, there is an angle dominantly controlling the observable oscillation amplitude and a mass difference dominantly controlling the observable frequency.

In detail, for 2 light neutrino flavours U^{lep} is parametrised by a single angle θ and the oscillation formula is then quite simple:

$$P_{\alpha\beta} = \delta_{\alpha\beta} - (2\delta_{\alpha\beta} - 1) \sin^2 2\theta \sin^2 \frac{\Delta m^2 L}{4E}, \quad (2.63)$$

where Δm^2 is the squared mass difference between the considered mass eigenstates. In this case, the oscillation probability is symmetric under the exchange $\theta \leftrightarrow \frac{\pi}{2} - \theta$ and/or $\Delta m^2 \leftrightarrow -\Delta m^2$. Furthermore, no physical CP violating phase is left here. More-than-two neutrino mixing as well as matter effects (see below) break all these symmetries.

2.2.4 Flavour transitions in matter

The oscillation probability calculation in Eq. (2.61) assumed that neutrinos travelled in vacuum. Even though their inelastic scattering cross section is very small, coherent forward elastic scattering on dense matter gets accumulated over long distances, as scattered and unscattered waves interfere.

In more detail, the matrix elements of the Hamiltonian operator in Eq. (2.60) have to be computed among states containing all particles present in the medium. Then, the interaction operators among neutrinos and fermions in the Lagrangian (2.9) will contribute to the Hamiltonian matrix elements, generating an effective potential V .

As an example, in a medium with electrons, the charged current interaction Hamiltonian will contribute to the ee matrix element in flavour space. If these have spin s and momentum \vec{p}_e distributed as $f(\vec{p}_e, s, \vec{x})$, the matrix element is computed as [99]

$$\begin{aligned} V_{ee} &= \sum_s \int d^3\vec{p}_e f(\vec{p}_e, s, \vec{x}) \langle \nu_e, e(\vec{p}_e, s) | \hat{H}_{\text{CC}} | \nu_e, e(\vec{p}_e, s) \rangle \\ &= 2\sqrt{2}G_F \sum_s \int d^3\vec{p}_e d^3x f(\vec{p}_e, s, \vec{x}) \langle \nu_e, e(\vec{p}_e, s) | \bar{e}(x) \gamma^\mu P_L \nu_e(x) \bar{\nu}_e(x) \gamma_\mu P_L e(x) | \nu_e, e(\vec{p}_e, s) \rangle, \end{aligned} \quad (2.64)$$

where $G_F = \frac{\sqrt{2}}{8} \frac{g^2}{M_W^2} \simeq 1.166 \times 10^{-5} \text{ GeV}^{-2}$ is the Fermi constant. Notice that coherence implies that the spins and momenta of all initial and final particles are equal. As a consequence, the momentum transfer among neutrinos and electrons is zero³, much smaller than the W boson mass, and the effective Fermi Lagrangian can be used instead of the Lagrangian (2.9) to compute the Hamiltonian. After Fierz rearrangement,

$$V_{ee} = 2\sqrt{2}G_F \sum_s \int d^3\vec{p}_e d^3x \langle \nu_e | \bar{\nu}_e(x) \gamma^\mu P_L \nu_e(x) | \nu_e \rangle f(\vec{p}_e, s, \vec{x}) \langle e(\vec{p}_e, s) | \bar{e}(x) \gamma_\mu P_L e(x) | e(\vec{p}_e, s) \rangle. \quad (2.65)$$

³Technically, if ν_i and ν_j have different masses the momentum transfer cannot be zero. Nevertheless, coherence holds as long as it is much smaller than the typical electron quantum mechanical momentum spread, $\mathcal{O}(\text{eV})$.

Expanding the electron fields in plane waves, standard Dirac algebra gives

$$\langle e(\vec{p}_e, s) | \bar{e}(x) \gamma_\mu P_L e(x) | e(\vec{p}_e, s) \rangle = \frac{1}{2E_e} \bar{u}_s(p_e) \gamma_\mu P_L u_s(p_e), \quad (2.66)$$

with E_e the electron energy. The one-particle states have been normalised as $|e(\vec{p}, s)\rangle = a_{\vec{p}}^{s\dagger} |0\rangle$, with $a_{\vec{p}}^s$ an annihilation operator with momentum \vec{p} and spin s and $|0\rangle$ the vacuum.

For an isotropic and unpolarised medium, $f(\vec{p}_e, s, \vec{x}) = \frac{1}{2} f(p_e, \vec{x})$ and thus

$$\begin{aligned} & \sum_s \int d^3 \vec{p}_e f(\vec{p}_e, s, \vec{x}) \langle e(\vec{p}_e, s) | \bar{e}(x) \gamma_\mu P_L e(x) | e(\vec{p}_e, s) \rangle \\ &= \frac{1}{2} \int d^3 \vec{p}_e f(p_e, \vec{x}) \sum_s \frac{1}{2E_e} \bar{u}_s(p_e) \gamma_\mu P_L u_s(p_e) = \frac{1}{2} \int d^3 \vec{p}_e f(p_e, \vec{x}) \text{Tr} \left[\frac{m_e + \not{p}}{2E_e} \gamma_\mu P_L \right] \\ &= \frac{1}{2} \int d^3 \vec{p}_e f(p_e, \vec{x}) \frac{p_\mu}{E_e}, \end{aligned} \quad (2.67)$$

where m_e is the electron mass, and the Dirac equation $\sum_s u_s(p) \bar{u}_s(p) = \not{p} + m$ has been used. Because of isotropy, $\int d^3 \vec{p}_e \vec{p}_e = 0$, and only the $\mu = 0$ term survives. Furthermore, $\int d^3 \vec{p}_e f(p_e, \vec{x}) = n_e(x)$, the electron number density in the medium. Thus,

$$\sum_s \int d^3 \vec{p}_e f(\vec{p}_e, s, \vec{x}) \langle e(\vec{p}_e, s) | \bar{e}(x) \gamma_\mu P_L e(x) | e(\vec{p}_e, s) \rangle = \frac{1}{2} n_e(x) \delta_\mu^0. \quad (2.68)$$

Finally, the neutrino matrix element

$$\langle \nu_e | \bar{\nu}_e(x) \gamma^\mu P_L \nu_e(x) | \nu_e \rangle \quad (2.69)$$

gives, for neutrino wavepackets centered at a position \vec{x}_0 , a term $\propto \delta^3(\vec{x} - \vec{x}_0)$. Putting everything together,

$$V_{ee}(\vec{x}_0) = \sqrt{2} G_F n_e(\vec{x}_0). \quad (2.70)$$

For antineutrinos, there is one additional anticommutation when computing the matrix element, and the result changes sign.

Finally, neutral current interactions will also contribute to the matrix elements. A similar calculation gives

$$V_{\alpha\beta}(\vec{x}_0) = -\delta_{\alpha\beta} \frac{G_F}{\sqrt{2}} [(n_e(\vec{x}_0) - n_p(\vec{x}_0))(1 - 4 \sin^2 \theta_W) + n_n(\vec{x}_0)], \quad (2.71)$$

where n_p and n_n are the proton and neutron number densities. Notice that this contribution to the Hamiltonian matrix is proportional to the identity, and thus unobservable in this scenario.

All in all, we have seen that matter effects lead to an effective potential difference between electron neutrinos and other flavours

$$V_{\text{eff}} = \pm \sqrt{2} G_F n_e, \quad (2.72)$$

where the $+$ ($-$) sign refers to neutrinos (antineutrinos). Adding it to the free Hamiltonian, the oscillation probability for 3 light neutrinos travelling through matter of constant density is given by

$$P_{\alpha\beta} = |\mathcal{M}_{\beta\alpha}|^2, \quad (2.73)$$

with

$$\mathcal{M} = \exp \left\{ -iL \left[\begin{pmatrix} \sqrt{2}G_F n_e & 0 & 0 \\ 0 & 0 & 0 \\ 0 & 0 & 0 \end{pmatrix} + \frac{1}{2E} U^{\text{lep}} \begin{pmatrix} 0 & 0 & 0 \\ 0 & \Delta m_{21}^2 & 0 \\ 0 & 0 & \Delta m_{31}^2 \end{pmatrix} U^{\text{lep}\dagger} \right] \right\}, \quad (2.74)$$

where U^{lep} is the leptonic mixing matrix Eq. (2.56). In general there is no compact exact expression for this probability.

As a consequence, a two neutrino scenario gets significantly modified by matter effects (take for example $\nu_\mu \leftrightarrow \nu_e$ oscillations by setting $\theta_{13} = \theta_{23} = 0$). There, the presence of the matter potential allows to distinguish the sign of Δm_{12}^2 (or, equivalently, whether θ_{12} is below or above 45°). It also induces a different oscillation probability between neutrinos and antineutrinos, this is, matter breaks CP because it contains only electrons and not positrons.

Non-uniform density: the MSW effect

If the matter density cannot be considered constant along neutrino propagation, which is the case for solar neutrinos, the derivation of the relevant oscillation probability is more involved. As rigorously derived in Refs. [112–114] from field theory first principles, the evolution equation for n light neutrino mass eigenstates is given by

$$i \frac{d}{dx} \begin{pmatrix} \nu_1 \\ \vdots \\ \nu_n \end{pmatrix} = H \begin{pmatrix} \nu_1 \\ \vdots \\ \nu_n \end{pmatrix}, \quad (2.75)$$

where x is the coordinate along the neutrino trajectory and H is the Hamiltonian matrix

$$H = \frac{1}{2E} \text{diag}(m_1^2, \dots, m_n^2) + U^{\text{lep}\dagger} V U^{\text{lep}}, \quad (2.76)$$

where V is the effective potential matrix in the flavour basis. For the particular case of three SM neutrinos with just SM interactions in a medium made of electrons, protons and neutrons,

$$V = \begin{pmatrix} 2\sqrt{2}G_F n_e(x) & 0 & 0 \\ 0 & 0 & 0 \\ 0 & 0 & 0 \end{pmatrix}. \quad (2.77)$$

For antineutrinos, the leptonic mixing matrix has to be replaced by its complex conjugate, and the SM matter potential flips sign.

To solve this equation⁴, we first switch to the basis of instantaneous mass eigenstates in matter, i.e., the eigenstates of the full Hamiltonian (2.76) for a fixed x ,

$$H(x) \begin{pmatrix} \nu_1^m \\ \vdots \\ \nu_n^m \end{pmatrix} = \frac{1}{2E} \text{diag}(\mu_1^2(x), \dots, \mu_n^2(x)) \begin{pmatrix} \nu_1^m \\ \vdots \\ \nu_n^m \end{pmatrix}, \quad (2.78)$$

where the instantaneous mass eigenstates are related to the flavour eigenstates $(\nu_\alpha \ \dots)^T$ as

$$\begin{pmatrix} \nu_\alpha \\ \vdots \end{pmatrix} = \tilde{U}(x) \begin{pmatrix} \nu_1^m \\ \vdots \\ \nu_n^m \end{pmatrix}. \quad (2.79)$$

⁴The derivation here closely follows Refs. [72, 99].

For the particular case of two neutrino flavours α and β ,

$$\mu_{1,2}^2(x) = \frac{m_1^2 + m_2^2}{2} + E(V_\alpha(x) + V_\beta(x)) \mp \frac{1}{2} \sqrt{(\Delta m^2 \cos 2\theta - A(x))^2 + (\Delta m^2 \sin 2\theta)^2}, \quad (2.80)$$

where $A(x) \equiv 2E(V_\alpha(x) - V_\beta(x))$ and V_α and V_β are the matter potentials of ν_α and ν_β . θ is the angle parametrising the 2×2 mixing matrix

$$\begin{pmatrix} \nu_\alpha \\ \nu_\beta \end{pmatrix} = \begin{pmatrix} \cos \theta & \sin \theta \\ -\sin \theta & \cos \theta \end{pmatrix} \begin{pmatrix} \nu_1 \\ \nu_2 \end{pmatrix}. \quad (2.81)$$

On top of that, the mixing angle parametrising $\tilde{U}(x)$ is given by

$$\tan 2\theta_m(x) = \frac{\Delta m^2 \sin 2\theta}{\Delta m^2 \cos 2\theta - A(x)}. \quad (2.82)$$

From here, we notice that for the *resonance condition*

$$V_\alpha - V_\beta = \frac{\Delta m^2}{2E} \cos 2\theta, \quad (2.83)$$

the effective mixing angle is maximal.

We can now write the evolution equation in the instantaneous mass basis. Taking the derivative of Eq. (2.79) and using Eq. (2.75),

$$i \frac{d}{dx} \begin{pmatrix} \nu_1^m \\ \vdots \\ \nu_n^m \end{pmatrix} = \left[\frac{1}{2E} \text{diag}(\mu_1^2, \dots, \mu_n^2) - i \tilde{U}^\dagger(x) \frac{d\tilde{U}(x)}{dx} \right] \begin{pmatrix} \nu_1^m \\ \vdots \\ \nu_n^m \end{pmatrix}. \quad (2.84)$$

If the potential varies slowly enough, the second term can be neglected. Then, the instantaneous mass eigenstates are energy eigenstates at every position x and they do not mix in the evolution. Instead, they just pick a phase $\propto \frac{\mu_i^2}{2E}$ and the transition probability takes a simple form, similar to the vacuum one [72],

$$P_{\alpha\beta} = \left| \sum_i \tilde{U}_{\alpha i}^*(0) \tilde{U}_{\beta i}(L) \exp\left(-i \frac{1}{2E} \int_0^L \mu_i^2(x') dx'\right) \right|^2. \quad (2.85)$$

This is known as the *adiabatic approximation*. Physically, it means that the potential varies slowly enough so that the effective mixing in matter changes in scales much larger than the oscillation length. If, on the contrary, there are regions where the potential has strong variations, the adiabatic approximation breaks down and there can be transitions among instantaneous mass eigenstates. In these regions, one has to resort for instance to the WKB approximation to solve the evolution equation analytically [115].

For the two-neutrino case, the adiabaticity condition reads [99]

$$\frac{2EA(x)\Delta m^2 \sin 2\theta}{\Delta(x)^3} \left| \frac{1}{A} \frac{dA}{dx} \right| \ll 1, \quad (2.86)$$

with $\Delta(x) \equiv \mu_1^2(x) - \mu_2^2(x)$. For small mixing angles θ , the left-hand side is largest at the resonance. If the adiabaticity condition is always satisfied, for very large L

$$P_{\alpha\alpha} = 1 - P_{\alpha\beta} = \frac{1}{2}(1 + \cos 2\theta_{m,0} \cos 2\theta_{m,L}), \quad (2.87)$$

where $\theta_{m,0}$ and $\theta_{m,L}$ are the effective mixing angles at production and detection, respectively. Notice that with constant matter effects $\theta_{m,0}$ and $\theta_{m,L}$ have the same sign, and so $P_{\alpha\alpha} \geq \frac{1}{2}$. However, as can be seen from Eq. (2.82), if neutrinos cross the resonance along their path, θ_m changes its octant. Thus, $\cos 2\theta_{m,0} \cos 2\theta_{m,L} < 0$ and $P_{\alpha\alpha} < \frac{1}{2}$. This is referred to as the Mikheev-Smirnov-Wolfenstein (MSW) effect [116,117], and plays a fundamental role in explaining the observed deficit of solar neutrinos. This will be further explored in Section 3.1.

2.2.5 Leptonic CP violation as a consequence of neutrino masses

Besides flavour oscillations, another important consequence of neutrino masses and mixing is the possibility of having CP violation in the leptonic sector. As in the quark sector, flavour mixing between 3 particle flavours opens the door to breaking this symmetry. In particular, a non zero value for any of the phases in the parametrisation (2.56) will introduce a phase in the Lagrangian that violates CP. For the rest of this work, the Majorana phases will be ignored: they depend on the Dirac or Majorana nature of neutrino mass eigenstates but, as discussed above, they are irrelevant for neutrino flavour oscillations.

The fact that a non zero value of δ_{CP} can lead to CP violation is directly present in the oscillation formula (2.61): due to the chiral structure of the SM, antineutrinos (right-handed) are the CP conjugates of neutrinos (left-handed); any difference in $P_{\alpha\beta}$ between neutrinos and antineutrinos is a sign of CP violation. Since Eq. (2.61) accounts for antineutrino flavour oscillations just by substituting $U^{\text{lep}} \rightarrow U^{\text{lep}*}$, only the terms in the second sum

$$\text{Im} \left[U_{\alpha i}^{\text{lep}*} U_{\beta i}^{\text{lep}} U_{\alpha j}^{\text{lep}*} U_{\beta j}^{\text{lep}} \right], \quad i < j, \quad \alpha \neq \beta \quad (2.88)$$

violate CP. It is immediate to see that if $\delta_{\text{CP}} \neq 0$ these elements are different from zero. Furthermore, for three light neutrinos the matrix element products (2.88) can be shown to be all equal, up to signs, to

$$J_{\text{CP}} \equiv J_{\text{CP}}^{\text{max}} \sin \delta_{\text{CP}} = c_{12} c_{23} c_{13}^2 s_{12} s_{23} s_{13} \sin \delta_{\text{CP}}. \quad (2.89)$$

A quantity completely equivalent to the Jarlskog invariant in Eq. (2.41). Indeed, the same procedure followed there could be applied here: the presence of neutrino masses makes the transformation (2.21) physical as there is an additional flavour matrix as in the quark sector. In the end, the same condition for CP conservation would be obtained: for Dirac neutrinos, CP violation requires all three neutrino masses to be different (so that the mixing angles are physical), all three charged lepton masses to be different (so that the concept of neutrino flavour is meaningful), and the invariant in Eq. (2.89) not to vanish. This will be explicitly shown for the more general case in which there is new physics in addition to neutrino masses in Chapter 5.

2.3 Summary

The paradigmatic fundamental theory of Nature until the end of the 20th century was the SM of Particle Physics. Although it was ultimately confirmed with the discovery of the Higgs boson, it predicts leptonic flavours to be exactly conserved, and as a consequence neutrinos are strictly massless. The former has been experimentally checked to fail. This may be an indication of neutrino masses, our first laboratory evidence for BSM physics. Furthermore, assuming the SM to be a theory valid up to some high energy scale, the first observable effect of new physics is actually *predicted* to be neutrino masses and leptonic flavour mixing.

An immediate experimental consequence is that neutrinos change their flavour as they travel, a phenomenon known as neutrino oscillations. The experimental scrutiny of this process allows

to measure the first properties of a theory more fundamental than the SM. Because of that, there is a strong experimental programme that will be overviewed in the next chapter.

In addition, mixing among three neutrino flavours induces a new source of CP violation. This could be linked to the matter-antimatter asymmetry of the Universe, and so it is interesting on its own. Current experiments are slowly starting to show a hint that CP could be violated in the leptonic sector. Rigorously assessing the significance of this signal and its robustness is the main goal of this thesis.

Chapter 3

Three-neutrino fit to oscillation experiments: framework

In that simple statement is the key to science. It does not make any difference how beautiful your guess is. It does not make any difference how smart you are, who made the guess, or what his name is — if it disagrees with experiment it is wrong.

— Richard P. Feynman

*Mientras en el mar o en el cielo haya un abismo,
que al cálculo resista;
Mientras la humanidad siempre avanzando,
no sepa a dó camina;
Mientras haya un misterio para el hombre,
¡habrá poesía!*

— Gustavo A. Bécquer

As mentioned in the previous chapter, data from neutrino experiments conclusively show that each of the leptonic flavours is violated, and thus that there is BSM physics. In principle, neutrino masses could provide the source for leptonic flavour violation. However, any other mechanism introducing a distinction between interaction and propagation eigenstates could explain the same phenomenon. Some alternatives, that generically introduce a dependence of the flavour transition probability on the energy different from $\sim \sin \frac{L}{E}$ [118], include neutrino decay [119], quantum decoherence [120], or Lorentz invariance violation [121,122]. Nevertheless, the precise analysis of neutrino spectra conclusively proved that the observed phenomena were mass-induced flavour-oscillations [118,120,123].

Once mass-induced neutrino oscillations are experimentally established, the next step is their quantitative characterisation. Currently, there exist some tensions in the experimental data: the so-called short baseline reactor anomaly [124–129], the gallium anomaly [130,131], and the LSND [132] and MiniBooNE [133] short baseline accelerator results. Since they have low statistical significance and they are not fully consistent among themselves [134,135], they will be ignored in what follows. Apart from these anomalies, all the existing oscillation data can be explained by a three light neutrino paradigm parametrised by the mixing matrix in Eq. (2.56).

The convention regarding the numbering of mass eigenstates, diagrammatically shown in Fig. 3.1, makes use of the experimental fact (see description of the data below) that two of them have masses close to each other ($|\Delta m^2| \sim 10^{-5} \text{ eV}^2$) whereas the third one is further away ($|\Delta m^2| \sim 10^{-3} \text{ eV}^2$). Based on this, one can always choose a convention in which the close eigenstates are denoted as ν_1 and ν_2 with $m_1 < m_2$ keeping the ranges of angles and phases as $\theta_{12}, \theta_{13}, \theta_{23} \in [0, 90^\circ]$, and $\delta_{\text{CP}} \in [0, 2\pi]$. The other eigenstate is denoted as ν_3 . It is currently unknown whether $m_3 > m_1$ (known as Normal Ordering, NO) or $m_3 < m_1$ (known as Inverted Ordering, IO).

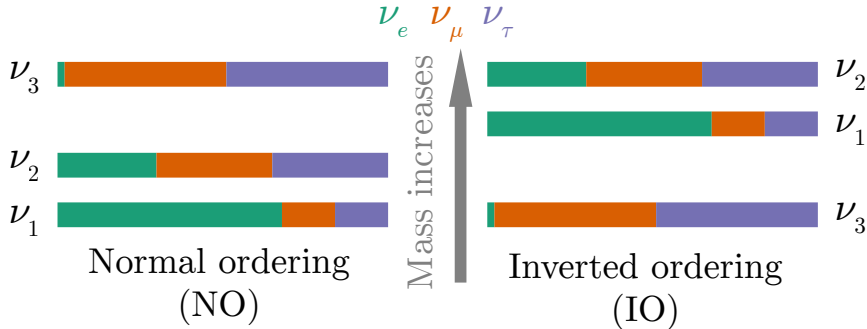


Figure 3.1: Convention for the numbering of mass eigenstates and possible orderings (NO on left, IO on right). The colours indicate the amount of mixing between mass and flavour eigenstates.

The current picture of neutrino flavour transitions has been built by combining a variety of experimental results. Indeed, due to the different oscillation regimes described in Section 2.2.3 and explicitly seen in Fig. 2.1, there are qualitatively different experiments that look for different sectors of the neutrino mixing matrix. They will be explored in the rest of this chapter.

3.1 Solar neutrinos

Neutrinos coming from the Sun provided the first experimental hint for neutrino flavour transitions. Solar neutrinos are copiously generated in the thermonuclear reactions that fuel our star. These reactions occur through two main chains, the pp chain and the CNO cycle: the relevant processes producing neutrinos are shown in Fig. 3.2. The resulting spectrum, with energies $\mathcal{O}(\text{MeV})$ as is typical in nuclear reactions, is shown in Fig. 3.3. Its precise computation requires a detailed knowledge of the Sun and its evolution, and the Solar Models rely on observational parameters that in turn give the normalisation uncertainties shown in the Figure [136, 137].

Solar neutrinos were first detected by the Chlorine experiment in 1968 [77]. Since then, they have been detected in many experiments that can be generically classified as [72]

- *Radiochemical experiments*: these experiments detect solar neutrinos through inverse beta decay

$$n + \nu_e \rightarrow e^- + p, \quad (3.1)$$

which modifies the chemical composition of the detector. The amount of generated nuclei is measured after a certain period of time, which allows to extract the solar neutrino flux.

The detectors either exploit the

$${}^{37}\text{Cl} + \nu_e \rightarrow {}^{37}\text{Ar} + e^- \quad (3.2)$$

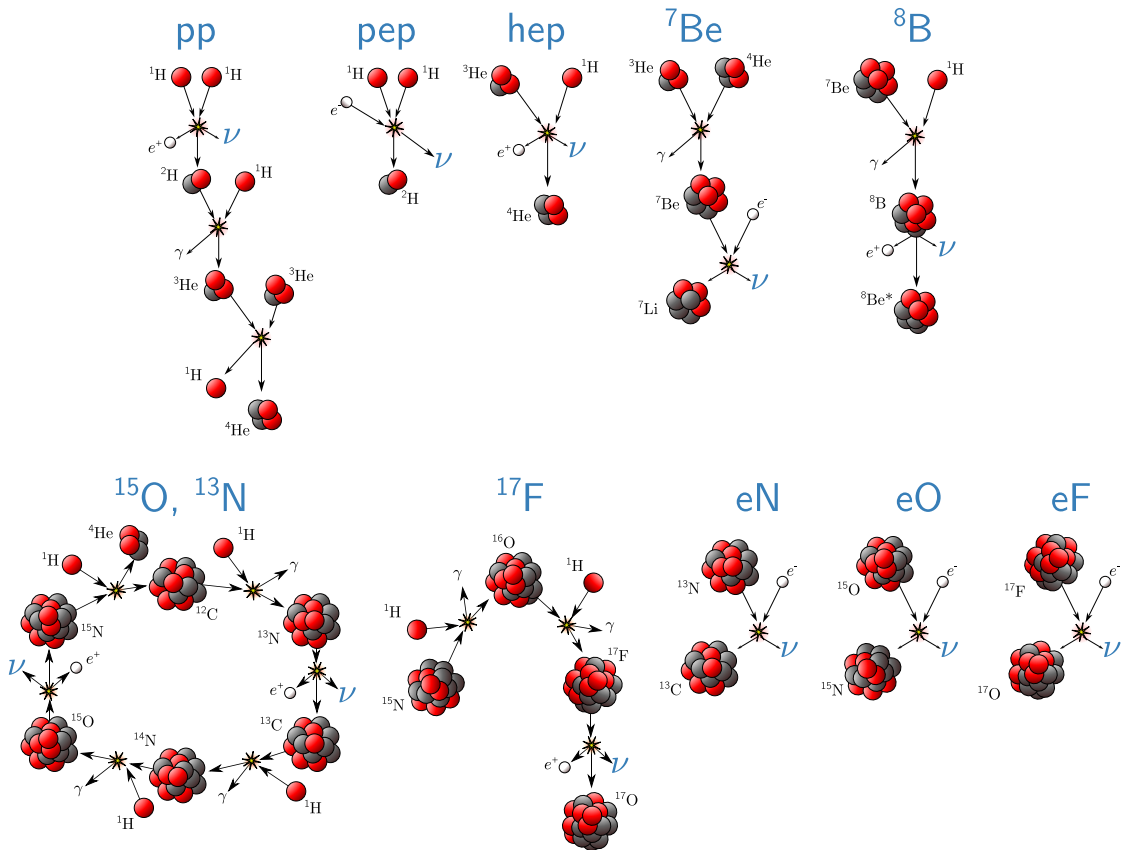


Figure 3.2: Nuclear reactions in the Sun that produce neutrinos. The top row corresponds to the pp cycle, and the bottom row to the CNO cycle. Above each reaction, the name with which the neutrinos produced there are denoted is indicated. Adapted from Refs. [138, 139].

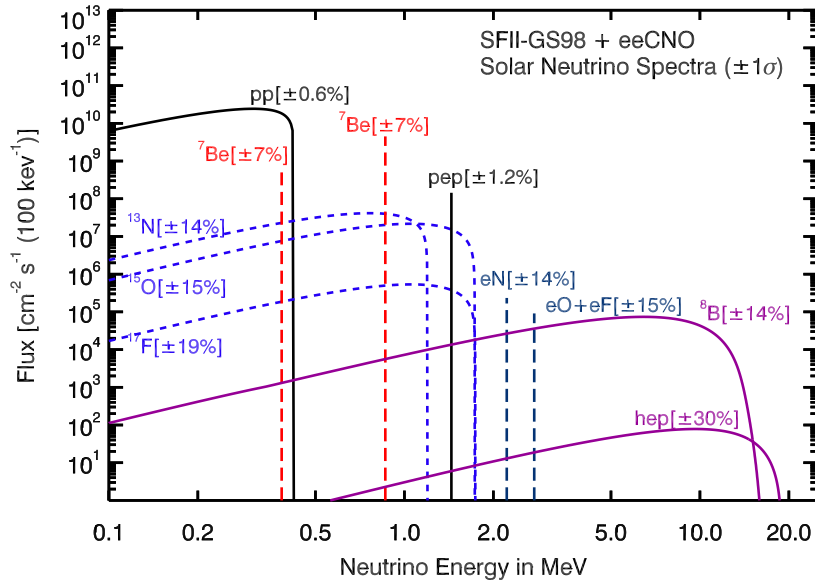


Figure 3.3: Solar neutrino spectrum. Above each line, the reaction in which neutrinos are generated is indicated (see Fig. 3.2). Extracted from Ref. [140]. The theoretical computations and uncertainties on flux normalisations are given in Refs. [136, 137]. Monochromatic fluxes, corresponding to electron capture processes, are given in units of $\text{cm}^{-2} \text{s}^{-1}$.

reaction [23], that with a threshold of 0.814 MeV is mostly sensitive to ${}^7\text{Be}$ and ${}^8\text{B}$ neutrinos; or the



reaction [24–26], that has a lower threshold (0.233 MeV) and a larger capture cross section, thus detecting as well pp neutrinos. The former set of experiments detected a $\sim 70\%$ deficit of solar neutrinos, whereas the latter observed a $\sim 45\%$ deficit, indicating that the solar neutrino deficit is energy dependent.

- *Real time experiments:* unlike radiochemical experiments, these are capable of detecting the solar neutrino interaction in real time. In addition, they can measure the energy and incoming direction of each event. Therefore, they are sensitive to the energy dependence of flavour transitions, as well as to transitions induced by the Earth matter discussed in Section 2.2.4.

The real time experiments that have detected solar neutrinos are

- Kamiokande [27] and Super-Kamiokande [28], water tanks that detect the Cherenkov light emitted by electrons elastically scattered in the $\nu_\alpha + e^- \rightarrow \nu_\alpha + e^-$ process. Requiring the electrons to emit enough Cherenkov light sets a threshold $E_\nu \gtrsim 5$ MeV, and so the experiments are mostly sensitive to ${}^8\text{B}$ neutrinos. A deficit $\sim 60\%$ was observed in these experiments.
- SNO [29], a heavy water (D_2O) Cherenkov detector. Interestingly, in addition to elastic scattering $\nu_\alpha + e^- \rightarrow \nu_\alpha + e^-$, SNO could measure both charged current interactions of electron neutrinos, $\nu_e + {}^2\text{H} \rightarrow p + p + e^-$, and neutral current interactions of all interacting neutrinos, $\nu_\alpha + {}^2\text{H} \rightarrow n + p + \nu_\alpha$. Comparing the reaction rates (see

Fig. 3.4), SNO checked that the solar neutrino deficit was due to electron neutrinos transitioning to other flavours.

- KamLAND [30] and Borexino [31] are detectors filled with liquid scintillator that detect neutrinos through elastic scattering with electrons. Unlike with Cherenkov detectors, there is no physical barrier for detecting low energy neutrinos other than the scintillator being sensitive to low energy electrons. This allowed to detect ${}^7\text{Be}$ and pp neutrinos.

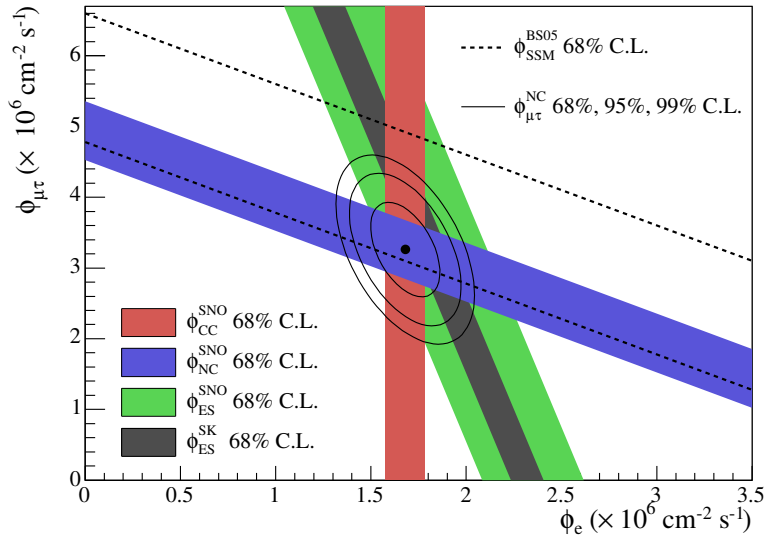


Figure 3.4: $\nu_\mu + \nu_\tau$ flux vs ν_e flux, as measured by the SNO neutral current (purple), charged current (red), and elastic scattering (green) data. The region between the dashed lines corresponds to the prediction in Ref. [141] assuming neutrino flavour oscillations. The contours correspond to the joint confidence regions. Also shown in grey is the Super-Kamiokande measurement [142]. The hypothesis of no flavour transitions ($\phi_{\mu\tau} = 0$) is clearly excluded. Figure from Ref. [15].

3.1.1 Analysis and interpretation of solar neutrino data

Since solar neutrinos traverse large non-uniform densities before leaving the Sun, the results of the experiments above must be analysed by properly taking into account the effects of non-uniform matter discussed in Section 2.2.4. As experiments with a higher energy threshold observed $P_{ee} < \frac{1}{2}$, the MSW effect reviewed there is expected to play a significant role in explaining the data.

Solar neutrino experiments measure the $\nu_e \rightarrow \nu_e$ transition probability and matter affects identically ν_μ and ν_τ , and so we can consider to a good approximation transitions between ν_e and ν_X , where the latter is some linear combination of ν_μ and ν_τ . These transitions are parametrised in terms of a single squared mass difference Δm^2 and a single mixing angle θ . When analysing all solar neutrino data, the region of masses and mixings that best describes the experiments is shown in Fig. 3.5. As can be seen, the squared mass difference is $\sim 10^{-5} \text{ eV}^2$, and the mixing angle is $\sim 32^\circ$.

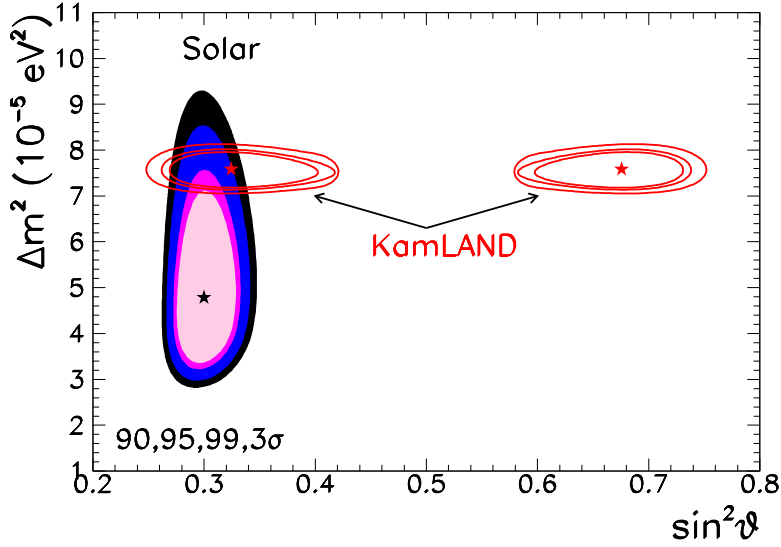


Figure 3.5: Allowed regions of Δm^2 and $\sin^2 \theta$ that best describe solar data. The red regions correspond to the KamLAND reactor experiment, to be discussed later. Figure courtesy of M. C. Gonzalez-García and M. Maltoni.

The energy dependence of the transition probability can be easily understood from the allowed parameters, for which the adiabatic approximation (2.86) always holds [99]. Recalling Eq. (2.87),

$$P_{ee} = \frac{1}{2}(1 + \cos 2\theta_{m,0} \cos 2\theta), \quad (3.4)$$

where

$$\tan 2\theta_m = \frac{\tan 2\theta}{1 - A/(\Delta m^2 \cos 2\theta)}. \quad (3.5)$$

For the best fit parameters in Fig. 3.5,

$$\frac{A}{\Delta m^2 \cos 2\theta} \simeq 0.72 \left(\frac{E}{\text{MeV}} \right) \left(\frac{4.8 \times 10^{-5} \text{ eV}^2}{\Delta m^2} \right), \quad (3.6)$$

where E is the neutrino energy, and we have taken a solar density $\sim 100 \text{ gm/cm}^3$, representative of its core.

Thus, for $E \ll \text{MeV}$, matter effects are not important and $P_{ee} \simeq \frac{1}{2}(1 + \cos^2 2\theta) \simeq 0.6$. For $E \gg \text{MeV}$, however, $P_{ee} \simeq \frac{1}{2}(1 - \cos 2\theta) \simeq 0.3$. At $E \sim \text{MeV}$, the transition between both regimes takes place. The exact transition probability as a function of the neutrino energy, as well as the experimental data, is shown in Fig. 3.6. As can be seen, Nature was kind to provide solar neutrinos with energies around the transition between vacuum-dominated and MSW-dominated oscillations, $\sim \text{MeV}$, so that the squared mass splitting could be determined.

In addition, matter effects allow to determine the octant of θ , as the MSW effect only happens when $1 - \frac{A}{\Delta m^2 \cos 2\theta}$ changes sign along neutrino propagation. That is, for $\theta < 45^\circ$ ¹.

¹In our convention, we set $\Delta m^2 > 0$, as one can always change the sign of Δm^2 by simultaneously changing the octant of θ . The whole procedure is equivalent to relabelling the mass eigenstates.

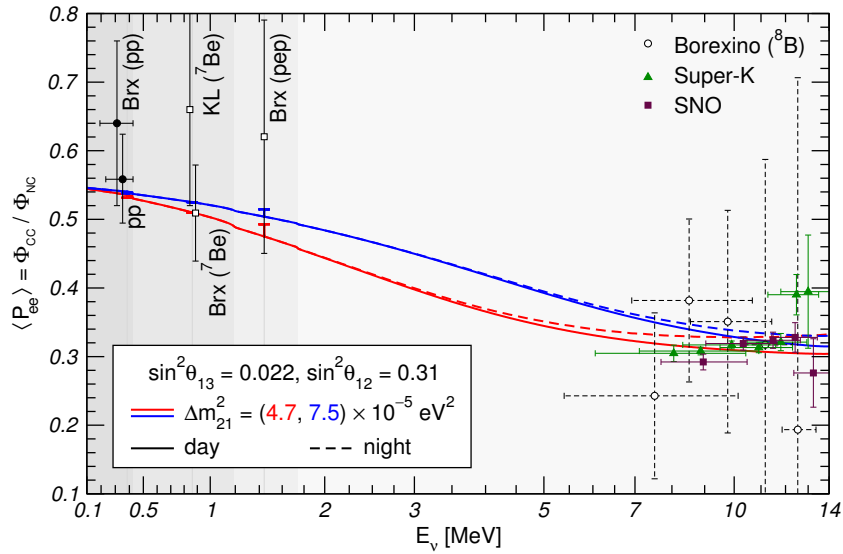


Figure 3.6: Solar ν_e survival probability as a function of the neutrino energy, as well as some experimental data. Brx means Borexino and KL KamLAND. Earth matter effects, which induce a small day-night asymmetry, are also included. The transition between the vacuum-dominated regime, at lower energies and with $P_{ee} > \frac{1}{2}$; and the MSW-dominated regime, at higher energies and with $P_{ee} < \frac{1}{2}$, is clearly visible. Extracted from Ref. [143].

3.2 Atmospheric neutrinos

Besides solar neutrinos, the other experiments that historically first established neutrino flavour oscillations were atmospheric neutrino experiments.

Muon and electron neutrinos and antineutrinos are abundantly produced in particle cascades created when cosmic rays hit the atmosphere at altitudes ~ 10 km. These cascades involve charged mesons, mainly pions, that decay to charged leptons and neutrinos as

$$\pi^\pm \rightarrow \mu^\pm + \bar{\nu}_\mu, \quad (3.7)$$

followed by muon decay

$$\mu^\pm \rightarrow e^\pm + \bar{\nu}_\mu + \bar{\nu}_e. \quad (3.8)$$

Realistic calculations introduce decays of other subdominant mesons, mostly kaons, producing a neutrino flux depicted in Fig. 3.7.

Atmospheric neutrinos were first detected in underground experiments, where plastic scintillators detected the muons produced by atmospheric ν_μ in charged current interactions [145, 146]. In the 1980s, large underground experiments searching for nucleon decay started observing atmospheric neutrinos. There are two main kind of such experiments

- *Water Cherenkov detectors*: these experiments detect the Cherenkov light emitted by muons and electrons generated in charged current interactions of neutrinos with nuclei. They can estimate the neutrino energy and incoming direction, as well as discern between electrons and muons, as the former generate an electromagnetic shower that blurs the Cherenkov ring. The main experiments are IMB [147], Kamiokande [17] and Super-Kamiokande [18]. On top of them, in the last years the IceCube experiment [89] has also detected atmospheric neutrino oscillations using the Antarctic ice as a Cherenkov detector.

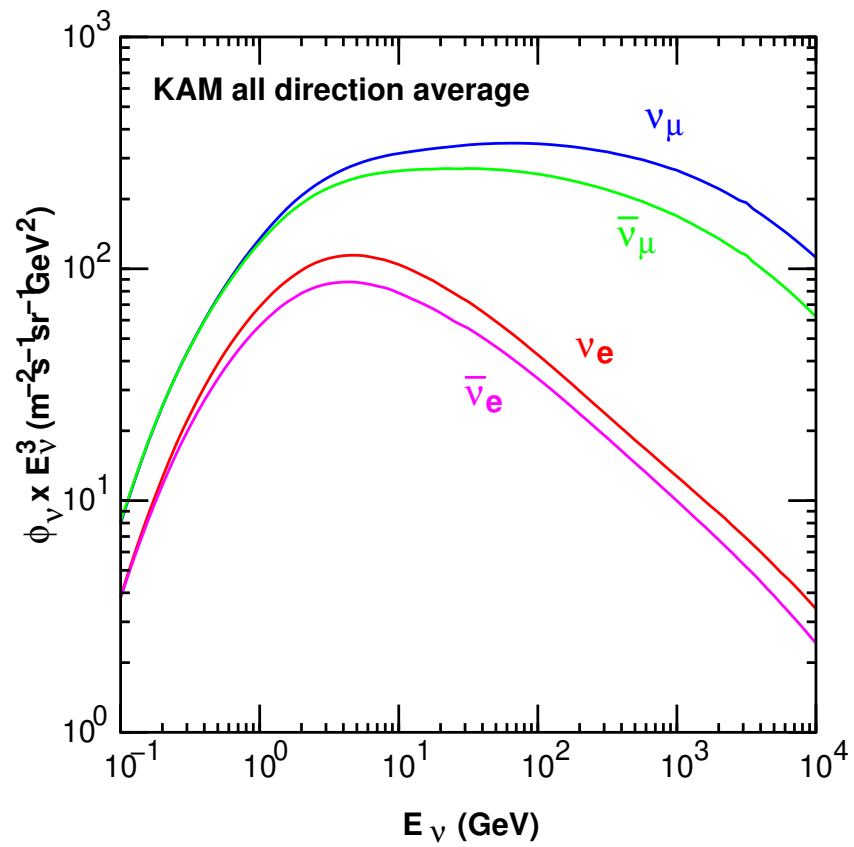


Figure 3.7: Atmospheric neutrino flux at the Super-Kamiokande site, averaged over all directions and over one year. Extracted from Ref. [144].

Both IMB and Kamiokande reported a 60–70% deficit in muon neutrinos, and no significant deficit in electron neutrinos. The Super-Kamiokande experiment explored this anomaly as a function of the energy and arrival direction of the neutrinos. The results, which will be discussed below, confirmed the deficit with large significance.

- *Iron calorimeters*: these detectors are sensitive to the energy deposition of neutrino-generated electrons and muons as they traverse a large iron volume. The Frejus [148] and NUSEX [149] experiment did not observe any atmospheric neutrino deficit (although the results were compatible with IMB and Kamiokande within $\sim 2\sigma$). Nevertheless, some years later the MACRO [32] and Soudan-2 [33] calorimetric experiments independently confirmed the Super-Kamiokande results on a significant ν_μ deficit.

Since atmospheric neutrinos have energies $\mathcal{O}(\text{GeV})$ the oscillation length induced by the “solar” squared mass splitting, $\mathcal{O}(10^{-5} \text{ eV}^2)$, is $\sim 2 \times 10^4 \text{ km}$, very large even for neutrinos that traverse the entire Earth. Thus, it can be safely ignored when analysing the data. Furthermore, since the data show no evidence for ν_e appearance, the process can be understood in terms of $\nu_\mu \rightarrow \nu_\tau$ oscillations. As both flavours have the same interactions with matter, matter effects are subdominant and the ν_μ survival probability is simply given by

$$P_{\mu\mu} = 1 - \sin^2 2\theta_{\text{atm}} \sin^2 \frac{\Delta m_{\text{atm}}^2 L}{4E}, \quad (3.9)$$

parametrised by a single mixing angle θ_{atm} and a single squared mass splitting Δm_{atm}^2 . Notice that here, since matter effects are irrelevant, there is no sensitivity to the octant of θ_{atm} or to the sign of Δm_{atm}^2 .

Interestingly, atmospheric neutrinos allow to directly test the oscillatory behaviour of Eq. (3.9) by exploiting that neutrinos with different incoming directions have travelled different distances before reaching the detector. This is parametrised in terms of the zenith angle, i.e., the angle between the neutrino direction and the vertical. The amount of ν_e and ν_μ events observed by Super-Kamiokande as a function of this angle is shown in Fig. 3.8.

The data shows a clear preference for ν_μ disappearance, and no significant ν_e appearance or disappearance. Furthermore, the deficit grows for larger zenith angles, i.e., muon neutrinos travelling for larger distances are more likely to disappear. Finally, neutrinos with larger energies are less likely to disappear: this is particularly visible in the “UpThrough” sample, which shows no significant ν_μ depletion; and in the “Multi-GeV” sample at smaller zenith angles.

These properties are exactly what is expected from Eq. (3.9). When interpreted in terms of $\nu_\mu \rightarrow \nu_\tau$ oscillations, the allowed regions for the squared mass splitting and the effective mixing angle are shown in Fig. 3.9.

3.3 Reactor neutrinos

Nuclear reactors produce copious amounts of electron anti-neutrinos in beta decay processes. Indeed, the first experimentally detected neutrinos came from a reactor [146]. Their typical energies are $\mathcal{O}(\text{MeV})$, as is characteristic in nuclear processes, and their spectrum is shown in Fig. 3.10. They are relatively easy to detect, as low-energy $\bar{\nu}_e$ induce inverse beta decay

$$\bar{\nu}_e + p \rightarrow e^+ + n, \quad (3.10)$$

a process with a very characteristic signature: e^+ annihilation into two photons with a total energy $\sim E_\nu + m_p - m_n + m_e$, where E_ν is the antineutrino energy and m_p , m_n and m_e are

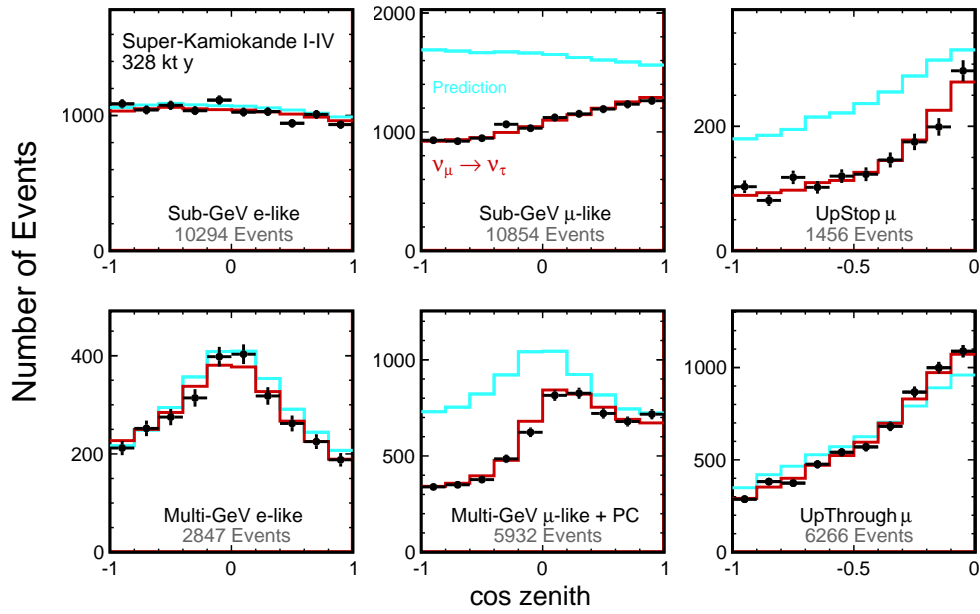


Figure 3.8: Super-Kamiokande neutrino events as a function of the zenith angle. The blue (red) lines shown the expectations without (with) $\nu_\mu \rightarrow \nu_\tau$ neutrino oscillations. The data points show a clear preference for ν_μ disappearance. The events are classified as “Sub-GeV” (“Multi-GeV”) if their deposited energy was < 1.33 GeV (> 1.33 GeV). The third column corresponds to up-going muons, generated by neutrino interactions with the surrounding rock, and classified as “UpStop” or “UpThrough” depending on whether the muons stopped inside the detector or not, respectively. The latter are generated by much more energetic neutrinos. Figure from Ref. [72].

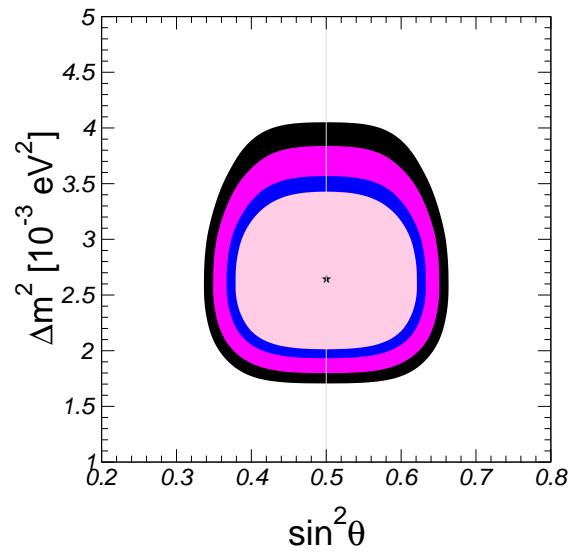


Figure 3.9: Allowed regions of $|\Delta m^2|$ and $\sin^2 \theta$ that best describe atmospheric data at 90% CL, 95% CL, 99% CL and 3σ . Figure courtesy of M. C. Gonzalez-García and M. Maltoni.

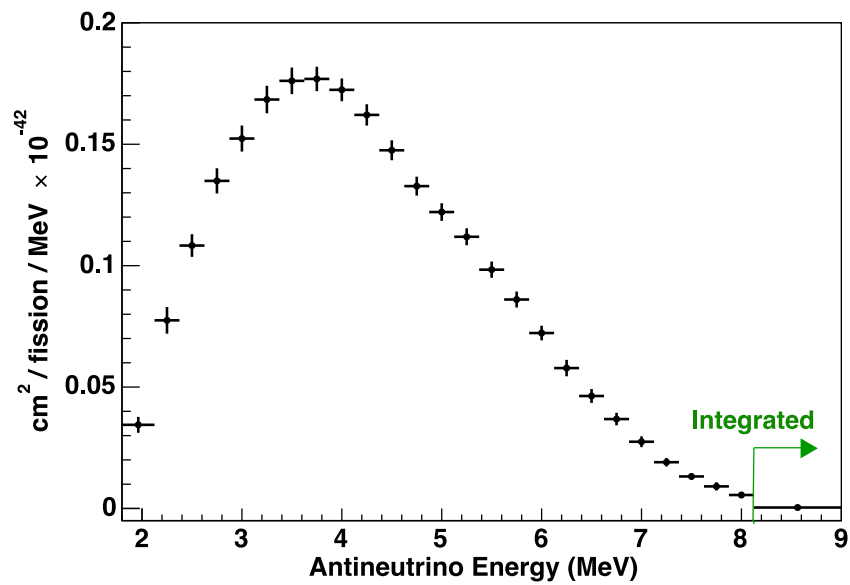


Figure 3.10: Reactor $\bar{\nu}_e$ spectrum, as measured by the Daya Bay collaboration [150].

the proton, neutron and electron masses; as well as neutron capture if the detector material is sensitive to it. e^+ annihilation also allows to cleanly measure the antineutrino energy.

As reactor antineutrinos have low energies, they are sensitive to rather low squared mass splittings. In this sense, we can distinguish two types of reactor neutrino experiments

- *Long baseline reactor experiments:* these experiments look for reactor $\bar{\nu}_e$ disappearance at baselines $\mathcal{O}(100 \text{ km})$. I.e., they are sensitive to squared mass splittings $\mathcal{O}(10^{-5} \text{ eV}^2)$, and so they can independently confirm the neutrino oscillation solution to the solar neutrino deficit.

With this idea, the KamLAND liquid scintillator detector [91] was built in the Kamioka mine in Japan, about 100 km away from several Japanese nuclear power plants. The ratio between the observed number of events and the expectation without $\bar{\nu}_e$ disappearance is shown in Fig. 3.11. As can be seen, the data clearly shows the oscillatory pattern expected from mass-induced neutrino flavour transitions. The resulting allowed region in parameter space is shown in Fig. 3.5 (where the octant degeneracy associated with vacuum experiments is also visible). The compatibility casts no doubt on the interpretation of the solar neutrino deficit.

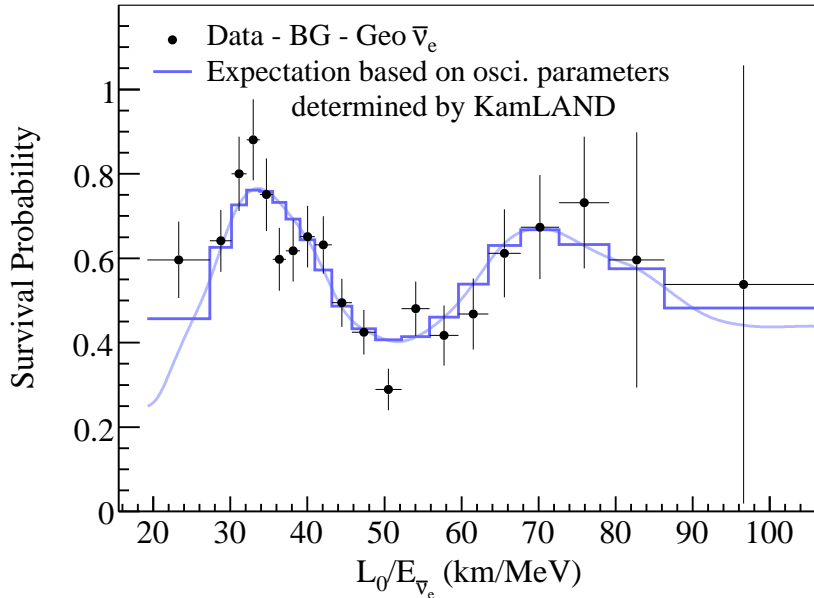


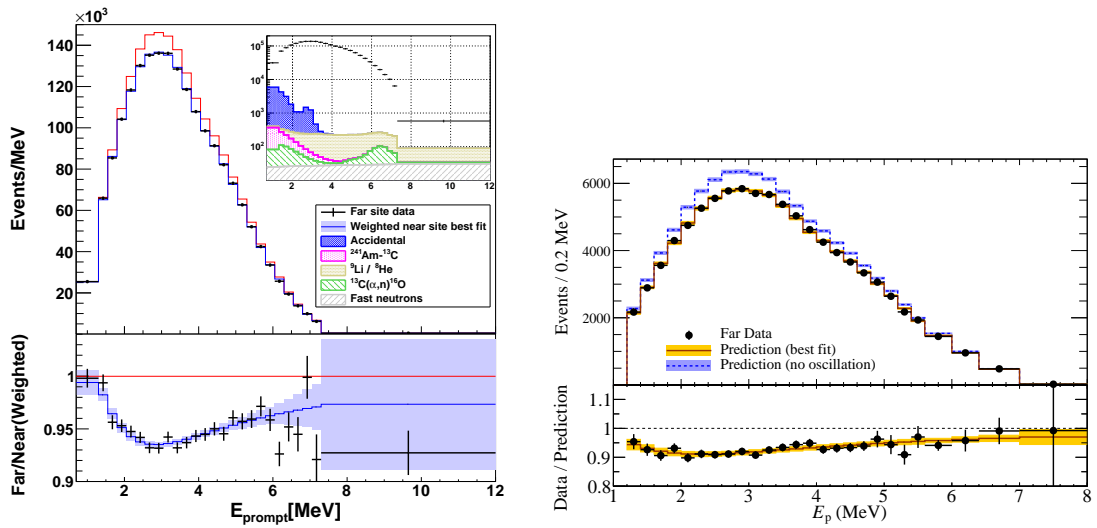
Figure 3.11: Ratio between the observed number of $\bar{\nu}_e$ events and the expectation without oscillations, as a function of $L_0/E_{\bar{\nu}_e}$. L_0 is the flux-weighted average distance to nuclear reactors, and $E_{\bar{\nu}_e}$ the antineutrino energy. The blue line corresponds to the expectation from oscillations. Figure from Ref. [34].

- *Medium baseline reactor experiments:* reactor antineutrino experiments can also look for $\bar{\nu}_e$ disappearance induced by the “atmospheric” squared mass splitting, $\mathcal{O}(10^{-3} \text{ eV}^2)$. The corresponding baseline has to be $\mathcal{O}(1 \text{ km})$, and so *a priori* the experiments look relatively easy to carry out. However, the atmospheric neutrino results showed no evidence for ν_e appearance nor disappearance, and so the mixing angle between ν_e and the mass eigenstates

involved in atmospheric ν_μ disappearance (ν_2 and ν_3 in our convention) must be tiny. In the parametrisation in Eq. (2.56), this angle is θ_{13} .

Originally, reactor experiments looking for a nonzero θ_{13} , such as CHOOZ [151] or Palo Verde [152], could only set limits $\sin^2 \theta_{13} \lesssim 0.03$. Being sensitive to smaller mixing angles required reducing the flux uncertainty below the 3% level. To this effect, a new generation of experiments was built: Double Chooz [37], Daya Bay [38] and RENO [39]. These experiments all had a detector near the reactor, that minimised systematics and flux uncertainties.

All these experiments have reported an energy-dependent $\bar{\nu}_e$ deficit shown in Fig. 3.12, pointing towards $\sin^2 \theta_{13} \sim 0.02$. The allowed region for $\sin^2 \theta_{13}$ and Δm_{32}^2 is shown in Fig. 3.13.



(a) Daya Bay results. Figure from Ref. [38].

(b) RENO results. Figure from Ref. [39].

Figure 3.12: Energy spectra of events at the RENO and Daya Bay far detectors. The lower panels show the ratio among observed and predicted number of events, as well as the prediction from neutrino oscillations. The energy is given in terms of the prompt event energy $\simeq E_{\bar{\nu}_e} - 0.78$ MeV, with $E_{\bar{\nu}_e}$ the antineutrino energy.

3.4 Accelerator neutrinos

Neutrino beams produced at proton accelerators played a significant role in the early development of the SM [11, 153–155]. The idea, which dates back to 1960 [156, 157] (see Ref. [158] for a review), is to collide high-energy protons onto a fixed target, generating a large amount of mesons (mostly pions) that decay as

$$\begin{aligned}
 p + \text{target} &\rightarrow \pi^\pm + X \\
 \pi^\pm &\rightarrow \mu^\pm + \bar{\nu}_\mu \\
 \mu^\pm &\rightarrow e^\pm + \bar{\nu}_\mu + \bar{\nu}_e.
 \end{aligned}
 \tag{3.11}$$

If the muons are stopped before they decay, a beam of muon neutrinos and antineutrinos will be generated. Furthermore, a magnetic field can be used to discard negative or positive pions,

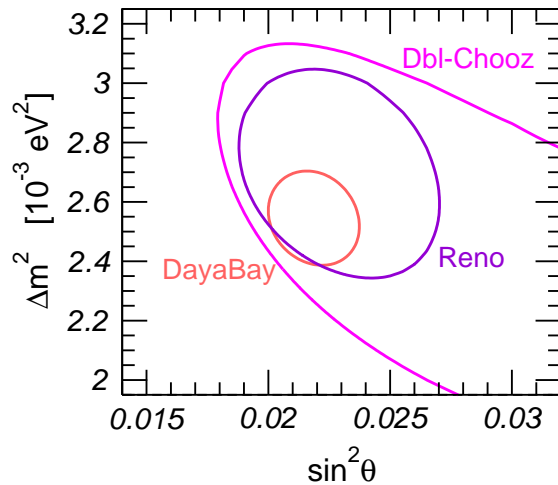


Figure 3.13: Allowed region of $|\Delta m^2|$ and $\sin^2 \theta$ at 95% CL for each relevant medium baseline reactor experiment. Figure courtesy of M. C. Gonzalez-García and M. Maltoni.

generating a beam of muon neutrinos or antineutrinos, respectively. This allows exploring matter effects and CP violation, that affect differently neutrinos and antineutrinos.

In addition, the orientation of the detector with respect to the beam can be exploited to precisely characterise neutrino oscillations. As pions are spinless particles and their muonic decays two-body decays, they emit in their rest frame neutrinos isotropically and with a fixed energy. Considering Lorentz boosts, however, the picture changes and isotropy is lost. In particular, in the laboratory frame the neutrino energy E_ν and flux ϕ_ν as a function of the angle θ with respect to the meson beam are given by

$$E_\nu(\theta) = \left(1 - \frac{m_\mu^2}{m_\pi^2}\right) \frac{E_\pi}{1 + \theta^2 \gamma^2}, \quad (3.12)$$

$$\phi_\nu(\theta) \propto \left(\frac{2\gamma}{1 + \theta^2 \gamma^2}\right)^2. \quad (3.13)$$

m_μ is the muon mass, m_π and E_π are the mass and energy of the parent pion, γ is its Lorentz factor, and L is the distance at which the flux is measured. The values of E_ν and ϕ_ν as a function of the parent pion energy are shown in Fig. 3.14. As can be seen there, an off-axis beam ($\theta \neq 0$) produces a quite monochromatic neutrino spectrum, allowing for a more precise exploration of neutrino oscillations, at the expense of reducing the flux.

Accelerator-produced neutrinos have typical energies $\sim \mathcal{O}(\text{GeV})$: a standard flux is shown in Fig. 3.15. Thus, by placing large detectors at distances $\sim \mathcal{O}(100 \text{ km})$, the neutrino oscillation interpretation of the atmospheric ν_μ deficit can be checked with a controlled beam. Due to the large baselines involved, these are usually referred to as long baseline (LBL) accelerator neutrino experiments.

The first experiments of this kind were K2K [35] and MINOS [36]. The former, with a baseline of about 235 km, sent neutrinos from the KEK facility to Super-Kamiokande. The latter, with a larger baseline of about 735 km, sent neutrinos from Fermilab to a detector in Soudan mine.

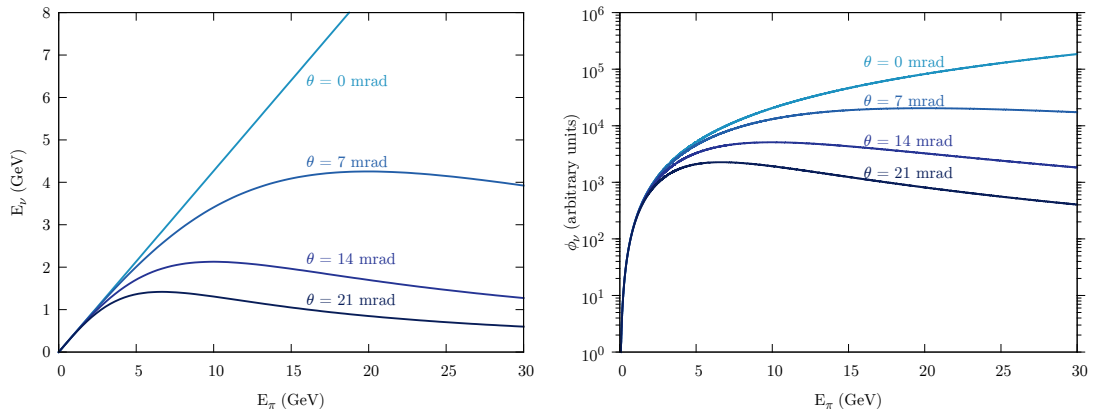


Figure 3.14: Neutrino energy (left) and flux (left) as a function of the parent pion energy at different angles θ with respect to the parent beam. Placing the neutrino detector off-axis ($\theta \neq 0$) significantly reduces the neutrino energy spread for a non-monochromatic parent beam. The neutrino flux is also reduced, though.

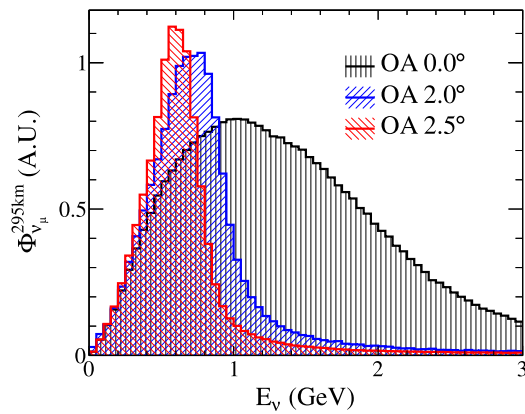
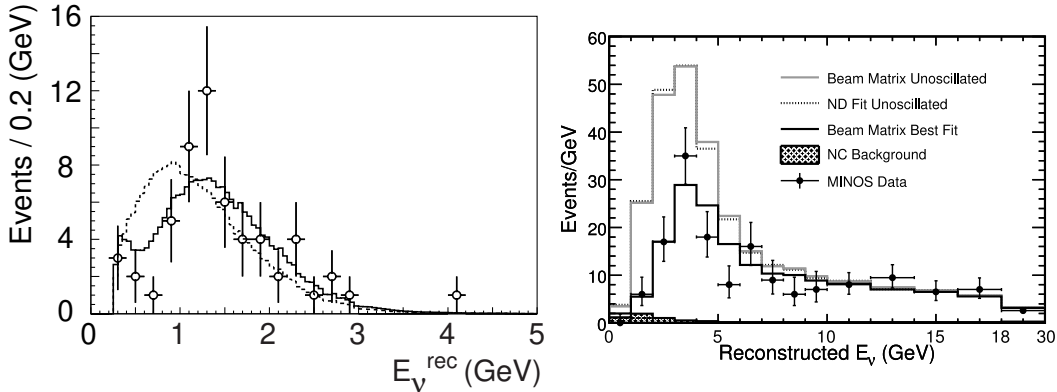


Figure 3.15: Muon neutrino flux at the T2K experiment. OA refers to the off-axis angle θ . Extracted from Ref. [159].

The spectra they observed along with the expectations without neutrino oscillations are shown in Fig. 3.16. As the Figure shows, they both confirmed muon neutrino disappearance with a controlled beam. The allowed parameter region is shown in Fig. 3.17, which also displays the compatibility with the atmospheric ν_μ disappearance results.



(a) K2K results. Figure from Ref. [160].

(b) MINOS results. Figure from Ref. [161].

Figure 3.16: Energy spectra of events at the K2K and MINOS detectors, along with the expectations, in solid and dark respectively. For K2K, the dashed line is the expected spectrum without oscillations *normalised to the observed number of events*. For MINOS, the clear line shows the expected number of events without oscillations.

All the data presented up to now robustly established the three-neutrino mixing paradigm. Nevertheless, there were still some open questions at the beginning of the 2010s:

- The “atmospheric” parameters were known with a rather low precision. In particular, it was not clear if the corresponding mixing angle, θ_{23} in the parametrisation (2.56), is maximal ($\theta_{23} = 45^\circ$) or not.
- The octant of θ_{23} was unknown.
- The sign of the “atmospheric” squared mass splitting, Δm_{32}^2 in our convention, was unknown. In other words, it was not known if the mass ordering was normal or inverted.
- Perhaps the physically most relevant question was whether CP is violated in the leptonic sector. This question became more significant when a non-zero θ_{13} was measured: CP violation in the quark sector is rather small because the mixing angles entering the invariant (2.41) are small. However, leptonic mixing angles are quite large, and so the Jarlskog invariant could be up to three orders of magnitude larger in the leptonic sector.

The first question is difficult to assess with atmospheric neutrino data, as Eq. (3.9) has a minimum at $\theta_{23} = 45^\circ$. Thus, determining the maximality of this angle accounts to measuring whether the ν_μ disappearance probability is exactly zero for $E = \frac{L}{4\Delta m_{\text{atm}}^2}$ or not. Such measurement can be easily spoiled by a not well-understood neutrino spectrum and by the unavoidable experimental energy resolution. The octant of θ_{23} and the sign of $|\Delta m^2|$ cannot be measured without three-neutrino mixing effects and/or matter effects. And, finally, CP violation is a three-flavour effect that requires sensitivity to three-neutrino mixing to be detectable.

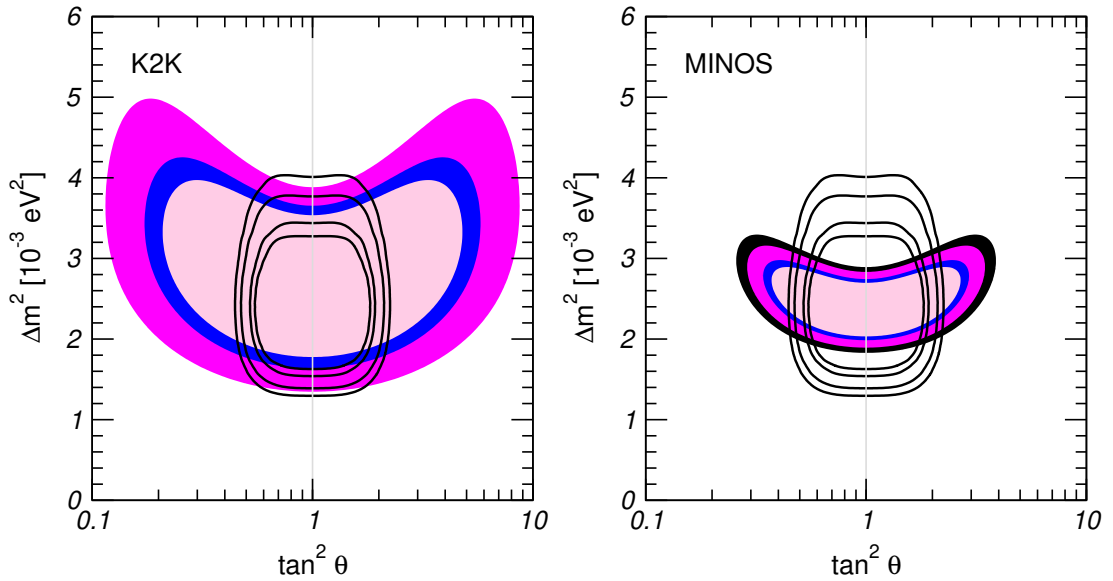


Figure 3.17: Allowed regions, in colour, of $|\Delta m^2|$ and $\tan^2 \theta$ that best describe K2K (left) and MINOS (right) data at 90% CL, 95% CL, 99% CL and 3σ . For comparison, the corresponding regions from atmospheric neutrino data are also shown in lines at the same CL. Figure from Ref. [100].

Luckily, LBL accelerator experiments can overcome these issues. By placing the detector off-axis, the neutrino beam can be quite monochromatic and relatively well-understood, as seen in Fig. 3.15. A near detector can also reduce flux uncertainties to improve the measurements. In addition, as oscillations driven by Δm_{32}^2 are mostly $\nu_\mu \rightarrow \nu_\tau$, detecting $\nu_\mu \rightarrow \nu_e$ transitions driven by this squared mass splitting directly tests three-neutrino effects. That is, ν_e appearance in LBL experiments is sensitive all to the θ_{23} octant, the mass ordering, and CP violation. Sensitivity to matter effects and CP violation can be enhanced by switching between a ν_μ and a $\bar{\nu}_\mu$ beam, as these affect differently neutrinos and antineutrinos.

With this in mind, the T2K and NO ν A experiments were built. T2K sends a neutrino beam from J-PARC to Super-Kamiokande, at 295 km; and NO ν A sends a beam from Fermilab to a far detector in Minnesota made out of liquid scintillator, at 810 km. The latter experiment has a higher energy and baseline, and thus it is more sensitive to matter effects. Their latest results are shown in Figs. 3.18 and 3.19. They clearly show $\bar{\nu}_\mu$ disappearance and $\bar{\nu}_e$ appearance. Assessing the significance, compatibility, robustness and physical consequences of the combined signal in a three-neutrino paradigm including all the neutrino experiments explained above is the main goal that this thesis pursues.

3.4.1 Simulation of long baseline accelerator experiments

As explained above, the current unknowns in leptonic flavour mixing are being explored through LBL accelerator experiments. However, since each of them has limited statistical significance, a definite answer only comes from combining the data. Furthermore, as most of the unknowns are assessed through 3-neutrino effects, it is essential to combine these experiments with solar, atmospheric, and reactor neutrino results in order to get the most out of the data and assess the true significance of the signals. Because of that, phenomenological simulations of the NO ν A and

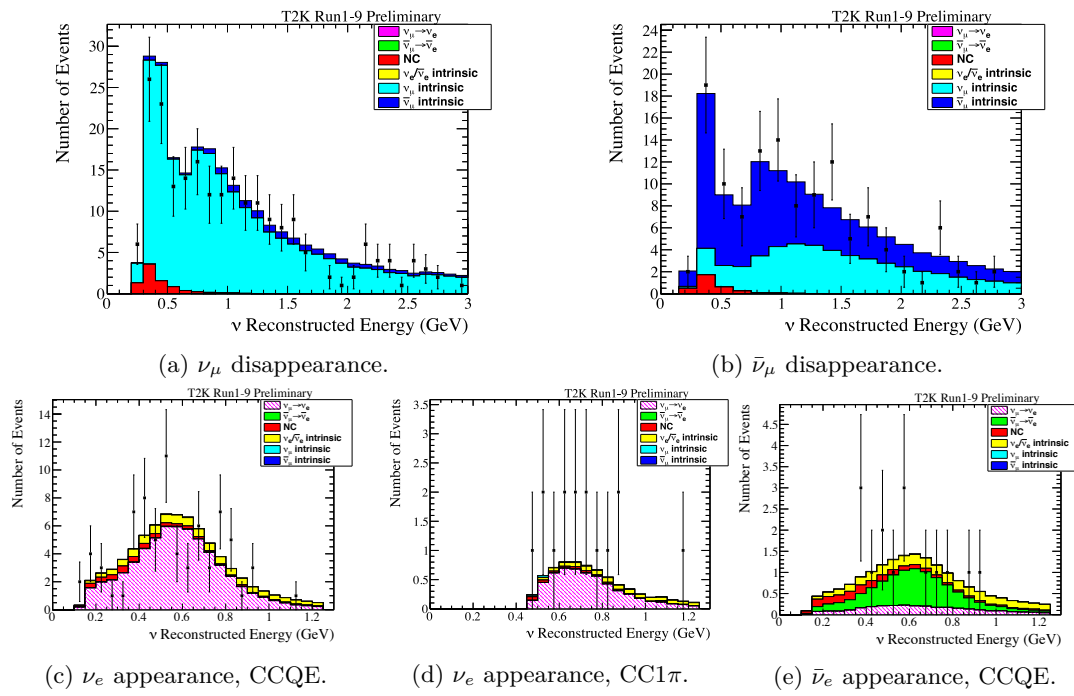


Figure 3.18: T2K results as of January 2019. The ν_e appearance results are separated as CCQE or CC1 π depending on whether the final state contains no visible pions or a single visible pion. Extracted from Ref. [96].

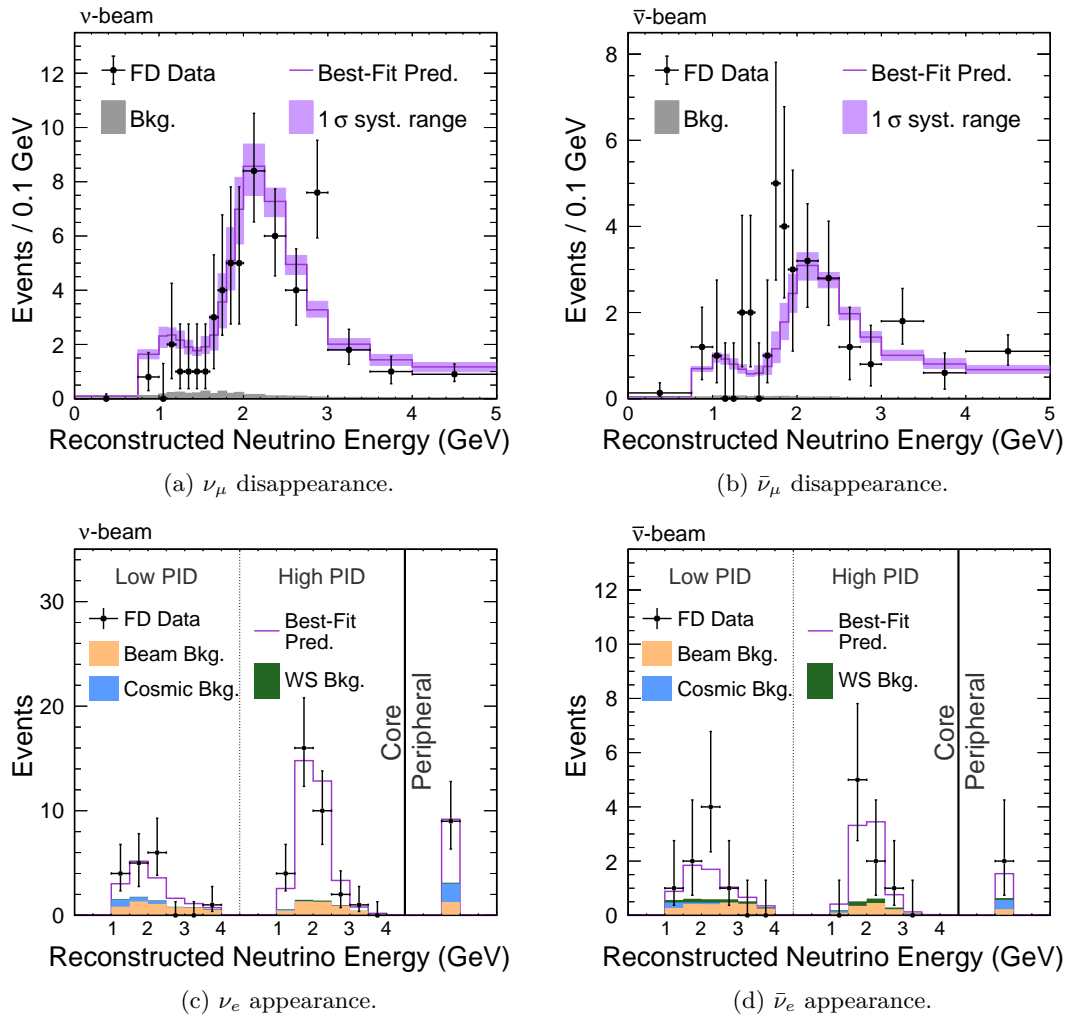


Figure 3.19: NO ν A results as of June 2019. The appearance events are classified in three bins from lowest to highest purity: “Peripheral”, “Low PID”, and “High PID”. Extracted from Ref. [97].

T2K experiments have been developed as part of this thesis. These simulations allow to analyse the data and approximately reproduce the results from each experiments, so that they can be embedded in a global framework.

Analysis framework

As in any statistical data analysis, the compatibility between data and different parameter values is determined through a log-likelihood test. In particular, for an experiment with data data_{exp} and for a set of parameters Θ , the log-likelihood for that experiment χ_{exp}^2 is given by

$$\chi_{\text{exp}}^2(\Theta) = -\ln \mathcal{P}(\text{data}_{\text{exp}}|\Theta), \quad (3.14)$$

where $\mathcal{P}(\text{data}_{\text{exp}}|\Theta)$ is the probability of obtaining the data points data_{exp} assuming the parameters to be Θ . The probabilistic nature stems both from systematic uncertainties in the experiment and from quantum mechanical fluctuations. The test statistic (3.14) is particularly useful because, for independent experiments, $\chi^2 = \sum_{\text{exp}} \chi_{\text{exp}}^2$. For the particular case of binned data n_i following a Poisson distribution with averages μ_i [72],

$$\chi_{\text{exp}}^2 = 2 \sum_i \mu_i - n_i + n_i \log \frac{n_i}{\mu_i}, \quad (3.15)$$

whereas if the data follow a Gaussian distribution with means μ_i and standard deviations σ_i ,

$$\chi_{\text{exp}}^2 = \sum_i \frac{(n_i - \mu_i)^2}{\sigma_i^2}. \quad (3.16)$$

The best fit parameters are chosen to be the ones that minimise $\chi^2(\Theta)$, whereas confidence intervals are obtained by evaluating

$$\Delta\chi^2(\Theta) = \chi^2(\Theta) - \min_{\Theta} \chi^2(\Theta). \quad (3.17)$$

According to Wilks' theorem [162], in the large sample limit (what is usually known as the *Gaussian limit*) the test statistic (3.17) is distributed following a χ^2 distribution whose number of degrees of freedom is the number of parameters in Θ . Therefore, in the Gaussian limit, a $\Delta\chi^2$ confidence interval $[0, \Delta\chi_\lambda^2]$ with confidence level (CL) λ fulfils

$$\int_0^{\Delta\chi_\lambda^2} \chi_{\text{dim } \Theta}^2(x) dx = \lambda, \quad (3.18)$$

where $\chi_{\text{dim } \Theta}^2(x)$ is a χ^2 distribution whose number of degrees of freedom is the number of parameters in Θ . Since $\chi^2 = \chi^2(\Theta)$, confidence intervals on χ^2 can be translated into confidence regions on Θ in a straightforward manner. Table 3.1 shows numerically obtained values of $\Delta\chi_\lambda^2$ for different confidence levels and degrees of freedom.

Finally, if Θ contains additional parameters apart from the ones on which we want to obtain confidence intervals, χ^2 is minimised over them and the number of degrees of freedom is accordingly reduced. Examples of such parameters include variables parametrising systematic uncertainties or additional model parameters.

CL (%)	$\Delta\chi_\lambda^2$				
	1 d.o.f.	2 d.o.f.	3 d.o.f.	4 d.o.f.	5 d.o.f.
68.27	1.00	2.30	3.53	4.72	5.89
90.00	2.71	4.61	6.25	7.78	9.24
95.00	3.84	5.99	7.81	9.49	11.07
95.45	4.00	6.18	8.02	9.72	11.31
99.00	6.63	9.21	11.34	13.28	15.09
99.73	9.00	11.83	14.16	16.25	18.21

Table 3.1: Value of $\Delta\chi_\lambda^2$ corresponding to a given confidence level (CL) for different degrees of freedom (d.o.f.) of the underlying χ^2 distribution.

Prediction of the number of events

The only ingredient left for simulating LBL accelerator experiments is the expected number of events in a given energy bin i and for a given channel α ($\alpha \in \{\nu_\mu, \nu_e, \bar{\nu}_\mu, \bar{\nu}_e\}$). This can generically be calculated as

$$N_i^\alpha = N_{\text{bkg},i} + \int_{E_i}^{E_{i+1}} dE_{\text{rec}} \int_0^\infty dE_\nu R(E_{\text{rec}}, E_\nu) \varepsilon(E_\nu) \sum_\beta \frac{d\Phi^\beta}{dE_\nu} \sigma_\alpha(E_\nu) P_{\nu_\beta \rightarrow \nu_\alpha}(E_\nu), \quad (3.19)$$

where

- $N_{\text{bkg},i}$ is the number of background events in that bin. If there is a neutrino component in the background, its oscillation has to be consistently included.
- $[E_i, E_{i+1}]$ are the bin limits.
- E_{rec} is the reconstructed neutrino energy.
- E_ν is the true neutrino energy.
- $R(E_{\text{rec}}, E_\nu)$ is the energy reconstruction function: the probability to observe a reconstructed energy E_{rec} if the true neutrino energy is E_ν . We take it to be Gaussian, i.e.,

$$R(E_{\text{rec}}, E_\nu) = \frac{1}{\sqrt{2\pi}\sigma_E E_\nu} \exp\left[-\frac{1}{2\sigma_E^2} \left(\frac{E_\nu - E_{\text{rec}}}{E_\nu}\right)^2\right], \quad (3.20)$$

that is, $\frac{E_\nu - E_{\text{rec}}}{E_\nu}$ is Gaussian-distributed around zero with standard deviation σ_E . The $\frac{1}{E_\nu}$ prefactor is for normalisation purposes.

- $\frac{d\Phi^\beta}{dE_\nu}$ is the incident neutrino flux with flavour β .
- σ_α is the ν_α detector cross-section.
- ε is the detection efficiency.
- $P_{\nu_\beta \rightarrow \nu_\alpha}(E_\nu)$ is the $\nu_\beta \rightarrow \nu_\alpha$ oscillation probability.

For the antineutrino channels, one has to switch ν by $\bar{\nu}$.

The number of background events, neutrino fluxes and cross sections, and energy resolutions can usually be obtained from the public information released by the experimental collaborations. The detection efficiencies can be adjusted to reproduce the official predicted spectra. Finally, we add overall systematic uncertainties on the global normalisation and on the reconstructed energy scale (i.e., we multiply the bin limits in reconstructed energy by a systematic parameter). These can sometimes be obtained from the collaborations, or otherwise they are adjusted to reproduce their confidence intervals.

3.5 Summary

In the last decades, the study of neutrino flavour transitions has tremendously progressed. What started as odd anomalies in solar and atmospheric neutrino fluxes has evolved into a precision science, where tiny distortions in well-controlled neutrino beams are detected and explored. Remarkably, all data from many different experiments, detection techniques, neutrino energies, baselines, traversed matter densities... fits within a simple 3 massive neutrino framework.

This effort of parametrising our first laboratory evidence for BSM physics is currently facing the challenge of determining its last unknowns. These are the maximality and octant of the mixing angle involved in atmospheric muon neutrino disappearance, the sign of the largest squared mass splitting, and the possible presence of CP violation. All these unknowns are to be assessed by LBL accelerator experiments which, at the same time, will serve as a validation of the 3 massive neutrino paradigm.

Due to the importance of these experiments in particular to assess leptonic CP violation, detailed simulations to describe their results have been developed. This will allow to combine their data with other experiments in a consistent framework in Chapter 4. Thus, a global picture will emerge that will precisely quantify our current experimental knowledge about neutrino flavour transitions and leptonic CP violation.

Chapter 4

Three-neutrino fit to oscillation data: results

Shut up and calculate.

— David Mermin

La vocación del arma es el blanco.

— Manuel Machado

In Chapter 3, we have summarised the results from the relevant neutrino experiments that have conclusively observed leptonic flavour transitions. Before the $\text{NO}\nu\text{A}$ and T2K experiments released data, each of them could be analysed to a good approximation in an effective two-neutrino framework. Because of that, there were three unknowns that cannot be assessed in this approximation: the octant of the mixing angle involved in atmospheric muon neutrino disappearance, the sign of the largest squared mass splitting, and the possible presence of CP violation.

LBL accelerator experiment address all these three questions. Once their data is analysed as described in Section 3.4.1, it can be combined in a three-neutrino framework with data from solar, atmospheric and reactor neutrinos as analysed by the NuFIT group. In this chapter, we will discuss the results, synergies and tensions that arise from that combination. We will begin with the results obtained at the beginning of this thesis, as the $\text{NO}\nu\text{A}$ experiment released its first data.

4.1 Global fit as of November 2016

4.1.1 Global analysis: determination of oscillation parameters

Data samples analyzed

In the analysis of solar neutrino data we consider the total rates from the radiochemical experiments Chlorine [23], Gallex/GNO [81] and SAGE [82], the results for the four phases of Super-Kamiokande [28, 83, 84, 163, 164], the data of the three phases of SNO included in the

form of the parametrization presented in [29], and the results of both Phase-I and Phase-II of Borexino [31, 87, 88].

Results from LBL accelerator experiments include the final energy distribution of events from MINOS [36, 94] in ν_μ and $\bar{\nu}_\mu$ disappearance and ν_e and $\bar{\nu}_e$ appearance channels, as well as the latest energy spectrum for T2K in the same four channels [165, 166] and for NO ν A on the ν_μ disappearance and ν_e appearance neutrino modes [167].

Data samples on $\bar{\nu}_e$ disappearance from reactor include the full results of the long baseline reactor data in KamLAND [168], as well as the results from medium baseline reactor experiments from CHOOZ [169] and Palo Verde [170]. Concerning running experiments we include the latest spectral data from Double-Chooz [171] and Daya-Bay [172], while for RENO we use the total rates obtained with their largest data sample corresponding to 800 days of data-taking [173].

In the analysis of the reactor data, the unoscillated reactor flux is determined as described in [174] by including in the fit the results from short baseline reactor data from ILL [175], G \ddot{o} s-gen [176], Krasnoyarsk [177, 178], ROVNO88 [179], ROVNO4 [180], Bugey3 [181], Bugey4 [182], and SRP [183].

For the analysis of atmospheric neutrinos we include the results from IceCube/DeepCore 3-year data [89].

The above data sets constitute the samples included in our NuFIT 3.0 analysis. For Super-Kamiokande atmospheric neutrino data from phases SK1–4 we will comment on our strategy in Sec. 4.1.2.

Results: oscillation parameters

The results of our standard analysis are presented in Figs. 4.1 and 4.2 where we show projections of the allowed six-dimensional parameter space.¹ In all cases when including reactor experiments we leave the normalization of reactor fluxes free and include data from short baseline (less than 100 m) reactor experiments. A previous analysis [185, 186] studied the impact of this choice versus that of fixing the reactor fluxes to the prediction of the latest calculations [124–126]. As expected, the overall description is better when the flux normalization f_{flux} is fitted against the data. We find $\chi^2(f_{\text{flux}} \text{ fix}) - \chi^2(f_{\text{flux}} \text{ fit}) \simeq 6$ which is just another way to quantify the well-known short baseline reactor anomaly to be $\sim 2.5\sigma$. However, the difference in the resulting parameter determination (in particular for θ_{13}) between these two reactor flux normalization choices has become marginal, since data from the reactor experiments with near detectors such as Daya-Bay, RENO and Double-Chooz (for which the near-far comparison allows for flux-normalization independent analysis) is now dominant. Consequently, in what follows we show only the $\Delta\chi^2$ projections for our standard choice with fitted reactor flux normalization.

The best fit values and the derived ranges for the six parameters at the 1σ (3σ) level are given in Tab. 4.1. For each parameter x the ranges are obtained after marginalizing with respect to the other parameters² and under the assumption that $\Delta\chi_{\text{marg}}^2(x)$ follows a χ^2 distribution. Hence the 1σ (3σ) ranges are given by the condition $\Delta\chi_{\text{marg}}^2(x) = 1$ (9). It is known that because of its periodic nature and the presence of parameter degeneracies the statistical distribution of the marginalised $\Delta\chi^2$ for δ_{CP} and θ_{23} (and consequently the corresponding CL intervals) may be modified [187, 188]. In Sec. 4.1.3 we will discuss and quantify these effects.

In Tab. 4.1 we list the results for three scenarios. In the first and second columns we assume that the ordering of the neutrino mass states is known *a priori* to be Normal or Inverted,

¹ $\Delta\chi^2$ tables from the global analysis corresponding to all 1-dimensional and 2-dimensional projections are available for download at the NuFIT website [184].

²We use the term “marginalization” over a given parameter as synonym for minimizing the χ^2 function with respect to that parameter.

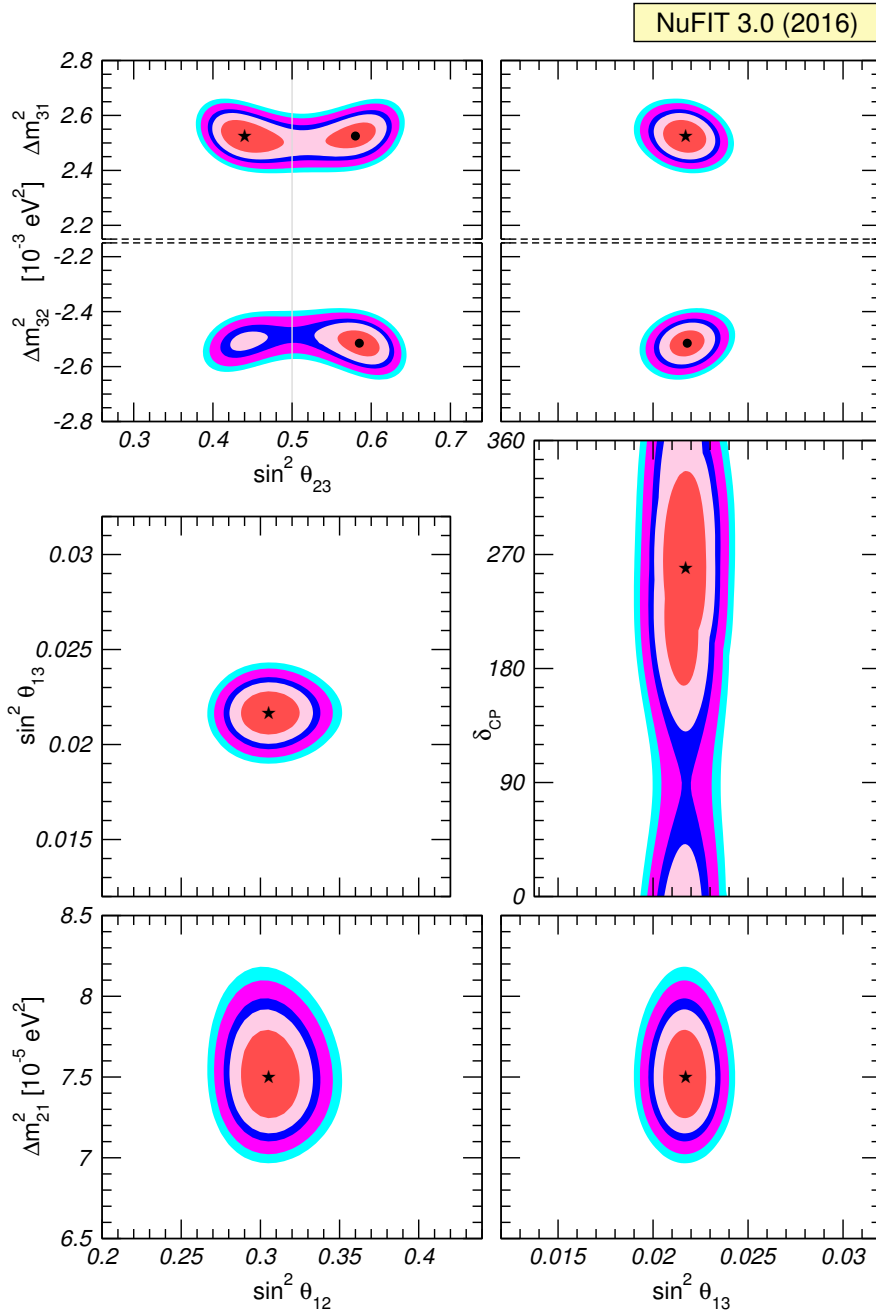


Figure 4.1: Global 3ν oscillation analysis. Each panel shows the two-dimensional projection of the allowed six-dimensional region after marginalization with respect to the undisplayed parameters. The different contours correspond to 1σ , 90%, 2σ , 99%, 3σ CL (2 dof). The normalization of reactor fluxes is left free and data from short baseline reactor experiments are included as explained in the text. Note that as atmospheric mass-squared splitting we use Δm^2_{31} for NO and Δm^2_{32} for IO. The regions in the four lower panels are obtained from $\Delta\chi^2$ minimised with respect to the mass ordering.

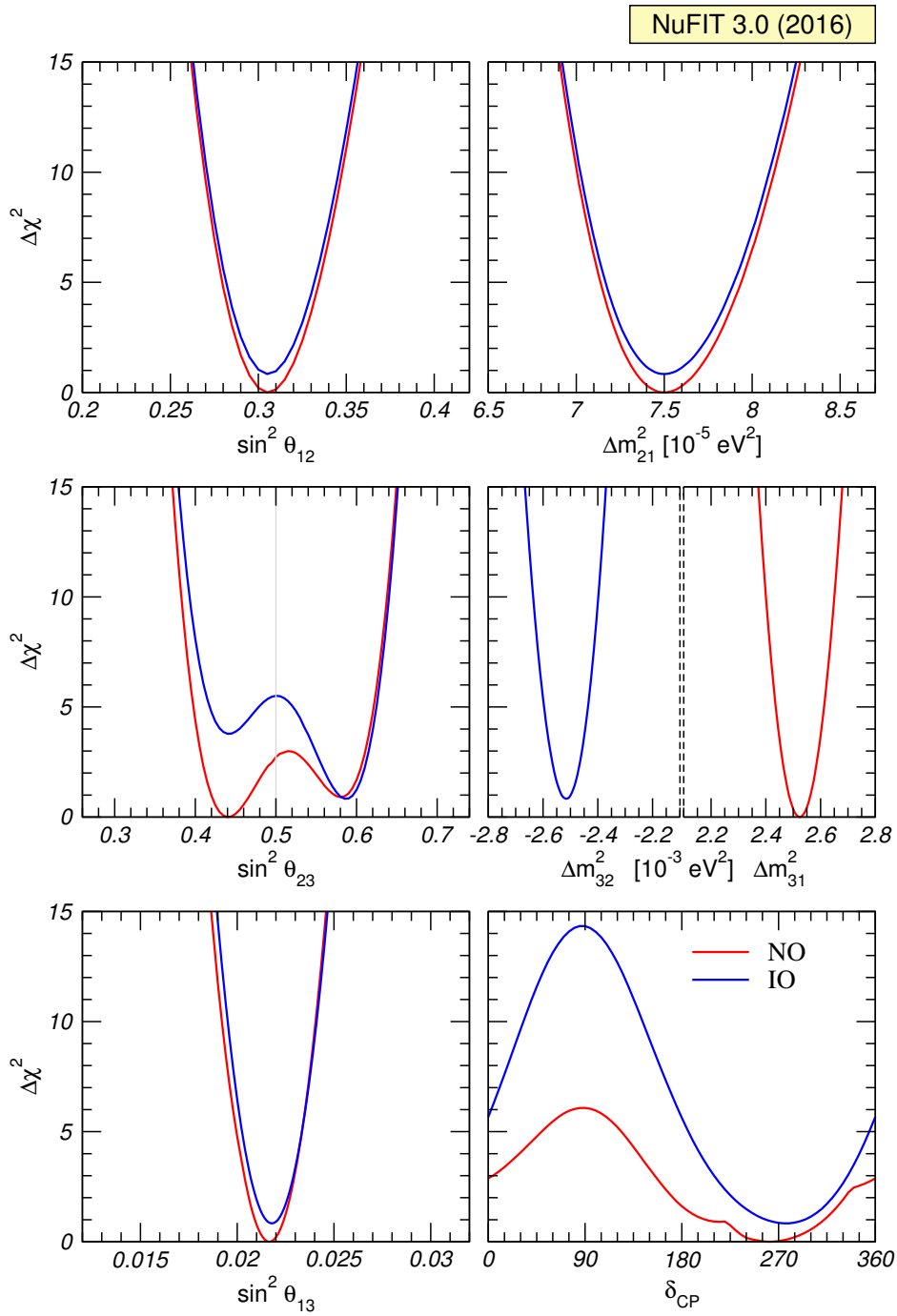


Figure 4.2: Global 3ν oscillation analysis. The red (blue) curves correspond to Normal (Inverted) Ordering. The normalization of reactor fluxes is left free and data from short baseline reactor experiments are included. Note that as atmospheric mass-squared splitting we use Δm_{31}^2 for NO and Δm_{32}^2 for IO.

	Normal Ordering (best fit)		Inverted Ordering ($\Delta\chi^2 = 0.83$)		Any Ordering 3 σ range
	bfp $\pm 1\sigma$	3 σ range	bfp $\pm 1\sigma$	3 σ range	
$\sin^2 \theta_{12}$	$0.306^{+0.012}_{-0.012}$	0.271 \rightarrow 0.345	$0.306^{+0.012}_{-0.012}$	0.271 \rightarrow 0.345	0.271 \rightarrow 0.345
$\theta_{12}/^\circ$	$33.56^{+0.77}_{-0.75}$	31.38 \rightarrow 35.99	$33.56^{+0.77}_{-0.75}$	31.38 \rightarrow 35.99	31.38 \rightarrow 35.99
$\sin^2 \theta_{23}$	$0.441^{+0.027}_{-0.021}$	0.385 \rightarrow 0.635	$0.587^{+0.020}_{-0.024}$	0.393 \rightarrow 0.640	0.385 \rightarrow 0.638
$\theta_{23}/^\circ$	$41.6^{+1.5}_{-1.2}$	38.4 \rightarrow 52.8	$50.0^{+1.1}_{-1.4}$	38.8 \rightarrow 53.1	38.4 \rightarrow 53.0
$\sin^2 \theta_{13}$	$0.02166^{+0.00075}_{-0.00075}$	0.01934 \rightarrow 0.02392	$0.02179^{+0.00076}_{-0.00076}$	0.01953 \rightarrow 0.02408	0.01934 \rightarrow 0.02397
$\theta_{13}/^\circ$	$8.46^{+0.15}_{-0.15}$	7.99 \rightarrow 8.90	$8.49^{+0.15}_{-0.15}$	8.03 \rightarrow 8.93	7.99 \rightarrow 8.91
$\delta_{\text{CP}}/^\circ$	261^{+51}_{-59}	0 \rightarrow 360	277^{+40}_{-46}	145 \rightarrow 391	0 \rightarrow 360
$\frac{\Delta m_{21}^2}{10^{-5} \text{ eV}^2}$	$7.50^{+0.19}_{-0.17}$	7.03 \rightarrow 8.09	$7.50^{+0.19}_{-0.17}$	7.03 \rightarrow 8.09	7.03 \rightarrow 8.09
$\frac{\Delta m_{3\ell}^2}{10^{-3} \text{ eV}^2}$	$+2.524^{+0.039}_{-0.040}$	+2.407 \rightarrow +2.643	$-2.514^{+0.038}_{-0.041}$	-2.635 \rightarrow -2.399	$[+2.407 \rightarrow +2.643]$ $[-2.629 \rightarrow -2.405]$

Table 4.1: Three-flavour oscillation parameters from our fit to global data after the NOW 2016 and ICHEP-2016 conferences. The numbers in the 1st (2nd) column are obtained assuming NO (IO), i.e., relative to the respective local minimum, whereas in the 3rd column we minimise also with respect to the ordering. Note that $\Delta m_{3\ell}^2 \equiv \Delta m_{31}^2 > 0$ for NO and $\Delta m_{3\ell}^2 \equiv \Delta m_{32}^2 < 0$ for IO.

respectively, so the ranges of all parameters are defined with respect to the minimum in the given scenario. In the third column we make no assumptions on the ordering, so in this case the ranges of the parameters are defined with respect to the global minimum (which corresponds to Normal Ordering) and are obtained marginalizing also over the ordering. For this third case we only give the 3 σ ranges. In this case the range of $\Delta m_{3\ell}^2$ is composed of two disconnected intervals, one containing the absolute minimum (NO) and the other the secondary local minimum (IO).

Defining the 3 σ relative precision of a parameter by $2(x^{\text{up}} - x^{\text{low}})/(x^{\text{up}} + x^{\text{low}})$, where x^{up} (x^{low}) is the upper (lower) bound on a parameter x at the 3 σ level, we read 3 σ relative precision of 14% (θ_{12}), 32% (θ_{23}), 11% (θ_{13}), 14% (Δm_{21}^2) and 9% ($|\Delta m_{3\ell}^2|$) for the various oscillation parameters.

Results: leptonic mixing matrix and CP violation

From the global χ^2 analysis described in the previous section and following the procedure outlined in Ref. [189] one can derive the 3 σ ranges on the magnitude of the elements of the leptonic mixing matrix:

$$|U^{\text{lep}}| = \begin{pmatrix} 0.800 \rightarrow 0.844 & 0.515 \rightarrow 0.581 & 0.139 \rightarrow 0.155 \\ 0.229 \rightarrow 0.516 & 0.438 \rightarrow 0.699 & 0.614 \rightarrow 0.790 \\ 0.249 \rightarrow 0.528 & 0.462 \rightarrow 0.715 & 0.595 \rightarrow 0.776 \end{pmatrix}. \quad (4.1)$$

Note that there are strong correlations between the elements due to the unitarity constraint.

The significance of leptonic CP violation is illustrated in Fig. 4.3. In the left panel we show the dependence of $\Delta\chi^2$ of the global analysis on the Jarlskog invariant, defined in Eq. (2.89), which gives a convention-independent measure of CP violation [69]. Thus the determination of the mixing angles yields a maximum allowed CP violation

$$J_{\text{CP}}^{\text{max}} = 0.0329 \pm 0.0007 \left({}^{+0.0021}_{-0.0024} \right) \quad (4.2)$$

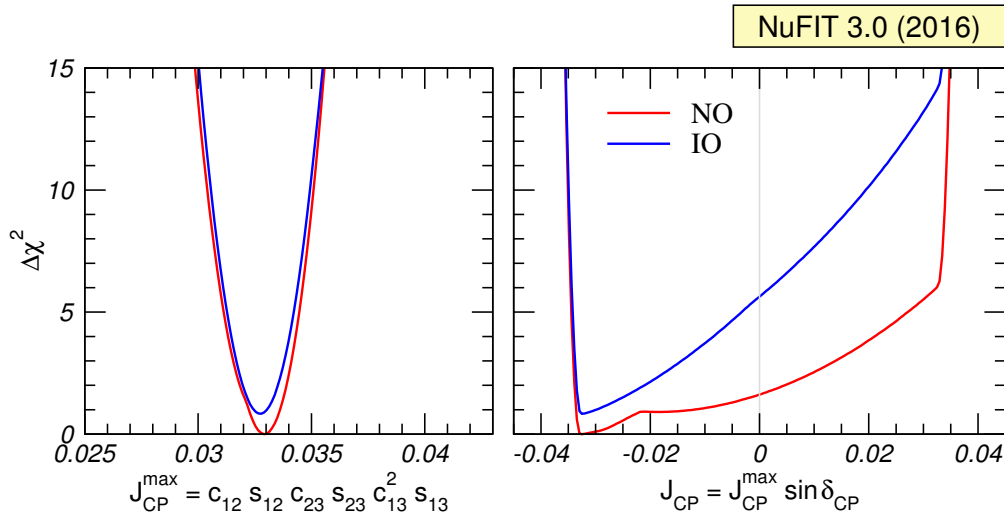


Figure 4.3: Dependence of the global $\Delta\chi^2$ function on the Jarlskog invariant. The red (blue) curves are for NO (IO).

at 1σ (3σ) for both orderings. The preference of the data for non-zero δ_{CP} implies a best fit value $J_{\text{CP}}^{\text{best}} = -0.033$, which is favoured over CP conservation with $\Delta\chi^2 = 1.7$. These numbers can be compared with the size of the Jarlskog invariant in the quark sector, which is determined to be $J_{\text{CP}}^{\text{quarks}} = (3.04^{+0.21}_{-0.20}) \times 10^{-5}$ [190].

In Fig. 4.4 we recast the allowed regions for the leptonic mixing matrix in terms of one leptonic unitarity triangle. Since in the analysis U^{lep} is unitary by construction, any given pair of rows or columns can be used to define a triangle in the complex plane. In the figure we show the triangle corresponding to the unitarity conditions on the first and third columns which is the equivalent to the one usually shown for the quark sector. In this figure the absence of CP violation implies a flat triangle, i.e., $\text{Im}(z) = 0$. As can be seen, for NO the horizontal axis crosses the 1σ allowed region, which for 2 dof corresponds to $\Delta\chi^2 \leq 2.3$. This is consistent with the preference for CP violation, $\chi^2(J_{\text{CP}} = 0) - \chi^2(J_{\text{CP}} \text{ free}) = 1.7$, mentioned above. We will comment on the statistical interpretation of this number in Sec. 4.1.3.

4.1.2 Issues in the analysis

The 3ν fit results in the previous section provide a statistically satisfactory description of all the neutrino oscillation data considered. There are however some issues in the determination of some of the parameters which, although not of statistical significance yet, deserve some attention.

Status of Δm_{21}^2 in solar experiments versus KamLAND

The analyses of the solar experiments and of KamLAND give the dominant contribution to the determination of Δm_{21}^2 and θ_{12} . It has been a result of global analyses for several years already, that the value of Δm_{21}^2 preferred by KamLAND is somewhat higher than the one from solar experiments. This tension arises from a combination of two effects which have not changed significantly over the last years: a) the well-known fact that none of the ^8B measurements performed by SNO, Super-Kamiokande and Borexino shows any evidence of the low energy spectrum turn-up expected in the standard LMA-MSW [116, 117] solution for the value of Δm_{21}^2 favoured by

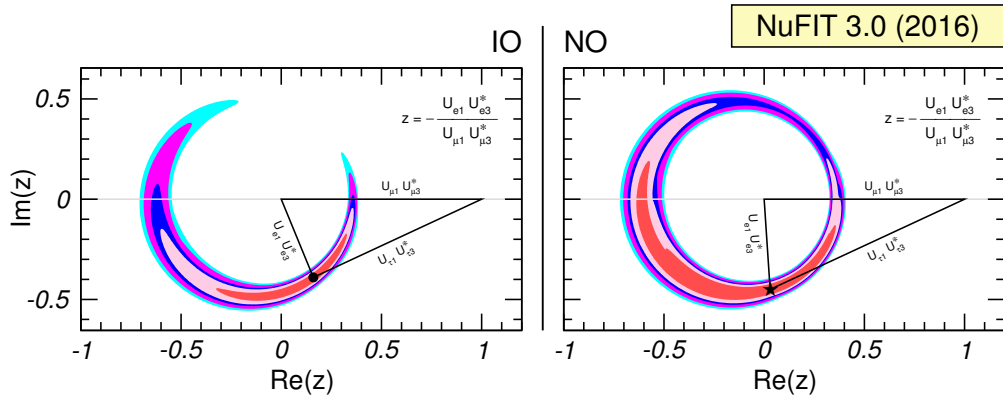


Figure 4.4: Leptonic unitarity triangle for the first and third columns of the mixing matrix. After scaling and rotating the triangle so that two of its vertices always coincide with $(0, 0)$ and $(1, 0)$ we plot the 1σ , 90%, 2σ , 99%, 3σ CL (2 dof) allowed regions of the third vertex. Note that in the construction of the triangle the unitarity of the U^{lep} matrix is always explicitly imposed. The regions for both orderings are defined with respect to the common global minimum which is in NO.

KamLAND; b) the observation of a non-vanishing day-night asymmetry in Super-Kamiokande, whose size is larger than the one predicted for the Δm_{21}^2 value indicated of KamLAND (for which Earth matter effects are very small). Ref. [185] discussed the differences in the physics entering in the analyses of solar and KamLAND data which are relevant to this tension, and to which we refer the reader for details. Here for sake of completeness we show in Fig. 4.5 the quantification of this tension in this global analysis. As seen in the figure, the best fit value of Δm_{21}^2 of KamLAND lays at the boundary of the 2σ allowed range of the solar neutrino analysis.

Also for illustration of the independence of these results with respect to the solar modelling, the solar neutrino regions are shown for two latest versions of the Standard Solar Model, namely the GS98 and the AGSS09 models [191] obtained with two different determinations of the solar abundances [192].

$\Delta m_{3\ell}^2$ determination in LBL accelerator experiments versus reactors

Figure 4.6 illustrates the contribution to the determination of $\Delta m_{3\ell}^2$ from the different data sets. In the left panels we focus on the determination from LBL experiments, which is mainly from ν_μ disappearance data. We plot the 1σ and 2σ allowed regions (2 dof) in the dominant parameters $\Delta m_{3\ell}^2$ and θ_{23} . As seen in the figure, although the agreement between the different experiments is reasonable, some “tension” starts to appear in the determination of both parameters among the LBL accelerator experiments. In particular we see that the results from NO ν A, unlike those from T2K, favour a non-maximal value of θ_{23} . It is important to notice that in the context of 3ν mixing the relevant oscillation probabilities for the LBL accelerator experiments also depend on θ_{13} (and on the θ_{12} and Δm_{21}^2 parameters which are independently well constrained by solar and KamLAND data). To construct the regions plotted in the left panels of Fig. 4.6, we adopt the procedure currently followed by the LBL accelerator experiments: we marginalise with respect to θ_{13} , taking into account the information from reactor data by adding a Gaussian penalty term to the corresponding χ_{LBL}^2 . This is not the same as making a combined analysis of LBL and reactor data as we will quantify in Sec. 4.1.2.

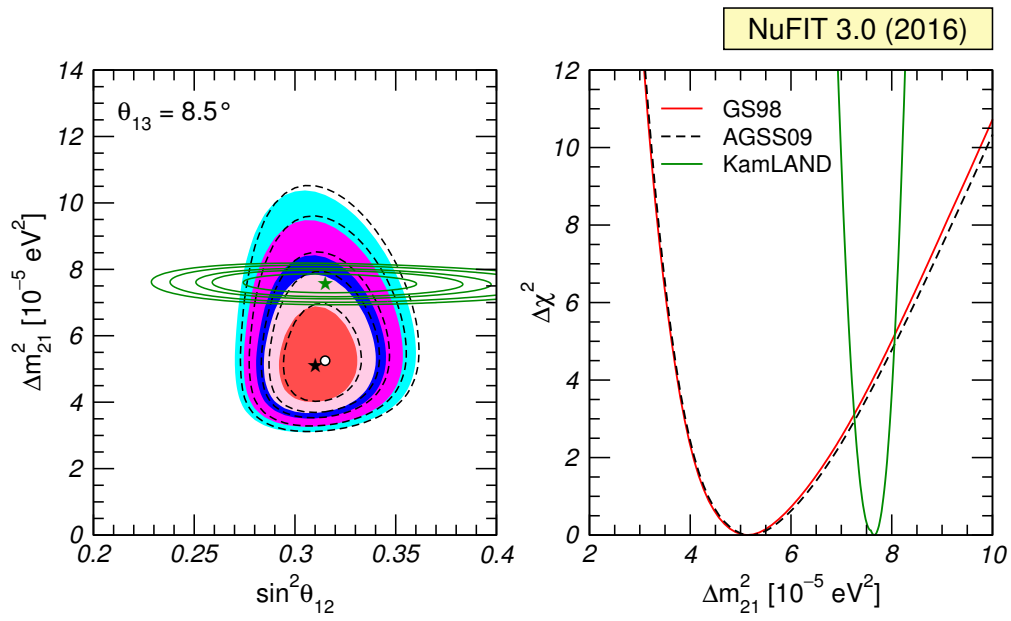


Figure 4.5: Left: Allowed parameter regions (at 1σ , 90%, 2σ , 99% and 3σ CL for 2 dof) from the combined analysis of solar data for GS98 model (full regions with best fit marked by black star) and AGSS09 model (dashed void contours with best fit marked by a white dot), and for the analysis of KamLAND data (solid green contours with best fit marked by a green star) for fixed $\theta_{13} = 8.5^\circ$. Right: $\Delta\chi^2$ dependence on Δm_{21}^2 for the same three analyses after marginalizing over θ_{12} .

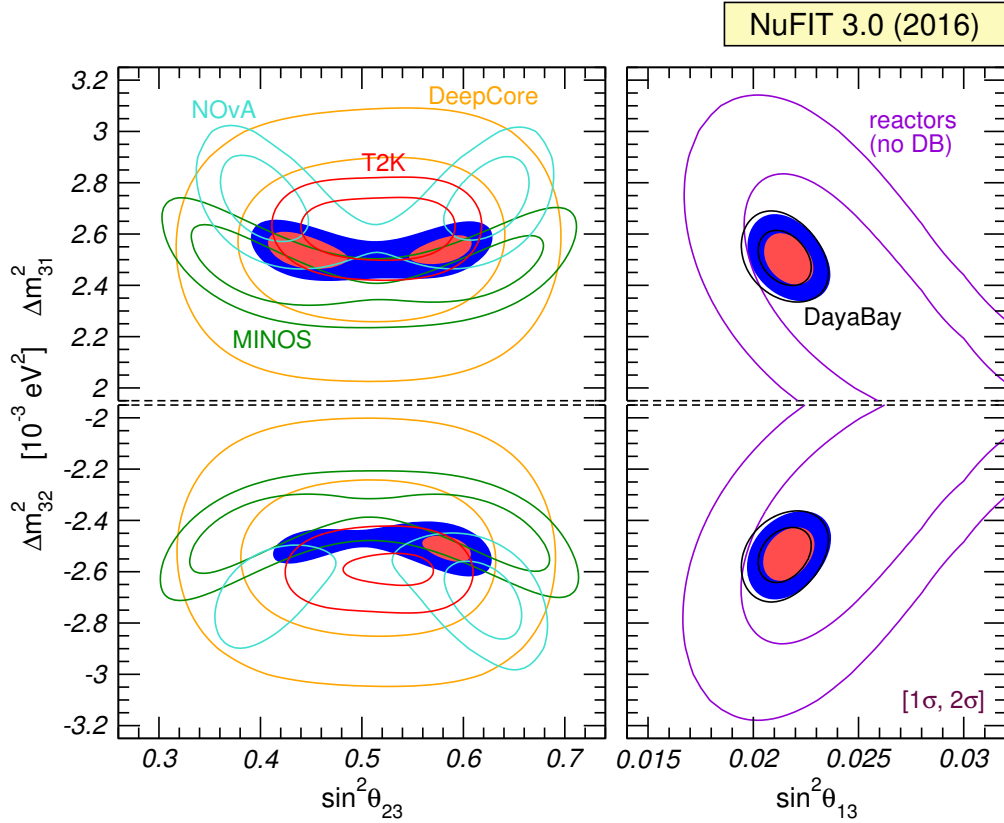


Figure 4.6: Determination of $\Delta m_{3\ell}^2$ at 1σ and 2σ (2 dof), where $\ell = 1$ for NO (upper panels) and $\ell = 2$ for IO (lower panels). The left panels show regions in the $(\theta_{23}, \Delta m_{3\ell}^2)$ plane using both appearance and disappearance data from MINOS (green line), T2K (red lines), NO ν A (light blue lines), as well as IceCube/DeepCore (orange lines) and the combination of them (colored regions). In these panels the constraint on θ_{13} from the global fit (which is dominated by the reactor data) is imposed as a Gaussian bias. The right panels show regions in the $(\theta_{13}, \Delta m_{3\ell}^2)$ plane using only Daya-Bay (black lines), reactor data without Daya-Bay (violet lines), and their combination (colored regions). In all panels solar and KamLAND data are included to constrain Δm_{21}^2 and θ_{12} . Contours are defined with respect to the global minimum of the two orderings.

Concerning ν_e disappearance data, the total rates observed in reactor experiments at different baselines can provide an independent determination of $\Delta m_{3\ell}^2$ [186, 193]. On top of this, the observation of the energy-dependent oscillation effect due to θ_{13} allows to further strengthen such measurement. In the right panels of Fig. 4.6 we show therefore the allowed regions in the $(\theta_{13}, \Delta m_{3\ell}^2)$ plane based on global data on ν_e disappearance. The violet contours are obtained from all the medium baselines reactor experiments with the exception of Daya-Bay; these regions emerge from the baseline effect mentioned above plus spectral information from Double-Chooz.³ The black contours are based on the energy spectrum in Daya-Bay, whereas the colored regions show the combination.

By comparing the left and right panels of Fig. 4.6 we observe that the combined ν_μ and ν_e disappearance experiments provide a consistent determination of $|\Delta m_{3\ell}^2|$ with similar precision. However when comparing the region for each LBL experiment with that of the reactor experiments we find some dispersion in the best fit values and allowed ranges. This is more clearly illustrated in the upper panels of Fig. 4.7, where we plot the one dimensional projection of the regions in Fig. 4.6 as a function of $\Delta m_{3\ell}^2$ after marginalization over θ_{23} for each of the LBL experiments and for their combination, together with that from reactor data after marginalization over θ_{13} . The projections are shown for NO(right) and IO(left). Let us stress that the curves corresponding to LBL experiments in the upper panels of Fig. 4.7 (as well as those in the upper panels of Figs. 4.8 and 4.9) have been obtained by a partial combination of the information on the shown parameter ($\Delta m_{3\ell}^2$ or θ_{23} or δ_{CP}) from LBL with that of θ_{13} from reactors, because in these plots only the θ_{13} constraint from reactors is imposed while the dependence on $\Delta m_{3\ell}^2$ is neglected. This corresponds to the 1-dim projections of the function:

$$\begin{aligned} \Delta\chi_{\text{LBL}+\theta_{13}^{\text{REA}}}^2(\theta_{23}, \delta_{\text{CP}}, \Delta m_{3\ell}^2) \\ = \min_{\theta_{13}} \left[\chi_{\text{LBL}}^2(\theta_{13}, \theta_{23}, \delta_{\text{CP}}, \Delta m_{3\ell}^2) + \min_{\Delta m_{3\ell}^2} \chi_{\text{REA}}^2(\theta_{13}, \Delta m_{3\ell}^2) \right] - \chi_{\text{min}}^2. \end{aligned} \quad (4.3)$$

However, since reactor data also depends on $\Delta m_{3\ell}^2$ the full combination of reactor and LBL results implies that one must add consistently the χ^2 functions of the LBL experiment with that of reactors evaluated the same value of $\Delta m_{3\ell}^2$, this is

$$\begin{aligned} \Delta\chi_{\text{LBL}+\text{REA}}^2(\theta_{23}, \delta_{\text{CP}}, \Delta m_{3\ell}^2) \\ = \min_{\theta_{13}} \left[\chi_{\text{LBL}}^2(\theta_{13}, \theta_{23}, \delta_{\text{CP}}, \Delta m_{3\ell}^2) + \chi_{\text{REA}}^2(\theta_{13}, \Delta m_{3\ell}^2) \right] - \chi_{\text{min}}^2. \end{aligned} \quad (4.4)$$

We discuss next the effect of combining consistently the information from LBL and reactor experiments in the determination of θ_{23} , δ_{CP} and the ordering.

Impact on the determination of θ_{23} , mass ordering, and δ_{CP} We plot in the lower panels of Figs. 4.7–4.9 the one dimensional projections of $\Delta\chi_{\text{LBL}+\text{REA}}^2$ for each of the parameters θ_{23} , δ_{CP} , $\Delta m_{3\ell}^2$ (marginalised with respect to the two undisplayed parameters) for the consistent LBL+REA combinations with both the information on θ_{13} and $\Delta m_{3\ell}^2$ from reactors included, Eq. (4.4). As mentioned before, the curves in the upper panels for these figures show the corresponding 1-dimensional projections for the partial combination, in which only the θ_{13} constraint from reactors is used, Eq. (4.3). For each experiment the curves in these figures are defined with respect to the global minimum of the two orderings, so the relative height of the minimum in one ordering vs the other gives a measure of the ordering favoured by each of the experiments.

³RENO also presented a spectral analysis based on an exposure of 500 days [194]. Here we prefer to include from RENO only the total rate measurement, based on the larger exposure of 800 days [173].

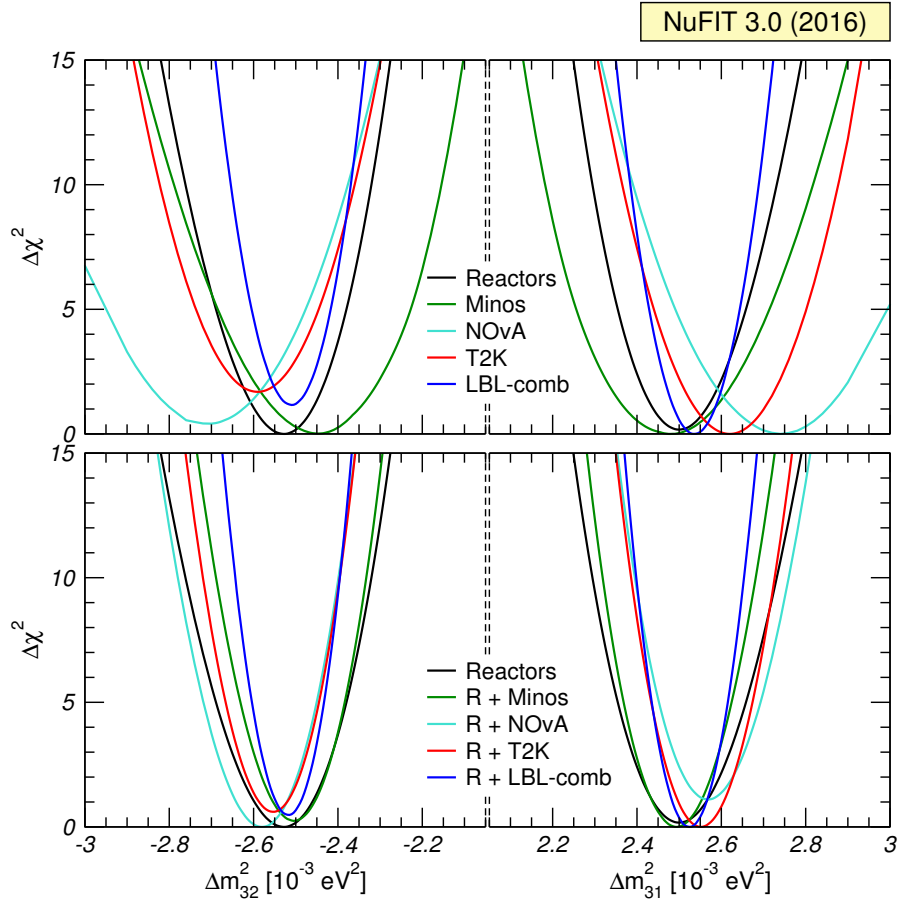


Figure 4.7: $\Delta m_{3\ell}^2$ determination from LBL accelerator experiments, reactor experiments and their combination. Left (right) panels are for IO (NO). The upper panels show the 1-dim $\Delta\chi^2$ from LBL accelerator experiments after constraining *only* θ_{13} from reactor experiments (this is, marginalizing Eq. (4.3) with respect to θ_{23} and δ_{CP}). For each experiment $\Delta\chi^2$ is defined with respect to the global minimum of the two orderings. The lower panels show the corresponding determination when the full information of LBL and reactor experiments is used in the combination (this is, marginalizing Eq. (4.4) with respect to θ_{23} and δ_{CP}).

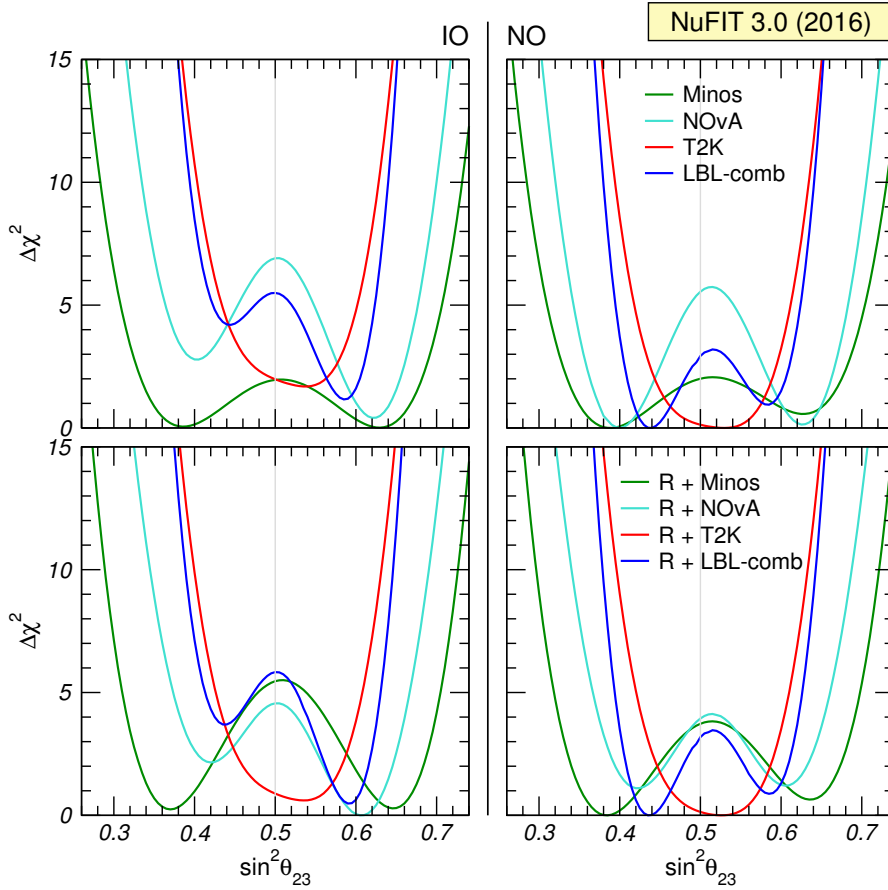


Figure 4.8: θ_{23} determination from LBL, reactor and their combination. Left (right) panels are for IO (NO). The upper panels show the 1-dim $\Delta\chi^2$ from LBL experiments after constraining *only* θ_{13} from reactor experiments (this is, marginalizing Eq. (4.3) with respect to $\Delta m_{3\ell}^2$ and δ_{CP}). For each experiment $\Delta\chi^2$ is defined with respect to the global minimum of the two orderings. The lower panels show the corresponding determination when the full information of LBL accelerator and reactor experiments is used in the combination (this is, marginalizing Eq. (4.4) with respect to $\Delta m_{3\ell}^2$ and δ_{CP}).

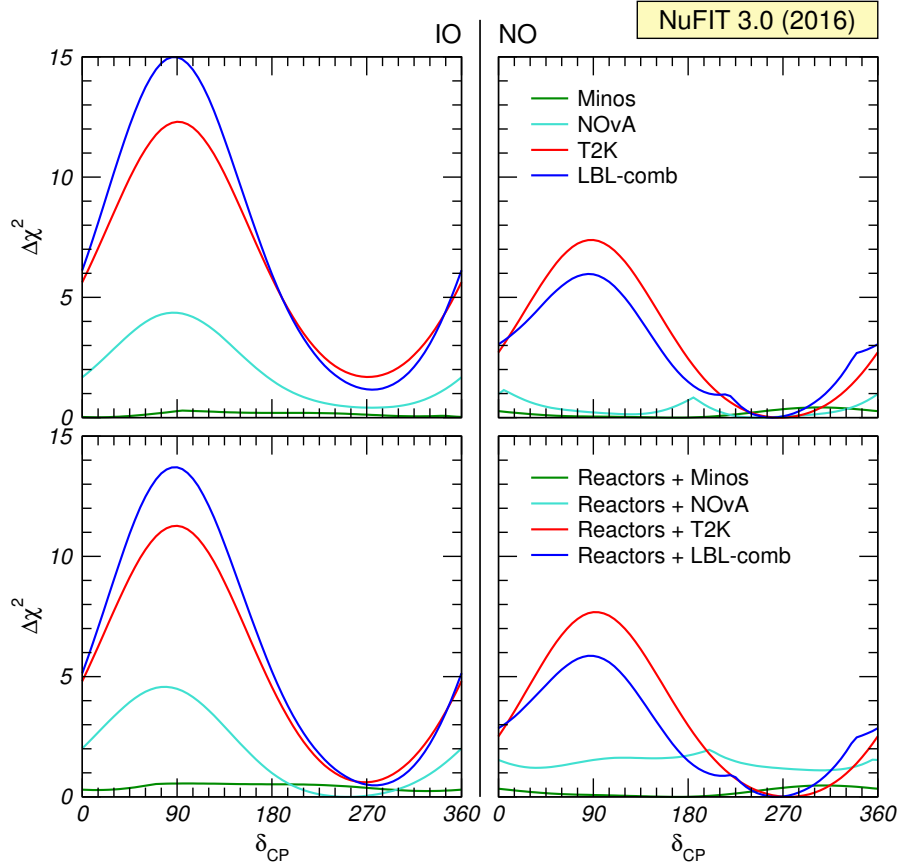


Figure 4.9: δ_{CP} determination from LBL, reactor and their combination. Left (right) panels are for IO (NO). The upper panels show the 1-dim $\Delta\chi^2$ from LBL experiments after constraining *only* θ_{13} from reactor experiments (this is, marginalizing Eq. (4.3) with respect to $\Delta m_{3\ell}^2$ and θ_{23}). For each experiment $\Delta\chi^2$ is defined with respect to the global minimum of the two orderings. The lower panels show the corresponding determination when the full information of LBL accelerator and reactor experiments is used in the combination (this is, marginalizing Eq. (4.4) with respect to $\Delta m_{3\ell}^2$ and θ_{23}).

Comparing the upper and lower panels in Figs. 4.7, 4.8 and 4.9 one sees how the contribution to the determination of the mass ordering, the octant and non-maximality of θ_{23} , and the presence of leptonic CP violation of each LBL experiment in the full LBL+REA combination (Eq. 4.4) can differ from those derived from the LBL results imposing only the θ_{13} constraint from reactors (Eq. 4.3). This is due to the additional information on $\Delta m_{3\ell}^2$ from reactors, which is missing in this last case. In particular:

- When only combining the results of the accelerator LBL experiments with the reactor bound of θ_{13} , both $\text{NO}\nu\text{A}$ and T2K favour NO by $\chi_{\text{LBL}+\theta_{13}^{\text{REA}}}^2(\text{IO}) - \chi_{\text{LBL}+\theta_{13}^{\text{REA}}}^2(\text{NO}) \simeq 0.4$ (1.7) for $\text{LBL} = \text{NO}\nu\text{A}$ (T2K). This is in agreement with the analyses shown by the collaborations for example in Refs. [165, 167]. However, when consistently combining with the reactor data, we find that the preference for NO by T2K+REA is reduced, and $\text{NO}\nu\text{A}+\text{REA}$ actually favours IO. This is due to the slightly lower value of $|\Delta m_{3\ell}^2|$ favoured by the reactor data, in particular in comparison with $\text{NO}\nu\text{A}$ for both orderings, and also with T2K for NO. Altogether we find that for the full combination of LBL accelerator experiments with reactors the “hint” towards NO is below 1σ .
- Figure 4.8 illustrates how both $\text{NO}\nu\text{A}$ and MINOS favour non-maximal θ_{23} . From this figure we see that while the significance of non-maximality in $\text{NO}\nu\text{A}$ seems more evident than in MINOS when only the information of θ_{13} is included (upper panels), the opposite holds for the full combination with the reactor data (lower panels). In particular,

$$\begin{aligned} \chi_{\text{LBL}+\theta_{13}^{\text{REA}}}^2(\theta_{23} = 45^\circ, \text{NO}) - \min_{\theta_{23}} \chi_{\text{LBL}+\theta_{13}^{\text{REA}}}^2(\theta_{23}, \text{NO}) &= 5.5 \quad (2.0), \\ \chi_{\text{LBL}+\theta_{13}^{\text{REA}}}^2(\theta_{23} = 45^\circ, \text{IO}) - \min_{\theta_{23}} \chi_{\text{LBL}+\theta_{13}^{\text{REA}}}^2(\theta_{23}, \text{IO}) &= 6.5 \quad (1.9), \\ \chi_{\text{LBL}+\text{REA}}^2(\theta_{23} = 45^\circ, \text{NO}) - \min_{\theta_{23}} \chi_{\text{LBL}+\text{REA}}^2(\theta_{23}, \text{NO}) &= 2.8 \quad (3.7), \\ \chi_{\text{LBL}+\text{REA}}^2(\theta_{23} = 45^\circ, \text{IO}) - \min_{\theta_{23}} \chi_{\text{LBL}+\text{REA}}^2(\theta_{23}, \text{IO}) &= 4.6 \quad (5.2), \end{aligned} \quad (4.5)$$

for $\text{LBL} = \text{NO}\nu\text{A}$ (MINOS). The T2K results, though, are compatible with $\theta_{23} = 45^\circ$ for any ordering. Altogether we find that for NO the full combination of LBL accelerator experiments and reactors disfavour maximal θ_{23} mixing by $\Delta\chi^2 = 3.2$.

- Regarding the octant of θ_{23} , for IO all LBL accelerator experiments are better described with $\theta_{23} > 45^\circ$, adding up to a $\sim 1.8\sigma$ preference for that octant. Conversely, for NO $\theta_{23} < 45^\circ$ is favoured at $\sim 1\sigma$.
- From Fig. 4.9 we see that the “hint” for a CP phase around 270° is mostly driven by T2K data, with some extra contribution from $\text{NO}\nu\text{A}$ in the case of IO. Within the precision of the data samples in this section, the favoured ranges of δ_{CP} in each ordering by the combination of LBL accelerator experiments are pretty independent on the inclusion of the $\Delta m_{3\ell}^2$ information from reactors.

Analysis of Super-Kamiokande atmospheric data

In all the results discussed so far we have not included information from Super-Kamiokande atmospheric data. The reason is that our oscillation analysis could reproduce that of the collaboration presented in their talks (see for example Ref. [196]).

Already since SK2 the Super-Kamiokande collaboration has been presenting its experimental results in terms of a growing number of data samples. The rates for some of those samples cannot

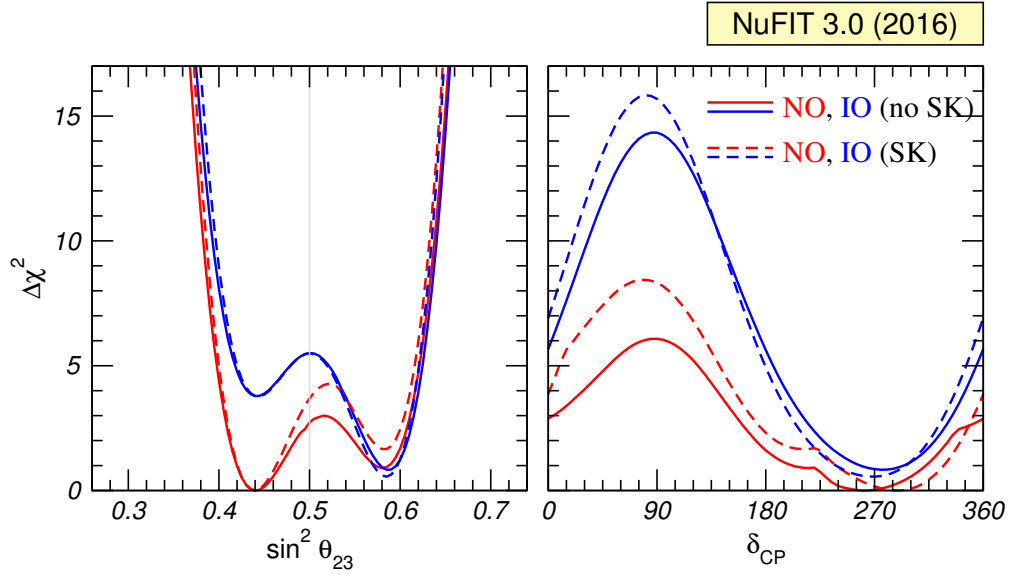


Figure 4.10: Impact of our re-analysis of Super-Kamiokande atmospheric neutrino data [195] (70 bins in energy and zenith angle) on the determination of $\sin^2 \theta_{23}$, δ_{CP} , and the mass ordering. The impact on all other parameters is negligible.

	Normal Ordering (best fit)		Inverted Ordering ($\Delta\chi^2 = 0.56$)		Any Ordering 3 σ range
	bfp $\pm 1\sigma$	3 σ range	bfp $\pm 1\sigma$	3 σ range	
$\sin^2 \theta_{23}$	$0.440^{+0.024}_{-0.019}$	$0.388 \rightarrow 0.630$	$0.584^{+0.019}_{-0.022}$	$0.398 \rightarrow 0.634$	$0.388 \rightarrow 0.632$
$\theta_{23}/^\circ$	$41.5^{+1.4}_{-1.1}$	$38.6 \rightarrow 52.5$	$49.9^{+1.1}_{-1.3}$	$39.1 \rightarrow 52.8$	$38.6 \rightarrow 52.7$
$\delta_{\text{CP}}/^\circ$	289^{+38}_{-51}	$0 \rightarrow 360$	269^{+40}_{-45}	$146 \rightarrow 377$	$0 \rightarrow 360$

Table 4.2: Three-flavour oscillation parameters from our fit to global data, including also our re-analysis of SK1–4 (4581 days) atmospheric data. The numbers in the 1st (2nd) column are obtained assuming NO (IO), i.e., relative to the respective local minimum, whereas in the 3rd column we minimise also with respect to the ordering. The omitted parameters are identical to Tab. 4.1.

be predicted (and therefore included in a statistical analysis) without a detailed simulation of the detector, which can only be made by the experimental collaboration itself. The NuFIT analysis of Super-Kamiokande data has been always based on the “classical” set of samples for which the simulations were reliable enough: sub-GeV and multi-GeV e -like and μ -like fully contained events, as well as partially contained, stopping and through-going muon data, each divided into 10 angular bins for a total of 70 energy and zenith angle bins (details on the simulation of the data samples and the statistical analysis are given in the Appendix of Ref. [100]). Despite the limitations, until recently these results represented the most up-to-date analysis of the atmospheric neutrino data which could be performed outside the collaboration, and they were able to reproduce with reasonable precision the oscillation results of the full analysis presented by Super-Kamiokande — both for what concerns the determination of the dominant parameters $\Delta m_{3\ell}^2$ and θ_{23} , as well as their rather marginal sensitivity to the subdominant ν_e appearance effects driven by θ_{13} (and consequently to δ_{CP} and the ordering). Thus the NuFIT collaboration confidently included their own implementation of the Super-Kamiokande χ^2 in the global fit.

However, in the last years Super-Kamiokande has developed a new analysis method in which a set of neural network based selections are introduced, some of them with the aim of constructing $\nu_e + \bar{\nu}_e$ enriched samples which are then further classified into ν_e -like and $\bar{\nu}_e$ -like subsamples, thus increasing the sensitivity to subleading parameters such as the mass ordering and δ_{CP} [195, 197]. The selection criteria are constructed to exploit the expected differences in the number of charged pions and transverse momentum in the interaction of ν_e versus $\bar{\nu}_e$. With this new analysis method Super-Kamiokande has been reporting in talks an increasing sensitivity to the ordering and to δ_{CP} : for example, the preliminary results of the analysis of SK1–4 (including 2520 days of SK4) [196] in combination with the reactor constraint of θ_{13} show a preference for NO with a $\Delta\chi^2(\text{IO}) = 4.3$ and variation of $\chi^2(\delta_{\text{CP}})$ with the CP phase at the level of $\sim 1.7\sigma$.

Unfortunately, with publicly available information this analysis is not reproducible outside the collaboration. Conversely the “traditional” analysis based on their reproducible data samples continues to show only marginal dependence on these effects. This is illustrated in Fig. 4.10 and Tab. 4.2 where we show the impact of inclusion of our last re-analysis of Super-Kamiokande atmospheric data using the above mentioned 70 bins in energy and zenith angle.⁴ We only show the impact on the determination of $\sin^2 \theta_{23}$, δ_{CP} , and the mass ordering as the effect on all other parameters is negligible. We observe that $\Delta\chi^2$ for maximal mixing and the second θ_{23} octant receive an additional contribution of about 1 unit in the case of NO, whereas the θ_{23} result for IO is practically unchanged. Values of $\delta_{\text{CP}} \simeq 90^\circ$ are slightly more disfavoured, whereas there is basically no effect on the mass ordering discrimination.

In summary, with the information at hand we are not able to reproduce the elements driving the main dependence on the subdominant effects of the official (though preliminary and unpublished) Super-Kamiokande results, while the dominant parameters are currently well determined by LBL experiments. For these reasons we have decided not to include our re-analysis of Super-Kamiokande data in our preferred global fit presented in the previous section. Needless to say that when enough quantitative information becomes available to allow a reliable simulation of the subdominant ν_e -driven effects, we will proceed to include it in our global analysis.

4.1.3 Monte Carlo evaluation of confidence levels for θ_{23} , δ_{CP} and ordering

From the analysis presented in Chapter 3 we see that the three least known neutrino oscillation parameters are the Dirac CP violating phase δ_{CP} , the octant of θ_{23} and the mass ordering (which

⁴We use the same data and statistical treatment as in the previous global fit NuFIT 2.0 [185] as well as in versions 2.1 and 2.2 [184] which is based on 4581 days of data from SK1–4 [195] (corresponding to 1775 days of SK4).

in what follows we will denote by “O”). In order to study the information from data on these parameters one can use two $\Delta\chi^2$ test statistics [188, 198]:

$$\Delta\chi^2(\delta_{\text{CP}}, \text{O}) = \min_{x_1} \chi^2(\delta_{\text{CP}}, \text{O}, x_1) - \chi_{\text{min}}^2, \quad (4.6)$$

$$\Delta\chi^2(\theta_{23}, \text{O}) = \min_{x_2} \chi^2(\theta_{23}, \text{O}, x_2) - \chi_{\text{min}}^2, \quad (4.7)$$

where the minimization in the first equation is performed with respect to all oscillation parameters except δ_{CP} and the ordering ($x_1 = \{\theta_{12}, \theta_{13}, \theta_{23}, \Delta m_{21}^2, |\Delta m_{3\ell}^2|\}$), while in the second equation the minimization is over all oscillation parameters except θ_{23} and the ordering ($x_2 = \{\theta_{12}, \theta_{13}, \delta_{\text{CP}}, \Delta m_{21}^2, |\Delta m_{3\ell}^2|\}$). Here χ_{min}^2 indicates the χ^2 minimum with respect to all oscillation parameters including the mass ordering.

We have plotted the values of these test statistics in the lower right and central left panels in Fig. 4.2. We can use them not only for the determination of δ_{CP} and θ_{23} , respectively, but also of the mass ordering. For instance, using Eq. (4.6) we can determine a confidence interval for δ_{CP} at a given CL for both orderings. However, below a certain CL no interval will appear for the less favoured ordering. In this sense we can exclude that ordering at the CL at which the corresponding interval for δ_{CP} disappears. Note that a similar prescription to test the mass ordering can be built for any other parameter as well, e.g., for θ_{23} using Eq. (4.7).⁵

In Sec. 4.1.1 we have presented confidence intervals assuming that the test statistics follow a χ^2 -distribution with 1 dof, relying on Wilks’ theorem to hold [162] (this is what we call the Gaussian limit). However, the test statistics in Eqs. (4.6) and (4.7) are expected not to follow Wilks’ theorem because of several reasons [198]:

- Sensitivity of the data presented in this section to δ_{CP} is still limited, as can be seen in Fig. 4.2: all values of δ_{CP} have $\Delta\chi^2 < 14$, and for NO not even $\Delta\chi^2 = 6$ is attained.
- Regarding θ_{23} , its precision is dominated by ν_μ disappearance experiments. Since the relevant survival probability depends dominantly on $\sin^2 2\theta_{23}$, there is both a physical boundary of their parameter space at $\theta_{23} = 45^\circ$ (because $\sin 2\theta_{23} < 1$), as well as a degeneracy related to the octant.
- The mass ordering is a discrete parameter.
- The dependence of the theoretical predictions on δ_{CP} is significantly non-linear, even more considering the periodic nature of this parameter. Furthermore, there are complicated correlations and degeneracies between δ_{CP} , θ_{23} , and the mass ordering (see Fig. 4.11 for illustration).

Therefore, one may expect deviations from the Gaussian limit of the $\Delta\chi^2$ distributions, and confidence levels for these parameters should be cross checked through a Monte Carlo simulation of the relevant experiments. We consider in the following the combination of the T2K, NO ν A, MINOS and Daya-Bay experiments, which are most relevant for the parameters we are interested in this section. For a given point of assumed true values for the parameters we generate a large number (10^4) of pseudo-data samples for each of the experiments. For each pseudo-data sample we compute the two statistics given in Eqs. (4.6) and (4.7) to determine their distributions numerically. In Ref. [198] it has been shown that the distribution of test statistics for 2-dimensional parameter region (such as for instance the middle panels of Fig. 4.11) are more close to Gaussianity than 1-dimensional ones such as Eqs. (4.6) and (4.7). Therefore we focus here on the 1-dimensional cases.

⁵Let us mention that this method to determine the mass ordering is different from the one based on the test statistic T discussed in Ref. [199].

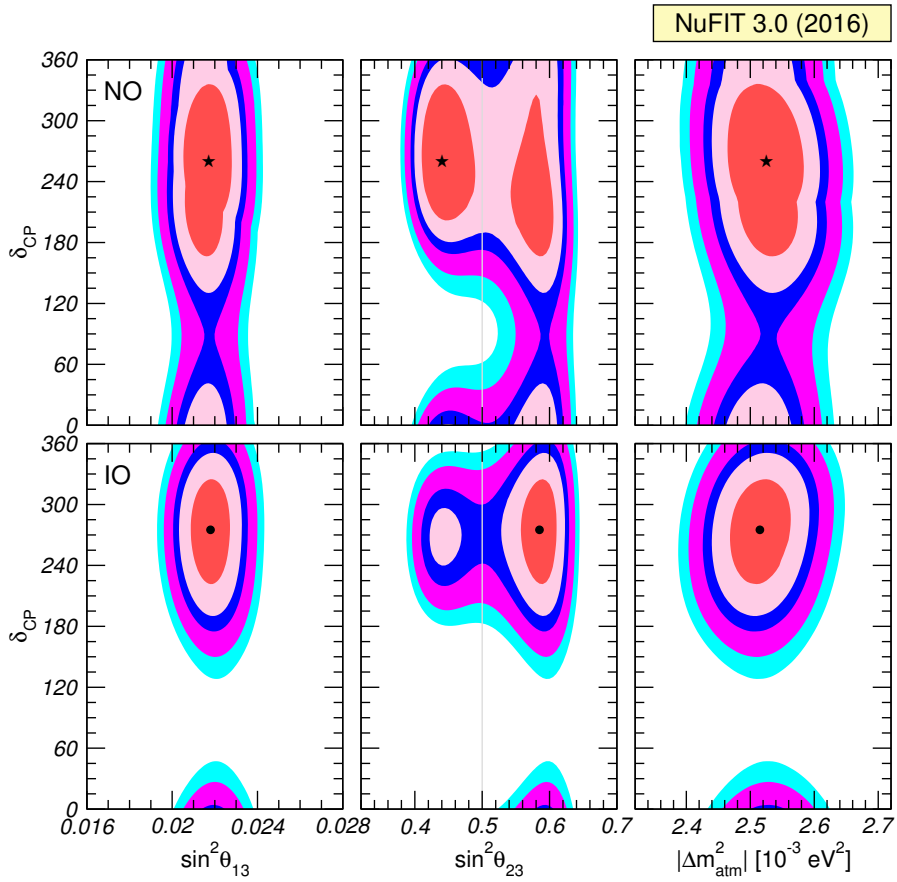


Figure 4.11: Allowed regions from the global data at 1σ , 90%, 2σ , 99% and 3σ CL (2 dof). We show projections onto different planes with δ_{CP} on the vertical axis after minimizing with respect to all undisplayed parameters. The lower (upper) panels correspond to IO (NO). Contour regions are derived with respect to the global minimum which occurs for NO and is indicated by a star. The local minimum for IO is shown by a black dot.

First, let us note that in order to keep calculation time manageable one can fix all parameters which are known to be uncorrelated with the three we are interested in (i.e., θ_{23} , δ_{CP} , O). This is certainly the case for Δm_{21}^2 and θ_{12} which are determined independently by solar and KamLAND data. As for θ_{13} , the most precise information arises from reactor data whose results are insensitive to δ_{CP} and θ_{23} . Consequently, marginalizing over θ_{13} within reactor uncertainties or fixing it to the best fit value gives a negligible difference in the simulations. Concerning $|\Delta m_{3\ell}^2|$ we observe that there are no strong correlations or degeneracies with δ_{CP} (see Fig. 4.11), and we assume that the distributions of the test statistics do not significantly depend on the assumed true value. Therefore we consider only the global best fit values for each ordering as true values for $|\Delta m_{3\ell}^2|$ to generate pseudo-data. However, since the relevant observables *do* depend non-trivially on its value, it is important to keep $|\Delta m_{3\ell}^2|$ as a free parameter in the fit and to minimise the χ^2 for each pseudo-data sample with respect to it. Hence, we approximate the test statistics in Eqs. (4.6) and (4.7) by using

$$\chi^2(\delta_{\text{CP}}, \text{O}, x_1) \equiv \min_{\theta_{23}, |\Delta m_{3\ell}^2|} \chi^2(\theta_{23}, \delta_{\text{CP}}, \text{O}, |\Delta m_{3\ell}^2|), \quad (4.8)$$

$$\chi^2(\theta_{23}, \text{O}, x_2) \equiv \min_{\delta_{\text{CP}}, |\Delta m_{3\ell}^2|} \chi^2(\theta_{23}, \delta_{\text{CP}}, \text{O}, |\Delta m_{3\ell}^2|), \quad (4.9)$$

with the other oscillation parameters kept fixed at their best fit points: $\Delta m_{21}^2 = 7.5 \times 10^{-5} \text{ eV}^2$, $\sin^2 \theta_{12} = 0.31$, and $\sin^2 \theta_{13} = 0.022$.

δ_{CP} and the mass ordering

The value of the test statistics (4.6) is shown in Fig. 4.12 for the combination of T2K, NO ν A, MINOS and Daya-Bay as a function of δ_{CP} for both mass orderings. In the generation of the pseudo-data we have assumed three representative values of $\theta_{23, \text{true}}$ as shown in the plots. The broken curves show, for each set of true values, the values of $\Delta\chi^2(\delta_{\text{CP}}, \text{O})$ which are larger than 68%, 95%, and 99% of all generated data samples.

From the figure we read that if the $\Delta\chi^2$ from real data (solid curve, identical in the three panels) for a given ordering is above the $x\%$ CL lines for that ordering for a given value of δ_{CP} , that value of δ_{CP} and the mass ordering can be rejected with $x\%$ confidence. So if the minimum of the $\Delta\chi^2$ curve for one of the orderings (in this case IO is the one with non-zero minimum) is above the $x\%$ CL line one infers that that ordering is rejected at that CL.

For the sake of comparison we also show in Fig. 4.12 the corresponding 68%, 95% and 99% Gaussian confidence levels as horizontal lines. There are some qualitative deviations from Gaussianity that have already been reported [198]:

- For $\theta_{23} < 45^\circ$, $\delta_{\text{CP}} = 90^\circ$, and IO as well as for $\theta_{23} > 45^\circ$, $\delta_{\text{CP}} = 270^\circ$ and NO, the confidence levels decrease. This effect arises because at those points in parameter space the $\nu_\mu \rightarrow \nu_e$ oscillation probability has a minimum or a maximum, respectively. Therefore, statistical fluctuations leading to less (or more) events than predicted cannot be accommodated by adjusting the parameters. $\Delta\chi^2$ is small more often and the confidence levels decrease. This is an effect always present at boundaries in parameter space, usually referred to as an effective decrease in the number of degrees of freedom in the model.
- Conversely for $\delta_{\text{CP}} \sim 90^\circ$ for $\theta_{23} > 45^\circ$, and $\delta_{\text{CP}} \sim 270^\circ$ for $\theta_{23} < 45^\circ$, the confidence levels increase. This is associated with the prominent presence of the octant degeneracy. Degeneracies imply that statistical fluctuations can drive you away from the true value, $\Delta\chi^2$ increases, and the confidence levels increase. This is usually referred to as an effective increase in the number of degrees of freedom in the model due to degeneracies.

- Overall we find that with the data presented in this section confidence levels are clearly closer to Gaussianity than found in Refs. [185,198], where similar simulations have been performed with less data available. For those data sets confidence levels were consistently below their Gaussian limit. This was mainly a consequence of the limited statistics and the cyclic nature of δ_{CP} which lead to an effective decrease in the number of degrees of freedom. We now find that when the full combination of data currently available is included this effect is reduced, as expected if experiments become more sensitive.
- For all true values considered, IO is not rejected even at 1σ . In particular we find IO disfavoured at 30% – 40% for $\sin^2 \theta_{23} = 0.44 - 0.60$.

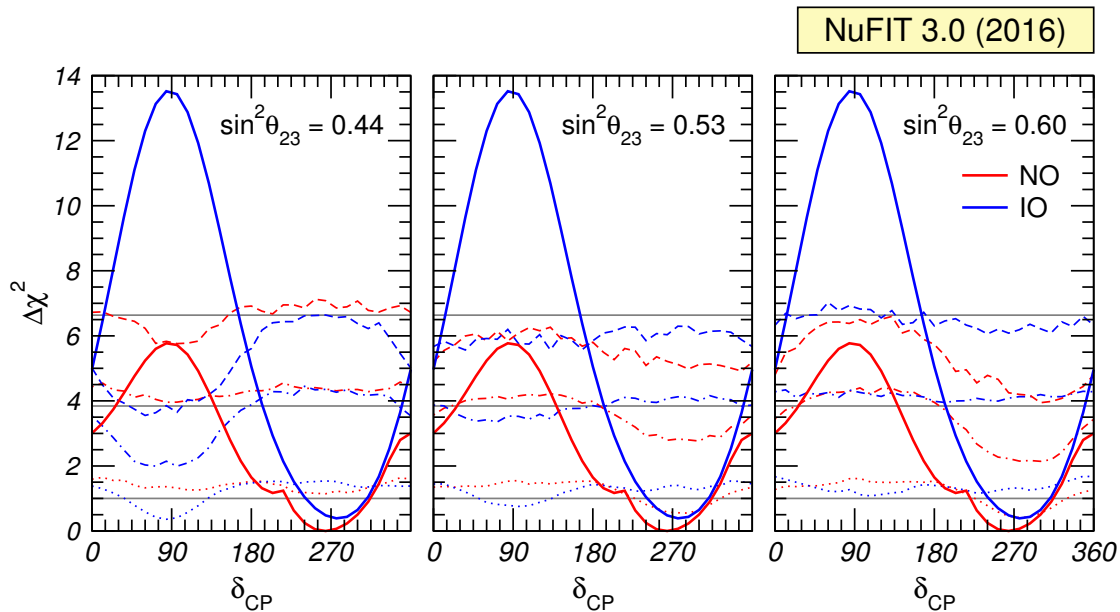


Figure 4.12: 68%, 95% and 99% confidence levels (broken curves) for the test statistics (4.6) along with its value (solid curves) for the combination of T2K, NO ν A, MINOS and reactor data. The value of $\sin^2 \theta_{23}$ given in each panel corresponds to the assumed true value chosen to generate the pseudo-experiments and for all panels we take $\Delta m_{3\ell, \text{true}}^2 = -2.53 \times 10^{-3} \text{ eV}^2$ for IO and $+2.54 \times 10^{-3} \text{ eV}^2$ for NO. The solid horizontal lines represent the 68%, 95% and 99% CL predictions from Wilks' theorem.

Quantitatively we show in Tab. 4.3 the CL at which CP conservation ($\delta_{\text{CP}} = 0, 180^\circ$) is disfavoured as well as the 90% and 95% confidence intervals for δ_{CP} . We find that the CL of rejection of CP conservation as well as the allowed ranges do not depend very significantly on $\theta_{23, \text{true}}$. This can be understood from Fig. 4.12: the dependence on $\theta_{23, \text{true}}$ occur mostly for $\delta_{\text{CP}} \sim 90^\circ$ and IO, a region discarded with a large CL, and for $\delta_{\text{CP}} \sim 270^\circ$ and NO, a region around the best fit.

Note that in the table the intervals for δ_{CP} are defined for both orderings with respect to the global minimum (which happens for NO). Hence the intervals for IO include the effect that IO is slightly disfavoured with respect to NO. They cannot be directly compared to the intervals given in Tab. 4.1, where we defined intervals relative to the local best fit point for each ordering.

$\sin^2 \theta_{23, \text{true}}$	Ordering	CP cons.	90% CL range	95% CL range
0.44	NO	70%	$[0^\circ, 14^\circ] \cup [151^\circ, 360^\circ]$	$[0^\circ, 37^\circ] \cup [133^\circ, 360^\circ]$
	IO	98%	$[200^\circ, 341^\circ]$	$[190^\circ, 350^\circ]$
0.53	NO	70%	$[150^\circ, 342^\circ]$	$[0^\circ, 28^\circ] \cup [133^\circ, 360^\circ]$
	IO	98%	$[203^\circ, 342^\circ]$	$[193^\circ, 350^\circ]$
0.60	NO	70%	$[148^\circ, 336^\circ]$	$[0^\circ, 28^\circ] \cup [130^\circ, 360^\circ]$
	IO	97%	$[205^\circ, 345^\circ]$	$[191^\circ, 350^\circ]$
Gaussian	NO	80%	$[158^\circ, 346^\circ]$	$[0^\circ, 26^\circ] \cup [139^\circ, 360^\circ]$
	IO	97%	$[208^\circ, 332^\circ]$	$[193^\circ, 350^\circ]$

Table 4.3: Confidence level with which CP conservation ($\delta_{\text{CP}} = 0, 180^\circ$) is rejected (third column) and 90% and 95% confidence intervals for δ_{CP} (fourth and fifth column) for different sets of true values of the parameters and in the Gaussian approximation. Confidence intervals for δ_{CP} as well as the CL for CP conservation are defined for both orderings with respect to the global minimum (which happens for NO).

A similar comment applies also to the CL quoted in the table to reject CP conservation. For IO this is defined relative to the best fit point in NO. We find that for NO, CP conservation is allowed at 70% CL, i.e., slightly above 1σ (with some deviations from the Gaussian result of 80% CL), while for IO the CL for CP conservation is above 2σ . Note that values of $\delta_{\text{CP}} \simeq 90^\circ$ are disfavoured at around 99% CL for NO, while for IO the rejection is at even higher CL: the $\Delta\chi^2$ with respect to the global minimum is around 14, which would correspond to 3.7σ in the Gaussian limit. Our Monte Carlo sample of 10^4 pseudo-data sets is not large enough to confirm such a high confidence level.

θ_{23} and the mass ordering

Moving now to the discussion of θ_{23} , we show the value of the test statistics (4.7) in Fig. 4.13 for the combination of T2K, NO ν A, MINOS and Daya-Bay experiments as a function of θ_{23} , for both mass orderings. For the generation of the pseudo-data we have assumed three example values $\delta_{\text{CP}, \text{true}} = 0, 180^\circ, 270^\circ$. We do not show results for $\delta_{\text{CP}, \text{true}} = 90^\circ$, since this value is quite disfavoured by data, especially for IO.⁶ The broken curves show for each set of true values, the values of $\Delta\chi^2(\theta_{23}, \text{O})$ which are larger than 68%, 95%, and 99% of all generated data samples. From the figure we see that the deviations from Gaussianity are not very prominent and can be understood as follows:

- The confidence levels decrease around maximal mixing because of the boundary on the parameter space present at maximal mixing for disappearance data.
- There is some increase and decrease in the confidence levels for $\delta_{\text{CP}} = 270^\circ$, in the same parameter region as the corresponding ones in Fig. 4.12.

In Tab. 4.4 we show the CL at which the combination of LBL and reactor experiments can disfavour maximal θ_{23} mixing ($\theta_{23} = 45^\circ$) as well as the 90% and 95% confidence intervals for $\sin^2 \theta_{23}$ for both orderings with respect to the global best fit. We observe from the table that the Gaussian approximation is quite good for both, the CL of maximal mixing as well as for

⁶We are aware of the fact that this choice is somewhat arbitrary and implicitly resembles Bayesian reasoning. In the strict frequentist sense we cannot a priori exclude any true value of the parameters.

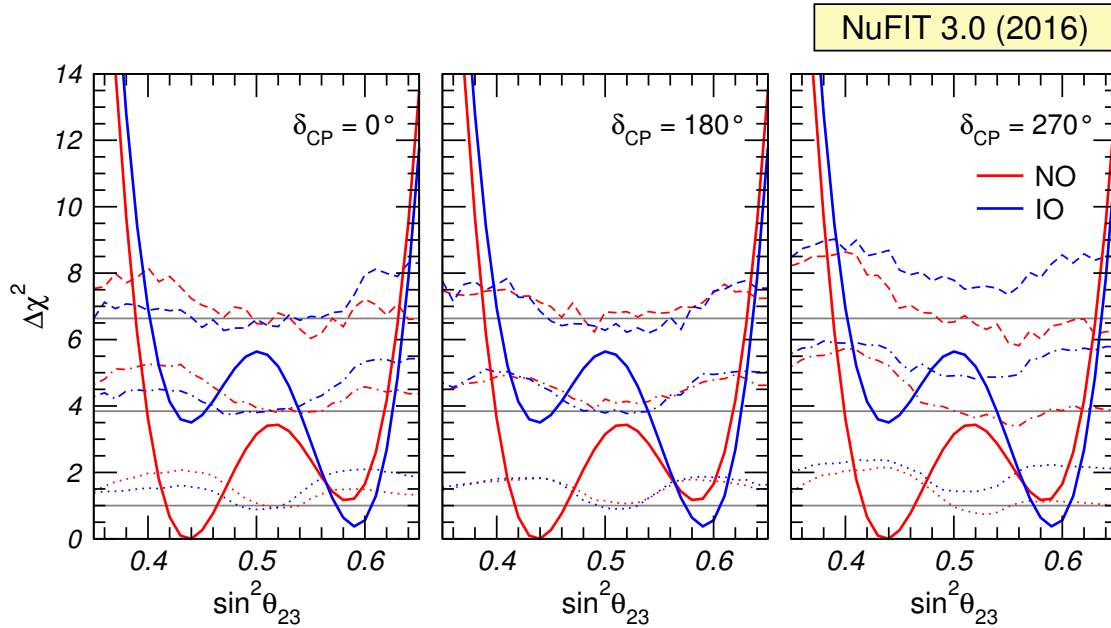


Figure 4.13: 68%, 95% and 99% confidence levels (broken curves) for the test statistics (4.7) along with its value (solid curves) for the combination of T2K, NO ν A, MINOS and reactor data. The value of δ_{CP} above each plot corresponds to the assumed true value chosen to generate the pseudo-experiments and for all panels we take $\Delta m_{3\ell, \text{true}}^2 = -2.53 \times 10^{-3} \text{ eV}^2$ for IO and $+2.54 \times 10^{-3} \text{ eV}^2$ for NO. The solid horizontal lines represent the 68%, 95% and 99% CL predictions from Wilks' theorem.

$\delta_{\text{CP}, \text{true}}$	Ordering	$\theta_{23} = 45^\circ$	90% CL range	95% CL range
0°	NO	92%	$[0.40, 0.49] \cup [0.55, 0.61]$	$[0.39, 0.62]$
	IO	98%	$[0.55, 0.62]$	$[0.42, 0.46] \cup [0.54, 0.63]$
180°	NO	91%	$[0.40, 0.50] \cup [0.54, 0.61]$	$[0.40, 0.62]$
	IO	98%	$[0.43, 0.44] \cup [0.55, 0.62]$	$[0.41, 0.46] \cup [0.54, 0.63]$
270°	NO	92%	$[0.40, 0.49] \cup [0.55, 0.61]$	$[0.39, 0.62]$
	IO	97%	$[0.42, 0.45] \cup [0.55, 0.62]$	$[0.41, 0.48] \cup [0.53, 0.63]$
Gaussian	NO	92%	$[0.41, 0.49] \cup [0.55, 0.61]$	$[0.40, 0.62]$
	IO	98%	$[0.56, 0.62]$	$[0.43, 0.45] \cup [0.54, 0.63]$

Table 4.4: CL for the rejection of maximal θ_{23} mixing (third column), and 90% and 95% CL intervals for $\sin^2 \theta_{23}$ for different sets of true parameter values and in the Gaussian approximation (last row).

$\delta_{\text{CP,true}}$	NO/2nd Oct.	IO/1st Oct.	IO/2nd Oct.
0°	62%	91%	28%
180°	56%	89%	32%
270°	70%	83%	27%
Gaussian	72%	94%	46%

Table 4.5: CL for the rejection of various combinations of mass ordering and θ_{23} octant with respect to the global best fit (which happens for NO and 1st octant). We quote the CL of the local minima for each ordering/octant combination, assuming three example values for the true value of δ_{CP} as well as for the Gaussian approximation (last row).

the confidence intervals. We conclude that the data presented in this section excludes maximal mixing at slightly more than 90% CL. Again we note that the intervals for $\sin^2 \theta_{23}$ for IO cannot be directly compared with the ones from Tab. 4.1, where they are defined with respect to the local minimum in each ordering.

In Tab. 4.5 we show the CL at which a certain combination of mass ordering and θ_{23} octant can be excluded with respect to the global minimum in the NO and 1st θ_{23} octant. We observe that the CL of the second octant for NO shows relatively large deviations from Gaussianity and dependence on the true value of δ_{CP} . In any case, the sensitivity is very low and the 2nd octant can be reject at most at 70% CL (1σ) for all values of δ_{CP} . The first octant for IO can be excluded at between 83% and 91% CL, depending on δ_{CP} . As discussed above, the exclusion of the IO/2nd octant case corresponds also to the exclusion of the IO, since at that point the confidence interval in IO would vanish. Also in this case we observe deviations from the Gaussian approximation and the CL of at best 32% is clearly less than 1σ (consistent with the results discussed in the previous subsection), showing that the considered data set has essentially no sensitivity to the mass ordering.

4.1.4 Conclusions

In this section we have presented the results of the analysis as of fall 2016 of relevant neutrino data in the framework of mixing among three massive neutrinos. Quantitatively the determination of the two mass differences, three mixing angles and the relevant CP violating phase obtained under the assumption that their log-likelihood follows a χ^2 distribution is listed in Tab. 4.1, and the corresponding leptonic mixing matrix is given in Eq. (4.1). We have found that the maximum allowed CP violation in the leptonic sector parametrised by the Jarlskog determinant is $J_{\text{CP}}^{\text{max}} = 0.0329 \pm 0.0007 \left(\begin{smallmatrix} +0.0021 \\ -0.0024 \end{smallmatrix} \right)$ at 1σ (3σ).

We have studied in detail how the sensitivity to the least-determined parameters θ_{23} , δ_{CP} and the mass ordering depends on the proper combination of the different data samples (Sec. 4.1.2). Furthermore we have quantified deviations from the Gaussian approximation in the evaluation of the confidence intervals for θ_{23} and δ_{CP} by performing a Monte Carlo study of the LBL accelerator and reactor results (Sec. 4.1.3). We can summarise the main conclusions in these sections as follows:

- The precision on the determination of $|\Delta m_{3\ell}^2|$ from ν_μ disappearance in LBL accelerator experiments NO ν A, T2K and MINOS is comparable to that from ν_e disappearance in reactor experiments, in particular with the spectral information from Daya-Bay. When comparing the region for each LBL experiment with that of the reactor experiments we find some dispersion in the best fit values and allowed ranges.

- The interpretation of the data from accelerator LBL experiments in the framework of 3ν mixing requires using information from the reactor experiments, in particular about the mixing angle θ_{13} . But since, as mentioned above, reactor data also constrain $|\Delta m_{3\ell}^2|$, the resulting CL of low confidence effects (in particular the non-maximality of θ_{23} and the mass ordering) is affected by the inclusion of this information in the combination.
- We find that the mass ordering favoured by $\text{NO}\nu\text{A}$ changes from NO to IO when the information on $\Delta m_{3\ell}^2$ from reactor experiments is correctly included in the LBL+REA combination, and the $\Delta\chi^2$ of NO in T2K is reduced from around 2 to 0.5 (see Fig. 4.7). Our MC study of the combination of LBL and reactor data shows that for all cases generated, NO is favoured but with a CL of less than 1σ .
- About the non-maximality of θ_{23} , we find that when the information on $\Delta m_{3\ell}^2$ from reactor experiments is correctly included in the LBL+REA combination, it is not $\text{NO}\nu\text{A}$ but actually MINOS which contributes most to the preference for non-maximal θ_{23} (see Fig. 4.8). Quantitatively our MC study of the combination of LBL and reactor data shows that for all the cases generated the CL for rejection of maximal θ_{23} is about 92% for NO. As seen in Fig. 4.13 and Tab. 4.4, the CL of maximal mixing as well as confidence intervals for $\sin^2\theta_{23}$ derived with MC simulations are not very different from the corresponding Gaussian approximation.
- The same study shows that for NO (IO) the favoured octant is $\theta_{23} < 45^\circ$ ($\theta_{23} > 45^\circ$). The CL for rejection of the disfavoured octant depends on the true value of δ_{CP} assumed in the MC study and it is generically lower than the one obtained in the Gaussian limit (see Tab. 4.5). For example, for NO the second octant is disfavoured at a confidence level between 0.9σ and 1.3σ depending on the assumed true value of δ_{CP} .
- The sensitivity to δ_{CP} is driven by T2K with a minor contribution from $\text{NO}\nu\text{A}$ for IO (see Fig. 4.9). The dependence of the combined CL of the “hint” towards leptonic CP violation and in particular for $\delta_{\text{CP}} \simeq 270^\circ$ on the true value of θ_{23} is shown in Fig. 4.12, from which we read that for all cases generated CP conservation is disfavoured only at 70% (1.05σ) for NO. Values of $\delta_{\text{CP}} \simeq 90^\circ$ are disfavoured at around 99% CL for NO, while for IO the rejection is at higher CL ($\Delta\chi^2 \simeq 14$ with respect to the global minimum).

Finally we comment that the increased statistics in SK4 and Borexino has had no major impact in the long-standing tension between the best fit values of Δm_{21}^2 as determined from the analysis of KamLAND and solar data, which remains an unresolved $\sim 2\sigma$ effect.

4.2 Results on δ_{CP} : from 2016 to present

The results presented above correspond to the status just after the first $\text{NO}\nu\text{A}$ data release. Along the following years, the LBL accelerator experiments (and also some reactor experiments) have continued releasing data. In this Section, we will overview how this has affected the status of the leptonic CP phase δ_{CP} . As has been shown, evaluating confidence intervals with a Monte Carlo simulation gives a similar result to using Wilks’ theorem, and so the latter will be assumed in what follows.

4.2.1 November 2017 update

About one year after the results presented in the previous Section, the T2K experiment released new data with twice as statistics in the neutrino mode and a $\sim 2\%$ increase in the antineutrino

mode data [200]. The $\bar{\nu}_\mu$ disappearance spectrum pointed towards $P_{\mu\mu} = 0$ at energies ~ 0.6 GeV, increasing the significance for maximal θ_{23} . In addition, the RENO experiment published spectral data, which slightly improved the precision on θ_{13} and $|\Delta m_{3\ell}^2|$.

The T2K $\bar{\nu}_e$ appearance results, though, significantly impacted δ_{CP} . This can be understood in terms of the approximate $\bar{\nu}_\mu \rightarrow \bar{\nu}_e$ transition probability [201–203]

$$P_{\bar{\nu}_\mu \rightarrow \bar{\nu}_e} \simeq 4 \sin^2 \theta_{13} \sin^2 \theta_{23} \frac{\sin^2 \Delta}{(1-A)^2} + \left(\frac{\Delta m_{21}^2}{\Delta m_{31}^2} \right)^2 \sin^2 2\theta_{12} \cos^2 \theta_{23} \frac{\sin^2 A \Delta}{A^2} + 8 \frac{\Delta m_{21}^2}{\Delta m_{31}^2} J_{\text{CP}}^{\text{max}} \cos(\Delta \pm \delta_{\text{CP}}) \frac{\sin \Delta A \sin \Delta (1-A)}{A(1-A)}, \quad (4.10)$$

where $J_{\text{CP}}^{\text{max}}$ is the maximum value of the leptonic Jarlskog invariant as defined in Eq. (2.89), $\Delta = \frac{\Delta m_{31}^2 L}{4E}$ and $A = \frac{2EV}{\Delta m_{31}^2}$ with V the matter potential in Eq. (2.72). The $+$ ($-$) sign applies to neutrinos (antineutrinos). The probability has been expanded at second order in the small parameters $\sin \theta_{13} \sim 0.15$ and $\frac{\Delta m_{21}^2}{\Delta m_{31}^2} \sim 0.03$.

The last term gives the sensitivity to δ_{CP} and is the most relevant for our discussion. Since T2K has a narrow neutrino spectrum peaked around maximal ν_μ disappearance, $\Delta \sim \frac{\pi}{2}$. Therefore, the ν_e appearance probability is maximised for $\delta_{\text{CP}} \sim \frac{3\pi}{2}$. At the same time, the $\bar{\nu}_e$ appearance probability is minimised for that value of δ_{CP} . Indeed, the T2K result presented in the previous Section, favouring maximal CP violation ($\delta_{\text{CP}} \sim \frac{3\pi}{2}$), was driven by an excess of ν_e events and a deficit of $\bar{\nu}_e$ events with respect to the expectations, as Table 4.6 shows. As a result, the significance for maximal CP violation was larger than the expected sensitivity.

Channel	$\delta_{\text{CP}} = 0$	$\delta_{\text{CP}} = \frac{\pi}{2}$	$\delta_{\text{CP}} = \pi$	$\delta_{\text{CP}} = \frac{3\pi}{2}$	Observed
ν_e	24.2	19.6	24.1	28.7	32
$\bar{\nu}_e$	6.9	7.7	6.8	6.0	4

Table 4.6: Expected and observed number of ν_e and $\bar{\nu}_e$ events in T2K, as of late 2016, for different values of δ_{CP} . The results are shown for NO, which increases the amount of ν_e events and decreases the amount of $\bar{\nu}_e$ events as the data indicates. The other mixing parameters are set to $\Delta m_{21}^2 = 7.53 \times 10^{-5} \text{ eV}^2$, $\sin^2 2\theta_{12} = 0.846$, $\sin^2 2\theta_{13} = 0.085$, $\Delta m_{32}^2 = 2.509 \times 10^{-3} \text{ eV}^2$ and $\sin^2 2\theta_{23} = 0.528$. Table adapted from Ref. [204].

The 2017 T2K results in those channels, which correspond to events in which only one electron Cherenkov ring was reconstructed in the final state, were closer to the expected values for $\delta_{\text{CP}} \sim \frac{3\pi}{2}$. However, the new results included data from an additional ν_e channel where a pion was also reconstructed in the final state. This channel (see Table 4.7) presented a $\sim 2\sigma$ upper fluctuation that increased the significance for $\delta_{\text{CP}} \sim \frac{3\pi}{2}$ above the expectations.

The combined $\Delta\chi^2$ as a function of δ_{CP} is shown in Fig. 4.14⁷. Comparing with Fig. 4.9, we notice that the significance for $\delta_{\text{CP}} \sim \frac{3\pi}{2}$ increased noticeably: the new results rejected $\delta_{\text{CP}} \sim \frac{\pi}{2}$ with more than 3σ . In the global combination, though, CP conservation was still allowed within 1σ , less than the T2K result alone. This was due to NO ν A and MINOS pushing θ_{23} away from 45° (see Fig. 4.8). As a consequence, for $\theta_{23} > 45^\circ$, the first term in Eq. (4.10) increases and the T2K excess could be explained without resorting to very large CP violation. This result emphasises that the hint towards maximal CP violation was *not* driven by directly observing CP violation, but by a ν_e excess requiring a very large ν_e appearance probability that maximal CP

⁷See <http://www.nu-fit.org/?q=node/150> for all the results in the global fit.

Channel	$\delta_{\text{CP}} = 0$	$\delta_{\text{CP}} = \frac{\pi}{2}$	$\delta_{\text{CP}} = \pi$	$\delta_{\text{CP}} = \frac{3\pi}{2}$	Observed
ν_e	61.4	49.9	61.9	73.5	74
ν_e (CC1 π)	6.0	4.9	5.8	6.9	15
$\bar{\nu}_e$	9.8	10.9	9.7	8.5	7

Table 4.7: Expected and observed number of ν_e and $\bar{\nu}_e$ events in T2K, as of late 2017, for different values of δ_{CP} . The results are shown for NO, which increases the amount of ν_e events and decreases the amount of $\bar{\nu}_e$ events as the data indicates. ν_e (CC1 π) refers to the channel where an electron and a single pion are detected in the final state. The other mixing parameters are set to $\Delta m_{21}^2 = 7.53 \times 10^{-5} \text{ eV}^2$, $\sin^2 \theta_{12} = 0.304$, $\sin^2 \theta_{13} = 0.0219$, $\Delta m_{32}^2 = 2.509 \times 10^{-3} \text{ eV}^2$ and $\sin^2 2\theta_{23} = 0.528$. Table adapted from Ref. [200].

violation attains. The hint for NO also had the same origin, and because of that the 2017 update increased its significance. These hints, being indirect and coming from statistical fluctuations, are expected to be sensitive to the theoretical model under which the data is analysed. This will be explored in the next chapters.

4.2.2 January 2018 update

Shortly after the update mentioned above, NO ν A released new data with $\sim 50\%$ more statistics [205]. They also observed a large amount of events in the ν_e channel, increasing the significance for maximal CP violation and NO. Their results are shown in Fig. 4.15a: unlike for T2K, they were well within the expectations.

In addition, they also improved the simulation of the energy response of their detector by including propagation of Cherenkov light inside it. As has been discussed, the issue of whether $\theta_{23} = 45^\circ$ or not is related to observing a minimum in the ν_μ spectrum. Thus, it is rather sensitive to energy mismodelling. Indeed, after this improvement the NO ν A results became perfectly compatible with $\theta_{23} = 45^\circ$. As a consequence, the ν_e excess in T2K and NO ν A could no longer be explained with a large θ_{23} , and so the significance of CP violation in the combined analysis grew up to $\sim 2\sigma$. This effect, along with the NO ν A preference for maximal CP violation, can be seen in Fig. 4.15b⁸.

4.2.3 November 2018 update

At the end of 2018, Daya Bay and RENO published new results with increased statistics, T2K increased the statistics of their antineutrino sample [206], and NO ν A released their first antineutrino data [207]. This is particularly relevant, as comparing neutrino and antineutrino data constitutes a direct check of CP violation. The whole global fit is discussed in detail in Ref. [3], and here we will explore the results affecting δ_{CP} .

This information is mostly driven by the appearance signals, depicted in Fig. 4.16a. As shown there, the T2K $\bar{\nu}_e$ sample still showed a slight downward fluctuation with respect to the expectations, driving δ_{CP} towards $\frac{3\pi}{2}$. The NO ν A data, however, did *not* show a deficit of electron antineutrinos. As a consequence, when combining the NO ν A neutrino and antineutrino samples, they did not point towards $\delta_{\text{CP}} \sim \frac{3\pi}{2}$.

Furthermore, the NO ν A $\bar{\nu}_\mu$ sample rejected maximal $\bar{\nu}_\mu$ disappearance with $\sim 3\sigma$. As has been discussed earlier in this Section, this reduces the T2K significance for CP violation. The

⁸See <http://www.nu-fit.org/?q=node/166> for all the results of the global fit.

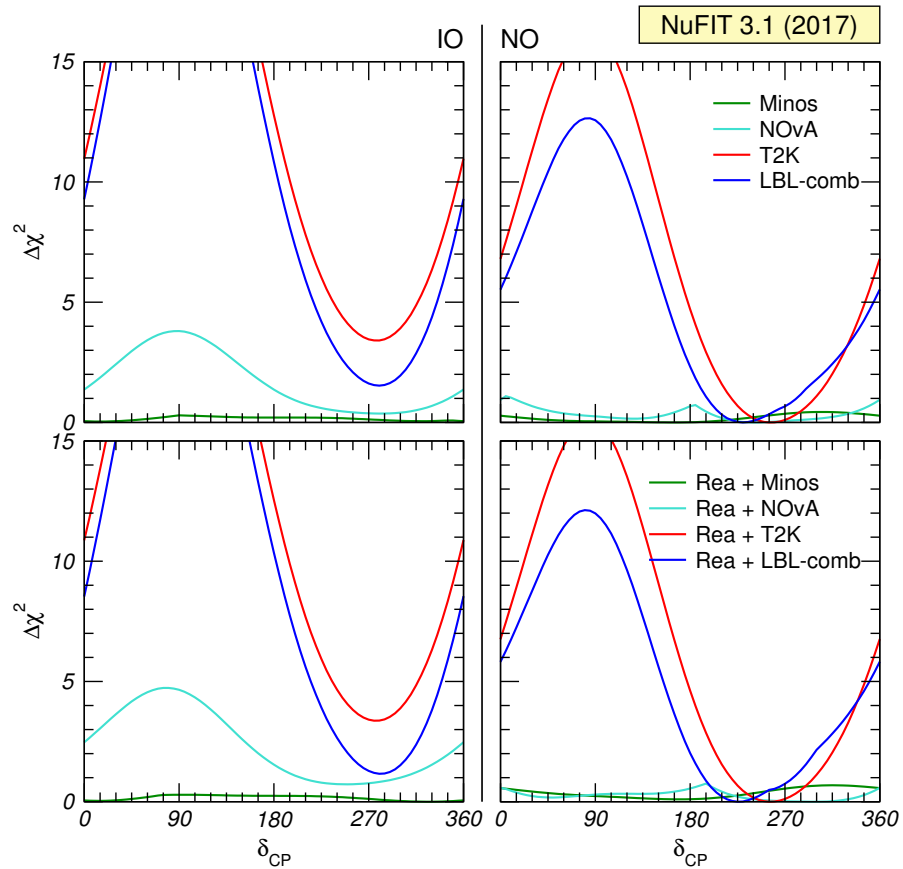
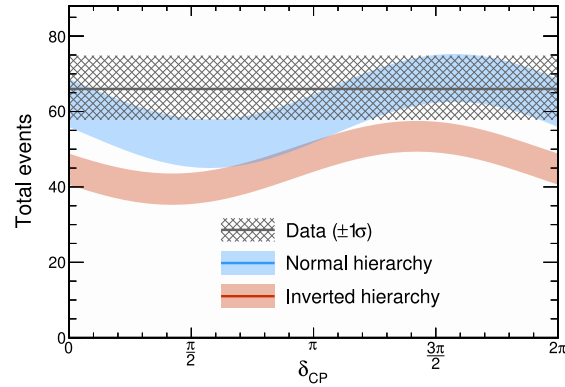
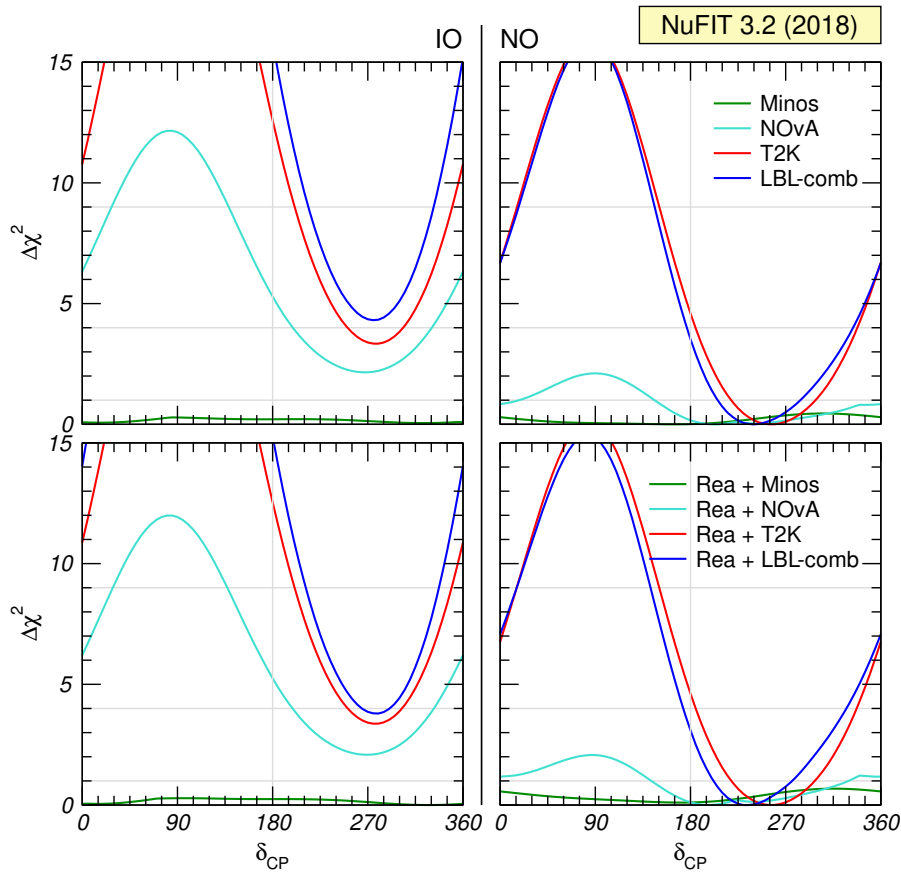


Figure 4.14: δ_{CP} determination as of November 2017. Left (right) panels are for IO (NO). The upper panels constrain only θ_{13} from reactor experiments, whereas the lower panels include the full information from them: see Fig. 4.9 and its description in the text for the difference among both procedures.



(a) Total number of observed ν_e events at NO ν A (gray). The prediction (colour) is shown as a function of δ_{extCP} for both mass orderings (here named as “hierarchy”). The bands represent the variation as $\sin^2 \theta_{23}$ changes from 0.43 to 0.60. Adapted from Ref. [205].



(b) δ_{CP} determination. Left (right) panels are for IO (NO). The upper panels constrain only θ_{13} from reactor experiments, whereas the lower panels include the full information from them: see Fig. 4.9 and its description in the text for the difference among both procedures.

Figure 4.15: Updated NO ν A results on δ_{CP} and global combination as of January 2018.

global combination is shown in Fig. 4.16b. There, we also see that it was just with the combination of neutrino and antineutrino samples that $\text{NO}\nu\text{A}$ rejected $\delta_{\text{CP}} \sim \frac{3\pi}{2}$ with $\sim 2\sigma$. CP conservation was only rejected with $\sim 1\sigma$.

4.2.4 July 2019 update

The last update before this thesis was complete took place in summer 2019, as the T2K [96] and $\text{NO}\nu\text{A}$ [97] experiments released new antineutrino data. The observed and expected number of events in the appearance channels are shown in Fig. 4.17a. As can be seen, the T2K $\bar{\nu}_e$ appearance signal has moved towards the expectation. The $\text{NO}\nu\text{A}$ $\bar{\nu}_e$ data, when combined with the ν_e signal, also keeps pointing towards $\delta_{\text{CP}} \neq \frac{3\pi}{2}$ and normal mass ordering.

In addition, the $\text{NO}\nu\text{A}$ $\bar{\nu}_\mu$ spectrum now allows $\theta_{23} = 45^\circ$ within less than 2σ : the previous indication for non-maximal θ_{23} was probably a statistical fluctuation due to the limited statistics. This has slightly increased the significance for CP violation.

The combined $\Delta\chi^2$ as a function of δ_{CP} is shown in Fig. 4.17b. As can be seen, there is still a slight tension among T2K, that prefers $\delta_{\text{CP}} \sim \frac{3\pi}{2}$ due to the large amount of observed ν_e events; and $\text{NO}\nu\text{A}$, that does not observe a significant ν_e excess and $\bar{\nu}_e$ deficit. As a consequence, the T2K $\sim 2\sigma$ hint for leptonic CP violation gets diluted to $\sim 1.5\sigma$ when all the data is combined.

Finally, as a summary of the current status of three-neutrino mixing, in Figs. 4.18 and 4.19 we show the current projections of the allowed six-dimensional parameter space⁹. The results are shown with and without the Super-Kamiokande atmospheric neutrino data: even though, as explained in Section 4.1.2, we cannot reproduce their results, they have provided a $\Delta\chi^2$ table that allows to include them in a global fit.

These figures are to be compared with Figs. 4.1 and 4.2, the first global combination produced as part of this thesis. Because of all the data released mostly by LBL accelerator experiments, there is no longer an octant degeneracy in θ_{23} , although whether $\theta_{23} = 45^\circ$ or not is still unknown. The mass ordering, about which there was no clue, is now favoured to be normal at $2\text{--}3\sigma$. And, finally, we have gained a lot of information regarding the CP phase δ_{CP} . Values around $\frac{3\pi}{2}$ are still favoured, but now $\delta_{\text{CP}} \sim \frac{\pi}{2}$ is disfavoured with $\sim 4\sigma$. The issue of CP conservation, though, remains unclear as $\delta_{\text{CP}} = \pi$ is still allowed within $\sim 1.5\sigma$.

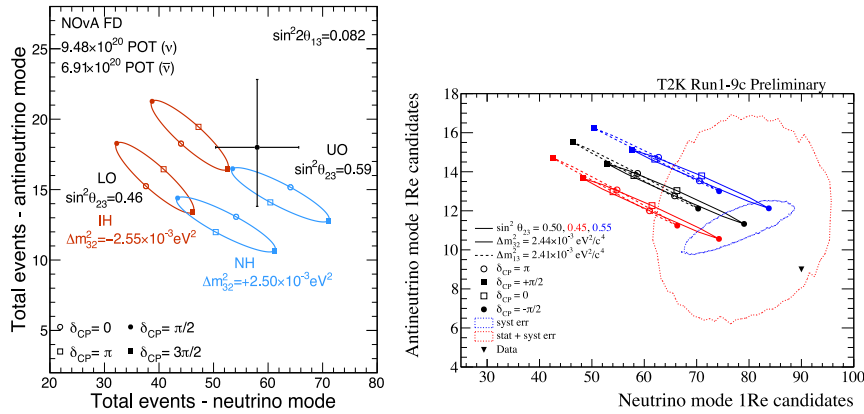
4.3 Summary and conclusions

The experimental programme for exploring neutrino flavour transitions successfully established the three massive neutrino framework as summarised in Chapter 3. Currently, it is determining its last unknowns, including leptonic CP violation, with LBL accelerator experiments.

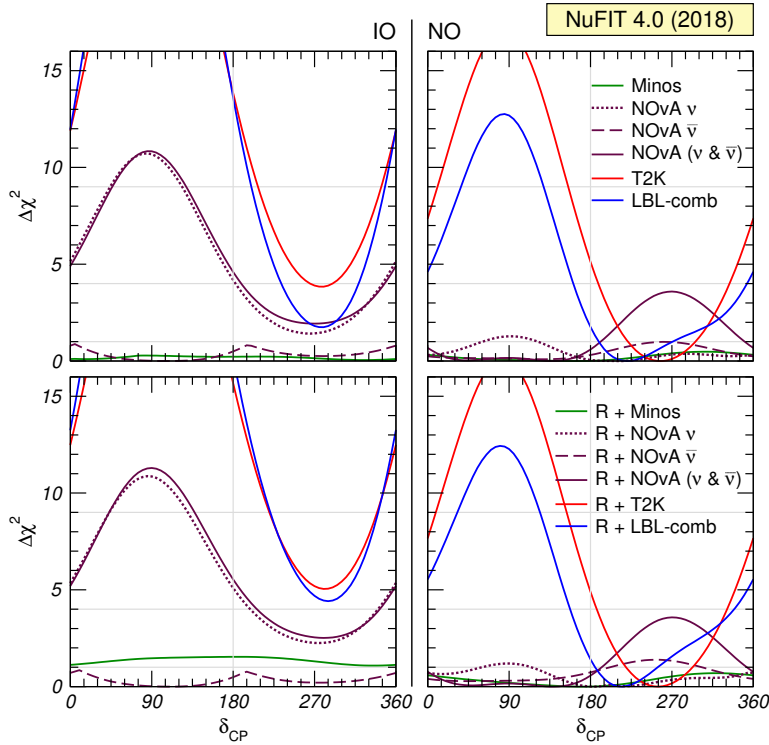
As a result of the interplay in these experiments between $\bar{\nu}_\mu$ disappearance, ν_e appearance and $\bar{\nu}_e$ appearance data, the unknowns start to clarify. There is no longer a strong degeneracy in the θ_{23} octant, normal mass ordering is currently favoured by the data, and there is a hint for $\delta_{\text{CP}} \sim \frac{3\pi}{2}$, i.e., maximal CP violation. $\delta_{\text{CP}} \sim \frac{\pi}{2}$ is disfavoured with $\sim 4\sigma$, but CP conservation is still allowed within $\sim 1.5\sigma$. We have also checked that Wilks' theorem can be safely applied to extract the corresponding confidence levels, as no significant deviation from gaussianity is expected in the currently favoured parameter regions.

This hint for maximal CP violation, which would imply that the strongest source of CP violation is provided by the lepton sector, is mostly driven by a ν_e excess in T2K. The excess has been consistently present for the last years, and within the 3-neutrino framework it can only be accommodated by large CP violation once information from other experiments is consistently

⁹More results are available in <http://www.nu-fit.org/?q=node/211>.

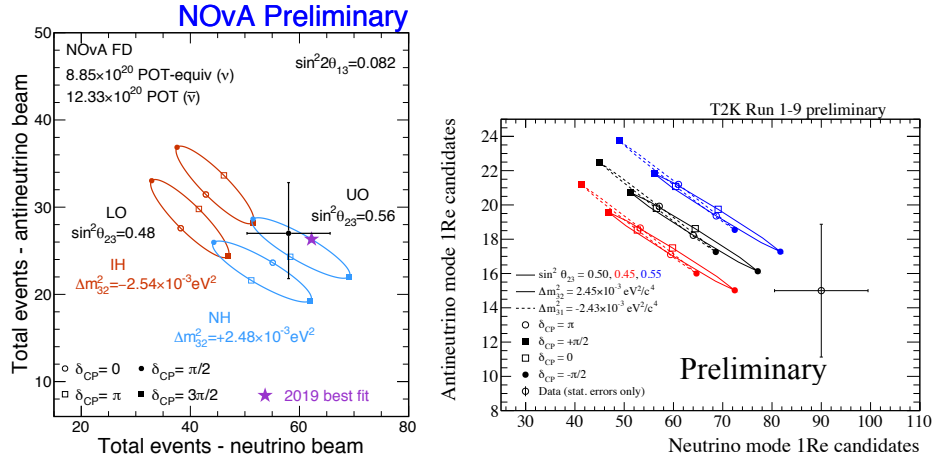


(a) Observed number of ν_e and $\bar{\nu}_e$ events at NO ν A (left) and T2K (right), extracted from Refs. [206,207]. The expectations are shown for different values of δ_{CP} , θ_{23} and the mass ordering. In the left panel, “UO” means Upper Octant ($\theta_{23} > 45^\circ$), “LO” Lower Octant ($\theta_{23} < 45^\circ$), “NH” Normal Ordering and “IH” Inverted Ordering. Notice that the NO ν A ellipses are more open and separated, giving more sensitivity to the θ_{23} octant, the mass ordering and δ_{CP} . This is due to the larger baseline of this experiment, that increases matter effects.

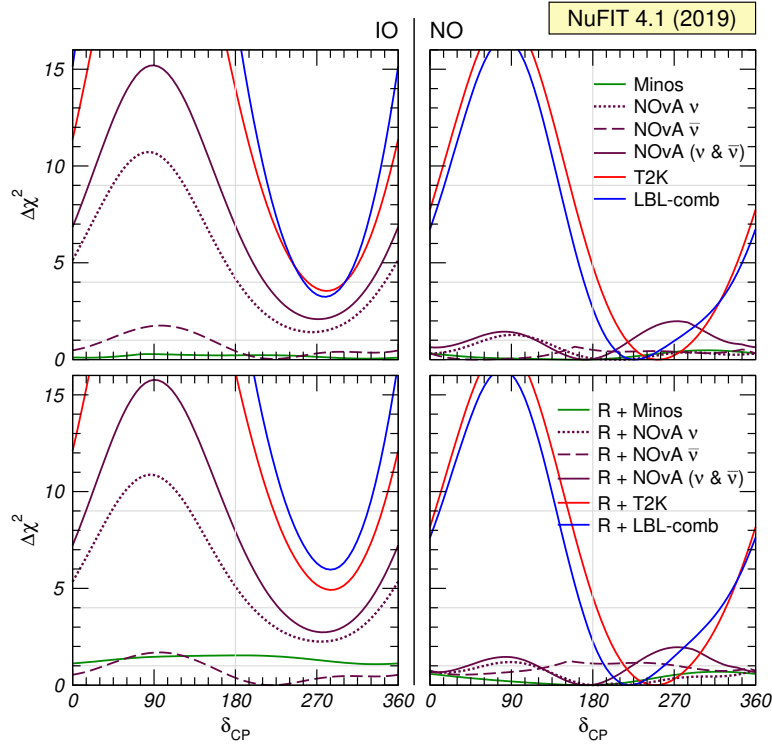


(b) δ_{CP} determination. Left (right) panels are for IO (NO). The upper panels constrain only θ_{13} from reactor experiments, whereas the lower panels include the full information from them: see Fig. 4.9 and its description in the text for the difference among both procedures. The NO ν A results are separated into neutrino and antineutrino samples.

Figure 4.16: Updated NO ν A and T2K $\bar{\nu}_e$ appearance results and global combination projection on δ_{CP} as of November 2018.



(a) Observed number of ν_e and $\bar{\nu}_e$ events at NO ν A (left) and T2K (right), extracted from Refs. [96,208]. The expectations are shown for different values of δ_{CP} , θ_{23} and the mass ordering. In the left panel, “UO” means Upper Octant ($\theta_{23} > 45^\circ$), “LO” Lower Octant ($\theta_{23} < 45^\circ$), “NH” Normal Ordering and “IH” Inverted Ordering.



(b) δ_{CP} determination. Left (right) panels are for IO (NO). The upper panels constrain only θ_{13} from reactor experiments, whereas the lower panels include the full information from them: see Fig. 4.9 and its description in the text for the difference among both procedures. The NO ν A results are separated into neutrino and antineutrino samples.

Figure 4.17: Updated NO ν A and T2K $\bar{\nu}_e$ appearance results and global combination projection on δ_{CP} as of July 2019.

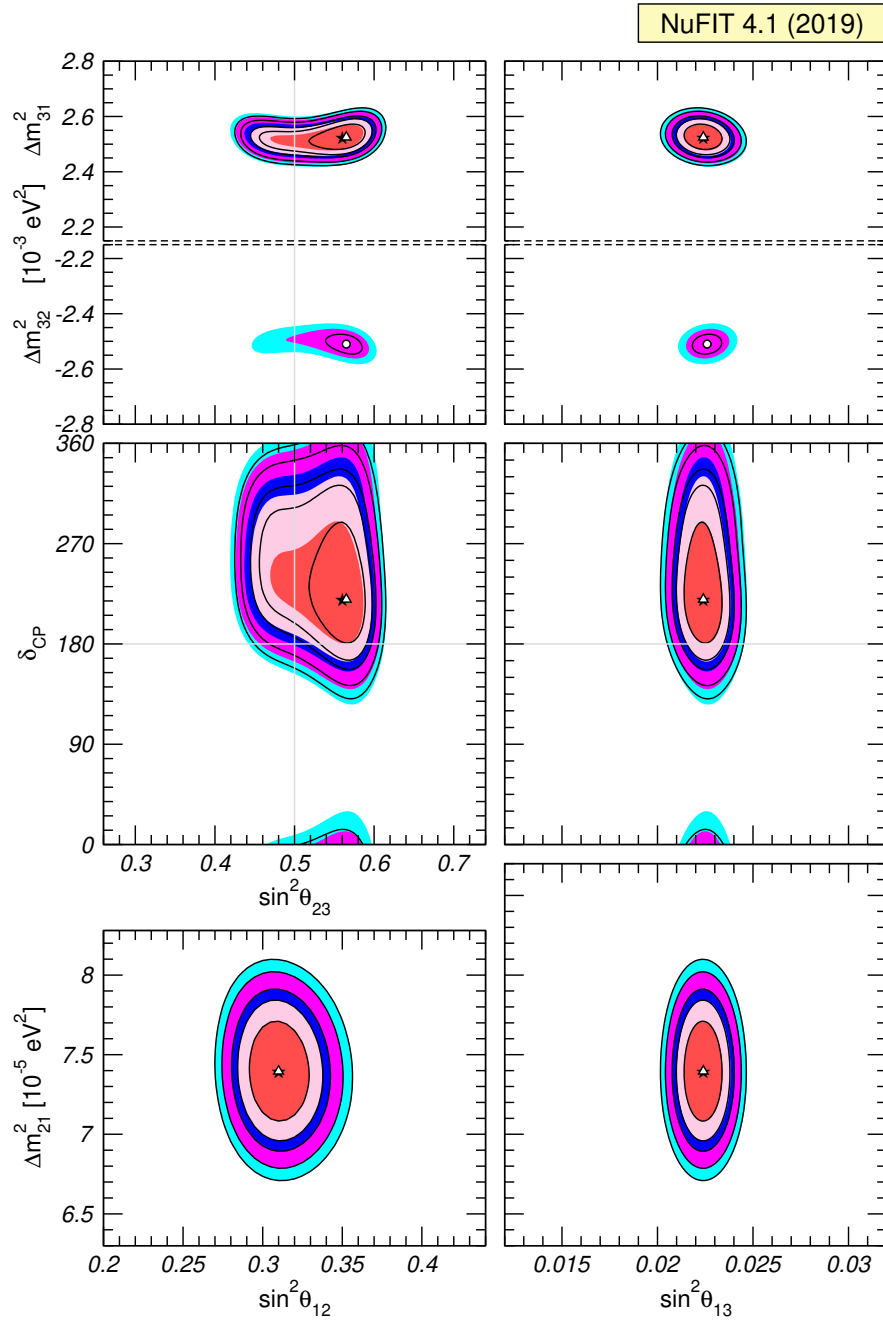


Figure 4.18: Global 3ν oscillation analysis. Each panel shows the two-dimensional projection of the allowed six-dimensional region after minimization with respect to the undisplayed parameters. The regions in the four lower panels are obtained from $\Delta\chi^2$ minimised with respect to the mass ordering. The different contours correspond to 1σ , 90%, 2σ , 99%, 3σ CL (2 dof). Coloured regions (black contour curves) are without (with) adding the Super-Kamiokande atmospheric results, provided as a $\Delta\chi^2$ table by the collaboration. Note that as atmospheric mass-squared splitting we use Δm_{31}^2 for NO and Δm_{32}^2 for IO.

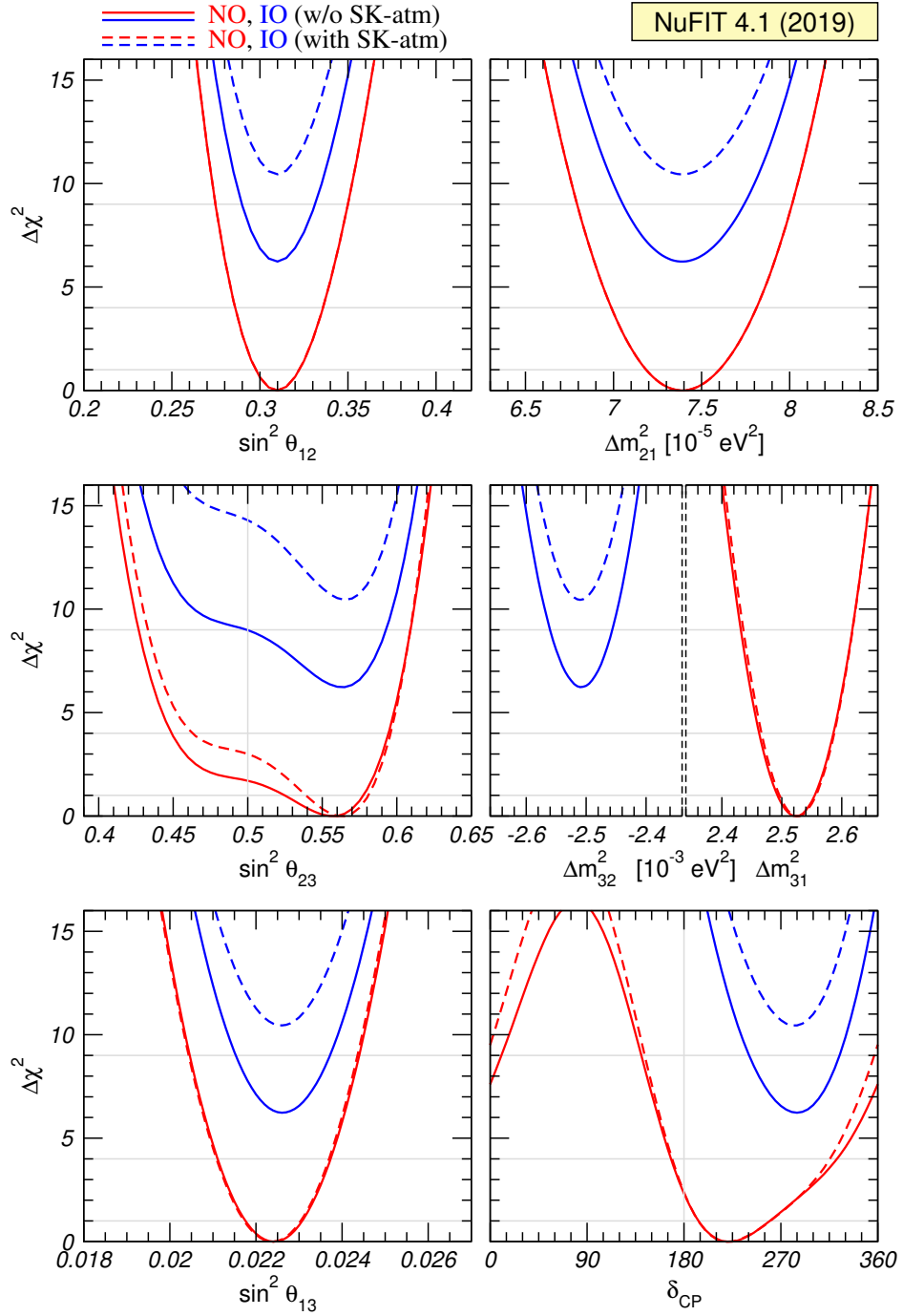


Figure 4.19: Global 3ν oscillation analysis. We show $\Delta\chi^2$ profiles minimised with respect to all undisplayed parameters. The red (blue) curves correspond to Normal (Inverted) Ordering. Solid (dashed) curves are without (with) adding the Super-Kamiokande atmospheric results, provided as a $\Delta\chi^2$ table by the collaboration. Note that as atmospheric mass-squared splitting we use Δm_{31}^2 for NO and Δm_{32}^2 for IO.

included. Nevertheless, as neutrino masses already constitute BSM physics, it is legitimate to ask whether we are detecting large leptonic CP violation or, on the contrary, whether other new physics could also accommodate the data. This is even more relevant considering that, in the near future, a new generation of LBL accelerator experiments will precisely explore the current hints coming from $\text{NO}\nu\text{A}$ and T2K [209–213]. Answering that question will be the main goal of the rest of this thesis.

Chapter 5

Beyond the three-neutrino paradigm: framework

Non-renormalizable interactions may also be detected. I doubt that they would not.

— Steven Weinberg

Sed tengo, y sal se vuelven tus arenas

— Blas de Otero

As discussed in the previous Chapter, there is a hint for maximal leptonic CP violation mostly coming from the T2K experiment. If their large $\nu_\mu \rightarrow \nu_e$ appearance signal is interpreted in the three light neutrino paradigm, it can only be accommodated by assuming large leptonic CP violation. Nevertheless, three light neutrinos is the consequence of extending the SM with the operator (2.49). Other operators of higher dimension are also expected if the SM is a theory valid up to certain energy scale Λ . If they are present, they could be masking the results and even introducing new degeneracies.

In this chapter, we will present the formalism for parametrising leptonic CP violation in these extended scenarios, in particular when including Non-Standard neutrino Interactions (NSI). We will end by describing the other relevant effect in the existing oscillation experiments, which is the appearance of intrinsic parameter degeneracies.

5.1 Formalism

The next operators with observable consequences at low energies come at dimension 6, and the ones affecting neutrinos include

- Operators modifying the neutrino kinetic term,

$$\left(\overline{L_L^\alpha \tilde{\Phi}}\right) i \not{\partial} \left(\tilde{\Phi}^\dagger L_L^\beta\right) + \text{h.c.} . \quad (5.1)$$

After spontaneous symmetry breaking, this operator generates non-unitary corrections to the leptonic mixing matrix [214–216]. Generically, it is a consequence of neutrinos mixing

with heavy mass eigenstates. Nevertheless, leptonic non-unitarity is strongly constrained by precision electroweak data [217]. Thus, its quantitative effect in present neutrino oscillation experiments is suppressed enough to be safely ignored in what follows [218].

- Four-fermion operators leading to so-called NSI [116,219,220] between neutrinos and matter (for recent reviews, see Refs. [221,222]), both in charged-current interactions (NSI-CC)

$$(\bar{\nu}_\alpha \gamma_\mu P_L \ell_\beta)(\bar{f}' \gamma^\mu P f) \quad (5.2)$$

and in neutral current interactions (NSI-NC)

$$(\bar{\nu}_\alpha \gamma_\mu P_L \nu_\beta)(\bar{f} \gamma^\mu P f). \quad (5.3)$$

Here α, β are lepton flavour indices, l_α is a charged lepton, f, f' are SM charged fermions and γ^μ are the Dirac gamma matrices; P_L is the left-handed projection operator while P can be either P_L or P_R (the right-handed projection operator). These operators are expected to arise generically from the exchange of some mediator state assumed to be heavier than the characteristic momentum transfer in the ν interaction process. They have all been written after spontaneous electroweak symmetry breaking: see Ref. [223] for a discussion of gauge invariant operators leading to them.

Since operators in both Eqs. (5.2) and (5.3) modify the inelastic neutrino scattering cross sections with other SM fermions they can be bounded by precision electroweak data (see for example Refs. [224–226]). In general these “scattering” bounds on NSI-CC operators are rather stringent, whereas the bounds on NSI-NC tend to be weaker. In turn, the operators in Eq. (5.3) can also modify the forward-coherent scattering (*i.e.*, at zero momentum transfer) of neutrinos as they propagate through matter, as discussed in Section 2.2.4. Consequently their effect can be significantly enhanced in oscillation experiments. Indeed, a global analysis of data from oscillation experiments in the framework of mass induced oscillations in presence of NSI provided some of the strongest constraints on the size of the NSI affecting neutrino propagation [227,228].

Of course, for models with a high energy new physics scale, electroweak gauge invariance generically implies that the NSI-NC parameters are still expected to be subject to tight constraints from charged lepton observables [223,229], leading to no visible effect in oscillations. However, more recently it has been argued that viable gauge models with light mediators (*i.e.*, below the electroweak scale) may lead to observable effects in oscillations without entering in conflict with other bounds [230–234] (see also Refs. [222,235] for discussions). In particular, for light mediators bounds from high-energy neutrino scattering experiments such as CHARM [236] and NuTeV [237] do not apply.

In this work we will consider NSI affecting neutral-current processes relevant to neutrino propagation in matter. The coefficients accompanying the new operators are usually parametrised in the form:

$$\mathcal{L}_{\text{NSI}} = -2\sqrt{2}G_F \sum_{f,P,\alpha,\beta} \varepsilon_{\alpha\beta}^{f,P} (\bar{\nu}_\alpha \gamma_\mu P_L \nu_\beta)(\bar{f} \gamma^\mu P f) + \text{h.c.}, \quad (5.4)$$

where G_F is the Fermi constant, α, β are flavour indices, $P \equiv P_L, P_R$ and f is a SM charged fermion. In this notation, $\varepsilon_{\alpha\beta}^{f,P}$ parametrises the strength of the new interaction with respect to the Fermi constant, $\varepsilon_{\alpha\beta}^{f,P} \sim \mathcal{O}(G_X/G_F)$. If we now assume that the neutrino flavour structure of the interactions is independent of the charged fermion type, we can factorise $\varepsilon_{\alpha\beta}^{f,P}$ as the product of two terms:

$$\varepsilon_{\alpha\beta}^{f,P} \equiv \varepsilon_{\alpha\beta} \xi^{f,P} \quad (5.5)$$

where the matrix $\varepsilon_{\alpha\beta}$ describes the neutrino part and the coefficients $\xi^{f,P}$ parametrise the coupling to the charged fermions. Under this assumption the Lagrangian in Eq. (5.4) takes the form:

$$\mathcal{L}_{\text{NSI}} = -2\sqrt{2}G_F \left[\sum_{\alpha,\beta} \varepsilon_{\alpha\beta} (\bar{\nu}_\alpha \gamma^\mu P_L \nu_\beta) \right] \left[\sum_{f,P} \xi^{f,P} (\bar{f} \gamma_\mu P f) \right] + \text{h.c.} . \quad (5.6)$$

If we follow the derivation of matter effects in Section 2.2.4, we immediately see that only vector NSI contribute to the matter potential in neutrino oscillations, as any γ_5 factor does not contribute to the trace in Eq. (2.67). It is therefore convenient to define:

$$\varepsilon_{\alpha\beta}^f \equiv \varepsilon_{\alpha\beta}^{f,L} + \varepsilon_{\alpha\beta}^{f,R} = \varepsilon_{\alpha\beta} \xi^f \quad \text{with} \quad \xi^f \equiv \xi^{f,L} + \xi^{f,R} . \quad (5.7)$$

5.1.1 Neutrino oscillations in the presence of NSI

In general, the evolution of the neutrino and antineutrino flavour state during propagation is governed by Eq. (2.75), with the Hamiltonian:

$$H^\nu = H_{\text{vac}} + H_{\text{mat}} \quad \text{and} \quad H^{\bar{\nu}} = (H_{\text{vac}} - H_{\text{mat}})^* , \quad (5.8)$$

where H_{vac} is the vacuum part which in the flavour basis $(\nu_e, \nu_\mu, \nu_\tau)$ reads

$$H_{\text{vac}} = U^{\text{lep}} D_{\text{vac}} U^{\text{lep}\dagger} \quad \text{with} \quad D_{\text{vac}} = \frac{1}{2E_\nu} \text{diag}(0, \Delta m_{21}^2, \Delta m_{31}^2) . \quad (5.9)$$

Here U^{lep} denotes the three-lepton mixing matrix in vacuum (2.56).

Concerning the matter part H_{mat} of the Hamiltonian which governs neutrino oscillations, if all possible operators in Eq. (5.4) are added to the SM Lagrangian we get:

$$H_{\text{mat}} = \sqrt{2}G_F N_e(x) \begin{pmatrix} 1 + \mathcal{E}_{ee}(x) & \mathcal{E}_{e\mu}(x) & \mathcal{E}_{e\tau}(x) \\ \mathcal{E}_{e\mu}^*(x) & \mathcal{E}_{\mu\mu}(x) & \mathcal{E}_{\mu\tau}(x) \\ \mathcal{E}_{e\tau}^*(x) & \mathcal{E}_{\mu\tau}^*(x) & \mathcal{E}_{\tau\tau}(x) \end{pmatrix} \quad (5.10)$$

where the “+1” term in the ee entry accounts for the standard contribution, and

$$\mathcal{E}_{\alpha\beta}(x) = \sum_{f=e,u,d} \frac{N_f(x)}{N_e(x)} \varepsilon_{\alpha\beta}^f \quad (5.11)$$

describes the non-standard part. Here $N_f(x)$ is the number density of fermion f as a function of the distance traveled by the neutrino along its trajectory. In Eq. (5.11) we have limited the sum to the charged fermions present in ordinary matter, $f = e, u, d$. Since quarks are always confined inside protons (p) and neutrons (n), it is convenient to define:

$$\varepsilon_{\alpha\beta}^p = 2\varepsilon_{\alpha\beta}^u + \varepsilon_{\alpha\beta}^d, \quad \varepsilon_{\alpha\beta}^n = 2\varepsilon_{\alpha\beta}^d + \varepsilon_{\alpha\beta}^u . \quad (5.12)$$

Taking into account that $N_u(x) = 2N_p(x) + N_n(x)$ and $N_d(x) = N_p(x) + 2N_n(x)$, and also that matter neutrality implies $N_p(x) = N_e(x)$, Eq. (5.11) becomes:

$$\mathcal{E}_{\alpha\beta}(x) = (\varepsilon_{\alpha\beta}^e + \varepsilon_{\alpha\beta}^p) + Y_n(x) \varepsilon_{\alpha\beta}^n \quad \text{with} \quad Y_n(x) \equiv \frac{N_n(x)}{N_e(x)} , \quad (5.13)$$

Since this matter term can be determined by oscillation experiments only up to an overall multiple of the identity, each $\varepsilon_{\alpha\beta}^f$ matrix introduces 8 new parameters: two differences of the three diagonal

real parameters (*e.g.*, $\varepsilon_{ee}^f - \varepsilon_{\mu\mu}^f$ and $\varepsilon_{\tau\tau}^f - \varepsilon_{\mu\mu}^f$) and three off-diagonal complex parameters (i.e., three additional moduli and three complex phases). The assumption (5.7) has only 8 parameters in $\varepsilon_{\alpha\beta}$ as well as three angles, characterising the relative strength of couplings with electrons, up quarks, and down quarks.

In summary, NSI-NC operators parametrised by Eqs. (5.6) and (5.7) could be present and affect neutrino oscillation experiments. In the following, we will discuss the new sources of CP violation and parameter degeneracies that they introduce.

5.2 Leptonic CP violation beyond the three-neutrino paradigm

As discussed in Section 2.1.2, CP violation arises whenever there are physical complex phases in the Lagrangian. In the SM and its minimal extension to include neutrino masses, flavour transformations can remove these phases and so the analysis is not straightforward. As described in Section 2.2.5, in the framework of three massive neutrinos all leptonic CP violating observables in neutrino oscillations depend on a unique physical parameter, which can be written in a basis independent form as the so-called leptonic Jarlskog invariant in Eq. (2.89).

In this section, we repeat the procedure to derive a set of flavour basis invariants that characterise leptonic CP violation in the presence of NSI (5.7). We follow the methodology introduced in Refs. [66, 67] for generalizing the construction of such invariants in quark sectors first introduced for three generations in [68, 69]. We will work with Dirac neutrinos, which is all it is needed when interested in CP violation in neutrino oscillations (see Ref. [238] for the invariants relevant for Majorana neutrinos).

The relevant parts of the Lagrangian that can contain complex phases and affect neutrino oscillations are:

$$\begin{aligned}
-\mathcal{L} = & (\bar{\nu}_{e,L} \quad \bar{\nu}_{\mu,L} \quad \bar{\nu}_{\tau,L}) M_D \begin{pmatrix} \nu_{e,R} \\ \nu_{\mu,R} \\ \nu_{\tau,R} \end{pmatrix} + (\bar{\nu}_{e,L} \quad \bar{\nu}_{\mu,L} \quad \bar{\nu}_{\tau,L}) M_e \begin{pmatrix} \nu_{e,R} \\ \nu_{\mu,R} \\ \nu_{\tau,R} \end{pmatrix} \\
& + 2\sqrt{2}G_F (\bar{\nu}_{e,L} \quad \bar{\nu}_{\mu,L} \quad \bar{\nu}_{\tau,L}) \varepsilon \gamma^\mu \begin{pmatrix} \nu_{e,L} \\ \nu_{\mu,L} \\ \nu_{\tau,L} \end{pmatrix} \left[\sum_f \xi^f (\bar{f} \gamma_\mu f) \right] - \text{h.c.} .
\end{aligned} \tag{5.14}$$

Unphysical flavour basis rotations leaving the fermion kinetic and gauge Lagrangian (2.1) invariant are given by the following field transformations (see Eqs. (2.26) and (2.27))

$$(e_L \quad \mu_L \quad \tau_L)^T \xrightarrow{\text{flavour}} P_{LL} (e_L \quad \mu_L \quad \tau_L)^T , \tag{5.15}$$

$$(\nu_{e,L} \quad \nu_{\mu,L} \quad \nu_{\tau,L})^T \xrightarrow{\text{flavour}} P_{LL} (\nu_{e,L} \quad \nu_{\mu,L} \quad \nu_{\tau,L})^T , \tag{5.16}$$

$$(e_R \quad \mu_R \quad \tau_R)^T \xrightarrow{\text{flavour}} P_{eR} (e_R \quad \mu_R \quad \tau_R)^T , \tag{5.17}$$

$$(\nu_{e,R} \quad \nu_{\mu,R} \quad \nu_{\tau,R})^T \xrightarrow{\text{flavour}} P_{\nu R} (\nu_{e,R} \quad \nu_{\mu,R} \quad \nu_{\tau,R})^T , \tag{5.18}$$

with all the $P \in SU(3)$. Correspondingly the matrices with flavour indices transform as

$$M_D \xrightarrow{\text{flavour}} P_{LL}^\dagger M_D P_{\nu R} , \quad M_e \xrightarrow{\text{flavour}} P_{LL}^\dagger M_e P_{eR} , \quad \varepsilon \xrightarrow{\text{flavour}} P_{LL}^\dagger \varepsilon P_{LL} . \tag{5.19}$$

So clearly the CP transformation, that changes these matrices into their complex conjugates, will be unphysical if (and only if) it is equivalent to some flavour rotation. That is, there is CP conservation if and only if there exists a set of matrices $\{P_{LL}, P_{\nu R}, P_{eR}\} \in SU(3)$ such that

$$P_{LL}^\dagger \varepsilon P_{LL} = \varepsilon^* , \quad P_{LL}^\dagger M_D P_{\nu R} = M_D^* , \quad P_{LL}^\dagger M_e P_{eR} = M_e^* . \tag{5.20}$$

Since given a matrix A , AA^\dagger determines A up to unitary rotations one can work with the “squares” of the mass matrices instead and find that there is CP conservation if and only if there exists a matrix $P \in SU(3)$ such that

$$P^\dagger \varepsilon P = \varepsilon^*, \quad P^\dagger S_\nu P = S_\nu^*, \quad P^\dagger S_e P = S_e^*, \quad (5.21)$$

with $S_e = M_e M_e^\dagger$ and $S_\nu = M_D M_D^\dagger$. In the charged lepton mass basis (i.e., where P_{L_L} and P_{e_R} are chosen to diagonalise the charged lepton mass matrix as in Sections 2.1.1 and 2.1.2), these matrices read

$$S_e = \begin{pmatrix} m_e^2 & 0 & 0 \\ 0 & m_\mu^2 & 0 \\ 0 & 0 & m_\tau^2 \end{pmatrix}, \quad S_\nu = U^{\text{lep}} \begin{pmatrix} m_1^2 & 0 & 0 \\ 0 & m_2^2 & 0 \\ 0 & 0 & m_3^2 \end{pmatrix} U^{\text{lep}\dagger}, \quad (5.22)$$

as U^{lep} is the product of the matrices that diagonalise S_e and S_ν .

This basis is particularly convenient, as there the last condition in Eq. (5.21) states that the matrices P and S_e commute. Therefore, P is also diagonal, and being an element of $SU(3)$ we can write it as $P = \text{diag}(e^{i\delta_1}, e^{i\delta_2}, e^{-i(\delta_1+\delta_2)})$. Thus, writing the other conditions and using the hermiticity of ε and S_ν , there is CP conservation if and only if there exist $\{\delta_1, \delta_2\} \in [0, 2\pi)$ such that

$$\varepsilon_{\mu e} e^{i(\delta_1 - \delta_2)} = \varepsilon_{\mu e}^*, \quad S_{\nu\mu e} e^{i(\delta_1 - \delta_2)} = S_{\nu\mu e}^*, \quad (5.23)$$

$$\varepsilon_{\tau e} e^{i(2\delta_1 + \delta_2)} = \varepsilon_{\tau e}^*, \quad S_{\nu\tau e} e^{i(2\delta_1 + \delta_2)} = S_{\nu\tau e}^*, \quad (5.24)$$

$$\varepsilon_{\tau\mu} e^{i(2\delta_2 + \delta_1)} = \varepsilon_{\tau\mu}^*, \quad S_{\nu\tau\mu} e^{i(2\delta_2 + \delta_1)} = S_{\nu\tau\mu}^*. \quad (5.25)$$

If we write each complex matrix element in polar form, we arrive to a linear system of six equations with two unknowns $\{\delta_1, \delta_2\}$. This system has a solution only if the phases are linearly dependent. Imposing it, we conclude that there is CP conservation if and only if

$$\text{Ph}(\varepsilon_{\mu e}) - \text{Ph}(\varepsilon_{\tau e}) + \text{Ph}(\varepsilon_{\tau\mu}) = 0, \quad (5.26)$$

$$\text{Ph}(S_{\nu\mu e}) + \text{Ph}(S_{\nu\tau e}) - \text{Ph}(S_{\nu\tau\mu}) = 0, \quad (5.27)$$

$$\text{Ph}(\varepsilon_{\mu e}) - \text{Ph}(S_{\nu\mu e}) = 0, \quad (5.28)$$

$$\text{Ph}(\varepsilon_{\mu\tau}) - \text{Ph}(S_{\nu\mu\tau}) = 0, \quad (5.29)$$

$$\text{Ph}(\varepsilon_{e\tau}) - \text{Ph}(S_{\nu e\tau}) = 0, \quad (5.30)$$

where $\text{Ph}(z)$ refers to the phase of the complex number z . These conditions can equivalently be written as

$$\text{Im}(\varepsilon_{\mu e} \varepsilon_{e\tau} \varepsilon_{\tau\mu}) = 0, \quad (5.31)$$

$$\text{Im}(S_{\nu\mu e} S_{\nu e\tau} S_{\nu\tau\mu}) = 0, \quad (5.32)$$

$$\text{Im}(\varepsilon_{\alpha\beta} S_{\nu\beta\alpha}) = 0. \quad (5.33)$$

where we have used the hermiticity of the ε and S_ν matrices, and the last condition has to be fulfilled for $\{\alpha\beta\} = \{e\mu\}, \{e,\tau\}, \{\mu,\tau\}$. However, since

$$\varepsilon_{\mu\tau} S_{\nu\tau\mu} = \frac{(\varepsilon_{e\mu} \varepsilon_{\mu\tau} \varepsilon_{\tau e})(S_{\nu e\mu} S_{\nu\mu\tau} S_{\nu\tau e})^* (\varepsilon_{e\tau} S_{\nu\tau e})(\varepsilon_{e\mu} S_{\nu\mu e})^*}{|\varepsilon_{e\mu}|^2 |\varepsilon_{e\tau}|^2 |S_{\nu e\mu}|^2 |S_{\nu e\tau}|^2} \quad (5.34)$$

there are only four independent conditions.

Using the projector technique [239] the four conditions can be expressed in a basis-invariant form. For example as:

$$\text{Im Tr} [S_e^2 S_\nu^2 S_e S_\nu] = \frac{2}{i} \text{Det}[S_e, S_\nu] = 0 \quad (5.35)$$

$$\text{Im Tr} [S_e^2 \varepsilon^2 S_e \varepsilon] = \frac{2}{i} \text{Det}[S_e, \varepsilon] = 0, \quad (5.36)$$

$$\text{Im Tr} [S_\nu S_e \varepsilon] = 0, \quad (5.37)$$

$$\text{Im Tr} [S_e S_\nu S_e^2 \varepsilon] = 0. \quad (5.38)$$

In the basis where the lepton mass matrix is diagonal these invariants read

$$\text{Im Tr} [S_e^2 S_\nu^2 S_e S_\nu] = v(m_e, m_\mu, m_\tau) \text{Im} [S_{\nu e \mu} S_{\nu \mu \tau} S_{\nu \tau e}] \quad (5.39)$$

$$\text{Im Tr} [S_e^2 \varepsilon^2 S_e \varepsilon] = v(m_e, m_\mu, m_\tau) \text{Im} [\varepsilon_{e\mu} \varepsilon_{\mu\tau} \varepsilon_{\tau e}], \quad (5.40)$$

$$\begin{aligned} \text{Im Tr} [S_\nu S_e \varepsilon] &= (m_\mu^2 - m_e^2) \text{Im} (S_{\nu e \mu} \varepsilon_{\mu e}) + (m_\tau^2 - m_e^2) \text{Im} (S_{\nu e \tau} \varepsilon_{\tau e}) \\ &\quad + (m_\tau^2 - m_\mu^2) \text{Im} (S_{\nu \mu \tau} \varepsilon_{\tau \mu}) \end{aligned} \quad (5.41)$$

$$\begin{aligned} \text{Im Tr} [S_e^2 \varepsilon^2 S_e \varepsilon] &= m_e m_\mu (m_\mu^2 - m_e^2) \text{Im} (S_{\nu e \mu} \varepsilon_{\mu e}) + m_e m_\tau (m_\tau^2 - m_e^2) \text{Im} (S_{\nu e \tau} \varepsilon_{\tau e}) \\ &\quad + m_\mu m_\tau (m_\tau^2 - m_\mu^2) \text{Im} (S_{\nu \mu \tau} \varepsilon_{\tau \mu}) \end{aligned} \quad (5.42)$$

with $v(m_e, m_\mu, m_\tau) = (m_\tau^2 - m_\mu^2)(m_\tau^2 - m_e^2)(m_\mu^2 - m_e^2)$.

Written in this form, the conditions for which the four independent phases are physically realizable becomes explicit, in particular the requirement of the non-zero difference between all or some of the charged lepton masses. We thus identify four invariants characterising CP violation in neutrino oscillations with NSI. In the charged lepton mass basis with the leptonic mixing matrix parametrised as in Eq. (2.56), they can be chosen as

- The standard Jarlskog invariant (2.89),

$$\begin{aligned} \text{Im Tr} (S_e^2 S_\nu^2 S_e S_\nu) &= \frac{2}{i} \text{Det}[S_e, S_\nu] = \frac{1}{4} v(m_e, m_\mu, m_\tau) \Delta m_{21}^2 \Delta m_{31}^2 \Delta m_{23}^2 \\ &\quad \times \sin(2\theta_{23}) \sin(2\theta_{12}) \sin(\theta_{13}) \cos^2(\theta_{13}) \sin \delta_{\text{CP}}. \end{aligned} \quad (5.43)$$

It parametrises CP violation in vacuum (e.g., in the T2K experiment to a good approximation), and as is well known it requires three-flavour effects to be non-zero. I.e., all three charged leptons must have different masses (to sensibly define neutrino flavour), all three neutrinos must have different masses (to sensibly define mixing angles), and all three mixing angles must be non-zero.

- An invariant characterising CP violation in neutrino propagation in matter in the $E_\nu \rightarrow \infty$ limit. That is, the source of CP violation induced solely by the NSI,

$$\begin{aligned} \text{Im Tr} (S_e^2 \varepsilon^2 S_e \varepsilon) &= \frac{2}{i} \text{Det}[S_e, \varepsilon] = v(m_e, m_\mu, m_\tau) \text{Im}(\varepsilon_{e\mu} \varepsilon_{\mu\tau} \varepsilon_{\tau e}) \\ &= v(m_e, m_\mu, m_\tau) |\varepsilon_{e\mu}| |\varepsilon_{e\tau}| |\varepsilon_{\mu\tau}| \sin(\phi_{e\mu} - \phi_{e\tau} + \phi_{\mu\tau}), \end{aligned} \quad (5.44)$$

where $\phi_{\alpha\beta}$ is the phase of $\varepsilon_{\alpha\beta}$. For it to be non-zero, all three charged leptons must have different masses (to sensibly define neutrino flavour), and all three flavour-violating NSI must be non-zero. Thus, it is also a three-flavour CP violating effect.

- The other two basis invariants involve both ε and S_ν and can be formed by two combinations of the rephasing invariants $\text{Im}(\varepsilon_{\alpha\beta} S_{\nu\beta\alpha})$ for $\alpha\beta = e\mu, e\tau, \mu\tau$ as shown, for example, in Eqs. (5.41) and (5.42). In the charged lepton mass basis they read:

$$\begin{aligned} \text{Im}(\varepsilon_{e\mu} S_{\nu\mu e}) &= \frac{1}{2} \cos\theta_{13} \varepsilon_{e\mu} [\Delta m_{21}^2 \cos\theta_{23} \sin 2\theta_{12} \sin(\delta_{\text{CP}} + \phi_{e\mu}) \\ &\quad + (2\Delta m_{31}^2 - \Delta m_{21}^2 + \Delta m_{21}^2 \cos 2\theta_{12}) \sin\theta_{13} \sin\theta_{23} \sin\phi_{e\mu}], \end{aligned} \quad (5.45)$$

$$\begin{aligned} \text{Im}(\varepsilon_{e\tau} S_{\nu\tau e}) &= \frac{1}{2} \cos\theta_{13} \varepsilon_{e\tau} [-\Delta m_{21}^2 \sin\theta_{23} \sin 2\theta_{12} \sin(\delta_{\text{CP}} + \phi_{e\tau}) \\ &\quad + (\Delta m_{31}^2 + \Delta m_{32}^2 + \Delta m_{21}^2 \cos 2\theta_{12}) \sin\theta_{13} \cos\theta_{23} \sin\phi_{e\tau}], \end{aligned} \quad (5.46)$$

and $\text{Im}(\varepsilon_{\mu\tau} S_{\nu\tau\mu})$ can be written in terms of the two above using the equality in Eq. (5.34).

Unlike for the case of the invariants in Eqs. (5.43) and (5.44), there is not a clear physical setup which could single out the contribution from Eq. (5.45) and Eq. (5.46) (or any combination of those) to a leptonic CP violating observable. Nevertheless, they are “interference” effects between vacuum CP-violation induced by lepton mixing and matter CP-violation induced by NSI. They are present whenever matter and vacuum oscillations are both relevant (for instance, in the $\text{NO}\nu\text{A}$ experiment), and they require only two-neutrino flavour mixing.

Admittedly the discussion above is only academic for the quantification of the effects induced by the NSI matter potential on neutrino propagation, because the relevant probabilities cannot be expressed in any practical form in terms of these basis invariants and one is forced to work in some specific parametrization. What these basis invariants clearly illustrate is that in order to study the possible effects (in experiments performed in matter) of NSI on the determination of the phase which parametrises CP violation in vacuum *without introducing an artificial basis dependence*, one needs to include in the analysis the most general complex NSI matter potential containing *all* the three additional arbitrary phases.

Furthermore, it also illustrates the origin of the four sources of CP violation: three-neutrino vacuum effects, three-neutrino matter effects, and two-neutrino interference effects among vacuum and matter. An experiment sensitive only to vacuum or only to matter could be analysed in terms of one single CP violation source. But experiments with relevant vacuum *and* matter effects, as LBL accelerator experiments, are sensitive to all sources of CP violation.

5.3 The generalised mass ordering degeneracy

Apart from explicitly introducing new sources of CP violation, NSI also introduce a degeneracy that affects the determination of δ_{CP} and the mass ordering [108, 228, 240, 241].

Neutrino evolution is invariant if the Hamiltonian $H^\nu = H_{\text{vac}} + H_{\text{mat}}$ is transformed as $H^\nu \rightarrow -(H^\nu)^*$. This transformation, that for the vacuum piece stems from CPT invariance, requires a simultaneous change of both the vacuum and the matter terms. The transformation of H_{vac} is implemented exactly (up to an irrelevant multiple of the identity) by the following transformation of the parameters:

$$\begin{aligned} \Delta m_{31}^2 &\rightarrow -\Delta m_{31}^2 + \Delta m_{21}^2 = -\Delta m_{32}^2, \\ \theta_{12} &\rightarrow \pi/2 - \theta_{12}, \\ \delta_{\text{CP}} &\rightarrow \pi - \delta_{\text{CP}}, \end{aligned} \quad (5.47)$$

which does not spoil the commonly assumed restrictions on the range of the vacuum parameters ($\Delta m_{21}^2 > 0$ and $0 \leq \theta_{ij} \leq \pi/2$). It involves a change in the octant of θ_{12} as well as a change in

the neutrino mass ordering (i.e., the sign of Δm_{31}^2), which is why it has been called “generalised mass ordering degeneracy” in Ref. [108]. This degeneracy was first explored for solar neutrino oscillation data, where it was called the LMA-D solution, standing for “Large Mixing Angle - Dark” as θ_{12} is quite large and bigger than 45° (named “the dark side” in Ref. [242]).

As for H_{mat} we need:

$$\begin{aligned} [\mathcal{E}_{ee}(x) - \mathcal{E}_{\mu\mu}(x)] &\rightarrow -[\mathcal{E}_{ee}(x) - \mathcal{E}_{\mu\mu}(x)] - 2, \\ [\mathcal{E}_{\tau\tau}(x) - \mathcal{E}_{\mu\mu}(x)] &\rightarrow -[\mathcal{E}_{\tau\tau}(x) - \mathcal{E}_{\mu\mu}(x)], \\ \mathcal{E}_{\alpha\beta}(x) &\rightarrow -\mathcal{E}_{\alpha\beta}^*(x) \quad (\alpha \neq \beta), \end{aligned} \tag{5.48}$$

see Refs. [108, 228, 240]. As seen in Eqs. (5.11) and (5.13) the matrix $\mathcal{E}_{\alpha\beta}(x)$ depends on the chemical composition of the medium, which may vary along the neutrino trajectory, so that in general the condition in Eq. (5.48) is fulfilled only in an approximate way. The degeneracy becomes exact in the following two cases:¹

- If the effective NSI coupling to neutrons vanishes, so that $\varepsilon_{\alpha\beta}^n = 0$ in Eq. (5.13). In terms of fundamental quantities this occurs when $\varepsilon_{\alpha\beta}^u = -2\varepsilon_{\alpha\beta}^d$, i.e., the NSI couplings are proportional to the electric charge of quarks.
- If the neutron/proton ratio $Y_n(x)$ is constant along the entire neutrino propagation path. This is certainly the case for reactor and LBL experiments, where only the Earth’s mantle is involved, and to a good approximation also for atmospheric neutrinos, since the differences in chemical composition between mantle and core can safely be neglected in the context of NSI [227]. In this case the matrix $\mathcal{E}_{\alpha\beta}(x)$ becomes independent of x and can be regarded as a new phenomenological parameter, as we will describe in Section 6.1.1.

Further details on the implications of this degeneracy for different classes of neutrino experiments (solar, atmospheric, etc.) will be provided later in Chapter 6.

Nevertheless, we already foresee that unless enough data from neutrino experiments with a non-constant chemical composition along the trajectory (essentially solar neutrino experiments) is available, this degeneracy is exact and thus completely spoils the sensitivity to the mass ordering.

Furthermore, the sensitivity to δ_{CP} may also get spoiled. Even though the transformation $\delta_{\text{CP}} \rightarrow \pi - \delta_{\text{CP}}$ does not change the Jarlskog invariant (2.89), it introduces a degenerate solution when determining δ_{CP} . A precise measurement of this parameter would thus be compromised.

5.4 Summary

Neutrino flavour transition data is usually analysed assuming that the only BSM physics affecting it are three light neutrino mass eigenstates. Nevertheless, there could be additional new physics in the form of higher-dimensional operators masking the results. Some of these operators can be constrained with electroweak precision observables, but others involve a two-neutrino vertex and are harder to explore. These include what are usually called NSI-NC.

Furthermore, these operators directly affect neutrino propagation in matter, and so they are expected to noticeably impact neutrino oscillation experiments. As we have seen, they introduce new sources of leptonic CP violation and an intrinsic degeneracy involving both δ_{CP} and the

¹Strictly speaking, Eq. (5.48) can be satisfied exactly for *any* matter chemical profile $Y_n(x)$ if $\varepsilon_{\alpha\beta}^u$, $\varepsilon_{\alpha\beta}^e$ and $\varepsilon_{\alpha\beta}^d$ are allowed to transform independently of each other. This possibility, however, is incompatible with the factorization constraint of Eq. (5.5), so it will not be discussed here.

mass ordering. Thus, their impact should be assessed to assure the robustness of leptonic CP violation measurements. This will be the goal of the following chapter.

Chapter 6

Beyond the three-neutrino paradigm: fit to oscillation data

We are boys playing on the sea-shore, and diverting ourselves in now and then finding a smoother pebble or a prettier shell than ordinary, whilst the great ocean of truth lay all undiscovered before us.

— Isaac Newton

*Despacito y buena letra,
que el hacer las cosas bien, importa más que el hacerlas*

— Antonio Machado

By analysing data from neutrino oscillation experiments in Chapter 4, we have obtained a hint for maximal CP violation in the leptonic sector. The hint, though, is indirect, and might be masked if other BSM operators apart from the Weinberg operator (2.49) are present. Among them, NSI-NC induced by rather light mediators are difficult to constraint but directly affect neutrino propagation in matter. Furthermore, they introduce new sources of CP violation and a degenerate solution known as LMA-D.

In this chapter, we confront these models with the bulk of data from neutrino oscillation experiments. Due to the large parameter space and variety of experiments involved, we will first assess the sensitivity of neutrino oscillation experiments to CP conserving NSI-NC. We will evaluate current bounds, the complementarity among different experiments, and the level at which the LMA-D solution can be tested. We will also evaluate how robustly are neutrino masses and mixing angles determined in the presence of the maximally allowed values for the NSI-NC.

Afterwards, we will assess whether experimentally allowed NSI-NC interactions can spoil the sensitivity to CP violation in LBL accelerator experiments. As detailed in the previous chapter, this requires introducing all possible CP-violating phases in the analysis. Therefore, we will explore the entire parameter space.

6.1 CP-conserving analysis: bounds on NSI moduli

In this section we revisit our current knowledge of the size and flavour structure of NSI-NC which affect the matter background in the evolution of solar, atmospheric, reactor and LBL accelerator neutrinos as determined by a global analysis of oscillation data. This updates and extends the analysis in Ref. [228] where NSI-NC with either up or down quarks were considered. Here we extend that analysis to account for the possibility of NSI with up *and* down quarks simultaneously, under the simplifying assumption that they carry the same lepton flavour structure. To this aim, in Sec. 6.1.1 we briefly summarise the framework of our study and discuss the simplifications used in the analysis of the atmospheric and LBL data on one side and of the solar and KamLAND sector on the other side. In Sec. 6.1.2 we present the results of the updated analysis of solar and KamLAND data and quantify the impact of the modified matter potential on the data description, as well as the status of the LMA-D solution [241] in presence of the most general NSI scenario considered here. In Sec. 6.1.3 we describe the constraints implied by the analysis of atmospheric, LBL and reactor experiments, and combine them with those arising from the solar+KamLAND data. We show how the complementarity and synergy of the different data sets is important for a robust determination of neutrino masses and mixing in the presence of these general NSI, and we derive allowed ranges on NSI couplings.

6.1.1 Formalism

We will consider NSI-NC mediated by the Lagrangian (5.6). Furthermore, we restrict ourselves to NSI with quarks, so that only ξ^u and ξ^d (see Eq. (5.7)) are relevant for neutrino propagation. The reason is that the presence of NSI with electrons would affect not only neutrino propagation in matter, but also the neutrino-electron cross section in experiments such as Super-Kamiokande and Borexino. Since here we are only interested in studying the propagation bounds, we limit ourselves to NSI with quarks. Also, Eq. (5.13) shows that from the phenomenological point of view the propagation effects of NSI with electrons can be mimicked by NSI with quarks by means of a suitable combination of up-quark and down-quark contributions. Our choice of neglecting $\varepsilon_{\alpha\beta}^e$ in this work does not therefore imply a loss of generality.

In what respects the parametrisation of the NSI couplings to quarks, from Eq. (5.5) it is clear that a global rescaling of both ξ^u and ξ^d by a common factor can be reabsorbed into a rescaling of $\varepsilon_{\alpha\beta}$, so that only the direction in the (ξ^u, ξ^d) plane is phenomenologically non-trivial. We parametrise such direction in terms of an angle η , which for later convenience we have related to the NSI couplings of protons and neutrons (see Eqs. (5.12) and (6.2) for a formal definition). In terms of the “quark” couplings introduced in Eq. (5.7) we have:

$$\xi^u = \frac{\sqrt{5}}{3}(2 \cos \eta - \sin \eta), \quad \xi^d = \frac{\sqrt{5}}{3}(2 \sin \eta - \cos \eta) \quad (6.1)$$

where we have chosen the normalisation so that $\eta = \arctan(1/2) \approx 26.6^\circ$ corresponds to NSI with up quarks ($\xi^u = 1, \xi^d = 0$) while $\eta = \arctan(2) \approx 63.4^\circ$ corresponds to NSI with down quarks ($\xi^u = 0, \xi^d = 1$). Note that the transformation $\eta \rightarrow \eta + \pi$ simply results in a sign flip of ξ^u and ξ^d , hence it is sufficient to consider $-\pi/2 \leq \eta \leq \pi/2$.

In terms of neutron and proton NSI, $\varepsilon_{\alpha\beta}^p = \varepsilon_{\alpha\beta} \xi^p$ and $\varepsilon_{\alpha\beta}^n = \varepsilon_{\alpha\beta} \xi^n$, which leads to:

$$\mathcal{E}_{\alpha\beta}(x) = \varepsilon_{\alpha\beta} [\xi^p + Y_n(x) \xi^n] \quad \text{with} \quad \xi^p = \sqrt{5} \cos \eta \quad \text{and} \quad \xi^n = \sqrt{5} \sin \eta \quad (6.2)$$

so that the phenomenological framework adopted here is characterised by 9 matter parameters: eight related to the matrix $\varepsilon_{\alpha\beta}$ plus the direction η in the (ξ^p, ξ^n) plane.

Matter potential in atmospheric and long baseline neutrinos

As discussed in Ref. [227], in the Earth the neutron/proton ratio $Y_n(x)$ which characterise the matter chemical composition can be taken to be constant to very good approximation. The PREM model [243] fixes $Y_n = 1.012$ in the Mantle and $Y_n = 1.137$ in the Core, with an average value $Y_n^\oplus = 1.051$ all over the Earth. Setting therefore $Y_n(x) \equiv Y_n^\oplus$ in Eqs. (5.11) and (5.13) we get $\mathcal{E}_{\alpha\beta}(x) \equiv \varepsilon_{\alpha\beta}^\oplus$ with:

$$\varepsilon_{\alpha\beta}^\oplus = \varepsilon_{\alpha\beta}^e + (2 + Y_n^\oplus)\varepsilon_{\alpha\beta}^u + (1 + 2Y_n^\oplus)\varepsilon_{\alpha\beta}^d = (\varepsilon_{\alpha\beta}^e + \varepsilon_{\alpha\beta}^p) + Y_n^\oplus \varepsilon_{\alpha\beta}^n. \quad (6.3)$$

If we drop $\varepsilon_{\alpha\beta}^e$ and impose quark-lepton factorization as in Eq. (6.2) we get:

$$\varepsilon_{\alpha\beta}^\oplus = \varepsilon_{\alpha\beta} (\xi^p + Y_n^\oplus \xi^n) = \sqrt{5} (\cos \eta + Y_n^\oplus \sin \eta) \varepsilon_{\alpha\beta}. \quad (6.4)$$

In other words, within this approximation the analysis of atmospheric and LBL neutrinos holds for any combination of NSI with up quarks, down quarks or electrons and it can be performed in terms of the effective NSI couplings $\varepsilon_{\alpha\beta}^\oplus$, which play the role of phenomenological parameters. In particular, the best-fit value and allowed ranges of $\varepsilon_{\alpha\beta}^\oplus$ are independent of η , while the bounds on the physical quantities $\varepsilon_{\alpha\beta}$ simply scale as $(\cos \eta + Y_n^\oplus \sin \eta)$. Moreover, it is immediate to see that for $\eta = \arctan(-1/Y_n^\oplus) \approx -43.6^\circ$ the contribution of NSI to the matter potential vanishes, so that no bound on $\varepsilon_{\alpha\beta}$ can be derived from atmospheric and LBL data in such case.

Following the approach of Ref. [227], the matter Hamiltonian H_{mat} , given in Eq. (5.10) after setting $\mathcal{E}_{\alpha\beta}(x) \equiv \varepsilon_{\alpha\beta}^\oplus$, can be parametrised in a way that mimics the structure of the vacuum term (5.9):

$$H_{\text{mat}} = Q_{\text{rel}} U_{\text{mat}} D_{\text{mat}} U_{\text{mat}}^\dagger Q_{\text{rel}}^\dagger \quad \text{with} \quad \begin{cases} Q_{\text{rel}} = \text{diag}(e^{i\alpha_1}, e^{i\alpha_2}, e^{-i\alpha_1 - i\alpha_2}), \\ U_{\text{mat}} = R_{12}(\varphi_{12}) R_{13}(\varphi_{13}) \tilde{R}_{23}(\varphi_{23}, \delta_{\text{NS}}), \\ D_{\text{mat}} = \sqrt{2} G_F N_e(x) \text{diag}(\varepsilon_\oplus, \varepsilon'_\oplus, 0) \end{cases} \quad (6.5)$$

where $R_{ij}(\varphi_{ij})$ is a rotation of angle φ_{ij} in the ij plane and $\tilde{R}_{23}(\varphi_{23}, \delta_{\text{NS}})$ is a complex rotation by angle φ_{23} and phase δ_{NS} . Note that the two phases α_1 and α_2 included in Q_{rel} are not a feature of neutrino-matter interactions, but rather a relative feature of the vacuum and matter terms. This is in accordance with the analysis in Section 5.2, where two CP violating invariants arose as ‘‘interference’’ among vacuum and matter terms. There is a single invariant for matter-only CP violation, parametrised here in terms of the phase δ_{NS} .

In order to simplify the analysis we neglect Δm_{21}^2 and also impose that two eigenvalues of H_{mat} are equal ($\varepsilon'_\oplus = 0$). The latter assumption is justified since, as shown in Ref. [244], strong cancellations in the oscillation of atmospheric neutrinos occur when two eigenvalues of H_{mat} are equal, and it is precisely in this situation that the weakest constraints can be placed. Setting $\Delta m_{21}^2 \rightarrow 0$ implies that the θ_{12} angle and the δ_{CP} phase disappear from the expressions of the oscillation probabilities, and the same happens to the φ_{23} angle and the δ_{NS} phase in the limit $\varepsilon'_\oplus \rightarrow 0$. Under these approximations the effective NSI couplings $\varepsilon_{\alpha\beta}^\oplus$ can be parametrised as:

$$\begin{aligned} \varepsilon_{ee}^\oplus - \varepsilon_{\mu\mu}^\oplus &= \varepsilon_\oplus (\cos^2 \varphi_{12} - \sin^2 \varphi_{12}) \cos^2 \varphi_{13} - 1, \\ \varepsilon_{\tau\tau}^\oplus - \varepsilon_{\mu\mu}^\oplus &= \varepsilon_\oplus (\sin^2 \varphi_{13} - \sin^2 \varphi_{12} \cos^2 \varphi_{13}), \\ \varepsilon_{e\mu}^\oplus &= -\varepsilon_\oplus \cos \varphi_{12} \sin \varphi_{12} \cos^2 \varphi_{13} e^{i(\alpha_1 - \alpha_2)}, \\ \varepsilon_{e\tau}^\oplus &= -\varepsilon_\oplus \cos \varphi_{12} \cos \varphi_{13} \sin \varphi_{13} e^{i(2\alpha_1 + \alpha_2)}, \\ \varepsilon_{\mu\tau}^\oplus &= \varepsilon_\oplus \sin \varphi_{12} \cos \varphi_{13} \sin \varphi_{13} e^{i(\alpha_1 + 2\alpha_2)}. \end{aligned} \quad (6.6)$$

With all this the relevant flavour transition probabilities for atmospheric and LBL experiments depend on eight parameters: $(\Delta m_{31}^2, \theta_{13}, \theta_{23})$ for the vacuum part, $(\varepsilon_{\oplus}, \varphi_{12}, \varphi_{13})$ for the matter part, and (α_1, α_2) as relative phases. Notice that in this case only the relative sign of Δm_{31}^2 and ε_{\oplus} is relevant for atmospheric and LBL neutrino oscillations: this is just a manifestation of the generalised mass ordering degeneracy described in Eqs. (5.47) and (5.48) once Δm_{21}^2 and ε'_{\oplus} are set to zero [227].

As further simplification, in order to keep the fit manageable we assume real NSI, which we implement by choosing $\alpha_1 = \alpha_2 = 0$ with φ_{ij} range $-\pi/2 \leq \varphi_{ij} \leq \pi/2$. It is important to note that with these approximations the formalism for atmospheric and LBL data is CP-conserving. We will go back to this point when discussing the experimental results included in the analysis.

In addition to atmospheric and LBL experiments, important information on neutrino oscillation parameters is provided also by reactor experiments with a baseline of about 1 km. Due to the very small amount of matter crossed, both standard and non-standard matter effects are completely irrelevant for these experiments, and the corresponding P_{ee} survival probability depends only on the vacuum parameters. However, in view of the high precision recently attained by both reactor and LBL experiments in the determination of the atmospheric mass-squared difference, combining them without adopting a full 3ν oscillation scheme requires a special care. In Ref. [245] it was shown that, in the limit $\Delta m_{21}^2 \ll \Delta m_{31}^2$ as indicated by the data, the $P_{\mu\mu}$ probability relevant for LBL-disappearance experiments can be accurately described in terms of a single effective mass parameter $\Delta m_{\mu\mu}^2 = \Delta m_{31}^2 - r_2 \Delta m_{21}^2$ with $r_2 = |U_{\mu 2}^{\text{lep}}|^2 / (|U_{\mu 1}^{\text{lep}}|^2 + |U_{\mu 2}^{\text{lep}}|^2)$. In the rest of this section we will therefore make use of $\Delta m_{\mu\mu}^2$ as the fundamental quantity parametrizing the atmospheric mass-squared difference. For each choice of the vacuum mixing parameters in U_{lep} , the calculations for the various data sets are then performed as follows:

- for atmospheric and LBL data we assume $\Delta m_{21}^2 = 0$ and set $\Delta m_{31}^2 = \Delta m_{\mu\mu}^2$;
- for reactor neutrinos we keep Δm_{21}^2 finite and set $\Delta m_{31}^2 = \Delta m_{\mu\mu}^2 + r_2 \Delta m_{21}^2$.

In this way the information provided by reactor and LBL data on the atmospheric mass scale is consistently combined in spite of the approximation $\Delta m_{21}^2 \rightarrow 0$ discussed above. Note that the correlations between solar and reactor neutrinos are properly taken into account in our fit, in particular for what concerns the octant of θ_{12} .

Matter potential for solar and KamLAND neutrinos

For the study of propagation of solar and KamLAND neutrinos one can work in the one mass dominance approximation, $\Delta m_{31}^2 \rightarrow \infty$ (which effectively means that $G_F \sum_f N_f(x) \varepsilon_{\alpha\beta}^f \ll \Delta m_{31}^2 / E_\nu$). In this approximation the survival probability P_{ee} can be written as [246, 247]

$$P_{ee} = c_{13}^4 P_{\text{eff}} + s_{13}^4 \quad (6.7)$$

The probability P_{eff} can be calculated in an effective 2×2 model described by the Hamiltonian $H_{\text{eff}} = H_{\text{vac}}^{\text{eff}} + H_{\text{mat}}^{\text{eff}}$, with:

$$H_{\text{vac}}^{\text{eff}} = \frac{\Delta m_{21}^2}{4E_\nu} \begin{pmatrix} -\cos 2\theta_{12} & \sin 2\theta_{12} e^{i\delta_{\text{CP}}} \\ \sin 2\theta_{12} e^{-i\delta_{\text{CP}}} & \cos 2\theta_{12} \end{pmatrix}, \quad (6.8)$$

$$H_{\text{mat}}^{\text{eff}} = \sqrt{2} G_F N_e(x) \left[\begin{pmatrix} c_{13}^2 & 0 \\ 0 & 0 \end{pmatrix} + [\xi^p + Y_n(x) \xi^n] \begin{pmatrix} -\varepsilon_D & \varepsilon_N \\ \varepsilon_N^* & \varepsilon_D \end{pmatrix} \right], \quad (6.9)$$

where we have imposed the quark-lepton factorization of Eq. (6.2) and used the parametrization convention of Eq. (2.56) for U^{lep} . The coefficients ε_D and ε_N are related to the original parameters

$\varepsilon_{\alpha\beta}$ by the following relations:

$$\begin{aligned} \varepsilon_D = & c_{13}s_{13} \operatorname{Re}(s_{23} \varepsilon_{e\mu} + c_{23} \varepsilon_{e\tau}) - (1 + s_{13}^2) c_{23}s_{23} \operatorname{Re}(\varepsilon_{\mu\tau}) \\ & - \frac{c_{13}^2}{2} (\varepsilon_{ee} - \varepsilon_{\mu\mu}) + \frac{s_{23}^2 - s_{13}^2 c_{23}^2}{2} (\varepsilon_{\tau\tau} - \varepsilon_{\mu\mu}), \end{aligned} \quad (6.10)$$

$$\varepsilon_N = c_{13}(c_{23} \varepsilon_{e\mu} - s_{23} \varepsilon_{e\tau}) + s_{13} [s_{23}^2 \varepsilon_{\mu\tau} - c_{23}^2 \varepsilon_{\mu\tau}^* + c_{23}s_{23}(\varepsilon_{\tau\tau} - \varepsilon_{\mu\mu})]. \quad (6.11)$$

Note that the δ_{CP} phase appearing in Eq. (6.8) could be transferred to Eq. (6.9) without observable consequences by means of a global rephasing. Hence, for each fixed value of η the relevant probabilities for solar and KamLAND neutrinos depend effectively on six quantities: the three real oscillation parameters Δm_{21}^2 , θ_{12} and θ_{13} , one real matter parameter ε_D , and one complex vacuum-matter combination $\varepsilon_N e^{-i\delta_{\text{CP}}}$. As stated in Sec. 6.1.1 in this section we will assume real NSI, implemented here by setting $\delta_{\text{CP}} = 0$ and considering only real (both positive and negative) values for ε_N .

Unlike in the Earth, the matter chemical composition of the Sun varies substantially along the neutrino trajectory, and consequently the potential depends non-trivially on the specific combinations of couplings with up and down quarks — i.e., on the value of η . This implies that the generalised mass-ordering degeneracy is not exact, except for $\eta = 0$ (in which case the NSI potential is proportional to the standard MSW potential and an exact inversion of the matter sign is possible). However, as we will see in Sec. 6.1.2, the generalised mass ordering transformation described in Eqs. (5.47) and (5.48) still results in a good fit to the global analysis of oscillation data for a wide range of values of η , and non-oscillation data are needed to break this degeneracy [248,249]. Because of the change in the θ_{12} octant implied by Eq. (5.47) and given that the standard LMA solution clearly favors $\theta_{12} < 45^\circ$, this alternative solution is characterised by a value of $\theta_{12} > 45^\circ$. In what follows we will denote it as “LMA-D” [241].

6.1.2 Analysis of solar and KamLAND data

Let us start by presenting the results of the updated analysis of solar and KamLAND experiments in the context of oscillations with the generalised matter potential in Eq. (6.9). We include the same data as the latest 3ν analysis in Chapter 4.

We present different projections of the allowed parameter space in Figs. 6.1–6.3. In the analysis we have fixed $\sin^2 \theta_{13} = 0.022$ which is the best-fit value from the global analysis of 3ν oscillations [1, 45].¹ So for each value of η there are four relevant parameters: Δm_{21}^2 , $\sin^2 \theta_{12}$, ε_D , and ε_N . As mentioned above, for simplicity the results are shown for real ε_N . Also strictly speaking the sign of ε_N is not physically observable in oscillation experiments, as it can be reabsorbed into a redefinition of the sign of θ_{12} . However, for definiteness we have chosen to present our results in the convention $\theta_{12} \geq 0$, and therefore we consider both positive and negative values of ε_N . Fig. 6.1 shows the two-dimensional projections on the oscillation parameters ($\theta_{12}, \Delta m_{21}^2$) for different values of η after marginalizing over the NSI parameters, while Fig. 6.2 shows the corresponding two-dimensional projections on the matter potential parameters ($\varepsilon_D, \varepsilon_N$) after marginalizing over the oscillation parameters. The one-dimensional ranges for the four parameters as a function of η are shown in Fig. 6.3.

The first thing to notice in the figures is the presence of the LMA-D solution for a wide range of values of η . This is a consequence of the approximate degeneracy discussed in the previous section. In particular, as expected, for $\eta = 0$ the degeneracy is exact and the LMA-D

¹Note that the determination of θ_{13} is presently dominated by reactor experiments, which have negligible matter effects and are therefore unaffected by the presence of NSI. Allowing for variations of θ_{13} within its current well-determined range has no quantitative impact on our results.

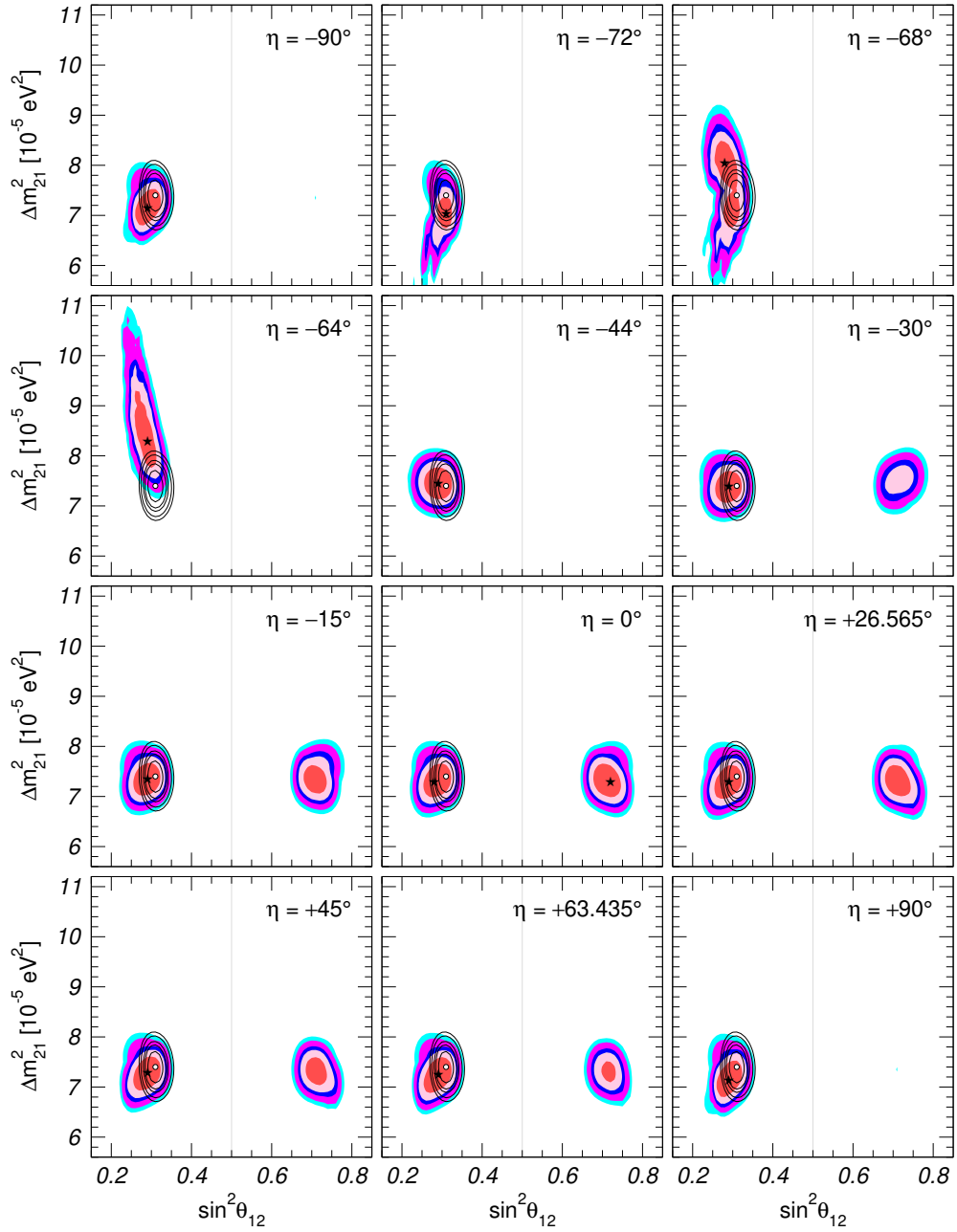


Figure 6.1: Two-dimensional projections of the 1σ , 90%, 2σ , 99% and 3σ CL (2 dof) allowed regions from the analysis of solar and KamLAND data in the presence of non-standard matter potential for the oscillation parameters $(\theta_{12}, \Delta m_{21}^2)$ after marginalizing over the NSI parameters and for θ_{13} fixed to $\sin^2 \theta_{13} = 0.022$. The best-fit point is marked with a star. The results are shown for fixed values of the NSI quark coupling parameter η . For comparison the corresponding allowed regions for the analysis in terms of 3ν oscillations without NSI are shown as black void contours. Note that, as a consequence of the periodicity of η , the regions in the first ($\eta = -90^\circ$) and last ($\eta = +90^\circ$) panels are identical.

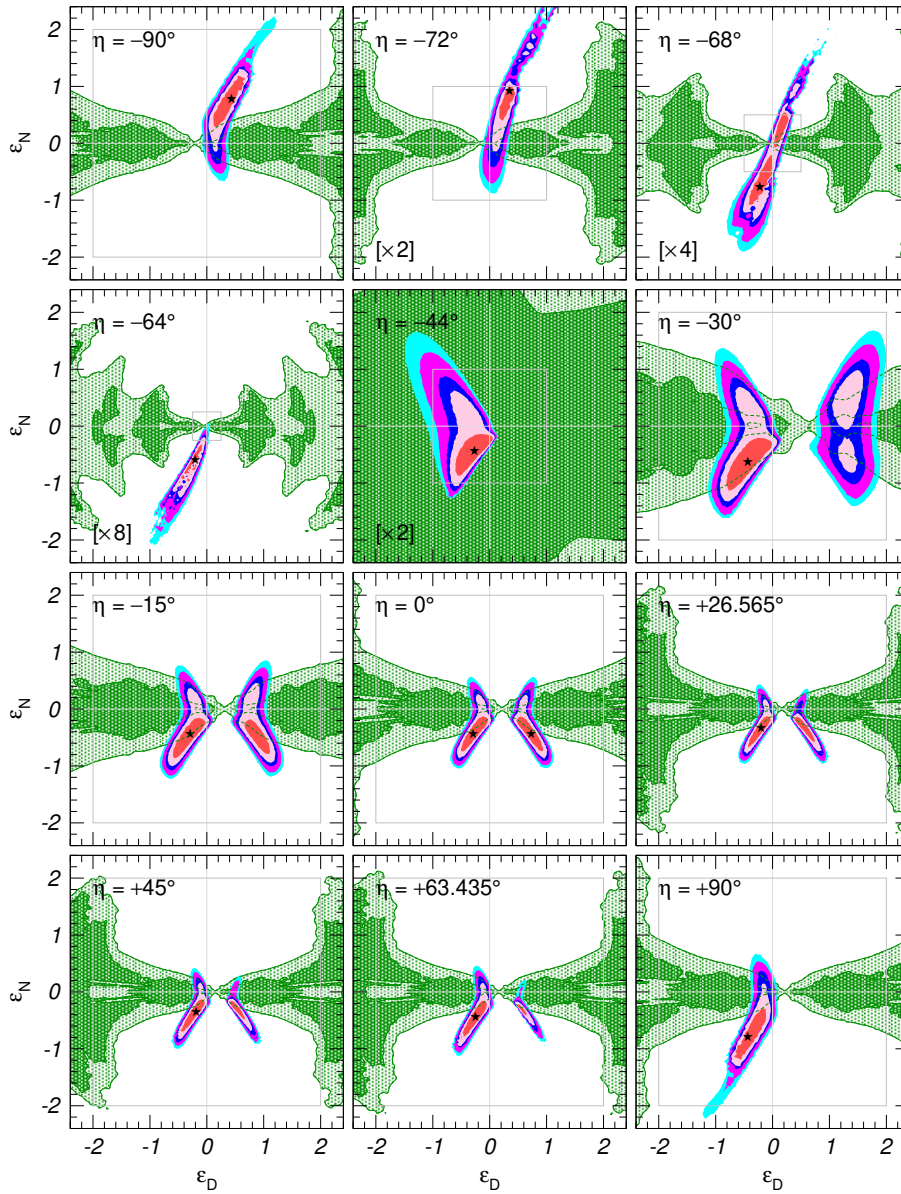


Figure 6.2: Two-dimensional projections of the 1σ , 90%, 2σ , 99% and 3σ CL (2 dof) allowed regions from the analysis of solar and KamLAND data in the presence of non-standard matter potential for the matter potential parameters $(\varepsilon_D, \varepsilon_N)$, for $\sin^2 \theta_{13} = 0.022$ and after marginalizing over the oscillation parameters. The best-fit point is marked with a star. The results are shown for fixed values of the NSI quark coupling parameter η . The panels with a scale factor “ $\times N$ ” in their lower-left corner have been “zoomed-out” by such factor with respect to the standard axis ranges, hence the grey square drawn in each panel always corresponds to $\max(|\varepsilon_D|, |\varepsilon_N|) = 2$ and has the same size in all the panels. For illustration we also show as shaded green areas the 90% and 3σ CL allowed regions from the analysis of the atmospheric and LBL data. Note that, as a consequence of the periodicity of η , the regions in the first ($\eta = -90^\circ$) and last ($\eta = +90^\circ$) panels are identical up to an overall sign flip.

region in Fig. 6.1 is perfectly symmetric to the LMA one with respect to maximal θ_{12} . Looking at the corresponding panels of Fig. 6.2 we note that the allowed area in the NSI parameter space is composed by two disconnected regions, one containing the SM case (i.e., the point $\varepsilon_D = \varepsilon_N = 0$) which corresponds to the “standard” LMA solution in the presence of the modified matter potential, and another which does not include such point and corresponds to the LMA-D solution. Although the appearance of the LMA-D region is a common feature, there is also a range of values of η for which such solution is strongly disfavored and does not appear at the displayed CLs.

In order to further illustrate the η dependence of the results, it is convenient to introduce the functions $\chi_{\text{LMA}}^2(\eta)$ and $\chi_{\text{LMA-D}}^2(\eta)$ which are obtained by marginalizing the χ^2 for a given value of η over both the oscillation and the matter potential parameters with the constraint $\theta_{12} < 45^\circ$ and $\theta_{12} > 45^\circ$, respectively. With this, in the left panel of Fig. 6.4 we plot the differences $\chi_{\text{LMA}}^2(\eta) - \chi_{\text{no-NSI}}^2$ (full lines) and $\chi_{\text{LMA-D}}^2(\eta) - \chi_{\text{no-NSI}}^2$ (dashed lines), where $\chi_{\text{no-NSI}}^2$ is the minimum χ^2 for standard 3ν oscillations (i.e., without NSI), while in the right panel we plot $\chi_{\text{LMA-D}}^2(\eta) - \chi_{\text{LMA}}^2(\eta)$ which quantifies the relative quality of the LMA and LMA-D solutions. From this plot we can see that even for the analysis of solar and KamLAND data alone (red lines) the LMA-D solution is disfavored at more than 3σ when $\eta \lesssim -40^\circ$ or $\eta \gtrsim 86^\circ$. Generically for such range of η the modified matter potential in the Sun, which in the presence of NSI is determined not only by the density profile but also by the chemical composition, does not allow for a degenerate solution compatible with KamLAND data. In particular, as discussed below, for a fraction of those η values the NSI contribution to the matter potential in the Sun becomes very suppressed and therefore the degeneracy between NSI and octant of θ_{12} cannot be realised. In what respects the LMA solution, we notice that it always provides a better fit (or equivalent for $\eta = 0$) than the LMA-D solution to solar and KamLAND data, for any value of η . This does not have to be the case in general, and indeed it is no longer so when atmospheric data are also included in the analysis. We will go back to this point in the next section.

From the left panel in Fig. 6.4 we see that the introduction of NSI can lead to a substantial improvement in the analysis of solar and KamLAND data, resulting in a sizeable decrease of the minimum χ^2 with respect to the standard oscillation scenario. The maximum gain occur for $\eta \simeq -64^\circ$ and is about 11.2 units in χ^2 (i.e., a 3.3σ effect), although for most of the values of η the inclusion of NSI improves the combined fit to solar and KamLAND by about 2.5σ . This is mainly driven by the well known 2.7σ tension between solar and KamLAND data in the determination of Δm_{21}^2 described in Section 4.1.2. Such tension can be alleviated in presence of a non-standard matter potential, thus leading to the corresponding decrease in the minimum χ^2 for most values of η — with the exception of the range $-70^\circ \lesssim \eta \lesssim -60^\circ$. Furthermore, as seen in the lower panel in Fig. 6.3 the allowed range of Δm_{21}^2 implied by the combined solar and KamLAND data is pretty much independent of the specific value of η , except again for $-70^\circ \lesssim \eta \lesssim -60^\circ$ in which case it can extend well beyond the standard oscillation LMA values.

The special behaviour of the likelihood of solar and KamLAND in the range $-70^\circ \lesssim \eta \lesssim -60^\circ$ is a consequence of the fact that for such values the NSI contributions to the matter potential in the Sun approximately cancel. As mentioned in the previous section, the matter chemical composition of the Sun varies substantially along the neutrino production region, with $Y_n(x)$ dropping from about $1/2$ in the center to about $1/6$ at the border of the solar core. Thus for $-70^\circ \lesssim \eta \lesssim -60^\circ$ (corresponding to $-2.75 \lesssim \tan \eta \lesssim -1.75$) the effective NSI couplings $\mathcal{E}_{\alpha\beta}(x) = \varepsilon_{\alpha\beta}^p + Y_n(x)\varepsilon_{\alpha\beta}^n \propto 1 + Y_n(x)\tan \eta \rightarrow 0$ vanish at some point inside the neutrino production region. This means that for such values of η the constraints on the NSI couplings from solar data become very weak, being prevented from disappearing completely only by the *gradient* of $Y_n(x)$. This is visible in the two upper panels in Fig. 6.3 and in the panels of Fig. 6.2 with η in such range, where a multiplicative factor 2–8 has to be included to make the regions

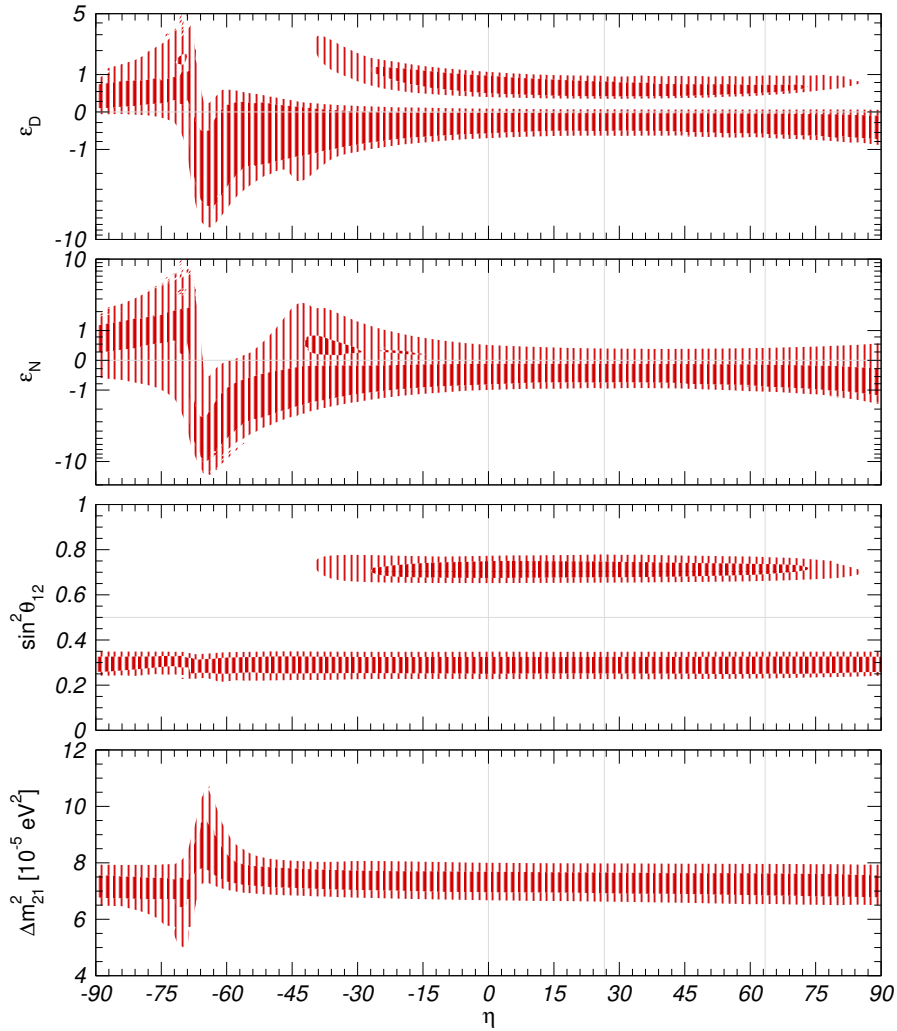


Figure 6.3: 90% and 3σ CL (1 dof) allowed ranges from the analysis of solar and KamLAND data in the presence of NSI, for the four relevant parameters (the matter potential parameters ε_D and ε_N as well as the oscillation parameters Δm_{21}^2 and $\sin^2\theta_{12}$) as a function of the NSI quark coupling parameter η , for $\sin^2\theta_{13} = 0.022$. In each panel the three undisplayed parameters have been marginalised.

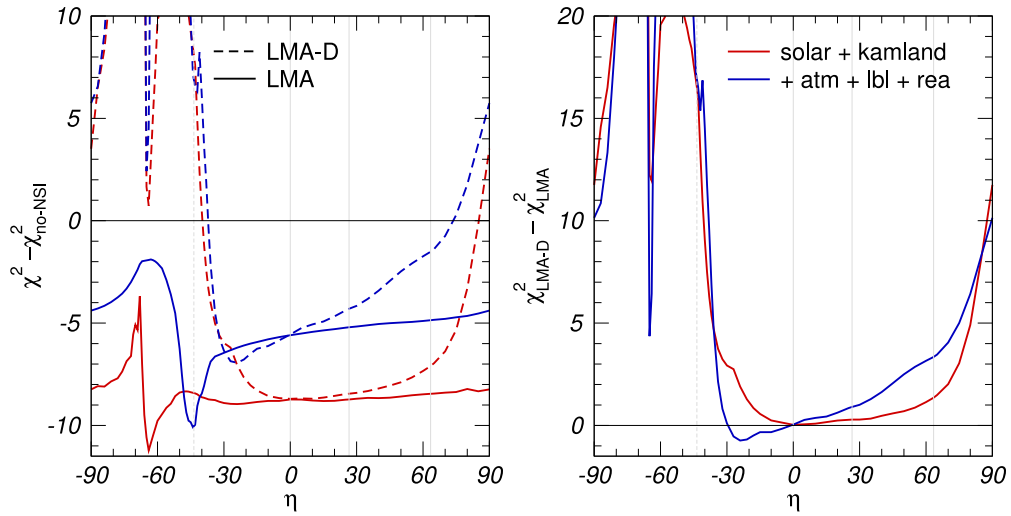


Figure 6.4: Left: $\chi_{\text{LMA}}^2(\eta) - \chi_{\text{no-NSI}}^2$ (full lines) and $\chi_{\text{LMA-D}}^2(\eta) - \chi_{\text{no-NSI}}^2$ (dashed lines) for the analysis of different data combinations (as labeled in the figure) as a function of the NSI quark coupling parameter η . Right: $\chi_{\text{LMA-D}}^2(\eta) - \chi_{\text{LMA}}^2(\eta)$ as a function of η . See text for details.

fit in the same axis range. Indeed for those values of η the allowed NSI couplings can be so large that their effect in the propagation of long baseline reactor neutrinos through the Earth becomes sizable, and can therefore lead to spectral distortions in KamLAND which affect the determination of Δm_{21}^2 — hence the “migration” and distortion of the LMA region observed in the corresponding panels in Fig. 6.1. In particular, it is precisely for $\eta = -64^\circ$ for which the “migration” of the KamLAND region leads to the best agreement with the solar determination of Δm_{12}^2 , whereas for $\eta = -68^\circ$ we find the worst agreement. In any case, looking at the shaded green regions in the corresponding panels of Fig. 6.2 we can anticipate that the inclusion of atmospheric and LBL oscillation experiments will rule out almost completely such very large NSI values.

As for θ_{12} , looking at the relevant panel in Fig. 6.3 we can see that its determination is pretty much independent of the value of η , however a comparison between coloured and void regions in Fig. 6.1 shows that its allowed range always extends to lower values than in the standard 3ν case without NSI. This is expected since the presence of non-diagonal NSI parametrised by ε_N provides another source of flavour transition, thus leading to a weakening of the lower bound on θ_{12} .

We finish this section by noticing that two of the panels in Figs. 6.1 and 6.2 correspond to the values of NSI only with $f = u$ ($\eta \approx 26.6^\circ$) and only with $f = d$ ($\eta \approx 63.4^\circ$) and can be directly compared with the results of the previous global OSC+NSI analysis in Ref. [228]. For illustration we also show in one of the panels the results for $\eta = -44^\circ$ which is close to the value for which NSI effects in the Earth matter cancel.

6.1.3 Results of the global oscillation analysis

In addition to the solar and KamLAND data discussed so far, in our global analysis we also consider the following data sets:

- atmospheric neutrino data: this sample includes the four phases of Super-Kamiokande (up

to 1775 days of SK4 [195]) in the form of the “classical” samples of e -like and μ -like events (70 energy and zenith angle bins), together with the complete set of DeepCore 3-year μ -like events (64 data points) presented in Ref. [89] and publicly released in Ref. [250]. The calculations of the event rates for both detectors are based on the atmospheric neutrino flux calculations described in Ref. [144]. In addition, we also include the results on ν_μ -induced upgoing muons reported by IceCube [251–253], based on one year of data taking;

- LBL experiments: we include here the ν_μ and $\bar{\nu}_\mu$ disappearance as well as the ν_e and $\bar{\nu}_e$ appearance data in MINOS [36] (39, 14, 5, and 5 data points, respectively); the ν_μ and $\bar{\nu}_\mu$ disappearance data in T2K [95] (39 and 55 data points, respectively), the latter as of January 2018; and the ν_μ disappearance data in NO ν A [254] (72 data points)². As mentioned in Sec. 6.1.1, in order to keep the fit manageable we restrict ourselves to the CP-conserving scenario. At present, the results of the full 3ν oscillation analysis with standard matter potential show a hint of CP violation [1, 45], which is mainly driven by the LBL ν_e and $\bar{\nu}_e$ appearance data at T2K [95] and NO ν A [254]. Conversely, allowing for CP violation has negligible impact on the determination of the CP-conserving parameters in the analysis of MINOS appearance data and of any LBL disappearance data samples, as well as in our analysis of atmospheric events mentioned above. Hence, to ensure full consistency with our CP-conserving parametrization we have chosen *not* to include in the present study the data from the ν_e and $\bar{\nu}_e$ appearance channels in NO ν A and T2K. This also renders our fit only marginally sensitive to the neutrino mass ordering. In what follows we will refer to the LBL data included here as LBL-CPC. Note that for simplicity we have omitted from our analysis the MINOS+ results on ν_μ disappearance, despite the fact that they probe higher neutrino energies than the other LBL experiments and are therefore, at least in principle, more sensitive to the NSI parameters than, e.g., MINOS [255]. The rationale behind this choice is that the LBL experiments which we include are crucial to determine the oscillation parameters in an energy range where NSI effects are subdominant, whereas at present MINOS+ data lack this capability. As for the NSI parameters involved in ν_μ disappearance, they are more strongly constrained by the atmospheric neutrino data of Super-Kamiokande and IceCube, which extends to energies well beyond those of MINOS+;
- medium baseline reactor experiments: since these experiments are largely insensitive to matter effects (either standard or non-standard), the results included here coincide with those of the standard 3ν analysis presented in Ref. [45] and illustrated in the black lines of the plot tagged “Synergies: determination of $\Delta m_{3\ell}^2$ ”. Such analysis is based on a reactor-flux-independent approach as described in Ref. [256], and includes the Double-Chooz FD-I/ND and FD-II/ND spectral ratios with 455-day (FD-I), 363-day (FD-II), and 258-day (ND) exposures [93] (56 data points), the Daya-Bay 1230-day EH2/EH1 and EH3/EH1 spectral ratios [257] (70 data points), and the Reno 1500-day FD/ND spectral ratios [258] (26 data points).

Let us begin by showing in Figure 6.5 the two-dimensional projections of the allowed regions in the Earth’s matter potential parameters ε_\oplus , φ_{12} and φ_{13} (i.e., in the parametrization of Eq. (6.6) with $\alpha_i = 0$) after marginalizing over the oscillation parameters. The green regions show the 90% and 3σ confidence regions (2 dof) from the analysis of atmospheric, LBL-CPC and medium baseline reactor experiments. Besides the increase in statistics on low-energy atmospheric events provided by the updated Super-Kamiokande and the new DeepCore data samples, the main

²We do not include the NO ν A antineutrino data or the latest T2K $\bar{\nu}_\mu$ results, because they were not available when the fit was performed. As the purpose of this section is just to understand the sensitivity to NSI of different experiments, these datasets will be included in the more complete fits in Sections 6.2 and 7.2.

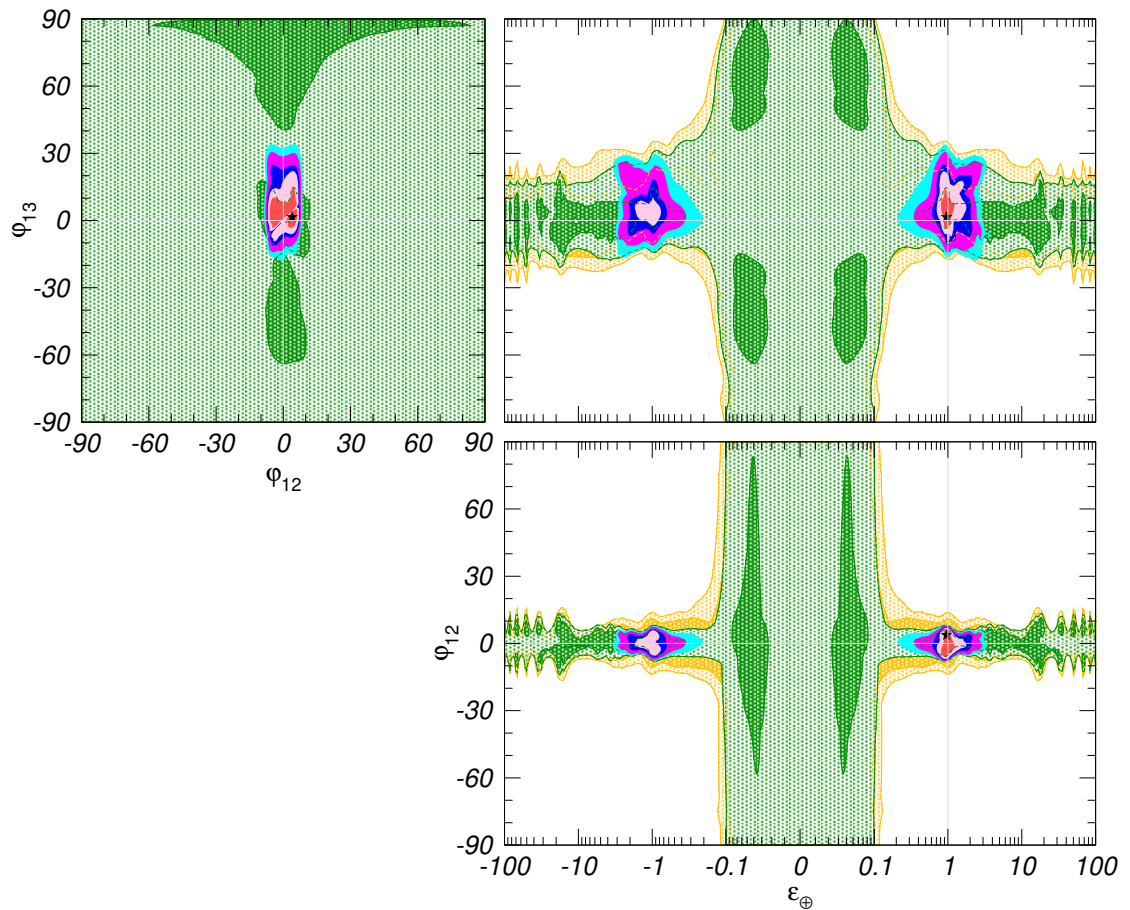


Figure 6.5: Two-dimensional projections of the allowed regions onto the matter potential parameters ε_{\oplus} , φ_{12} , and φ_{13} after marginalization with respect to the undisplayed parameters. The large green regions correspond to the analysis of atmospheric, LBL-CPC, and medium baseline reactor data at 90% and 3σ CL. For comparison we show in yellow the corresponding results when omitting IceCube and reactor data. The solid coloured regions show the 1σ , 90%, 2σ , 99% and 3σ CL allowed regions once solar and KamLAND data are included. The best-fit point is marked with a star.

difference with respect to the analysis in Refs. [227, 228] is the inclusion of the bounds on NSI-induced ν_μ disappearance provided by IceCube high-energy data as well as the precise information on θ_{13} and $|\Delta m_{31}^2|$ from medium baseline reactor experiments. To illustrate their impact we show as yellow regions the results obtained when IceCube and reactor data are omitted. For what concerns the projection over the matter potential parameters shown here, we have verified that the difference between the yellow and green regions is mostly driven by IceCube, which restricts the allowed values of the φ_{12} for $|\varepsilon_\oplus| \sim 0.1-1$. This can be understood since, for neutrinos with energies above $\mathcal{O}(100 \text{ GeV})$, the vacuum oscillation is very suppressed and the survival probability of atmospheric ν_μ arriving at zenith angle Θ_ν is dominated by the matter induced transitions

$$P_{\mu\mu} \simeq 1 - \sin^2(2\varphi_{\mu\mu}) \sin^2\left(\frac{d_e(\Theta_\nu)\varepsilon_\oplus}{2}\right) \quad \text{with} \quad \sin^2\varphi_{\mu\mu} = \sin^2\varphi_{12} \cos^2\varphi_{13} \quad (6.12)$$

where $d_e(\Theta_\nu) = \sqrt{2}G_F X_e(\Theta_\nu)$ and the column density $X_e(\Theta_\nu)$ is the integral of $N_e(x)$ along the neutrino path in the Earth [259]. Since $0.2 \lesssim d_e(\Theta_\nu) \lesssim 20$ for $-1 \leq \cos\Theta_\nu \leq -0.2$, the range $0.1 \lesssim |\varepsilon_\oplus| \lesssim 1$ corresponds to the first oscillation maximum for some of the trajectories. Also, the effective parameter $\varphi_{\mu\mu}$ entering in the expression of $P_{\mu\mu}$ depends linearly on φ_{12} and only quadratically on φ_{13} , which explains why the bounds on the mixings are stronger for φ_{12} than for φ_{13} .

As can be seen in Fig. 6.5, even with the inclusion of IceCube neither upper nor lower bounds on the overall strength of the Earth's matter effects, ε_\oplus , can be derived from the analysis of atmospheric, LBL-CPC and medium baseline reactor experiments [227, 244, 260].³ This happens because the considered data sample is mainly sensitive to NSI through ν_μ disappearance, and lacks robust constraints on matter effects in the ν_e sector. As a consequence, when marginalizing over ε_\oplus (as well as over the oscillation parameters) the full flavour projection ($\varphi_{12}, \varphi_{13}$) plane is allowed. On the other hand, once the results of solar and KamLAND experiments (which are sensitive to ν_e) are included in the analysis a bound on ε_\oplus is obtained and the flavour structure of the matter potential in the Earth is significantly constrained.

In Fig. 6.6 we show the two-dimensional projections of the allowed regions from the global analysis onto different sets of oscillation parameters. These regions are obtained after marginalizing over the undisplayed vacuum parameters as well as the NSI couplings. For comparison we also show as black-contour void regions the corresponding results with the standard matter potential, i.e., in the absence of NSI. As discussed in Sec. 6.1.1, in the right panels we have chosen to plot the regions in terms of the effective mass-squared difference relevant for ν_μ disappearance experiments, $\Delta m_{\mu\mu}^2$. Notice that, having omitted NO ν A and T2K appearance data and also set $\Delta m_{21}^2 = 0$ in atmospheric and LBL-CPC experiments, the impact of the mass ordering on the results of the fit is greatly reduced.

This figure clearly shows the robustness of the determination of the Δm_{21}^2 , $|\Delta m_{\mu\mu}^2|$ and θ_{23} vacuum oscillation parameters even in the presence of the generalised NSI. This result relies on the complementarity and synergies between the different data sets, which allows to constrain those regions of the parameter space where cancellations between standard and non-standard effects occur in a particular data set. To illustrate this we show as shaded regions the results obtained when some of the data are removed. For example, comparing the solid coloured regions with the shaded red ones in the left panel we see how, in the presence of NSI with arbitrary values of η , the precise determination of Δm_{21}^2 requires the inclusion of atmospheric, LBL-CPC and medium baseline reactor data: if these sets are omitted, the huge values of the NSI couplings allowed by solar data for $-70^\circ \lesssim \eta \lesssim -60^\circ$ destabilise KamLAND's determination of Δm_{21}^2 , as

³See Refs. [261, 262] for constraints in more restricted NSI scenarios.

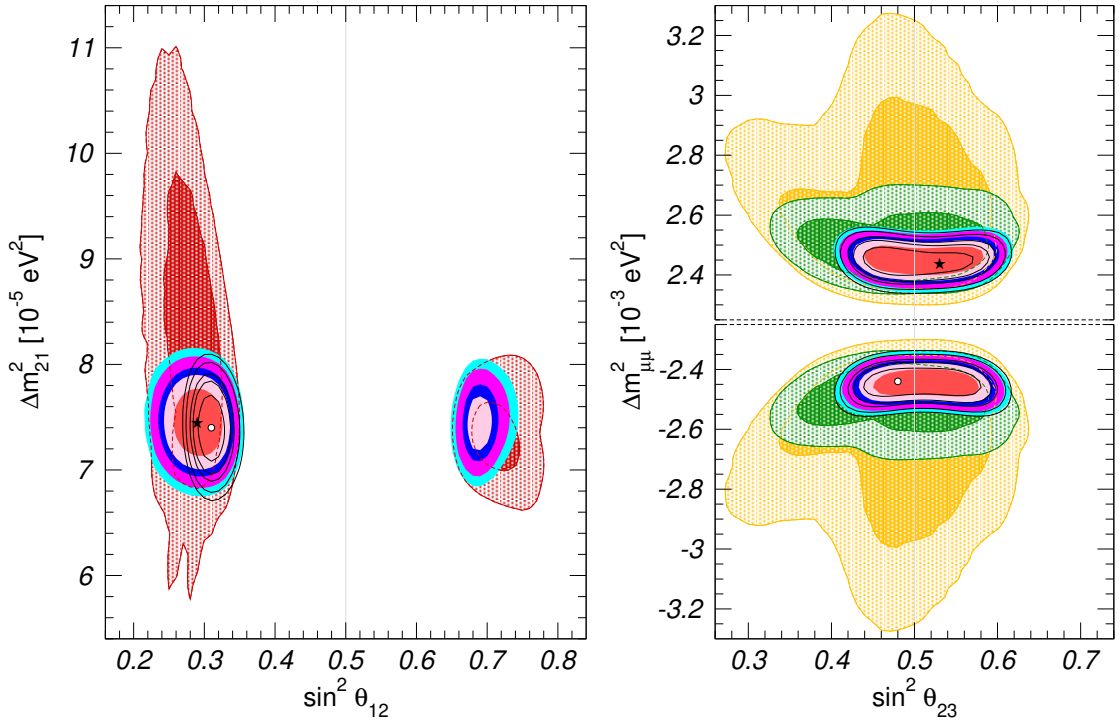


Figure 6.6: Two-dimensional projections of the allowed regions onto different vacuum parameters after marginalizing over the matter potential parameters (including η) and the undisplayed oscillation parameters. The solid coloured regions correspond to the global analysis of all oscillation data, and show the 1σ , 90%, 2σ , 99% and 3σ CL allowed regions; the best-fit point is marked with a star. The black void regions correspond to the analysis with the standard matter potential (i.e., without NSI) and its best-fit point is marked with an empty dot. For comparison, in the left panel we show in red the 90% and 3σ allowed regions including only solar and KamLAND results, while in the right panels we show in green the 90% and 3σ allowed regions excluding solar and KamLAND data, and in yellow the corresponding ones excluding also IceCube and reactor data.

discussed in Sec. 6.1.2. The inclusion of these sets also limits the margins for NSI to alleviate the tension between solar and KamLAND data on the preferred Δm_{21}^2 value, as can be seen by comparing the full dark-blue and red lines in the left panel of Fig. 6.4: indeed, in the global analysis the best-fit is achieved for $\eta \simeq -44^\circ$, which is precisely when the NSI effects in the Earth matter cancel so that no restriction on NSI contributions to solar and KamLAND data is imposed.

In the same way we see on the right panels that, if the solar and KamLAND data are removed from the fit, the determination of $\Delta m_{\mu\mu}^2$ and θ_{23} degrades because of the possible cancellations between NSI and mass oscillation effects in the relevant atmospheric and LBL-CPC probabilities. As NSI lead to energy-independent contributions to the oscillation phase, such cancellations allow for larger values of $|\Delta m_{\mu\mu}^2|$. Comparing the yellow and green regions we see the inclusion medium baseline reactor experiments, for which NSI effects are irrelevant due to the short baselines involved, is crucial to reduce the degeneracies and provide a NSI-independent measurement of $|\Delta m_{\mu\mu}^2|$. Even so, only the inclusion of solar and KamLAND allows to recover the full sensitivity of atmospheric and LBL-CPC experiments and derive limits on $\Delta m_{\mu\mu}^2$ and θ_{23} as robust as the standard ones.

The most dramatic implications of NSI for what concerns the determination of the oscillation parameters affect θ_{12} . In particular, for generic NSI with arbitrary η the LMA-D solution is still perfectly allowed by the global oscillation analysis, as indicated by the presence of the corresponding region in the left panel in Fig. 6.6. Turning to Fig. 6.4 we see that even after including all the oscillation data (dark-blue lines) the LMA-D solution is allowed at 3σ for $-38^\circ \lesssim \eta \lesssim 87^\circ$ (as well as in a narrow window around $\eta \simeq -65^\circ$), and indeed for $-28^\circ \lesssim \eta \lesssim 0^\circ$ it provides a slightly better global fit than LMA. From Fig. 6.6 we also see that the lower bound on θ_{12} in the presence of NSI is substantially weaker than the standard 3ν case. We had already noticed such reduction in the analysis of solar and KamLAND data for any value of η ; here we point out that the cancellation of matter effects in the Earth for $\eta \approx -43.6^\circ$ prevents any improvement of that limit from the addition of Earth-based oscillation experiments.

The bounds on the five relevant NSI couplings (two diagonal differences and three non-diagonal entries) from the global oscillation analysis are displayed in Fig. 6.7 as a function of η . Concretely, for each value of η we plot as vertical bars the 90% and 3σ allowed ranges (1 dof) after marginalizing with respect to the undisplayed parameters. The left and right panels correspond to the limits for θ_{12} within the LMA and LMA-D solution, respectively, both defined with respect to the same common minimum for each given η . For the sake of convenience and comparison with previous results we list in the first columns in Table 6.1 the 95% CL ranges for NSI with up-quarks only ($\eta \approx 26.6^\circ$), down-quarks only ($\eta \approx 63.4^\circ$) and couplings proportional to the electric charge ($\eta = 0^\circ$); in this last case we have introduced an extra $\sqrt{5}$ normalisation factor so that the quoted bounds can be directly interpreted in terms of $\varepsilon_{\alpha\beta}^p$. Let us point out that the sign of each non-diagonal $\varepsilon_{\alpha\beta}$ can be flipped away by a suitable change of signs in some of the mixing angles; it is therefore not an intrinsic property of NSI, but rather a relative feature of the vacuum and matter Hamiltonians. Thus, strictly speaking, once the results are marginalised with respect to all the other parameters in the most general parameter space, the oscillation analysis can only provide bounds on $|\varepsilon_{\alpha\neq\beta}|$. However, for definiteness we have chosen to restrict the range of the mixing angles to $0 \leq \theta_{ij} \leq \pi/2$ and to ascribe the relative vacuum-matter signs to the NSI couplings, so that the ranges of the non-diagonal $\varepsilon_{\alpha\beta}$ in Fig. 6.7 as well as in Table 6.1 are given for both signs.

From Fig. 6.7 and Tab. 6.1 we see that the allowed range for all the couplings (except $\varepsilon_{ee} - \varepsilon_{\mu\mu}$) obtained marginalizing over both θ_{12} octants, which we denote in the table as LMA \oplus LMA-D, is only slightly wider than what obtained considering only the LMA solution. Conversely, for $\varepsilon_{ee} - \varepsilon_{\mu\mu}$ the allowed range is composed by two disjoint intervals, each one corresponding to a

	LMA	LMA \oplus LMA-D
$\varepsilon_{ee}^u - \varepsilon_{\mu\mu}^u$	$[-0.020, +0.456]$	$\oplus[-1.192, -0.802]$
$\varepsilon_{\tau\tau}^u - \varepsilon_{\mu\mu}^u$	$[-0.005, +0.130]$	$[-0.152, +0.130]$
$\varepsilon_{e\mu}^u$	$[-0.060, +0.049]$	$[-0.060, +0.067]$
$\varepsilon_{e\tau}^u$	$[-0.292, +0.119]$	$[-0.292, +0.336]$
$\varepsilon_{\mu\tau}^u$	$[-0.013, +0.010]$	$[-0.013, +0.014]$
$\varepsilon_{ee}^d - \varepsilon_{\mu\mu}^d$	$[-0.027, +0.474]$	$\oplus[-1.232, -1.111]$
$\varepsilon_{\tau\tau}^d - \varepsilon_{\mu\mu}^d$	$[-0.005, +0.095]$	$[-0.013, +0.095]$
$\varepsilon_{e\mu}^d$	$[-0.061, +0.049]$	$[-0.061, +0.073]$
$\varepsilon_{e\tau}^d$	$[-0.247, +0.119]$	$[-0.247, +0.119]$
$\varepsilon_{\mu\tau}^d$	$[-0.012, +0.009]$	$[-0.012, +0.009]$
$\varepsilon_{ee}^p - \varepsilon_{\mu\mu}^p$	$[-0.041, +1.312]$	$\oplus[-3.327, -1.958]$
$\varepsilon_{\tau\tau}^p - \varepsilon_{\mu\mu}^p$	$[-0.015, +0.426]$	$[-0.424, +0.426]$
$\varepsilon_{e\mu}^p$	$[-0.178, +0.147]$	$[-0.178, +0.178]$
$\varepsilon_{e\tau}^p$	$[-0.954, +0.356]$	$[-0.954, +0.949]$
$\varepsilon_{\mu\tau}^p$	$[-0.035, +0.027]$	$[-0.035, +0.035]$

Table 6.1: 2σ allowed ranges for the NSI couplings $\varepsilon_{\alpha\beta}^u$, $\varepsilon_{\alpha\beta}^d$ and $\varepsilon_{\alpha\beta}^p$ as obtained from the global analysis of oscillation data. The results are obtained after marginalizing over oscillation and the other matter potential parameters either within the LMA only and within both LMA and LMA-D subspaces respectively (this second case is denoted as LMA \oplus LMA-D).

different θ_{12} octant. Note that for this coupling the interval associated with the LMA solution is not centered at zero due to the tension between the value of Δm_{21}^2 preferred by KamLAND and solar experiments, even after including the bounds from atmospheric and LBL data. In general, we find that the allowed ranges for all the couplings do not depend strongly on the value of η as long as η differs enough from the critical value $\eta \approx -43.6^\circ$. As already explained, at this point NSI in the Earth cancel out, so that no bound on the NSI parameters can be derived from any Earth-based experiment. This leads to a breakdown of the limits on $\varepsilon_{\alpha\beta}$, since solar data are only sensitive to the ε_D and ε_N combinations and cannot constrain the five NSI couplings simultaneously. In addition to the region around $\eta \approx -43.6^\circ$, there is also some mild weakening of the bounds on NSI couplings involving ν_e for $-70^\circ \lesssim \eta \lesssim -60^\circ$, corresponding to the window where NSI effects in the Sun are suppressed. Apart from these special cases, the bounds quoted in Table 6.1 are representative of the characteristic sensitivity to the NSI coefficients from present oscillation experiments, which at 95% CL ranges from $\mathcal{O}(1\%)$ for $|\varepsilon_{\mu\tau}|$ to $\mathcal{O}(30\%)$ for $|\varepsilon_{e\tau}|$ — the exception being, of course, $\varepsilon_{ee} - \varepsilon_{\mu\mu}$.

We finish by quantifying the results of our analysis in terms of the effective NSI parameters which describe the generalised Earth matter potential and are, therefore, the relevant quantities for the study of LBL experiments. The results are shown in Fig. 6.8 where we plot the dependence of the global χ^2 on each NSI effective couplings after marginalization over all other parameters⁴. Let us point out that, if only the results from Earth-based experiments such as atmospheric, LBL and reactor data were included in the analysis, the curves would be independent of η . However, when solar experiments are also considered the global χ^2 becomes sensitive to the value of η . Given that, what we quantify in Fig. 6.8 is our present knowledge of the matter

⁴Notice that the correlations among the allowed values for these parameters are important and they are required for reconstruction of the allowed potential at given CL.

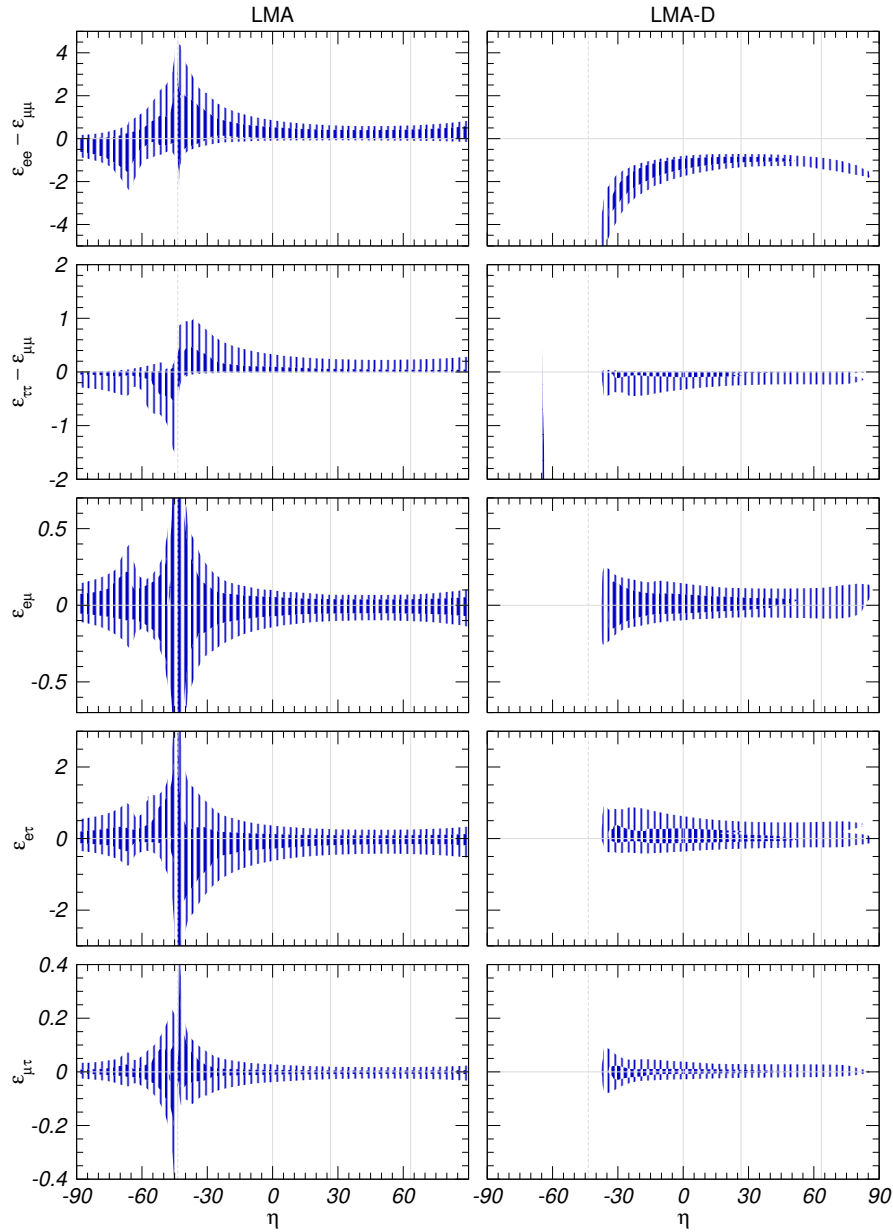


Figure 6.7: 90%, and 3σ CL (1 dof) allowed ranges for the NSI couplings from the global oscillation analysis in the presence of non-standard matter potential as a function of the NSI quark coupling parameter η . In each panel the undisplayed parameters have been marginalised. On the left panels the oscillation parameters have been marginalised within the LMA region while the right panels corresponds to LMA-D solutions. The ranges are defined with respect to the minimum for each η .

potential for neutrino propagation in the Earth for *any unknown value* of η . Technically this is obtained by marginalizing the results of the global χ^2 with respect to η as well, so that the $\Delta\chi^2$ functions plotted in the figure are defined with respect to the absolute minimum for any η (which, as discussed above and shown in Fig. 6.4, lies close to $\eta \sim -45^\circ$). In the upper panels the oscillation parameters have been marginalised within the LMA solution and in the lower ones within the LMA-D solution.

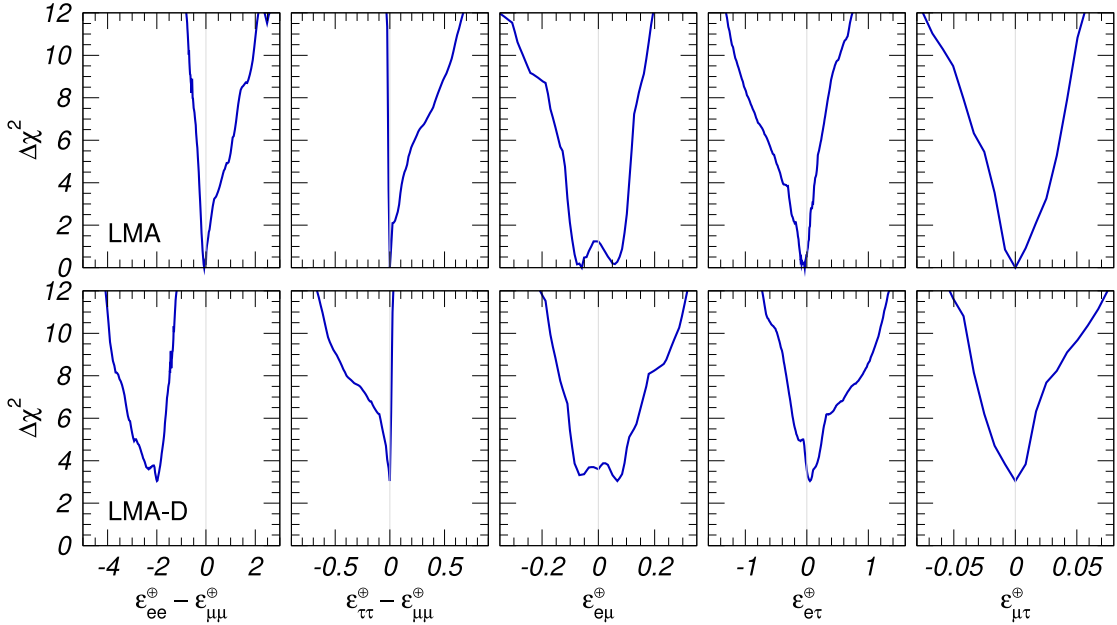


Figure 6.8: Dependence of the $\Delta\chi^2$ function on the effective NSI parameters relevant for matter effects in LBL experiments with arbitrary values of η , from the global analysis of solar, atmospheric, LBL-CPC and reactor data. The upper (lower) panels correspond to solutions within the LMA (LMA-D) subset of parameter space.

6.1.4 Summary

In this section we have presented an updated analysis of neutrino oscillation results with the aim of establishing how well we can presently determine the size and flavour structure of NSI-NC which affect the evolution of neutrinos in a matter background. In particular we have extended previous studies by considering NSI with an arbitrary ratio of couplings to up and down quarks (parametrised by an angle η) and a lepton-flavour structure independent of the quark type (parametrised by a matrix $\varepsilon_{\alpha\beta}$). We have included in our fit all the solar, atmospheric, reactor and accelerator data commonly used for the standard 3ν oscillation analysis, with the only exception of T2K and $\text{NO}\nu A$ appearance data whose recent hints in favor of CP violation are not easily accommodated within the CP-conserving approximation assumed in this fit. We have found that:

- classes of experiments which are sensitive to NSI only through matter characterised by a limited range of proton/neutron ratios Y_n unavoidably exhibit suppression of NSI effects for specific values of η . This is the case for solar data at $-70^\circ \lesssim \eta \lesssim -60^\circ$, and for Earth-

based (atmospheric, LBL, reactor) experiments at $\eta \approx -44^\circ$. Such cancellations limit the sensitivity to the NSI couplings;

- moreover, the interplay between vacuum and matter contributions to the flavour transition probabilities in classes of experiments with limited energy range and/or sensitive only to a specific oscillation channel spoils the accurate determination of the oscillation parameters achieved in the standard 3ν scenario. This is particularly visible in Δm_{21}^2 and θ_{12} as determined by solar and KamLAND data, as well as in Δm_{31}^2 and θ_{23} as determined by atmospheric, LBL-CPC and medium baseline reactor data;
- however, both problems can be efficiently resolved by combining together different classes of experiments, so to ensure maximal variety of matter properties, energy ranges, and oscillation channels. In particular, our calculations show that the precise determination of the vacuum parameters is fully recovered (except for θ_{12}) in a joint analysis of solar and Earth-based oscillation experiments, even when arbitrary values of η are considered;
- the well-known LMA-D solution, which arises in the presence of NSI as a consequence of the generalised mass ordering degeneracy, is allowed at 3σ for $-38^\circ \lesssim \eta \lesssim 87^\circ$ from the global analysis of oscillation data.

In addition, we have determined the allowed range of the NSI couplings $\varepsilon_{\alpha\beta}$ as a function of the up-to-down coupling η , showing that such constraints are generically robust except for a few specific values of η where cancellations occurs. Finally, in view of the possible implications that generic NSI-NC may have for future Earth-based facilities, we have recast the results of our analysis in terms of the effective NSI parameters $\varepsilon_{\alpha\beta}^\oplus$ which describe the generalised matter potential in the Earth, and are therefore the relevant quantities for the study of atmospheric and LBL experiments.

6.2 General analysis: robustness of LBL accelerator experiments under NSI

In the previous section, we have derived bounds on CP conserving NSI-NC from a global analysis of oscillation data. The obtained constraints are strong in general, but in some flavour channels $\mathcal{O}(0.1)$ NSI are still allowed. Being a fit to CP conserving effects, only ν_μ disappearance data from the T2K and NO ν A accelerator LBL experiments was included. But with the results we found, the allowed NSI could have an impact on the $\bar{\nu}_\mu \rightarrow \bar{\nu}_e$ appearance probability as well. This is mostly so because in appearance channels the standard contribution is suppressed by three-flavour mixing whereas the new physics contributions may not be [263].

We have seen that the $\bar{\nu}_e$ appearance channel is particularly relevant in assessing the questions still open in the three-neutrino analysis: the maximality and octant of θ_{23} , the ordering of the mass eigenstates, and leptonic CP violation. The clarification of these unknowns is the main focus of the running LBL experiments and its precise determination is at the center of the physics programme of the upcoming LBL facilities, in particular the Deep Underground Neutrino Experiment (DUNE) [42] and the Tokai to HyperKamiokande (T2HK) experiment [43].

In the presence of NSI, however, the task of exploring leptonic CP violation in LBL experiments becomes enriched (to the point of confusion) by new sources of CP violation and an intrinsic degeneracy in the Hamiltonian describing neutrino evolution, as explored in the previous chapter. This has resulted in an intense phenomenological activity to quantify these issues and to devise strategies to clarify them, first in proposed facilities like the Neutrino Factory [264–266] and most recently in the context of the upcoming experiments [218, 267–288].

Also very interestingly, it has been argued that NSI can already play a role in the significance of the “hints” of CP violation and of NO [289, 290]. In particular, in Ref. [289] it was pointed out the disconcerting possibility of confusing CP conserving NSI with a non-zero value of δ_{CP} in the analysis of ν_e and $\bar{\nu}_e$ appearance results at T2K and NO ν A. Clearly such confusion could lead to an incorrect claim of the observation of leptonic CP violation in a theory which is CP conserving.

As the analysis presented in the previous section only constrained the CP conserving part of the Hamiltonian — and for consistency the observables most sensitive to CP violating effects, i.e., ν_e and $\bar{\nu}_e$ appearance at LBL experiments, were not included in the fit —, the issue of the possible confusion between real NSI and leptonic CP violation could not be addressed. Furthermore, under the simplifying assumptions employed, the analysis could not either yield any conclusion on the status of the mass ordering determination in the presence of NSI.

So, in order to address these questions, in this section we extend the analysis to account for the effect of complex NSI in the observables sensitive to leptonic CP violation. We also include the effects of Δm_{21}^2 required to determine the sensitivity to the mass ordering. Our goal is to quantify the robustness of the present “hints” for these effects in the presence of NSI *which are consistent with the bounds imposed by the CP-conserving observables*.

6.2.1 Analysis framework

This section builds upon the results of the comprehensive global fit in the previous section, performed in the framework of three-flavour oscillations plus NSI with quarks. In addition, as discussed in Chapter 5, in order to study the possible effects (in experiments performed in matter) of NSI on the determination of the phase which parametrises CP violation in vacuum *without introducing an artificial basis dependence*, one needs to include in the analysis the most general complex NSI matter potential containing *all* the three additional arbitrary phases.

Thus, in principle, for each choice of the (ξ^p, ξ^n) couplings the analysis depends on six oscillations parameters plus eight NSI parameters, of which five are real and three are phases. To keep the fit manageable, in the previous section only real NSI were considered and Δm_{21}^2 effects were neglected in the fit of atmospheric and LBL experiments. This rendered such analysis independent of the CP phase in the leptonic mixing matrix and of the ordering of the states.

In this section we extend the previous analysis to include the effect of the four CP-phases in the Hamiltonian as well as the Δm_{21}^2 effects, in particular where they are most relevant which is the fit of the LBL experiments. In order to do so while still maintaining the running time under control, we split the global χ^2 in a part containing the latest data from the LBL experiments MINOS, T2K and NO ν A (accounting for both appearance and disappearance data in neutrinos and antineutrino modes, see Section 4.2), for which both the extra phases and the interference between Δm_{21}^2 and Δm_{31}^2 are properly included, and a part containing CP-conserving observables where the complex phases can be safely neglected and are therefore implemented as described in the previous section. In what follows we label as “OTH” (short for “others”) these non-LBL observables which include the results from solar neutrino experiments [23, 28, 29, 31, 81–84, 87, 88, 163], from the KamLAND reactor experiment [91], from medium baseline reactor experiments [93, 257, 258], from atmospheric neutrinos collected by IceCube [253] and its sub-detector DeepCore [89], and from our analysis of Super-Kamiokande atmospheric data [195].⁵

⁵As in the previous section, we include here our analysis of Super-Kamiokande atmospheric data in the form of the “classical” samples of e -like and μ -like events (70 energy and zenith angle bins). As discussed in Section 4.1.2 with such analysis in the framework of standard 3-nu oscillations we cannot reproduce the sensitivity to subdominant effects associated with the mass ordering and δ_{CP} found by Super-Kamiokande in their analysis of more dedicated samples [90]. For that reason we include Super-Kamiokande atmospheric data but only as part of the “OTH” group.

These correspond to the same data as the latest analysis in Section 4.2.

Schematically, if we denote by \vec{w} the five real oscillation parameters (i.e., the two mass differences and the three mixing angles), by η the direction in the (ξ^p, ξ^n) plane, by $|\varepsilon_{\alpha\beta}|$ the five real components of the neutrino part of the NSI parameters (two differences of the three diagonal entries of $\varepsilon_{\alpha\beta}$, as well as the modulus of the three non-diagonal entries⁶), and by $\phi_{\alpha\beta}$ the three phases of the non-diagonal entries of $\varepsilon_{\alpha\beta}$, we split the global χ^2 for the analysis as

$$\chi_{\text{GLOB}}^2(\vec{w}, \delta_{\text{CP}}, |\varepsilon_{\alpha\beta}|, \phi_{\alpha\beta}, \eta) = \chi_{\text{OTH}}^2(\vec{w}, |\varepsilon_{\alpha\beta}|, \eta) + \chi_{\text{LBL}}^2(\vec{w}, \delta_{\text{CP}}, |\varepsilon_{\alpha\beta}|, \phi_{\alpha\beta}, \eta) \quad (6.13)$$

so χ_{OTH}^2 and χ_{LBL}^2 depend on $5 + 5 + 1 = 11$ and $5 + 1 + 5 + 3 + 1 = 15$ parameters, respectively.

To make the analysis in such large parameter space treatable, we introduce a series of simplifications. First, we notice that in medium baseline reactor experiments the baseline is short enough to safely neglect the effects of the matter potential, so that we have:

$$\chi_{\text{OTH}}^2(\vec{w}, |\varepsilon_{\alpha\beta}|, \eta) = \chi_{\text{SOLAR+KAMLAND+ATM}}^2(\vec{w}, |\varepsilon_{\alpha\beta}|, \eta) + \chi_{\text{MBL-REA}}^2(\vec{w}). \quad (6.14)$$

Next, we notice that in LBL experiments the sensitivity to θ_{12} , Δm_{21}^2 and θ_{13} is marginal compared to solar and reactor experiments; hence, in χ_{LBL}^2 we can safely fix θ_{12} , θ_{13} and Δm_{21}^2 to their best fit value as determined by the experiments included in χ_{OTH}^2 . However, in doing so we must notice that, within the approximations used in the construction of $\chi_{\text{OTH}}^2(\vec{w}, |\varepsilon_{\alpha\beta}|, \eta)$, there still remains the effect associated to the NSI/mass-ordering degeneracy which leads to the appearance of a new solution in the solar sector with a mixing angle θ_{12} in the second octant, the so-called LMA-Dark (LMA-D) [241] solution. Although LMA-D is not totally degenerate with LMA, due to the variation of the matter chemical composition along the path travelled by solar neutrinos, it still provides a good fit to the data for a wide range of quark couplings, as found in the previous section. Concretely, after marginalization over η we get that the parameter region containing the LMA-D solution lies at

$$\chi_{\text{OTH,LMA-D}}^2 - \chi_{\text{OTH,LMA}}^2 = 3.15. \quad (6.15)$$

Therefore, when marginalizing over θ_{12} we consider two distinct parts of the parameter space, labelled by the tag ‘‘REG’’: one with $\theta_{12} < 45^\circ$, which we denote as REG = LIGHT, and one with $\theta_{12} > 45^\circ$, which we denote by REG = DARK. Correspondingly, the fixed value of θ_{12} used in the construction of $\chi_{\text{LBL,REG}}^2$ is the best fit value within either the LMA or the LMA-D region: $\sin^2 \bar{\theta}_{12}^{\text{LIGHT}} = 0.31$ or $\sin^2 \bar{\theta}_{12}^{\text{DARK}} = 0.69$, respectively. The best fit values for the other two oscillation parameters fixed in $\chi_{\text{LBL,REG}}^2$ are the same for LMA and LMA-D: $\Delta \bar{m}_{21}^2 = 7.4 \times 10^{-5} \text{ eV}^2$ and $\sin^2 \bar{\theta}_{13} = 0.0225$.

Further simplification arises from the fact that for LBL experiments the dependence on the NSI neutrino and quark couplings enters only via the effective Earth-matter NSI combinations $\varepsilon_{\alpha\beta}^{\oplus}$ defined in Eq. (6.4). It is therefore convenient to project also χ_{OTH}^2 over these combinations, and to marginalise it with respect to η . In addition we neglect the small correlations introduced by the common dependence of the atmospheric experiments in χ_{OTH}^2 and the LBL experiments on Δm_{31}^2 and θ_{23} , and we also marginalise the atmospheric part of χ_{OTH}^2 over these two parameters. This means that in our results we do not account for the information on Δm_{31}^2 and θ_{23} arising from atmospheric experiments, however we keep the information on Δm_{31}^2 from medium

⁶More precisely, in our analysis of OTH experiments we consider both the modulus and the sign of the non-diagonal $\varepsilon_{\alpha\beta}$, i.e., we explicitly account for the all the CP-conserving values of the three phases: $\phi_{\alpha\beta} = 0, \pi$. However, in the construction of χ_{OTH}^2 these signs are marginalised, so that only the modulus $|\varepsilon_{\alpha\beta}|$ is correlated with χ_{LBL}^2 .

baseline reactor experiments. With all this, we can define a function $\chi_{\text{OTH,REG}}^2$ depending on six parameters:

$$\chi_{\text{OTH,REG}}^2(\Delta m_{31}^2, |\varepsilon_{\alpha\beta}^\oplus|) \equiv \min_{\eta, \theta_{12} \in \text{REG}, \theta_{13}, \theta_{23}, \Delta m_{21}^2} \chi_{\text{OTH}}^2(\vec{w}, |\varepsilon_{\alpha\beta}^\oplus| / [\xi^p + Y_n^\oplus \xi^n], \eta) \quad (6.16)$$

while our final global $\chi_{\text{GLOB,REG}}^2$ is a function of eleven parameters which takes the form

$$\chi_{\text{GLOB,REG}}^2(\theta_{23}, \Delta m_{31}^2, \delta_{\text{CP}}, |\varepsilon_{\alpha\beta}^\oplus|, \phi_{\alpha\beta}) = \chi_{\text{OTH,REG}}^2(\Delta m_{31}^2, |\varepsilon_{\alpha\beta}^\oplus|) + \chi_{\text{LBL,REG}}^2(\theta_{23}, \Delta m_{31}^2, \delta_{\text{CP}}, |\varepsilon_{\alpha\beta}^\oplus|, \phi_{\alpha\beta} \parallel \bar{\theta}_{12}^{\text{REG}}, \bar{\theta}_{13}, \Delta \bar{m}_{21}^2) \quad (6.17)$$

with REG = LIGHT or DARK.

6.2.2 Results

In order to quantify the effect of the matter NSI on the present oscillation parameter determination we have performed a set of 12 different analyses in the eleven-dimensional parameter space. Each analysis corresponds to a different combination of observables. The results of the LBL experiment MINOS are always included in all the cases, so for convenience in what follows we define $\chi_{\text{OTHM}}^2 \equiv \chi_{\text{OTH}}^2 + \chi_{\text{MINOS}}^2$. To this we add χ_{LBL}^2 with LBL = T2K, NO ν A, and T2K+NO ν A. In addition, we perform the analysis in four distinctive parts of the parameter space: the solar octant ‘‘REG’’ being LIGHT or DARK, and the mass ordering being normal (NO) or inverted (IO).

To efficiently explore such a large dimensional parameter space, with potential flat directions and quasidegenerate minima, we have employed `MultiNest` [291–293] and the GNU `GSL` simplex minimiser [294].

For illustration we show in Figs. 6.9 and Fig. 6.10 all the possible one-dimensional and two-dimensional projections of the eleven-dimensional parameter space accounting for the new CP violating phases, parametrised as $\phi_{\alpha\beta}^\oplus \equiv \arg(\varepsilon_{\alpha\beta}^\oplus)$. In both figures we show the regions for the GLOBAL analysis including both T2K and NO ν A results. In Fig. 6.9 we present the results for the LIGHT sector and Normal Ordering, while in Fig. 6.10 we give the regions corresponding to the DARK sector and Inverted Ordering; in both cases the allowed regions are defined with respect to the local minimum of each solution. From these figures we can see that, with the exception of the required large value of $\varepsilon_{ee}^\oplus - \varepsilon_{\mu\mu}^\oplus$ in the DARK solution, there is no statistically significant feature for the $\varepsilon_{\alpha\beta}^\oplus$ parameters other than their bounded absolute values, nor there is any meaningful information on the $\phi_{\alpha\beta}$ phases. The most prominent non-trivial feature is the preference for a non-zero value of $\varepsilon_{e\mu}^\oplus$ at a $\Delta\chi^2 \sim 3$ level, associated with a $\phi_{e\mu}$ phase centered at the CP-conserving values π (0) for the LIGHT (DARK) solution. More on this below.

In order to quantify the effect of the matter NSI on the present determination of δ_{CP} and the mass ordering we plot in Fig. 6.11 the one-dimensional $\chi^2(\delta_{\text{CP}})$ function obtained from the above $\chi_{\text{GLOB,REG}}^2$ after marginalizing over the ten undisplayed parameters. In the left, central and right panels we focus on the GLOBAL analysis including T2K, NO ν A, and T2K+NO ν A respectively. In each panel we plot the curves obtained marginalizing separately in NO (red curves) and IO (blue curves) and within the REG = LIGHT (full lines) and REG = DARK (dashed) regions. For the sake of comparison we also plot the corresponding $\chi^2(\delta_{\text{CP}})$ from the 3ν oscillation analysis with the SM matter potential (labeled ‘‘NuFIT’’ in the figure).

For what concerns the analysis which includes T2K but not NO ν A, i.e., the left panels in Fig. 6.11, we find that:

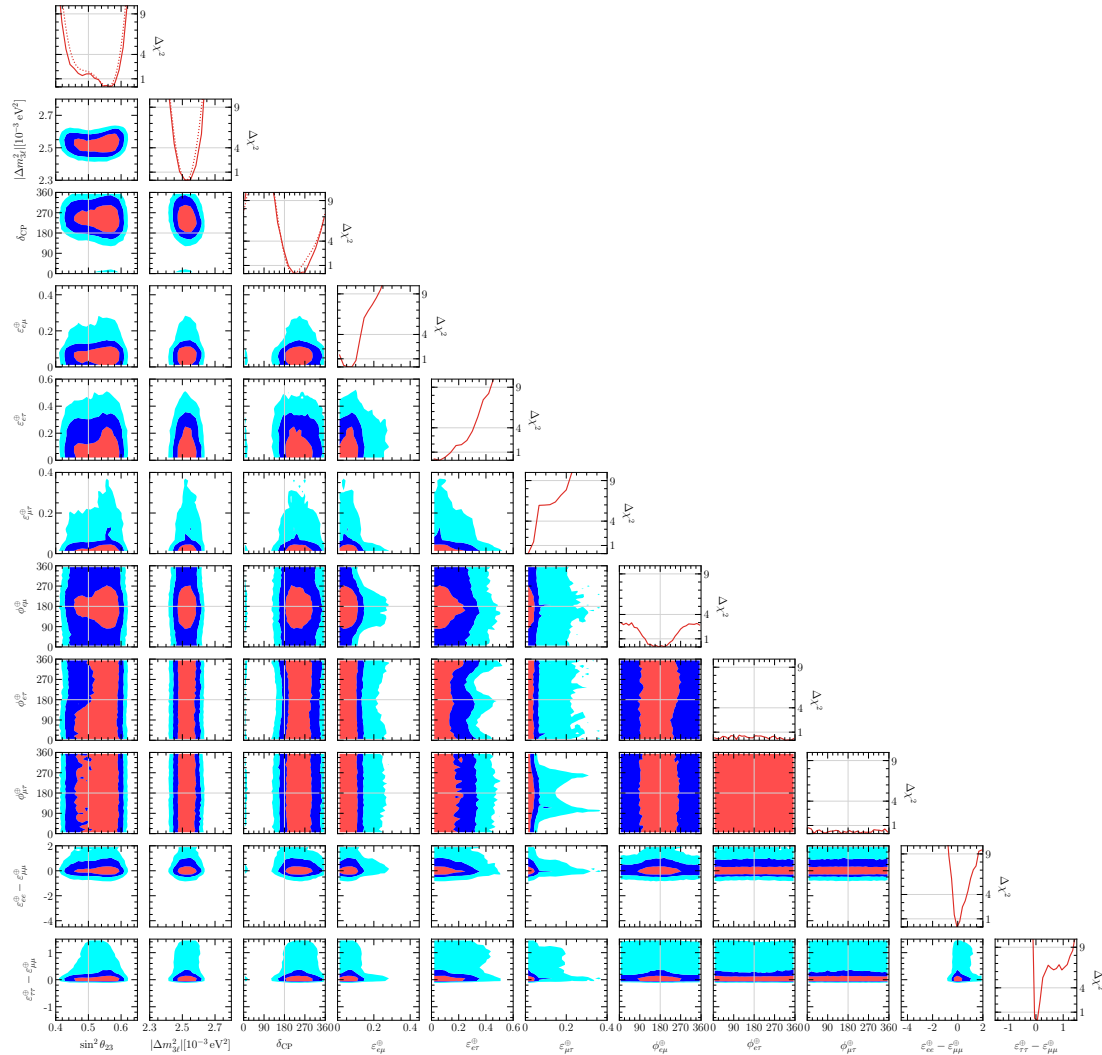


Figure 6.9: Global analysis of solar, atmospheric, reactor and accelerator oscillation experiments, in the LIGHT side of the parameter space and for Normal Ordering of the neutrino states. The panels show the two-dimensional projections of the allowed parameter space after marginalization with respect to the undisplayed parameters. The different contours correspond to the allowed regions at 1σ , 2σ and 3σ for 2 degrees of freedom. Note that as atmospheric mass-squared splitting we use $\Delta m_{3\ell}^2 = \Delta m_{31}^2$ for NO. Also shown are the one-dimensional projections as a function of each parameter. For comparison we show as dotted lines the corresponding one-dimensional dependence for the same analysis assuming only standard 3ν oscillation (i.e., setting all the NSI parameters to zero).

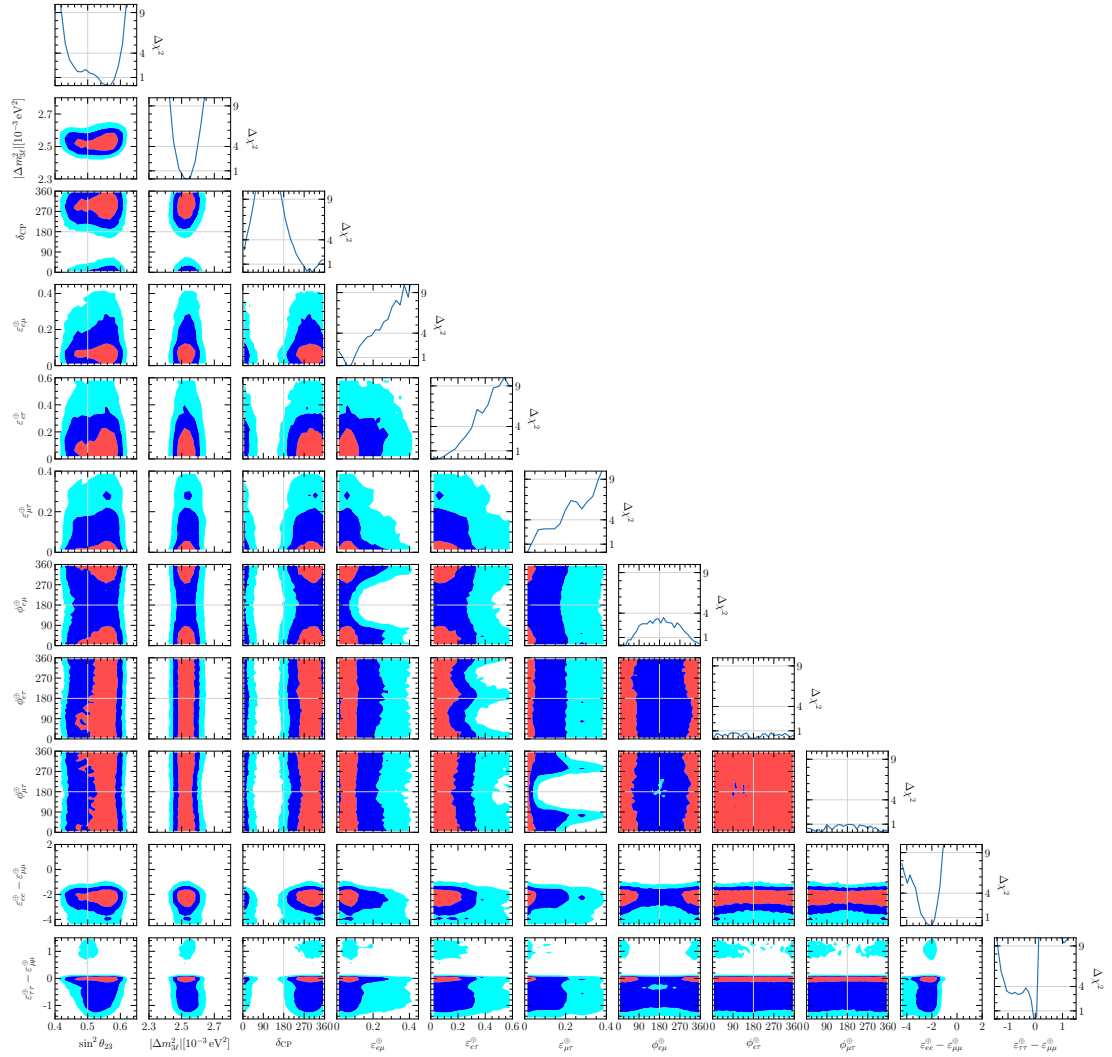


Figure 6.10: Same as Fig. 6.10 but for DARK-IO solution. In this case $\Delta m_{3\ell}^2 = \Delta m_{32}^2 < 0$ and we plot its absolute value. The regions and one-dimensional projections are defined with respect to the *local* minimum in this sector of the parameter space.

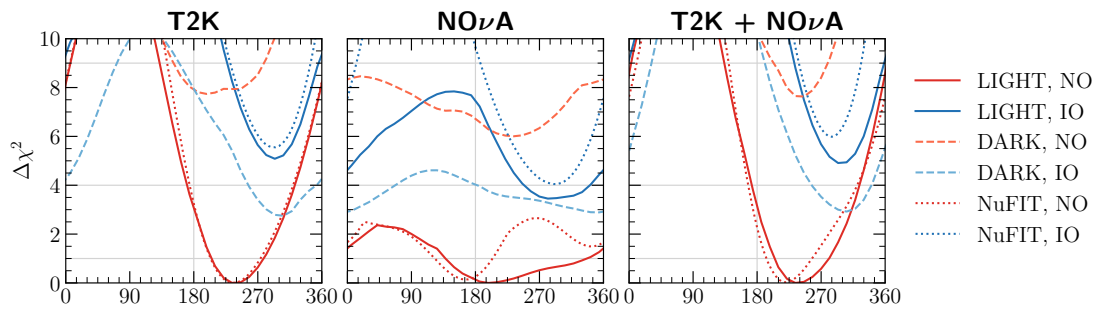


Figure 6.11: $\Delta\chi_{\text{GLOB}}^2$ as a function of δ_{CP} after marginalizing over all the undisplayed parameters, for different combination of experiments. We include SOLAR+KamLAND+ATM+MBL-REA+MINOS to which we add T2K (left), NOνA (center) and T2K + NOνA (right). The different curves are obtained by marginalizing within different regions of the parameter space, as detailed in the legend. See text for details.

- The statistical significance of the hint for a non-zero δ_{CP} in T2K is robust under the inclusion of the NSI-induced matter potential for the most favored solution (i.e., LIGHT-NO), as well as for LIGHT-IO.
- The $\Delta\chi^2$ for DARK solutions exhibits the expected inversion of the ordering as well as the $\delta_{\text{CP}} \rightarrow \pi - \delta_{\text{CP}}$ transformation when compared with the LIGHT ones. This is a consequence of the NSI-mass-ordering degeneracy discussed in Section 5.3.
- We notice that $\Delta\chi_{\text{min,OTHM+T2K,DARK,IO}}^2 \neq \Delta\chi_{\text{min,OTHM+T2K,LIGHT,NO}}^2$ because of the breaking of the NSI-mass-ordering degeneracy in the analysis of solar experiments as a consequence of the sizeable variation of the chemical composition of the matter crossed by solar neutrinos along their path. However as we see in the left panel

$$\chi_{\text{min,OTHM+T2K,DARK,IO}}^2 - \chi_{\text{min,OTHM+T2K,LIGHT,NO}}^2 \simeq 2.75 < 3.15 \quad (6.18)$$

so the DARK solutions become less disfavored when T2K is included. This suggests that the DARK-IO solution can provide a perfect fit to T2K data, i.e., there is an almost total loss of sensitivity to the ordering in T2K.

Indeed what the inequality above shows is that within the allowed DARK parameter space it is possible to find areas where the fit to T2K-only data for IO are slightly better than the fit for NO in the LIGHT sector (and than NO oscillations without NSI). For example, in DARK-NO we find that the best fit value for Δm_{31}^2 can be slightly larger than the best-fit $|\Delta m_{32}^2|$ in LIGHT-IO, which leads to a slightly better agreement with the results on Δm_{31}^2 from medium baseline reactors. These solutions, however, involve large NSI parameters, in particular $\varepsilon_{e\mu}$ and $\varepsilon_{e\tau}$.

- For the same reason, the statistical significance of the hint of CP violation in T2K is reduced for the DARK solutions with respect to the LIGHT ones. We find that CP conservation (CPC), that is, a fit with all phases either zero or π , lies at

$$\left. \begin{aligned} \chi_{\text{CPC,OTHM+T2K,DARK,IO}}^2 - \chi_{\text{min,OTHM+T2K,DARK,IO}}^2 &\simeq 1.5 \\ \chi_{\text{CPC,OTHM+T2K,LIGHT,NO}}^2 - \chi_{\text{min,OTHM+T2K,LIGHT,NO}}^2 &\simeq 3.2 \end{aligned} \right\} \Rightarrow 1.5 < 3.2. \quad (6.19)$$

- However we still find that

$$\begin{aligned} \chi_{\text{CPC,OTHM+T2K,LIGHT,NO}}^2 &\simeq \chi_{\text{OTHM+T2K,LIGHT,NO}}^2(\delta_{\text{CP}} = \pi), \\ \chi_{\text{CPC,OTHM+T2K,DARK,IO}}^2 &\simeq \chi_{\text{OTHM+T2K,DARK,IO}}^2(\delta_{\text{CP}} = 0). \end{aligned} \quad (6.20)$$

So the CL for CPC as naively read from the curves of δ_{CP} still holds, or what is the same, there is no leptonic CP violation “hidden” when there is no CP violation from δ_{CP} .

For the global combination including $\text{NO}\nu\text{A}$ without T2K (central panels in Fig. 6.11) we notice that:

- The sensitivity to δ_{CP} diminishes with respect to that of the oscillation only analysis both in the LIGHT and DARK sectors.
- Within the DARK sector, IO is the best solution as expected from the NSI/mass-ordering degeneracy, but it is still disfavored at $\Delta\chi_{\text{min,OTHM+NO}\nu\text{A,DARK,IO}}^2 \sim 3$ because of SOLAR + KamLAND, Eq. (6.15). By chance, this happens to be of the same order of the disfavouring of IO in the pure oscillation analysis, $\Delta\chi_{\text{min,OTHM+NO}\nu\text{A,OSC}}^2 \sim 3.5$ (although the physical effect responsible for this is totally different).

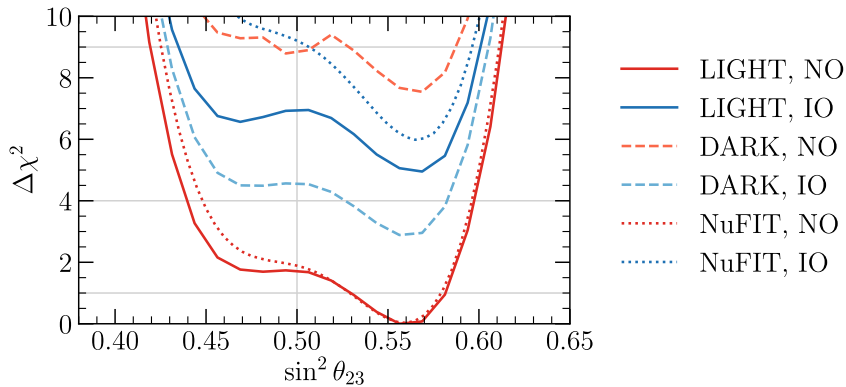


Figure 6.12: $\Delta\chi^2_{\text{GLOB}}$ as a function of $\sin^2\theta_{23}$ after marginalizing over all other parameters for the GLOBAL combination of oscillation experiments. The different curves correspond to marginalization within the different regions of the parameter space, as detailed in the legend. See text for details.

In the global analysis including both T2K and NO ν A (right panels in Fig. 6.11) we find qualitatively similar conclusions than for the analysis without NO ν A, albeit with a slight washout of the statistical significance for δ_{CP} due to the tensions between T2K and NO ν A discussed in Section 4.2. Such washout is already present in the oscillation-only analysis and within the LIGHT sector it is only mildly affected by the inclusion of NSI. For the same reason, the significance for the disfavouring of IO is also reduced by $\sim 0.2\sigma$, although this requires relatively large values of $\varepsilon_{e\tau}$.

However one also observes that in the favoured solution, LIGHT-NO, maximal $\delta_{\text{CP}} = 3\pi/2$ is more allowed than without NSI. This happens because, as mentioned above, in NO ν A the presence of NSI induces a loss of sensitivity on δ_{CP} , so in the global analysis with both T2K and NO ν A the behaviour observed in T2K dominates.

In the global analysis there remains, still, the DARK-IO solution at

$$\chi_{\text{min,GLOB,DARK,IO}}^2 - \chi_{\text{min,GLOB,LIGHT,NO}}^2 = 3. \quad (6.21)$$

The status of the non-maximality and octant determination for θ_{23} is displayed in Fig. 6.12 where we show the one-dimensional $\chi^2(\sin^2\theta_{23})$ obtained from $\chi^2_{\text{GLOB,REG}}$ including both T2K and NO ν A and after marginalizing over all the undisplayed parameters (so these are the corresponding projections to the left panels in Fig. 6.11). As seen in the figure the global analysis including NSI for both orderings, for both LIGHT and DARK sectors, still disfavors the maximal $\theta_{23} = \pi/4$ at a CL $\sim 1.5\sigma$. The main effect of the generalised NSI matter potential on θ_{23} is the mild improvement of the CL for the first octant. This is so because the disfavouring of the first octant in the global oscillation-only analysis is driven by the excess of appearance events in NO ν A. These events can now be fitted better with θ_{23} in the first octant when including a non-zero $\varepsilon_{e\mu}$ to enhance the $\nu_{\mu} \rightarrow \nu_e$ flavour transition probability.

6.2.3 Summary

In this section we have extended the analysis in Section 6.1 to account for the effect of NSI affecting neutrino propagation in matter on the observables sensitive to leptonic CP violation and to the mass ordering. We have quantified the robustness of the present hints for these effects in the presence of NSI as large as allowed by the global oscillation analysis itself. We conclude

that the CL for the preference for a CKM-like CP phase close to $3\pi/2$ in T2K, which is the one that drives the preference in the global analysis, remains valid even when including all other phases in the extended scenario. On the contrary the preference for NO in LBL experiments is totally lost when including NSI as large as allowed by the global analysis because of the intrinsic NSI/mass-ordering degeneracy in the Hamiltonian which implies the existence of an equally good fit to LBL results with IO and reversed octant of θ_{12} and $\delta_{CP} \rightarrow \pi - \delta_{CP}$ (so in this solution the favored δ_{CP} is also close to $3\pi/2$). In the global analysis the only relevant breaking of this degeneracy comes from the composition dependence of the matter potential in the Sun which disfavors the associated LMA-D with CL below 2σ . Finally, we have also studied the effect of NSI in the status of the non-maximality and octant determination for θ_{23} and find that for both orderings, for both LIGHT and DARK sectors, maximal $\theta_{23} = \pi/4$ is still disfavoured in the global fit at a CL $\sim 1.5\sigma$.

6.3 Summary and conclusions

In this chapter, we have performed a fit to neutrino oscillation data assuming there is BSM physics other than neutrino masses. In particular, we have introduced NSI-NC, very difficult to bound with other experiments but crucial for neutrino propagation in matter.

We have first obtained bounds on the moduli of the new parameters, i.e., their CP conserving part. We have found that individual experiments allow very large NSI, particularly when they are adjusted to be suppressed for the particular matter composition traversed by the neutrino beam. Consequently, the bounds on the oscillation parameters get weakened. However, different experiments are sensitive to different matter profiles, energy ranges and oscillation channels. When combining all data, we find that the oscillation parameters are robustly determined (except slightly for θ_{12}) and that $\mathcal{O}(1)$ NSI are disfavoured. Having observed neutrino oscillations in a large variety of environments is crucial for this.

Experimentally allowed NSI, though, could still spoil the sensitivity of LBL accelerator experiments to CP violation. To check whether this is the case, we have performed a generic fit to all experiments where CP-violating NSI are also allowed. We have found that, within the LMA solution, the results from the T2K experiment are quite robust: it has a relatively short baseline, and so NSI strong enough to affect it would have been detected by other experiments more sensitive to matter effects. Nevertheless, the $\text{NO}\nu\text{A}$ baseline is larger, and NSI within experimental bounds can significantly affect the interpretation of its data. Since the information on δ_{CP} is dominated by T2K, the global result within the LMA solution is robust.

Nevertheless, the generalised mass ordering degeneracy discussed in Section 5.3 implies a good fit at $\sim 2\sigma$ that spoils the global sensitivity to the mass ordering. Furthermore, it also has the potential of worsening the sensitivity to δ_{CP} .

These results are particularly worrisome in the context of future experiments. The Deep Underground Neutrino Experiment, for instance, is expected to determine CP violation with a very large statistical significance. This experiment is dominated by matter effects, and so it is potentially affected by the same sensitivity loss as $\text{NO}\nu\text{A}$. The advent of more neutrino oscillation experiments will not alleviate the situation, as part of the sensitivity loss comes from the generalised mass ordering degeneracy, exact for neutrino oscillations.

The only hope for lifting this degeneracy is bounding NSI with non-oscillation experiments. Traditional neutrino scattering experiments have large momentum transfers, and so bounds from them could be evaded if the mediator inducing NSI is light. Fortunately, in the recent years coherent neutrino-nucleus elastic scattering has been detected [295]. In this process, neutrinos interact coherently with an entire atomic nucleus by exchanging very low momenta, $\mathcal{O}(10 \text{ MeV})$.

Therefore, any light mediator-induced NSI could be bounded with these experiments. This will be the subject of the next chapter.

Chapter 7

COHERENT constraint of beyond three-neutrino scenarios

Our suggestion may be an act of hubris, because the inevitable constraints on interaction rate, resolution, and background pose grave experimental difficulties for elastic neutrino-nucleus scattering.

— Daniel Z. Freedman (1974)

We shall not cease from exploration. And the end of all our exploring will be to arrive where we started and know the place for the first time.

— T. S. Eliot

As explored in the previous chapters, there could be new physics in the form of NSI-NC affecting neutrino propagation in matter. Under its presence, the measurement of leptonic CP violation can get compromised. This is not only because of the additional parameters in the model, but also because NSI introduce a degeneracy exact at the oscillation probability level.

Therefore, robustly determining leptonic CP violation in present and next generation experiments would highly benefit from additional constraints on NSI-NC. In principle, these could come from neutral current neutrino scattering experiments such as CHARM [236] and NuTeV [237]. These experiments, however, probe typical momentum exchanges $\mathcal{O}(10 \text{ GeV})$, whereas neutrino matter effects are a coherent, zero momentum exchange process.

More explicitly, if NSI are mediated by a particle with mass M_X and coupling g , the coupling times propagator entering neutrino scattering will generically be

$$\sim \frac{g^2}{q^2 - M_X^2}, \quad (7.1)$$

with q the momentum transfer. Thus, neutrino matter effects are sensitive to g^2/M_X^2 , whereas for light mediators ($M_X \ll q$) scattering experiments can only bound g^2/q^2 . If the mediator is light enough, scattering bounds can consequently be avoided [222, 230–235]. Thus, bounding NSI that could spoil neutrino oscillation experiments requires a neutrino scattering experiment with very low momentum transfers.

Fortunately, such an experiment exists and has released data during the completion of this thesis. The COHERENT experiment [47], which will be further explained below, measures coherent elastic neutrino-nucleus scattering (CE ν NS), a process in which a neutrino interacts coherently with an entire atomic nucleus. Scattering amplitudes get enhanced by roughly the number of neutrons¹ N , and cross sections increase by a factor N^2 . Despite the large cross sections, coherent interaction with an entire nucleus only happens when the de Broglie wavelength of the exchanged mediator is of the order of the nuclear size, $\mathcal{O}(\text{MeV}^{-1})$. The only signal that the interaction leaves is thus a nucleus recoiling with tiny energies, $\mathcal{O}(\text{keV})$, very challenging to detect. The process is depicted in Fig. 7.1.

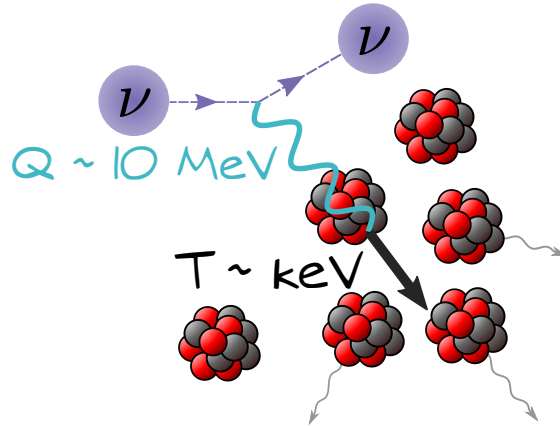


Figure 7.1: Schematic representation of coherent neutrino-nucleus elastic scattering. Here, Q is the momentum transfer, and T the recoil energy of the hit nucleus.

Nevertheless, modern low-threshold detectors are sensitive to such tiny recoils and in 2017 this process was detected [295]. In this chapter, we will develop a comprehensive analysis of data from the COHERENT experiment in the framework of NSI-NC. We will combine the results with the oscillation analyses from the previous chapter, to assess the importance of coherent scattering experiments in interpreting neutrino oscillation data.

Finally, we will also explore the prospects of a near future facility, the European Spallation Source, that can accumulate data one order of magnitude faster than the COHERENT experiment.

7.1 Analysis of COHERENT data

7.1.1 Coherent elastic neutrino-nucleus scattering

The COHERENT experiment uses neutrinos produced at the Spallation Neutron Source (SNS) sited at the Oak Ridge National Laboratory. There, an abundant flux of both π^+ and π^- is produced in proton-nucleus collisions in a mercury target. While the π^- are absorbed by nuclei before they can decay, the π^+ lose energy as they propagate and eventually decay at rest into $\pi^+ \rightarrow \mu^+ \nu_\mu$, followed by $\mu^+ \rightarrow e^+ \nu_e \bar{\nu}_\mu$. Since the muon lifetime is much longer than that of the pion, the ν_μ component is usually referred to as the prompt contribution to the flux, as opposed to the delayed contributions from μ^+ decay ($\bar{\nu}_\mu$ and ν_e).

¹Neutral current interactions with protons are suppressed by $1 - 4 \sin^2 \theta_W \simeq 0.05$ [72], see Eq. (2.9).

Given that the prompt neutrinos are a by-product of two-body decays at rest, their contribution to the total flux is a monochromatic line at $E_{\text{pr}} = (m_\pi^2 - m_\mu^2)/(2m_\pi) \simeq 29.7$ MeV, where m_π and m_μ refer to the pion and muon masses, respectively. Conversely, the delayed neutrino fluxes follow a continuous spectra at energies $E_{\nu_e, \bar{\nu}_\mu} < m_\mu/2 \simeq 52.8$ MeV. At a distance ℓ from the source, they read:

$$\begin{aligned} \frac{d\phi_{\nu_\mu}}{dE_\nu} &= \frac{1}{4\pi\ell^2} \delta(E_\nu - E_{\text{pr}}), \\ \frac{d\phi_{\bar{\nu}_\mu}}{dE_\nu} &= \frac{1}{4\pi\ell^2} \frac{64}{m_\mu} \left[\left(\frac{E_\nu}{m_\mu} \right)^2 \left(\frac{3}{4} - \frac{E_\nu}{m_\mu} \right) \right], \\ \frac{d\phi_{\nu_e}}{dE_\nu} &= \frac{1}{4\pi\ell^2} \frac{192}{m_\mu} \left[\left(\frac{E_\nu}{m_\mu} \right)^2 \left(\frac{1}{2} - \frac{E_\nu}{m_\mu} \right) \right], \end{aligned} \quad (7.2)$$

and are normalised to each proton collision on the target. For reference the distance ℓ at COHERENT is 19.3 m. These spectra are shown in Fig. 7.2.

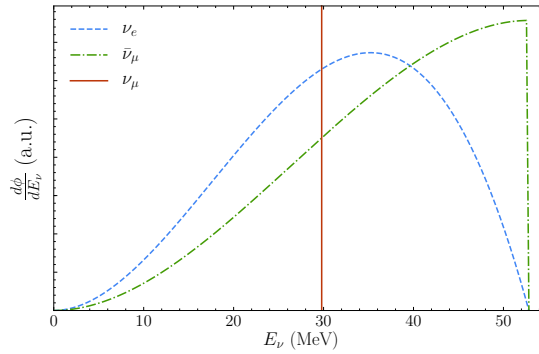


Figure 7.2: Neutrino flux spectra expected from π^+ decay at rest, in arbitrary units (a.u.), as a function of the neutrino energy in MeV. The three components of the flux are shown separately as indicated by the legend. The distributions have been normalised to one.

The differential cross section for coherent elastic neutrino-nucleus scattering, for a neutrino with incident energy E_ν interacting with a nucleus with Z protons and N neutrons, reads [296]:

$$\frac{d\sigma_{\text{SM}}(T, E_\nu)}{dT} = \frac{G_F^2}{2\pi} Q^2(Z, N) F^2(Q^2) M \left(2 - \frac{MT}{E_\nu^2} \right) \quad (7.3)$$

where G_F is the Fermi constant and Q^2 is the weak charge of the nucleus. In this notation, T is the recoil energy of the nucleus, M is its mass, and F is its nuclear form factor evaluated at the squared momentum transfer of the process, $Q^2 = 2MT$. In our calculations we have first used a Helm form factor ² parametrization [298]:

$$F(Q^2) = 3 \frac{j_1(QR_0)}{QR_0} e^{-Q^2 s^2/2} \quad (7.4)$$

²The collaboration used a slightly different form factor, taken from Ref. [297]. However, we have checked that the results of the fit using their parametrization gives identical results to those obtained using the Helm form factor.

where $s = 0.9$ fm [299] and $j_1(x)$ is the order-1 spherical Bessel function of the first kind. The value of R_0 relates to the value of s and the neutron radius R_n as

$$\frac{R_0^2}{5} = \frac{R_n^2}{3} - s^2. \quad (7.5)$$

In the absence of an experimental measurement of the neutron radius in CsI, we tune its value so that the prediction for the total number of events at COHERENT matches the official one provided in Refs. [295, 300] (173 events). However, by doing so we obtain $R_n = 4.83$ fm, a value that is unphysical as it approaches the proton radius [301] which all models predict to be smaller. Given that this is a phenomenological parametrization, though, and seeing the large differences in the prediction for the total number of events obtained with different values of R_n , it is worth asking whether this is accurate enough for CsI, and exploring the impact of the nuclear form factor on the results of the fit. Therefore, in Sec. 7.1.3 we will also show the results obtained using a state-of-the-art theoretical calculation for the nuclear form factor, taken from Refs. [302, 303] (calculated using the same methodology as in Refs. [304, 305]).

In the SM, the weak charge of a nucleus only depends on the SM vector couplings to protons (g_p^V) and neutrons (g_n^V) and is independent of the neutrino flavour:

$$\mathcal{Q}^2 \equiv (Zg_p^V + Ng_n^V)^2, \quad (7.6)$$

where $g_p^V = 1/2 - 2\sin^2\theta_w$ and $g_n^V = -1/2$, with θ_w being the weak mixing angle. For CsI, we obtain $\mathcal{Q}^2 \simeq 1352.5$ in the SM. However, in presence of NSI-NC, this effective charge gets modified³ by the new operators introduced as [306]:

$$\mathcal{Q}_\alpha^2(\vec{\varepsilon}) = [Z(g_p^V + 2\varepsilon_{\alpha\alpha}^u + \varepsilon_{\alpha\alpha}^d) + N(g_n^V + \varepsilon_{\alpha\alpha}^u + 2\varepsilon_{\alpha\alpha}^d)]^2 + \sum_{\beta \neq \alpha} [Z(2\varepsilon_{\alpha\beta}^u + \varepsilon_{\alpha\beta}^d) + N(\varepsilon_{\alpha\beta}^u + 2\varepsilon_{\alpha\beta}^d)]^2, \quad (7.7)$$

and in general its value may now depend on the NSI parameters $\vec{\varepsilon} \equiv \{\varepsilon_{\alpha\beta}^f\}$ as well as the incident neutrino flavour α . Since the COHERENT experiment observes interactions of both electron and muon neutrinos, its results are sensitive to both \mathcal{Q}_e^2 and \mathcal{Q}_μ^2 .

As can be seen from Eq. (7.7), the modification of NSI to the CE ν NS event rate comes in as a normalization effect. Therefore, adding nuclear recoil energy information to the analysis of the data is not expected to have a significant effect on the results of our fit to NSI.⁴ Conversely, the addition of timing information is crucial as it translates into a partial discrimination between neutrino flavours, thanks to the distinct composition of the prompt (ν_μ) and delayed ($\bar{\nu}_\mu$ and ν_e) neutrino flux. This translates into an enhanced sensitivity to NSI, since the fit will now be sensitive to a change in normalization affecting neutrino flavours differently.

³In practice, unless the ratio of the new couplings to up and down quarks remains the same as in the SM, the form factor of the nucleus would also be affected by the NP and should be recomputed including the NP terms. However, in the case of vector-vector interactions (as in the case of NSI) the modifications to the nuclear form factor are expected to be subleading, and the factorization of the NP effects into the weak charge approximately holds. We warmly thank Martin Hoferichter for pointing this out.

⁴In principle, a subleading effect can be observed for experiments with large statistics, due to the different maximum recoil energies expected for the prompt and delayed neutrino components of the beam as will be explored in Section 7.3. However, we find that the COHERENT experiment is insensitive to this effect with the current exposure.

7.1.2 Implementation of the COHERENT experiment

The COHERENT collaboration has released publicly both the energy and timing information of the events [300]. In this section we describe the procedure used to implement in our fit the information provided in such data release.

Computation of the signal

The differential event distribution at COHERENT, as a function of the nuclear recoil energy T , reads

$$\frac{dN}{dT} = N_{\text{pot}} f_{\nu/p} N_{\text{nuclei}} \sum_{\alpha} \int_{E_{\nu}^{\text{min}}}^{m_{\mu}/2} \frac{d\sigma_{\alpha}}{dT} \frac{d\phi_{\nu\alpha}}{dE_{\nu}} dE_{\nu}, \quad (7.8)$$

where N_{nuclei} is the total number of nuclei in the detector, $N_{\text{pot}} = 1.76 \cdot 10^{23}$ is the total number of protons on target considered, and $f_{\nu/p} = 0.08$ is the neutrino yield per proton. In Eq. (7.8) the sum runs over all neutrino flux components ($\nu_e, \nu_{\mu}, \bar{\nu}_{\mu}$), and the upper limit of the integral is given by the end-point of the spectrum from pion DAR, while the minimum neutrino energy that can lead to an event with a nuclear recoil energy T is given by

$$E_{\nu}^{\text{min}} = \sqrt{\frac{MT}{2}}. \quad (7.9)$$

At COHERENT, the observable that is actually measured is the number of photo-electrons (PE) produced by an event with a certain nuclear recoil. In fact, the nuclear recoil energy in CE ν NS events is typically dissipated through a combination of scintillation (that is, ionization) and secondary nuclear recoils (that is, heat). While secondary recoils are *the* characteristic signal of a nuclear recoil (as opposed to an electron recoil, which favours ionization instead), their measurable signal is much smaller than that of electron recoils. The ratio between the light yields from a nuclear and an electron recoil of the same energy is referred to as the Quenching Factor (QF).

Besides being a detector-dependent property, the QF may also depend non-trivially on the recoil energy of the nucleus. In general, the relation between PE and nuclear recoil T can be expressed as:

$$\text{PE} = T \cdot \text{LY} \cdot \text{QF}(T), \quad (7.10)$$

where LY is the light yield of the detector (that is, the number of PE produced by an electron recoil of one keV), and we have explicitly noted that the QF may depend on the nuclear recoil energy. Therefore, the expected number of events in a certain bin i in PE space can be computed as:

$$N_i = \int_{T(\text{PE}_i^{\text{min}})}^{T(\text{PE}_i^{\text{max}})} \frac{dN}{dT} dT, \quad (7.11)$$

where the limits of the integral correspond to the values of T obtained for the edges of the PE bin ($\text{PE}_i^{\text{min}}, \text{PE}_i^{\text{max}}$) from Eq. (7.10).

In their analysis, the COHERENT collaboration adopted an energy-independent QF throughout the whole energy range considered in the analysis, between 5 and 30 keV [295]. Also, given the tension observed between the different calibration measurements available at the time, they assigned large error bars to the assumed central value $\overline{\text{QF}} = 8.78\%$. Taking a central value for the light yield $\overline{\text{LY}} = 13.348$ PE per keV of electron recoil [300], this means that approximately 1.17 PE are expected per keV of nuclear recoil energy. Very recently, however, the authors of Ref. [307] have re-analyzed past calibration data used to derive this result. They concluded that the tension between previous measurements was partially due to an unexpected saturation of

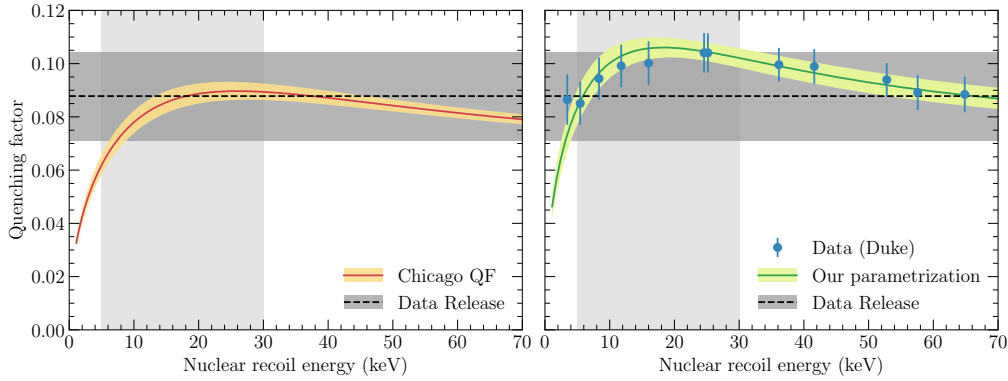


Figure 7.3: QF parametrizations used in our analysis of the COHERENT data. The left panel shows the curve provided in Ref. [307] (solid curve), while the right panel shows the corresponding result obtained for our fit to the calibration data of the Duke (TUNL) group [295], provided as part of the data release [300]. In both panels, the constant QF used in Ref. [295] is also shown for comparison. The three parametrizations are shown with a shaded band to indicate the values allowed at the 1σ CL in each case. For illustration, the vertical shaded area indicates approximately the range of nuclear recoil energies that enters the signal region used in the fit (the exact range varies with the nuisance parameters, and the exact QF parametrization used).

the photo-multipliers used in the calibration and, after correcting for this effect, a much better agreement was found between the different data sets. This allows for a significant reduction of the error bars associated to the QF, as well as for the implementation of an energy-dependent QF. Nevertheless, the COHERENT collaboration has not confirmed the claims of the authors of Ref. [307]. After repeating the calibration measurements, their new data still shows a good agreement [308] with the original measurements performed by the Duke (TUNL) group [295,300].

Given that this issue has not been settled yet, we will study and quantify the effect of these new measurements in the results of the fit in Sec. 7.1.3. We will present our results obtained for three different QF parametrizations: the original (constant) parametrization used in the data release [300]; the best-fit obtained by the authors of Ref. [307]; and the results from our fit to the calibration measurements performed by the TUNL group [295,300]. In order to fit the data of the Duke group, we use the phenomenological parametrization proposed in [307], which is based on a modification of the semi-empirical approach by Birks [309] and depends only on two parameters, E_0 and kB .⁵ Following this approach, we obtain a best-fit to the Duke group data for $E_0 = 9.54 \pm 0.84$ and $kB = 3.32 \pm 0.10$, with a correlation $\rho_{kB,E_0} = -0.69$. The three QF parametrizations used in our calculations are shown in Fig. 7.3, as a function of the recoil energy of the nucleus.

Once the expected event distribution in PE has been computed following Eq. (7.11), the expected number of events in each bin has to be smeared according to a Poisson distribution, to account for the probability that a given event yields a different number of PE than the average. On top of that, signal acceptance efficiencies are applied to each bin:

$$\eta(\text{PE}) = \frac{\eta_0}{1 + e^{-k(\text{PE} - \text{PE}_0)}} \Theta(\text{PE} - 5), \quad (7.12)$$

⁵In brief, the fitted functional form of the QF as a function of the nuclear recoil energy T is $\text{QF}(T) = [1 - \exp(-T/E_0)]/[kB dE/dR(T)]$ where $dE/dR(T)$ is the energy loss per unit length of the ions. For simplicity, we take it to be the average between that of Cs and I, obtained from SRIM-2013 [310]. We have also verified that using a simple polynomial parametrization for $\text{QF}(T)$ leads to very similar results.

where the function Θ is defined as:

$$\Theta(\text{PE} - 5) = \begin{cases} 0 & \text{if } \text{PE} < 5, \\ 0.5 & \text{if } 5 < \text{PE} < 6, \\ 1 & \text{if } 6 < \text{PE}. \end{cases} \quad (7.13)$$

Following Ref. [300], the central values of the signal acceptance parameters are set to $\bar{\eta}_0 = 0.6655$, $\bar{k} = 0.4942$, $\bar{PE}_0 = 10.8507$.

Finally, once the predicted energy spectrum has been computed, one should consider the arrival times expected for the different contributions to the signal. This is implemented using the distributions provided by the COHERENT collaboration in the data release [300], which are normalised to one.

This final prediction can be compared with the published data. This is provided in two different time windows for each trigger in the data acquisition system (that is, for each proton pulse). On the one hand, the region where signals and beam-induced backgrounds associated with the SNS beam are expected is referred to as the coincidence (C) region, which can therefore be considered a “signal” region. Conversely, the region where no contribution from the SNS beam is expected is referred to as the anti-coincidence (AC) region and could be considered a “background” region. While the collaboration provides data separately for the beam-ON and beam-OFF data taking periods, in this chapter we only use the beam-ON samples. The total exposure considered in this chapter corresponds to 308.1 live-days of neutrino production, which correspond to 7.48 GW-hr ($\sim 1.76 \times 10^{23}$ protons on target). The residual event counts for this period, i.e., the C data with the AC data subtracted, are shown in Fig. 7.4, projected onto the time and PE axes, for different choices of the QF and form factor as indicated by the labels.

As can be seen from the comparison between the upper and lower panels, the change in QF between a constant approximation (Data Release) and the energy-dependent result obtained by the TUNL group (QF-D) does not affect significantly the predicted event distributions. This will lead to a minor change in the results of the numerical fit to the data in Sec. 7.1.3. A larger difference is observed with respect to the predictions using the QF by the Chicago group (QF-C, middle panels): in this case, the very different central values at $T \sim 10$ keV (corresponding to $PE \sim 10$) lead to a reduced number of events, which will have a larger impact on the results.

Computation of the background

The COHERENT measurement is affected by three main background sources: (i) the steady-state background, coming from either cosmic rays or their by-products entering the detector; (ii) prompt neutrons produced in the target station and exiting it, and (iii) neutrino-induced neutrons (NINs) that originate in the shielding surrounding the detector. While the latter is irreducible, it has been shown to be negligible at the COHERENT experiment and is therefore ignored here.

The procedure used to compute the expected number of background events for the steady-state and the prompt neutron components follows the prescription given in Ref. [300]. For both backgrounds, it is assumed that the temporal and energy dependence on the number of events can be factorised as

$$N_{\text{bg}}(t, \text{PE}) = f(t) \cdot g(\text{PE}), \quad (7.14)$$

where f contains the temporal dependence of the signal and g its energy dependence.

For the prompt neutron background, the collaboration provides both its expected energy distribution before acceptance efficiencies are applied (that is, $g(\text{PE})$), and the total expected counts as a function of time (that is, $f(t)$). The expected 2D distribution can be obtained simply

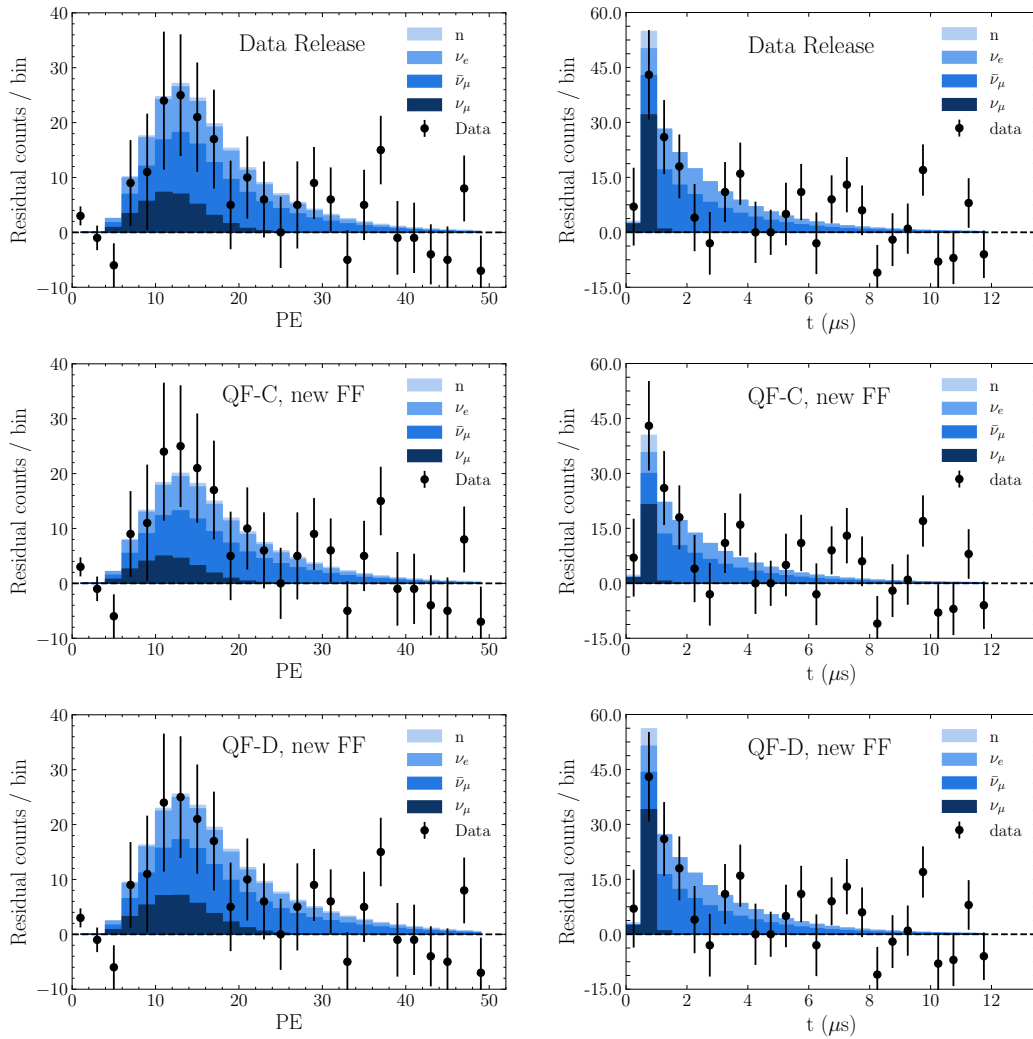


Figure 7.4: Residual events per bin obtained after subtracting C and AC data for the beam-ON sample, after being projected onto the PE (left panels) and time (right panels) axes and using the same cuts in PE as time as those applied to Fig. 3 in Ref. [295]. The observed data points are indicated with statistical error bars, as in Ref. [295]. In the upper panels the shaded histograms show the predicted event rates in the SM using the QF and nuclear form factor from Ref. [300]. In the middle panels they correspond to the predictions with the QF from the Chicago group (QF-C) in Ref. [307] and the nuclear form factor (FF) from Ref. [302, 303]. The lower panels have been obtained with the same form factor, but changing the QF to match the Duke (TUNL) measurements in Ref. [295] (QF-D). In all panels the prompt neutron background prediction is also shown for completeness. All the event histograms shown in this figure correspond to the SM prediction.

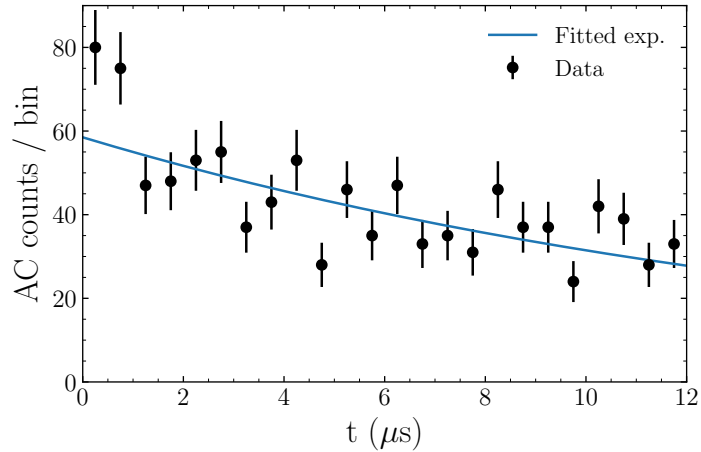


Figure 7.5: Total AC counts per bin, compared to the results of the exponential fit employed in Ref. [300] and described in Sec. 7.1.2 used to model the steady-state background. No cuts on the observed number of PE have been applied to this figure.

by multiplying the two distributions. After the number of events in each bin has been computed, the same acceptance efficiency as for the signal, Eq. (7.12), is applied to determine the expected number of events in each bin.

The steady-state is the most significant background source to this analysis, and it has the largest impact on the fit. In this case, the functions $g(\text{PE})$ and $f(t)$ are not provided in Ref. [300] but inferred from the data, which is provided per bin in energy and time. In particular, the projected data onto the PE axis is then used directly as $g(\text{PE})$, while $f(t)$ is assumed to follow an exponential:

$$f_{\text{ss}}(t) = a_{\text{ss}} e^{-b_{\text{ss}} t}. \quad (7.15)$$

By taking the AC data and projecting it into the time axis, a best-fit to the steady-state background is obtained for $a_{\text{ss}} = 58.5$ and $b_{\text{ss}} = 0.062$. The value of $f(t)$ is then normalised so that its integral over the whole range in time is equal to one. Since in this case the expected background events are inferred from a measurement, the signal acceptance has already been included into the calculation and there is no need to apply it here.

The procedure outlined above for the steady-state component is meant to eliminate biases in the fit due to the limited statistics of the data sample used. However, by treating the background in this way the analysis is rather sensitive to a mismodelling of its temporal component. In particular, if we plot the separate C and AC event distribution as a function of time, instead of looking at their difference, it is easy to see that there is an excess in the first two bins in the data, which cannot be accommodated by the simplified exponential fit. This is shown in Fig. 7.5, where we show the total AC counts (which should include only the steady-state background as measured by the detector) together with the exponential that gives a best fit to the data. As clearly seen, the first two bins are not well fitted by a simple exponential model.

Interestingly enough, both the C and AC samples seem to observe a similar excess in the first two temporal bins, which suggests that this contribution is not related to the neutrino signal but to some mismodelling of the background. A possible way to correct for this is to directly use the measured time dependence of the AC sample as a direct prediction for the expected behaviour of the steady-state background in the C sample. Doing this on a bin-per-bin basis

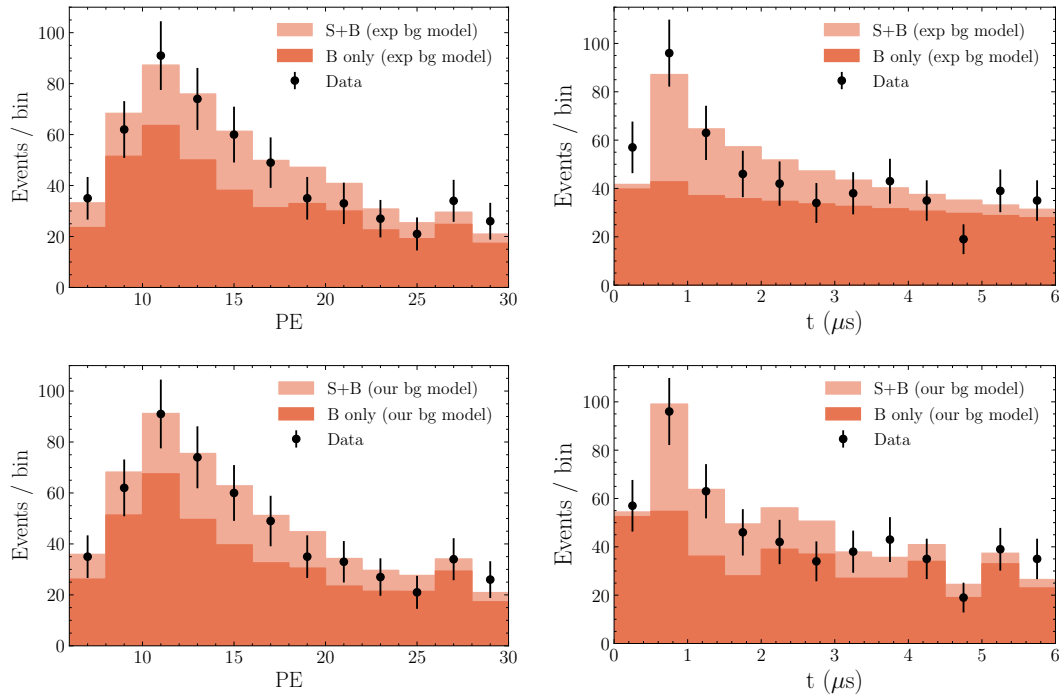


Figure 7.6: Total events per bin in the beam-ON C sample, after being projected onto the time (left) and PE (right) and imposing the cuts $5 < PE \leq 30$ and $t < 6 \mu s$. The observed data points are indicated with statistical error bars as in Fig. 7.4. The dark histograms show the expected background events for the steady-state contribution only. The upper panels have been obtained assuming that the time dependence of the background follows an exponential model, as in Ref. [300], while the lower panels have been obtained using our model (which follows the time dependence of the AC events, see text for details). The light histograms show the predicted total number of events, after adding all signal and background contributions. To ease the comparison among different panels, in this figure the signal has been computed in all cases using the same form factor and QF as in the data release [300]. All histograms shown correspond to the SM predicted event rates.

would not provide a good predictor for the expected number of events in each bin, due to the limited statistics. However, the projected data onto the time axis may still be used, as in the case of the exponential fit, to get a prediction for the function $f(t)$. In other words, the prediction for $f(t)$ may be obtained following the same procedure as was done for $g(\text{PE})$, i.e., projecting the events onto the corresponding axis. Figure 7.6 shows the observed total event counts for the beam-ON, C sample (which includes both signal and background) projected onto PE (left) and time (right), compared with the predictions using these two different background models.

As can be seen from this figure, both background models are able to reproduce the observed spectrum in PE relatively well, and give very similar results. However, the event rates obtained with this second method provide a better fit to the data when projected onto the time axis and, as clearly observed from the figure, the effect is specially noticeable in the first two bins. Therefore, in Sec. 7.1.3 we will show two sets of results: with and without using an exponential model for the background.

Systematic errors and implementation of the χ^2

Once the predicted event distributions for the signal and backgrounds have been computed, a χ^2 function is built as:

$$\chi^2[P_{ij}(\vec{\xi})] = \sum_{ij} 2 \left[P_{ij}(\vec{\xi}) - O_{ij} + O_{ij} \ln \left(\frac{O_{ij}}{P_{ij}(\vec{\xi})} \right) \right], \quad (7.16)$$

where O_{ij} stands for the observed number of events in PE bin i and time bin j , while P_{ij} stands for the total number of predicted events in that bin, including the signal plus all background contributions. Following Ref. [300], we consider only the events with $5 < \text{PE} \leq 30$ and $t < 6 \mu\text{s}$ in the analysis. The predicted number of events depends on the nuisance parameters $\vec{\xi} \equiv \{\xi_a\}$ included in the fit, which account for the systematic uncertainties affecting the QF, signal acceptance, neutrino production yield, and normalisation of the backgrounds. These are implemented replacing the original quantity as $x \rightarrow (1 + \sigma_x \xi_x) \bar{x}$, where \bar{x} denotes the central value assumed for x prior to the experiment and σ_x denotes the relative uncertainty for nuisance parameter ξ_x summarised in Tab. 7.1 for convenience. More specifically:

$$P_{ij}(\vec{\xi}) = (1 + \sigma_{\text{ss}} \xi_{\text{ss}}) N_{ij}^{\text{ss}} + \eta(\text{PE}_i | \xi_{\eta_0}, \xi_k, \xi_{\text{PE}_0}) [(1 + \sigma_n \xi_n) N_{ij}^{\text{n}} + (1 + \sigma_{\text{sig}} \xi_{\text{sig}}) N_{ij}^{\text{sig}}(\xi_{\text{QF}})], \quad (7.17)$$

where N_{ij}^{ss} , N_{ij}^{n} and N_{ij}^{sig} stand for the predicted number of events for the steady-state background, the prompt neutron background and the signal. In Eq. (7.17) we have generically denoted as ξ_{QF} the set of nuisance parameters characterizing the uncertainty on the QF employed. For the constant parametrization used in the data release [300] we introduce a unique nuisance parameter with constant uncertainty. For QF-C we introduce also a unique nuisance parameter, but with an energy-dependent uncertainty inferred from the uncertainty band in Fig. 1 of Ref. [307] (also shown in the left panel of Fig. 7.3), which varies from 6.5% to 3.5% in the range of recoil energies relevant for COHERENT. For QF-D we introduce two nuisance parameters characterizing the uncertainty on parameters E_0 and kB with their corresponding correlation.⁶

⁶We have verified that, in practice, it is equivalent to using a single nuisance parameter with an energy-dependent uncertainty ranging between 8% and 3% (corresponding to the shaded band shown in the right panel in Fig. 7.3).

Parameter	Uncertainty (%)
Steady-state norm.	5.0
Prompt n norm.	25.0
Signal norm.	11.2
η_0	4.5
k	4.7
PE_0	2.7
QF (data release)	18.9
QF (our fit, QF-C)	6.5 – 3.5
kB (our fit, QF-D)	3.0
E_0 (our fit, QF-D)	8.8
$\rho_{E_0, kB}$ (our fit, QF-D)	–0.69

Table 7.1: Systematic uncertainties considered in the fit on acceptance efficiency parameters (Eq. (7.12)), normalisation of the signal and background contributions, and the QF. The steady-state normalisation uncertainty includes the statistical error of the sample (AC data). The quoted uncertainties on the QF also includes the error on the light yield (0.14%), which is however subdominant. For details on the QF parametrization, see Sec. 7.1.2.

Altogether the likelihood for some physics model parameters $\vec{\varepsilon}$, leading to a given set of predictions $P_{ij}^{\vec{\varepsilon}}(\vec{\xi})$ for the events in bin ij , is obtained including the effects of the nuisance parameters as in Eq. (7.17) and minimizing over those within their assumed uncertainty. This is ensured by adding a pull term to the χ^2 function in Eq. (7.16) for each of the nuisance parameters introduced:

$$\chi_{\text{COH}}^2(\vec{\varepsilon}) = \min_{\vec{\xi}} \left\{ \chi^2 [P_{ij}^{\vec{\varepsilon}}(\vec{\xi})] + \sum_{ab} \xi_a (\rho^{-1})_{ab} \xi_b \right\}, \quad (7.18)$$

where ρ is the correlation matrix, whose entries are $\rho_{ab} = \delta_{ab}$ for all parameters except those entering our parametrization of the QF of the Duke group (the corresponding correlation coefficient can be found in Tab. 7.1).

As validation of our χ^2 construction we have performed a fit to extract the total number of signal $\text{CE}\nu\text{NS}$ events when using the same assumptions on the background, systematics and energy and time dependence of the signal as those employed by COHERENT in their data release [300]. This can be directly compared with their corresponding likelihood extracted from Figure S13 of Ref. [295]. The result of this comparison is shown in Fig. 7.7. Strictly speaking, the χ^2 function plotted in Fig. 7.7 depends on the assumed energy dependence of the signal. Therefore it is expected to vary if, instead of using the QF and form factor quoted in the data release, we employed a different QF parametrization and nuclear form factor. Quantitatively, within the systematic uncertainties used in the construction of the shown $\chi^2(N_{\text{CE}\nu\text{NS}})$, we find that changing the QF and form factor has a negligible effect on this curve. Conversely, we find a stronger dependence on the systematic uncertainties introduced, and therefore Fig. 7.7 serves as validation of our implementation for these. For illustration, we also indicate the predicted event rates in the SM predicted by the collaboration (173 events) as well as our result obtained using the Chicago QF parametrization [307], as shown in the left panel of Fig. 7.3 and the new nuclear form factor from Refs. [302, 303]. In both cases the vertical lines correspond to the prediction without accounting for systematic uncertainties. The predicted result using the Duke QF and the new form factor from Refs. [302, 303] is very similar to the one obtained by the collaboration (168 events) and is therefore not shown here.

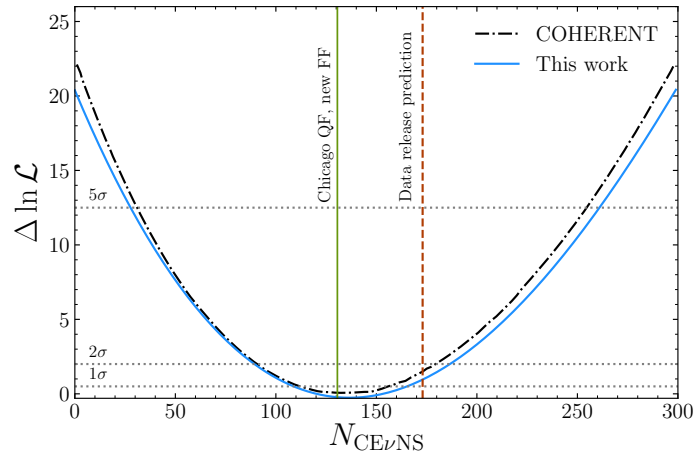


Figure 7.7: Comparison of our χ^2 for the COHERENT timing and energy data as a function of the number of signal $\text{CE}\nu\text{NS}$ events under the same assumptions on the background, systematics and expected time and energy dependence of signal, compared to that provided by COHERENT in figure S13 of Ref. [295]. For comparison, the vertical lines indicate the predicted event rates in the SM (with no systematic uncertainties), for different choices of QF and form factor used: dashed red corresponds to the prediction provided in the data release of 173 events [300], while solid green indicates our prediction using the QF from Ref. [307] (left panel in Fig. 7.3) and nuclear form factor of [302, 303].

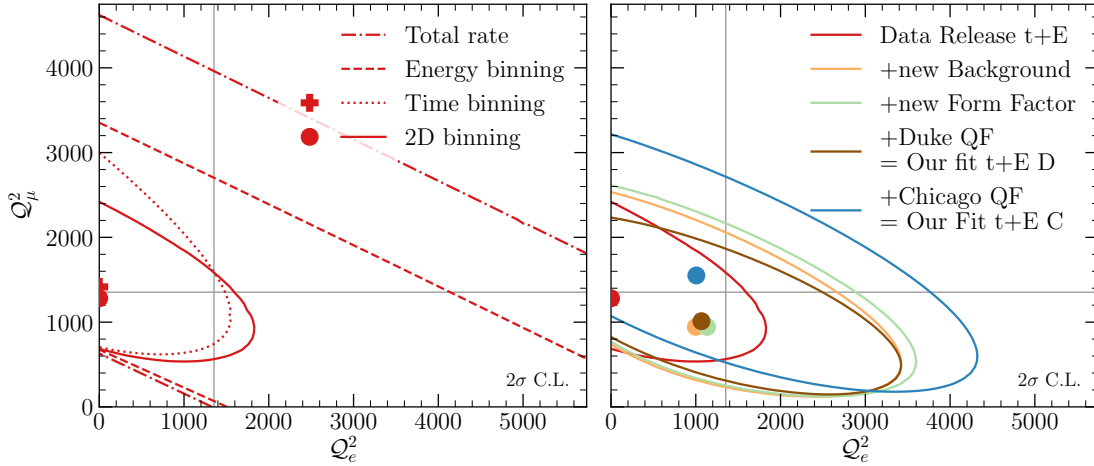


Figure 7.8: 2σ allowed regions for the flavour-dependent weak charges for a variety of fits to COHERENT data as labeled in the figure. In all cases shown in the left panel, the QF, nuclear form factor and background assumptions are those employed in the data release [300]. On the right panel we show the dependence on the steady background modelling, nuclear form factor, and QF. The vertical lines indicate the SM value $Q_e^2 = Q_\mu^2 = 1353.5$. The coloured dots and the red cross mark the position of the best-fit for the various cases.

7.1.3 Results: Fit to COHERENT data

In this section we present our results. We discuss in detail the improvements coming from the inclusion of energy and timing information in the fit, and investigate the impact of the different choices of QF, nuclear form factor and background implementation.

In order to study the dependence of the results on the different assumptions, we have performed a set of fits to COHERENT data in terms of two effective flavour-dependent weak charges Q_α^2 (assumed to be energy-independent). Figure 7.8 shows the corresponding allowed regions at 2σ from the fit to COHERENT data alone. In the left panel we illustrate the effect of including the energy and timing information in the fit, by comparing the allowed values of the weak charges obtained: (i) using only the total rate information (dot-dashed); (ii) adding only the energy information (dashed); (iii) using only the event timing information (dotted); and (iv) fitting the data binned in both timing and energy (solid). In all cases shown in the left panel, the QF, nuclear form factor and background have been implemented following closely the prescription given in the data release [300]. It is well-known that, when only the total event rate information is considered, there is a degeneracy in the determination of the flavour-dependent weak charges, since the number of predicted events approximately behaves as

$$Q_e^2 f_{\nu_e} + Q_\mu^2 (f_{\nu_\mu} + f_{\bar{\nu}_\mu}) \approx \frac{1}{3} Q_e^2 + \frac{2}{3} Q_\mu^2 \quad (7.19)$$

where f_α indicates the fraction of expected SM events from interactions of ν_α in the final event sample and we have assumed that one neutrino of each species is produced for each pion DAR. Under these assumptions, the allowed region in the (Q_e^2, Q_μ^2) plane is a straight band with a negative slope, $\arctan(-0.5) \approx -27^\circ$. This behaviour is also observed from our exact fit to the data, as shown by the dot-dashed lines in the left panel in Fig. 7.8.

As expected, the timing information is most relevant in breaking of this degeneracy: since

the prompt component of the beam contains only ν_μ , the inclusion of time information allows for a partial discrimination between \mathcal{Q}_e^2 and \mathcal{Q}_μ^2 . Notice, however, that in this case the best fit is obtained at the edge of the physically allowed region, $\mathcal{Q}_e^2 \simeq 0$ (in fact, it would probably take place for a negative value, but this is not the case since we are effectively imposing the restriction $\mathcal{Q}_\alpha^2 > 0$ in the fit). This is driven by the small excess for the event rates in the first two time bins (with respect to the SM prediction) when using the exponential fit model for the steady-state background, as described in Sec. 7.1.2 (see Fig. 7.6). Such excess can be accommodated thanks to the overall normalisation uncertainty of the signal, combined with a decrease of the ν_e contribution as required to match the distribution observed for the delayed events. Within the systematic uncertainties in the analysis, this results into a higher rate at short times without a major distortion of the PE spectrum. We also observe that, including only the PE spectrum in the fit, the degeneracy still remains but the width of the band in this plane decreases. For values of \mathcal{Q}_α^2 in the non-overlapping region, the fit using the event rate information alone is able to fit the data, albeit at the price of very large nuisance parameters and, in particular, of the QF-related uncertainties (which affect the shape of the event distributions in PE space). Therefore, once the PE information is added the allowed regions are consequently reduced.

The right panel in Fig. 7.8 shows the dependence of the allowed region on the assumed background model, nuclear form factor and QF choice in the fit, for the 2D fit using both time and PE information. As seen in the figure, if one uses the steady-state background prediction without the exponential model for its temporal dependence the region becomes considerably larger, and the best fit moves closer to the SM. This is expected because, with this background, there is no excess of events in the first time bins with respect to the SM prediction (see Fig. 7.6). This also leads to a better overall fit, with $\chi_{\min}^2 = 145.24$ (for $12 \times 12 = 144$ data points) compared to $\chi_{\min}^2 = 150.8$ obtained for the exponential model of the steady-state background. Altogether we observe that modifying the nuclear form factor has a very small effect on the current results, as can be seen from the comparison between the orange and green lines in the figure. Changing the QF does not have a dominant impact either, once the exponential fit to the background has been removed. This can be seen from the comparison between the green, brown and blue lines in the figure, which all provide similar results. Overall, we find a slightly better agreement with the SM result for the QF-C parametrization, albeit the effect is small.

In the framework of NSI, the constraints on the weak charges derived above can be directly translated into constraints on the effective Wilson coefficients. This is shown in Fig. 7.9, where we plot the allowed regions for the two relevant flavour-diagonal NSI couplings after setting the flavour-changing ones to zero. In doing so we notice that the fact that the neutron/proton ratio in the two target nuclei is very similar ($N_{\text{Cs}}/Z_{\text{Cs}} \simeq 1.419$ for cesium and $N_{\text{I}}/Z_{\text{I}} \simeq 1.396$ for iodine) allows to approximate Eq. (7.7) as:

$$\mathcal{Q}_\alpha^2(\vec{\varepsilon}) \propto [(g_p^V + Y_n^{\text{coh}} g_n^V) + \varepsilon_{\alpha\alpha}^{\text{coh}}]^2 + \sum_{\beta \neq \alpha} (\varepsilon_{\alpha\beta}^{\text{coh}})^2 \quad (7.20)$$

with an average value $Y_n^{\text{coh}} = 1.407$ and

$$\varepsilon_{\alpha\beta}^{\text{coh}} \equiv \varepsilon_{\alpha\beta}^p + Y_n^{\text{coh}} \varepsilon_{\alpha\beta}^n, \quad \varepsilon_{\alpha\beta}^p \equiv 2\varepsilon_{\alpha\beta}^u + \varepsilon_{\alpha\beta}^d, \quad \varepsilon_{\alpha\beta}^n \equiv 2\varepsilon_{\alpha\beta}^d + \varepsilon_{\alpha\beta}^u. \quad (7.21)$$

From Eq. (7.7) it is evident that COHERENT can only be sensitive to a certain combination of NSI operators $\varepsilon_{\alpha\beta}^{\text{coh}}$, which are ultimately determined by just two factors: (a) the value of Y_n^{coh} , which depends on the nuclei in the detector, and (b) the strength of the coupling of the new interaction to up and down quarks (or, equivalently, to protons and neutrons). In fact, using the η parametrization in Eqs. (6.1) and (6.2), $\varepsilon_{\alpha\beta}^{\text{coh}}$ can be written as:

$$\varepsilon_{\alpha\beta}^{\text{coh}} = \sqrt{5} (\cos \eta + Y_n^{\text{coh}} \sin \eta) \varepsilon_{\alpha\beta}^\eta. \quad (7.22)$$

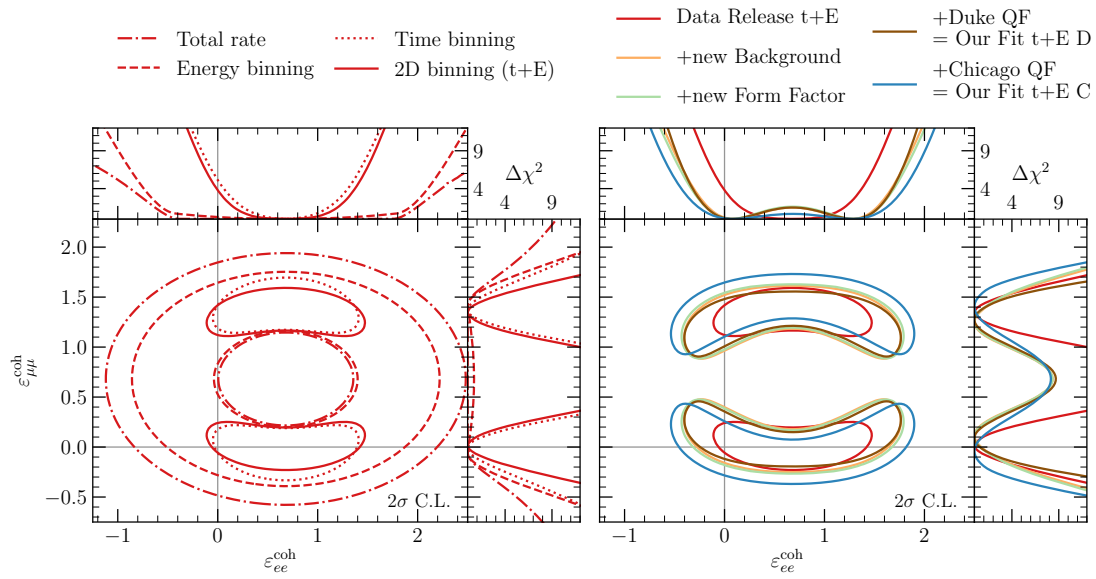


Figure 7.9: 2σ allowed regions for the flavour-diagonal NSI coefficients $\varepsilon_{\alpha\beta}^{\text{coh}}$ (assuming zero non-diagonal couplings) for a variety of fits to COHERENT data as labelled in the figure. In all cases shown in the left panel, the QF, nuclear form factor and background assumptions are those employed in the data release [300]. On the right panel we show the dependence on the assumptions for steady background modelling, nuclear form factor, and QF. For simplicity, in this figure we set all off-diagonal NSI parameters to zero, but it should be kept in mind that the results of our global analysis presented in Sec. 7.2.1 have been obtained allowing all operators simultaneously in the fit.

It is clear from the expressions above that the best-fit value and allowed ranges of $\varepsilon_{\alpha\beta}^{\text{coh}}$ implied by COHERENT are independent of η . Once these have been determined, the corresponding bounds on the associated couplings $\varepsilon_{\alpha\beta}^{\eta}$ for a given NSI model (identified by a particular value of η) can be obtained in a very simple way, by just rescaling the values of $\varepsilon_{\alpha\beta}^{\text{coh}}$ as $[\sqrt{5}(\cos\eta + Y_n^{\text{coh}} \sin\eta)]^{-1}$. For example, the results in Fig. 7.9 can be immediately translated in the corresponding ranges for NSI models where the new interaction couples only to $f = u$, $f = d$, or $f = p$ ($\eta \approx 26.6^\circ$, 63.4° , and 0 , respectively), after rescaling the bounds on $\varepsilon_{\alpha\beta}^{\text{coh}}$ by the corresponding factors of 0.293, 0.262, and 1 in each case. Furthermore, from Eq. (7.22) it becomes evident that, for NSI models with $\eta = \arctan(-1/Y_n^{\text{coh}}) \approx -35.4^\circ$, no bound can be derived from COHERENT data. This could be improved by measuring CE ν NS in nuclei with different neutron/proton ratios, which could be achieved in the future as explored in Section 7.3.

The impact of the timing information on the fit can be readily observed from the left panel in Fig. 7.9. In the absence of any timing information and using total rate information alone, it is straightforward to show that, if the experiment observes a result compatible with the SM expectation, the allowed confidence regions in this plane should obey the equation of an ellipse. This automatically follows from Eqs. (7.19) and (7.20):

$$\frac{1}{3}[R + \varepsilon_{ee}^{\text{coh}}]^2 + \frac{2}{3}[R + \varepsilon_{\mu\mu}^{\text{coh}}]^2 = R^2, \quad (7.23)$$

where $R \equiv g_p^V + Y_n^{\text{coh}} g_n^V \approx -0.68$. This is also shown by our numerical results in the left panel of Fig. 7.9 which do not include timing information in the fit (dashed and dot-dashed contours).

While the inclusion of a non-zero $\varepsilon_{ee}^{\text{coh}}$ can be compensated by a change in $\varepsilon_{\mu\mu}^{\text{coh}}$ that brings the total number of events in the opposite direction without significantly affecting the delayed events, this would be noticed in the prompt event distribution once timing information is added to the fit. In particular, too large/small values of $\varepsilon_{ee}^{\text{coh}}$ would require a consequent modification of the $\varepsilon_{\mu\mu}^{\text{coh}}$ to recover the same event rate in the delayed time bins, which is however not allowed by the prompt events observed. Thus, once timing information is included in the fit the ellipse is broken in this plane and two separate minima are obtained (dotted and solid lines).

It should also be noted that the central region in Fig. 7.9 (around the centre of the ellipse in Eq. (7.23), $\varepsilon_{ee}^{\text{coh}} = \varepsilon_{\mu\mu}^{\text{coh}} = -R$) can be excluded at COHERENT *only* in the case when the off-diagonal NSI operators are not included in the fit. This is so because in this region the effect of the diagonal parameters leads to a destructive interference in the total cross section and therefore to a reduction of the number of events, in contrast with the experimental observation. Once the off-diagonal operators are introduced this is no longer the case and the central region becomes allowed [311]. However, since global neutrino oscillation data provide tight constraints on the off-diagonal NSI operators, in our results the two minima remain separate even after the off-diagonal operators are allowed in the fit, as we will show in Sec. 7.2.1.

7.1.4 Summary

In this section, we analysed the latest results obtained for coherent neutrino-nucleus scattering data at the COHERENT experiment, which provide both energy and timing information.

We have quantified the dependence of our results for COHERENT with respect to the choice of QF, nuclear form factor, and the treatment of the backgrounds. We find that the implementation of the steady-state background has a strong impact on the results of the analysis of COHERENT due to a slight background excess in the first two bins, which is present in both the coincident and anti-coincident data samples provided by the collaboration. Once this effect has been accounted for in the modelling of the expected backgrounds, the choice of QF and nuclear form factor has a minor impact on the results obtained from the fit.

7.2 Combining COHERENT and oscillation data

Once the results from the COHERENT experiments are properly understood and analysed, their bounds on NSI can be combined with the global analyses of oscillation data in Chapter 6. This will allow to quantitatively assess the current complementarity between CE ν NS and neutrino oscillation experiments.

7.2.1 Including COHERENT in the CP-conserving analysis of Section 6.1

As a start, we present the results of the global CP-conserving analysis of oscillation plus COHERENT data. We will show two main sets of results, which quantify: (1) the quality of the global fit once NSI are allowed, compared to the fit obtained under the SM hypothesis; and (2) the status of the LMA-D solution after the inclusion of COHERENT energy and timing data in the global fit. Both sets of results are presented for a wide range of NSI models (that is, for different values of η). Finally, we also provide the allowed ranges obtained for the Wilson coefficients for three particular NSI models, assuming that the new mediator couples predominantly to either up/down quarks or to protons.

To this end we construct a combined χ^2 function

$$\chi_{\text{global}}^2(\vec{\varepsilon}) = \min_{\vec{\omega}} [\chi_{\text{OSC}}^2(\vec{\omega}, \vec{\varepsilon}) + \chi_{\text{COH}}^2(\vec{\varepsilon})], \quad (7.24)$$

where we denote by $\vec{\omega} \equiv \{\theta_{ij}, \delta_{\text{CP}}, \Delta m_{ji}^2\}$ the “standard” 3ν oscillation parameters. For the detailed description of methodology and data included in χ_{OSC}^2 we refer to the comprehensive global fit in Section 6.1 performed in the framework of three-flavour oscillations plus NSI with quarks parametrised as Eqs. (6.1) and (6.2). In this section we minimally update the results from Section 6.1 to account for the latest LBL data samples discussed in Section 4.2. To keep the fit manageable in Section 6.1 only the CP-conserving case with real NSI and $\delta_{\text{CP}} \in \{0, \pi\}$ was considered, and consequently the T2K and NO ν A appearance data (which exhibit substantial dependence on the leptonic CP phase) were not included in the fit. Here we follow the same approach and consistently update only the disappearance samples from these experiments.⁷

Figure 7.10 shows the impact of COHERENT on the global fit (left panel) as well as on the LMA-D degeneracy (right panel). In doing so, we have defined the functions $\chi_{\text{LMA}}^2(\eta)$ and $\chi_{\text{LMA-D}}^2(\eta)$, obtained by marginalizing $\chi_{\text{global}}^2(\vec{\omega}, \vec{\varepsilon})$ over both $\vec{\omega}$ and $\vec{\varepsilon}$ for a given value of η , with the constraint $\theta_{12} < 45^\circ$ (in the LMA case) and $\theta_{12} > 45^\circ$ (for LMA-D). With these definitions, we show in the left panel the differences $\chi_{\text{LMA}}^2(\eta) - \chi_{\text{no-NSI}}^2$ (full lines) and $\chi_{\text{LMA-D}}^2(\eta) - \chi_{\text{no-NSI}}^2$ (dashed lines), where $\chi_{\text{no-NSI}}^2$ is the minimum χ^2 for standard 3ν oscillations (i.e., setting all the NSI parameters to zero). Then, in the right panel we show the values of $\chi_{\text{LMA-D}}^2(\eta) - \chi_{\text{LMA}}^2(\eta)$, which quantifies the relative quality of the LMA and LMA-D solutions as a function of η .

First, from the left panel in Fig. 7.10 we notice that the introduction of NSI leads to a substantial improvement of the fit already for the LMA solution (solid lines) with respect to the oscillation data analysis, resulting in a sizable decrease of the minimum χ_{LMA}^2 with respect to the standard oscillation scenario. This is mainly driven by a well-known tension (although mild, at the level of $\Delta\chi^2 \sim 7.4$ in the present analysis) between solar and KamLAND data in the determination of Δm_{21}^2 (see Sections 4.1.2 and 6.1.2). As seen in the figure, the inclusion of NSI improves the combined fit by about 2.2σ over a broad range of values of η . The improvement is maximised for NSI models with values of η for which the effect is largest in the Sun without entering in conflict with terrestrial experiments. This occurs for $\eta \simeq -44^\circ$ (as for this value the NSI in the Earth matter essentially cancel) and leads to an improvement of about 10 units

⁷For a discussion of CP violation in the presence of NSI, see Chapter 5 and Sections 6.2 and 7.2.2.

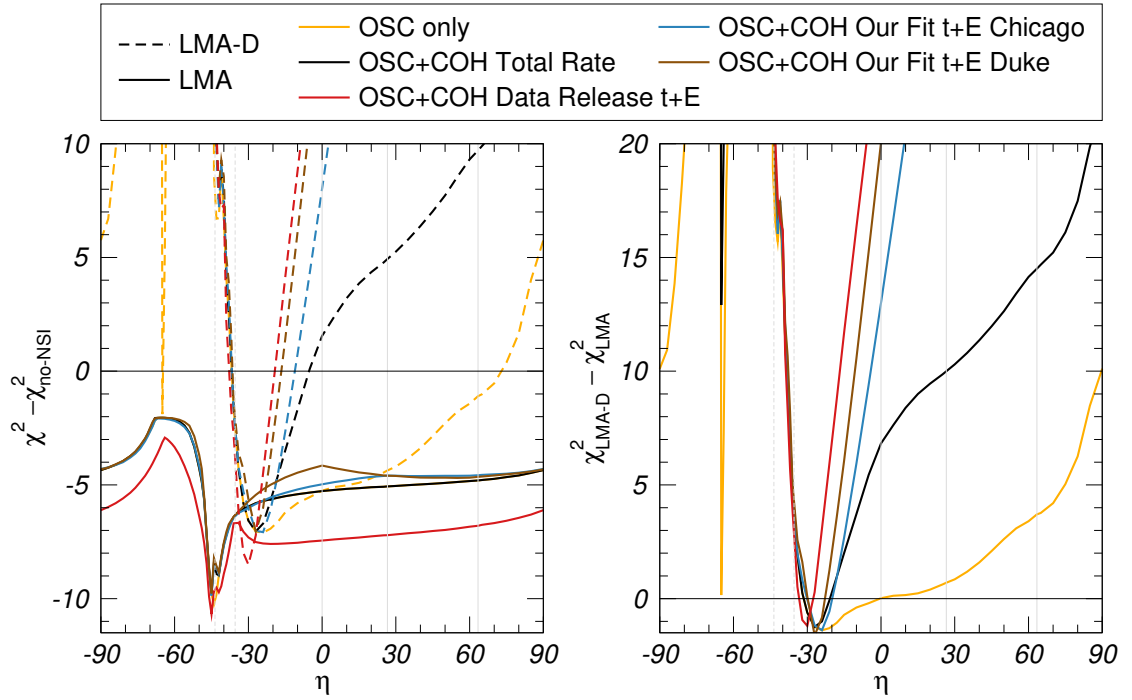


Figure 7.10: Left: $\chi^2_{\text{LMA}}(\eta) - \chi^2_{\text{no-NSI}}$ (full lines) and $\chi^2_{\text{LMA-D}}(\eta) - \chi^2_{\text{no-NSI}}$ (dashed lines) for the analysis of different data combinations (as labeled in the figure) as a function of the NSI quark coupling parameter η . Right: $\chi^2_{\text{dark}} - \chi^2_{\text{light}} \equiv \chi^2_{\text{LMA-D}}(\eta) - \chi^2_{\text{LMA}}(\eta)$ as a function of η . See text for details.

in χ^2 (i.e., a $\sim 3.2\sigma$ effect). From the figure we also conclude that adding the information from COHERENT on rate only, as well as on timing and energy (t+E), still allows for this improved fit in the LMA solution for most values of η . Indeed, the maximum effect at $\eta \simeq -44^\circ$ still holds after the combination since it falls very close to -35.4° , for which NSI effects cancel at COHERENT as seen in Eq. (7.22). Interestingly, the improvement is slightly larger for the combination with COHERENT t+E data using the data release assumptions. This is so because, as described in the previous section, in this case the fit pulls the weak charge Q_e^2 towards zero (see Fig. 7.8) while leaving the value of Q_μ^2 around the SM expectation. Such situation can be easily accommodated by invoking diagonal NSI operators and, in particular, favours the non-standard values $\varepsilon_{ee}^\eta - \varepsilon_{\mu\mu}^\eta \neq 0$, thus bringing the fit to a better agreement with solar+KamLAND oscillation data.

Most importantly, Fig. 7.10 shows that the main impact of including COHERENT data in the analysis is on the status of the LMA-D degeneracy. We see in the figure that with oscillation data alone the LMA-D solution is still allowed at 3σ for a wide range of NSI models ($-38^\circ \lesssim \eta \lesssim 87^\circ$, as well as a narrow window around $\eta \simeq -65^\circ$) and, in fact, for $-31^\circ \lesssim \eta \lesssim 0^\circ$ it provides a slightly better global fit than the LMA solution. The addition of COHERENT to the analysis of oscillation data disfavors the LMA-D degeneracy for most values of η , and the inclusion of the timing and energy information makes this conclusion more robust. More quantitatively we find that, when COHERENT results are taken into account, LMA-D is allowed below 3σ only for values of η in the following ranges:

$$\begin{aligned}
-38^\circ &\lesssim \eta \lesssim 15^\circ && \text{COHERENT Total Rate,} \\
-38^\circ &\lesssim \eta \lesssim -18^\circ && \text{COHERENT t+E Data Release,} \\
-38^\circ &\lesssim \eta \lesssim -6^\circ && \text{COHERENT t+E Our Fit Chicago,} \\
-38^\circ &\lesssim \eta \lesssim -12^\circ && \text{COHERENT t+E Our Fit Duke.}
\end{aligned} \tag{7.25}$$

Finally, we provide in Fig. 7.11 the χ^2 profiles for each of the six NSI coefficients after marginalization over the undisplayed oscillation parameters and the other five NSI coefficients not shown in a given panel. We show these results for three representative cases of NSI models including couplings to up quarks only, down quarks only and to protons. The corresponding 2σ ranges are also provided in Tab. 7.2 for convenience. This figure shows that the LMA-D solution for NSI models that couple only to protons ($\eta = 0$) can only be excluded beyond 3σ if both energy and timing information are included for COHERENT, in agreement with Eq. (7.25). From this figure we also see that for the LMA solution the allowed ranges for the off-diagonal NSI couplings are only moderately reduced by the addition of the COHERENT results and, moreover, the impact of the energy and timing information is small in these cases. This is because they are already very well constrained by oscillation data alone.

More interestingly, the addition of COHERENT data allows to derive constraints on each of the diagonal parameters separately and, for those, the timing (and to less degree energy) information has a quantitative impact. In particular we see in the figure the appearance of the two minima corresponding to the degenerate solutions for $\varepsilon_{\mu\mu}^{\text{coh}}$ in Fig. 7.9, obtained after the inclusion of timing information for COHERENT. Noticeably, now the non-standard solution (obtained for $\varepsilon_{\mu\mu}^f \neq 0$) is partially lifted by the combination with oscillation data, but it remains well allowed around $\sim 2\sigma$ depending on the assumptions for the COHERENT analysis. Figure 7.11 also shows the corresponding two minima for $\varepsilon_{\tau\tau}^f$ arising from the combination of the information on $\varepsilon_{\tau\tau}^f - \varepsilon_{\mu\mu}^f$ and $\varepsilon_{ee}^f - \varepsilon_{\mu\mu}^f$ from the oscillation experiments with the constraints on $\varepsilon_{\mu\mu}^f$ from the COHERENT t+E data. In particular, in all the three cases $f = u, d, p$ shown in the figure the bound on $\varepsilon_{\tau\tau}^f$ becomes about two orders of magnitude stronger than previous indirect (loop-induced) limits [224] when the t+E analysis with the data release assumptions is used. Indeed

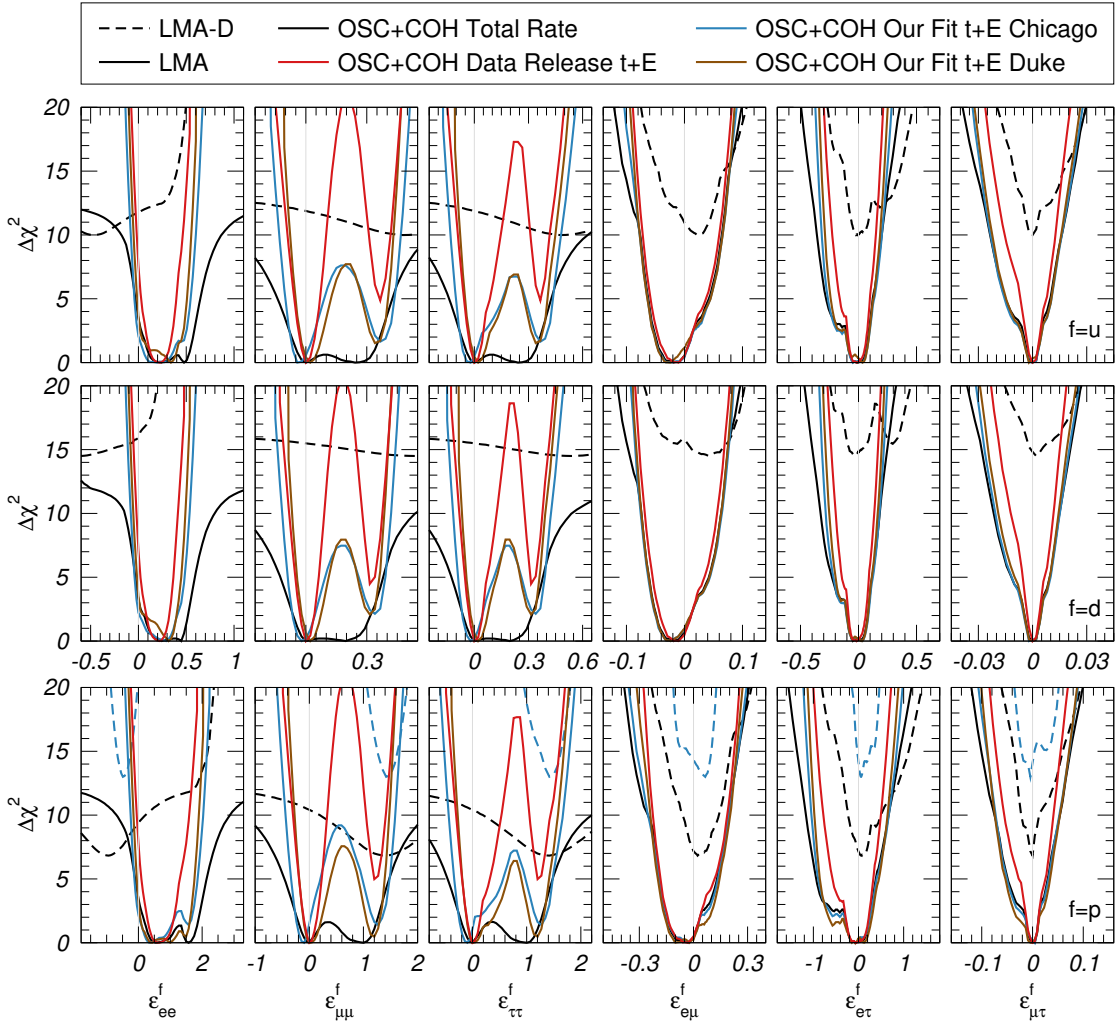


Figure 7.11: Dependence of the $\Delta\chi_{\text{global}}^2$ function on the NSI couplings with up quarks (upper row), down quark (central row) and, protons (lower row) for the global analysis of oscillation and COHERENT data. In each panel χ_{global}^2 is marginalised with respect to the other five NSI couplings not shown and with respect to the oscillation parameters for the LMA (solid) and LMA-D (dashed) solutions. The different curves correspond to the different variants of the COHERENT analysis implemented in this chapter: total rate (black), t+E Data Release (red), t+E with QF-C (blue), and t+E with QF-D (brown); see text for details.

	Total Rate	Data Release t+E	Our Fit t+E Chicago	Our Fit t+E Duke
ϵ_{ee}^u	$[-0.012, +0.621]$	$[+0.043, +0.384]$	$[-0.032, +0.533]$	$[-0.004, +0.496]$
$\epsilon_{\mu\mu}^u$	$[-0.115, +0.405]$	$[-0.050, +0.062]$	$[-0.094, +0.071] \oplus [+0.302, +0.429]$	$[-0.045, +0.108] \oplus [+0.290, +0.399]$
$\epsilon_{\tau\tau}^u$	$[-0.116, +0.406]$	$[-0.050, +0.065]$	$[-0.095, +0.125] \oplus [+0.302, +0.428]$	$[-0.045, +0.141] \oplus [+0.290, +0.399]$
$\epsilon_{e\mu}^u$	$[-0.059, +0.033]$	$[-0.055, +0.027]$	$[-0.060, +0.036]$	$[-0.060, +0.034]$
$\epsilon_{e\tau}^u$	$[-0.250, +0.110]$	$[-0.141, +0.090]$	$[-0.243, +0.118]$	$[-0.222, +0.113]$
$\epsilon_{\mu\tau}^u$	$[-0.012, +0.008]$	$[-0.006, +0.006]$	$[-0.013, +0.009]$	$[-0.012, +0.009]$
ϵ_{ee}^d	$[-0.015, +0.566]$	$[+0.036, +0.354]$	$[-0.030, +0.468]$	$[-0.006, +0.434]$
$\epsilon_{\mu\mu}^d$	$[-0.104, +0.363]$	$[-0.046, +0.057]$	$[-0.083, +0.077] \oplus [+0.278, +0.384]$	$[-0.037, +0.099] \oplus [+0.267, +0.356]$
$\epsilon_{\tau\tau}^d$	$[-0.104, +0.363]$	$[-0.046, +0.059]$	$[-0.083, +0.083] \oplus [+0.279, +0.383]$	$[-0.038, +0.104] \oplus [+0.268, +0.354]$
$\epsilon_{e\mu}^d$	$[-0.058, +0.032]$	$[-0.052, +0.024]$	$[-0.059, +0.034]$	$[-0.058, +0.034]$
$\epsilon_{e\tau}^d$	$[-0.198, +0.103]$	$[-0.106, +0.082]$	$[-0.196, +0.107]$	$[-0.181, +0.101]$
$\epsilon_{\mu\tau}^d$	$[-0.008, +0.008]$	$[-0.005, +0.005]$	$[-0.008, +0.008]$	$[-0.007, +0.008]$
ϵ_{ee}^p	$[-0.035, +2.056]$	$[+0.142, +1.239]$	$[-0.095, +1.812]$	$[-0.024, +1.723]$
$\epsilon_{\mu\mu}^p$	$[-0.379, +1.402]$	$[-0.166, +0.204]$	$[-0.312, +0.138] \oplus [+1.036, +1.456]$	$[-0.166, +0.337] \oplus [+0.952, +1.374]$
$\epsilon_{\tau\tau}^p$	$[-0.379, +1.409]$	$[-0.168, +0.257]$	$[-0.313, +0.478] \oplus [+1.038, +1.453]$	$[-0.167, +0.582] \oplus [+0.950, +1.382]$
$\epsilon_{e\mu}^p$	$[-0.179, +0.112]$	$[-0.174, +0.086]$	$[-0.179, +0.120]$	$[-0.187, +0.131]$
$\epsilon_{e\tau}^p$	$[-0.877, +0.340]$	$[-0.503, +0.295]$	$[-0.841, +0.355]$	$[-0.817, +0.386]$
$\epsilon_{\mu\tau}^p$	$[-0.041, +0.025]$	$[-0.020, +0.019]$	$[-0.044, +0.026]$	$[-0.048, +0.030]$

Table 7.2: 2σ allowed ranges for the NSI couplings $\epsilon_{\alpha\beta}^u$, $\epsilon_{\alpha\beta}^d$ and $\epsilon_{\alpha\beta}^p$ as obtained from the global analysis of oscillation plus COHERENT data. See text for details.

this conclusion holds for most η values, with exception of $\eta \sim -45^\circ$ to -35° for which NSI effects are suppressed in either the Earth matter or in COHERENT. In particular, for $\eta = -35.4^\circ$ the NSI effects in COHERENT totally cancel, as described above, and consequently no separate determination of the three diagonal parameters is possible around such value.

Summary

In this section, we have combined neutrino oscillation data with the latest results from the COHERENT experiment. The results of our analysis are used to constrain the Wilson coefficients of the whole set of neutral current operators leading to CP-conserving NSI involving up and down quarks simultaneously.

We have found that the inclusion of COHERENT timing information affects the global fit significantly and, most notably, has a large impact on the constraints that can be derived for the flavour-diagonal NSI operators, for which separate constraints can only be derived after combination of COHERENT and oscillation data.

Furthermore, the presence of NSI is known to introduce a degeneracy in the oscillation probabilities for neutrinos propagating in matter, leading in particular to the appearance of the LMA-D solution. We find that the inclusion of COHERENT to the analysis of oscillation data disfavors the LMA-D degeneracy for NSI models over a wide range of η , and the addition of the timing and energy information makes this conclusion more robust, see Eq. (7.25) and Fig. 7.10. In particular, the LMA-D solution for NSI models that couple only to protons ($\eta = 0$) can only be excluded beyond 3σ once both energy and timing information are included for the COHERENT data.

Finally, the introduction of NSI is known to alleviate the well-known (albeit mild) tension between solar and KamLAND data in the determination of the Δm_{21}^2 , thus leading to an overall improvement in the quality of the global fit to oscillation data. We find that this still remains the case after the inclusion of COHERENT results.

7.2.2 Including COHERENT in the CP violation and mass ordering analysis of Section 6.2

The results from the COHERENT experiment impose relevant constraints on NSI that could improve the robust determination of leptonic CP violation in LBL accelerator experiments. In this section, we will add the bounds from COHERENT to the analysis in Section 6.2. We will use the time and energy information; and for the background, nuclear form factor and QF we use the procedure named as “Our fit t+E Duke” in the previous section. Nevertheless, the results of the fit do not significantly depend on the nuclear form factor and QF assumed.

To begin with, in Figs. 7.12 and 7.13 we show all the possible one-dimensional and two-dimensional projections of the eleven-dimensional parameter space after including COHERENT data. Comparing with Figs. 6.9 and 6.10, we see that COHERENT improves the constraints on large NSI moduli. This will be relevant for CP violation.

To quantify the impact, in Fig. 7.14 we plot the one-dimensional $\chi^2(\delta_{CP})$ function after marginalizing over the ten undisplayed parameters. In the left, central and right panels we include T2K, NO ν A, and T2K+NO ν A respectively. In each panel we plot the curves obtained marginalizing separately in NO (red curves) and IO (blue curves) for the LMA and LMA-D solutions. For the sake of comparison we also plot the corresponding $\chi^2(\delta_{CP})$ from the 3ν oscillation analysis with the SM matter potential (labeled “NuFIT” in the figure). These results can be compared with the ones in Fig. 6.11, that do not include COHERENT.

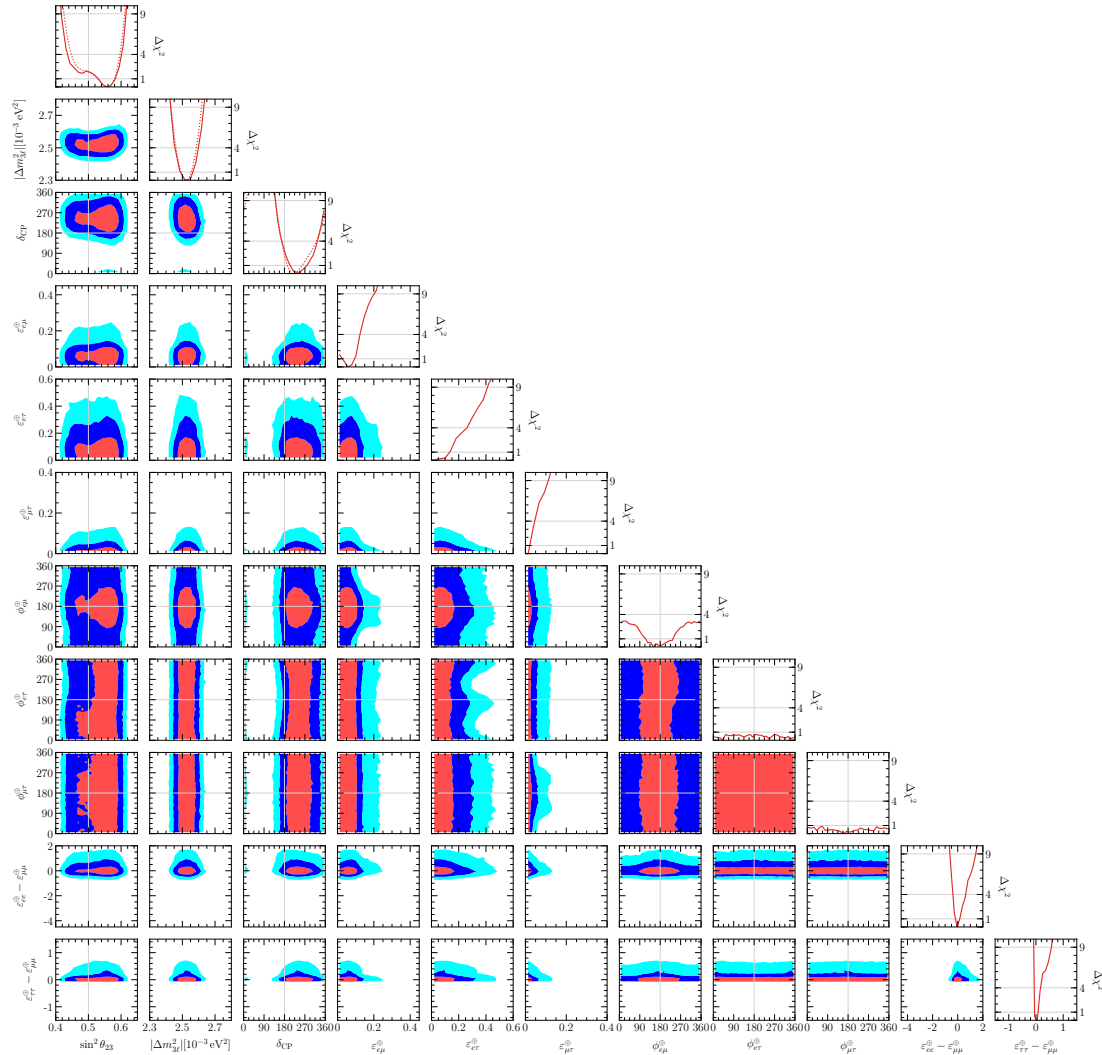


Figure 7.12: Global analysis of solar, atmospheric, reactor and accelerator oscillation experiments plus COHERENT, in the LIGHT side of the parameter space and for Normal Ordering of the neutrino states. The panels show the two-dimensional projections of the allowed parameter space after marginalization with respect to the undisplayed parameters. The different contours correspond to the allowed regions at 1σ , 2σ and 3σ for 2 degrees of freedom. Note that as atmospheric mass-squared splitting we use $\Delta m_{3\ell}^2 = \Delta m_{31}^2$ for NO. Also shown are the one-dimensional projections as a function of each parameter. For comparison we show as dotted lines the corresponding one-dimensional dependence for the same analysis assuming only standard 3ν oscillation (i.e., setting all the NSI parameters to zero).

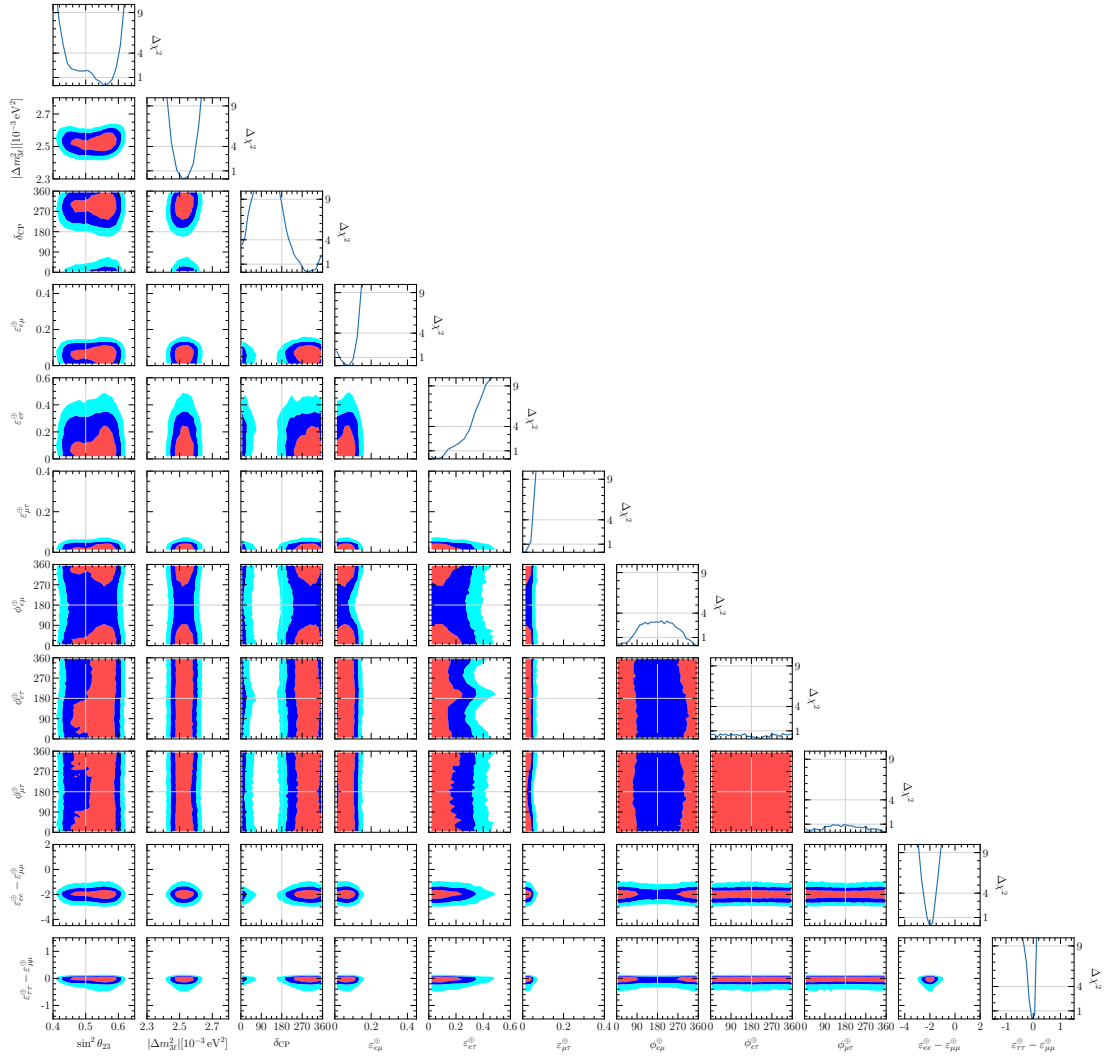


Figure 7.13: Same as Fig. 6.10 but for DARK-IO solution. In this case $\Delta m_{3\ell}^2 = \Delta m_{32}^2 < 0$ and we plot its absolute value. The regions and one-dimensional projections are defined with respect to the *local* minimum in this sector of the parameter space.

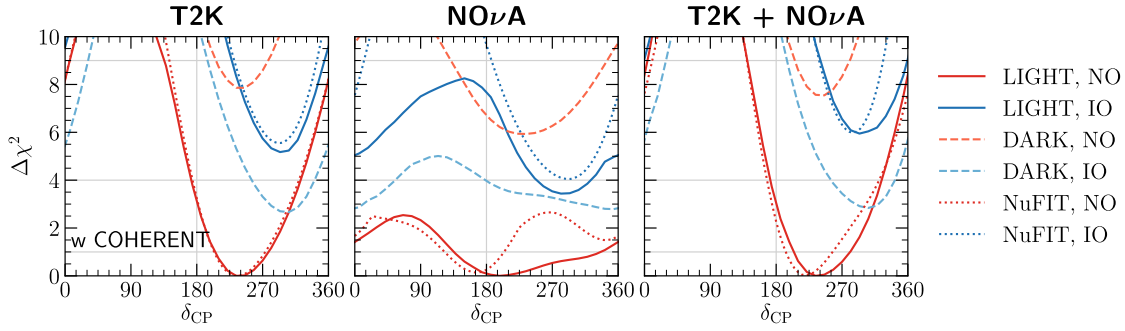


Figure 7.14: $\Delta\chi^2$ as a function of δ_{CP} after marginalizing over all the undisplayed parameters, for different combination of experiments. We include SOLAR + KamLAND + ATM + MBL-REA + MINOS + COHERENT to which we add T2K (left), NO ν A (center) and T2K + NO ν A (right). The different curves are obtained by marginalizing within different regions of the parameter space, as detailed in the legend. See Fig. 6.11 and the text around it for details.

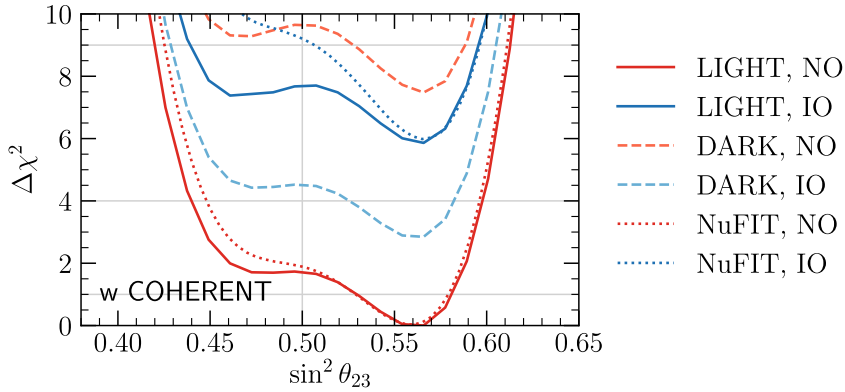


Figure 7.15: $\Delta\chi^2$ as a function of $\sin^2 \theta_{23}$ after marginalizing over all other parameters for the global combination of oscillation experiments + COHERENT. The different curves correspond to marginalization within the different regions of the parameter space, as detailed in the legend. See Fig. 6.12 and the text around it for details.

We see that, regarding T2K, when including COHERENT,

- The robustness of its hint for maximal CP violation still holds.
- For T2K without COHERENT, the DARK, IO solution provided a better fit than LIGHT, NO for several values of δ_{CP} (see Fig. 6.11). These solutions involved large $\varepsilon_{e\mu}$ and $\varepsilon_{e\tau}$, that are no longer allowed after including COHERENT data. As a consequence, the statistical significance of the hint for CP violation in T2K is now essentially the same for the DARK solutions as for the LIGHT ones.

For NO ν A, including COHERENT has a marginal effect, and it mostly reduces to excluding the DARK, NO solution with higher statistical significance. In other words, the NSI required to spoil the NO ν A results are not yet within the reach of COHERENT. Finally, in the global analysis, COHERENT plays a significant role in excluding the DARK, IO solution. This is due to the relatively large NSI that this solution requires, constrained by COHERENT.

In addition, in Fig. 7.15 we show the one-dimensional $\chi^2(\theta_{23})$ after including COHERENT data, to be compared with Fig. 6.12. The main effect is that $\theta_{23} < 45^\circ$ for the DARK-NO solution and $\theta_{23} > 45^\circ$ for DARK-IO, which required large NSI, are now much more constrained.

Overall, we see that the current COHERENT data significantly enhances the robustness of the fit regarding the LMA-D solutions. These, that could flatten $\Delta\chi^2$ and reduce the sensitivity of LBL experiments to the currently unknown parameters, are efficiently explored by COHERENT. Nevertheless, COHERENT cannot significantly exclude the LMA-D solution with respect to LMA. The reason for this is that the analysis presented in this section marginalises over η , whose best-fit value in the LMA-D solution, $\eta \sim -30^\circ$, lies close to $\eta = \arctan(-1/Y_n^{\text{coh}}) \approx -35.4^\circ$ where NSI at COHERENT cancel. This could be overcome by measuring CE ν NS with different nuclei, a possibility that will be explored below.

7.3 Future prospects: coherent elastic neutrino-nucleus scattering at the European Spallation Source

As shown by the analyses above, the first data release from COHERENT already increased the robustness with which LBL accelerator experiments can assess leptonic CP violation. This programme should be further pursued in the near future to have better bounds when DUNE and Hyper-Kamiokande start taking data. COHERENT, though, is still limited by statistical uncertainties as seen in Fig. 7.4.

Luckily, one can perform high-statistics CE ν NS measurements provided by the upcoming European Spallation Source (ESS) sited in Lund, Sweden. The ESS will combine the world's most powerful superconducting proton linac with an advanced hydrogen moderator, generating the most intense neutron beams for multi-disciplinary science (see Fig. 7.16). The operating principle of the facility is the same as for the SNS, whose neutrinos COHERENT detects. However, the ESS will provide an order of magnitude increase in neutrino flux with respect to the SNS due to a higher proton energy and luminosity. This will facilitate CE ν NS measurements not limited in their sensitivity to new physics by poor signal statistics, while still employing non-intrusive, compact (few kg) neutrino detectors, able to operate without interference with ESS neutron activities.

Furthermore, as the facility is still under construction, large areas could be allocated for detectors. These could be more modern, sensitive to smaller nuclear recoils where the CE ν NS cross section (7.3) increases, and of different materials to increase the sensitivity to different NSI models. The detailed proposal and detector details are explained in Ref. [6] and summarised in Table 7.3.

Here, we quote the main results concerning NSI after three years of data-taking. We have assumed an 80% detector acceptance and a 10% signal normalisation systematic uncertainty. Apart from that, the number of neutrino events is calculated exactly as for COHERENT (see Sections 7.1.1 and 7.1.2), although due to longer beam pulses (see Fig. 7.16) no useful timing information is available at the ESS.

In what follows, we focus on the determination of the flavour-diagonal NSI coefficients, $\epsilon_{\alpha\alpha}^f$ ($f = u, d$), although it should be kept in mind that coherent neutrino scattering is also sensitive to all the off-diagonal NSI operators as well, and competitive bounds should also be expected for those.

Figure 7.17 shows our results on the expected allowed regions at 90% CL in the plane ($\epsilon_{ee}^u, \epsilon_{\mu\mu}^u$) for the six detectors under consideration. In this figure for simplicity, we have assumed that the NSI take place only with up-type quarks; however, similar results are obtained if the NSI are assumed to take place with down-type quarks instead. For illustration we show as well the

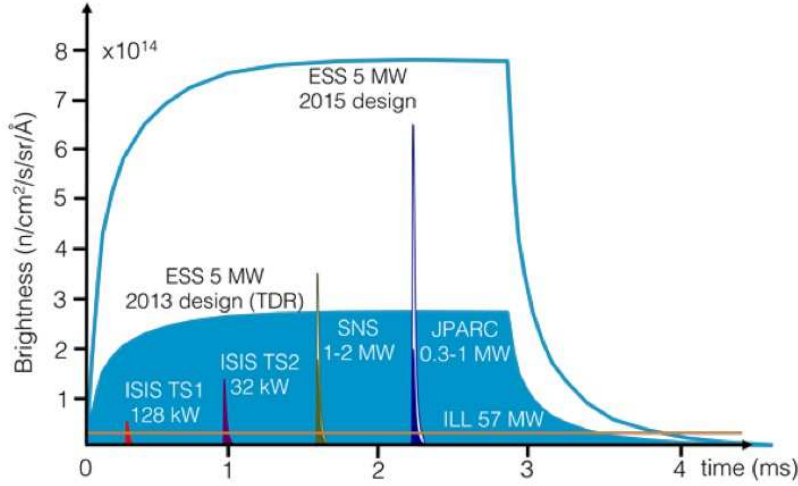


Figure 7.16: (Source: ESS) Neutron production from existing and planned spallation sources. The nominal SNS power is 1 MW at proton energy 1 GeV, with a plan to reach 2 MW by 2026. The ESS power will be 5 MW at 2 GeV circa 2023, with the ability to further upgrade. Differences in the duration of the protons-on-target (POT) pulse are visible in the figure. The ESS will generate an increase in neutron brightness by a factor 30-100 with respect to previous spallation sources, and an order of magnitude larger neutrino yield than the SNS.

Detector Technology	Target nucleus	Mass (kg)	Steady-state background	E_{th} (keV _{nr})	$\frac{\Delta E}{E}$ (%) at E_{th}	E_{max} (keV _{nr})	CE ν NS $\frac{NR}{yr}$ @20m, $> E_{th}$
Cryogenic scintillator	CsI	22.5	10 ckkd	1	30	46.1	8,405
Charge-coupled device	Si	1	0.2 ckkd	0.16	60	212.9	80
High-pressure gaseous TPC	Xe	20	10 ckkd	0.9	40	45.6	7,770
p-type point contact HPGe	Ge	7	3 ckkd	0.6	15	78.9	1,610
Scintillating bubble chamber	Ar	10	0.1 c/kg-day	0.1	~ 40	150.0	1,380
Standard bubble chamber	C ₃ F ₈	10	0.1 c/kg-day	2	40	329.6	515

Table 7.3: Summary of detector properties for CE ν NS at the ESS. We show the target nuclei and mass of different detectors, the steady-state background, the minimum detectable nuclear recoil energy E_{th} , the relative energy resolution $\Delta E/E$ at E_{th} , the maximum detectable nuclear recoil energy E_{max} , and the amount of CE ν NS events per year above threshold for a detector at 20 m from the source. Backgrounds listed do not include a 4×10^{-2} reduction by the pulsed character of the ESS beam. The background for bubble chambers is integrated above nucleation threshold (in counts per kg and day), and only the total event rate is used in the simulations. Other backgrounds are given in counts per keV, kg and day (ckkd). We conservatively adopt the background at E_{th} , which is typically maximal, for all higher energies. The relative energy resolution is assumed to depend on the nuclear recoil energy as $\propto \sqrt{E}$.

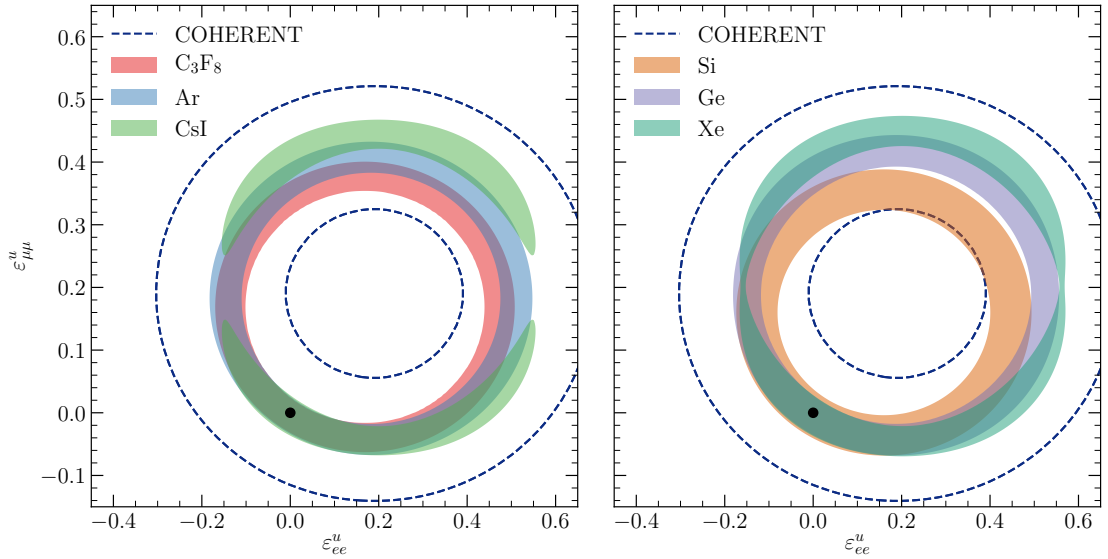


Figure 7.17: Expected allowed regions in the $(\epsilon_{ee}^u, \epsilon_{\mu\mu}^u)$ plane at the 90% confidence level (C.L.) for two degrees of freedom (d.o.f.) after three years of running. The different regions correspond to the expected results for the different detectors listed in Table 7.3, as indicated by the legend. In all cases, the simulated data has been generated for the SM (that is, setting all the operator coefficients to zero), and the results are then fitted assuming NSI. For simplicity, the rest of the NSI parameters not shown in the figure have been assumed to be zero. For comparison, the dashed lines show the allowed regions at 90% CL in this plane, as obtained in Ref. [249] from an analysis of current data from the COHERENT experiment [295], see text for details.

90% CL allowed region from the analysis of the total event rate observed at the COHERENT experiment in Ref. [249], following the prescription provided in Ref. [295] to perform a fit to NSI using the total event rates. In principle, adding the timing and energy information provided in Ref. [300] can help to tighten their constraints to some degree [311,312]; however, the final result is subject to uncertainties in the treatment of the background and systematic errors assumed as explored in Section 7.1.

The different areas in the two panels in Fig. 7.17 correspond to the results obtained with the detector configurations listed in Tab. 7.3. As seen in the figure, in most cases the shape of the allowed regions is an ellipse in this plane. This can be easily understood as follows. From Eqs. (7.2), (7.3), (7.8) and (7.7) one can trivially compute the expected total number of events in each energy bin as a function of the two NSI coefficients. Requiring that the NSI-induced correction is of the same relative size in all bins and that the total number of events is compatible with the SM expectation, it is straightforward to show that the allowed confidence regions in the plane $\epsilon_{ee}^u - \epsilon_{\mu\mu}^u$ obey the equation of an ellipse:

$$[R + \epsilon_{ee}^{u,V}]^2 + 2[R + \epsilon_{\mu\mu}^{u,V}]^2 = 3R^2 \quad (7.26)$$

where $R \equiv \frac{Zg_{V,p} + Ng_{V,n}}{2Z+N}$ only depends on the target nucleus and the SM weak couplings to protons and neutrons. In the SM, given that $g_{V,p} \ll g_{V,n}$ this constant can be safely approximated to $R \simeq g_{V,n}/(2r+1)$, where $r \equiv Z/N$ is the ratio of protons to neutrons in the nucleus. From Eq. (7.26) it follows that the shape of the allowed confidence regions in this plane will be very

Nucleus	Z	N	r	$M(\text{a.m.u.})$
^{132}Xe	54	78	0.69	131.29
^{40}Ar	18	22	0.81	39.95
^{72}Ge	32	40	0.8	75.92
^{28}Si	14	14	1.0	27.98
^{12}C	6	6	1.0	12.01
^{19}F	9	10	0.9	19.00
^{133}Cs	55	78	0.71	132.91
^{127}I	53	74	0.72	126.90
^{20}Ne	10	10	1.0	20.18

Table 7.4: Main properties of the nuclei for the different target nuclei considered in this section. The different columns indicate the isotope considered, together with the number of protons and neutrons, the ratio between them r , and the value of the nuclear mass in atomic mass units (a.m.u.). For the detectors using CsI and C_3F_8 we take the weighted average between the two elements in the molecule.

similar for different target nuclei as long as they have a similar value of r . For reference Table 7.4 summarises the values of Z , N , r , and the nuclear masses assumed for different nuclei.

As seen in Fig. 7.17, the allowed regions are in good agreement with Eq. (7.26), for most of the detectors under consideration. However, from the figure we also see that for some detectors, in particular for the CsI target (and also in part for Xe target), the degeneracy in the allowed region in the $(\epsilon_{ee}^{u,V}, \epsilon_{\mu\mu}^{u,V})$ plane implied by Eq. (7.26) is partly broken. This is so because Eq. (7.26) has been obtained under the approximation of a constant — flavour- and energy-independent — shift of the event rates in all bins. Clearly the degeneracy will be broken if somehow the experiment is capable of discriminating between muon and electron neutrino flavours at some level. A possibility to do this, is through the addition of timing information, which allows to distinguish between the prompt component of the beam (which contains just ν_μ) and the delayed component (which contains a mixture of ν_e and $\bar{\nu}_\mu$). Unfortunately, due to the very long proton pulses this would not be possible at the ESS source.

One must notice, however, that the prompt signal is also characterised by a lower neutrino energy ($E_{\nu_\mu} \sim 30 \text{ MeV}$), as can be seen in Fig. 7.2. Therefore, it should be possible to distinguish its contribution using a detector with good energy resolution that allows to observe not only the bulk of events at low energies (which receives equal contributions from the three components of the beam) but also the tail at high recoil energies, above the maximum recoil allowed for the prompt signal (see Eq. (7.9)). For large enough statistics, this would allow to obtain partial flavour discrimination, by comparing the event rates below and the maximum recoil allowed for the prompt flux. For illustration, we show in Fig. 7.18 the expected event rates, where the contribution per flavour is shown separately. As shown in this figure, above the maximum recoil energy allowed for the prompt component the event rates are given almost exclusively by ν_e and $\bar{\nu}_\mu$ scattering (albeit with a small contribution from ν_μ in the first bin, due to smearing by the energy resolution). Consequently in the case of detectors with high statistics, good energy resolution and no saturation, the ellipse is broken in this plane. This is the case for the CsI and Xe detectors, as seen in Fig. 7.17.

Furthermore, from Eq. (7.26) it is clear that an alternative form of breaking this degeneracy is through the combination of data obtained using different target nuclei, as long as they have different values of r . This is true even if only information on the total event rates is available (without any time nor energy information). While the combination can be done using different

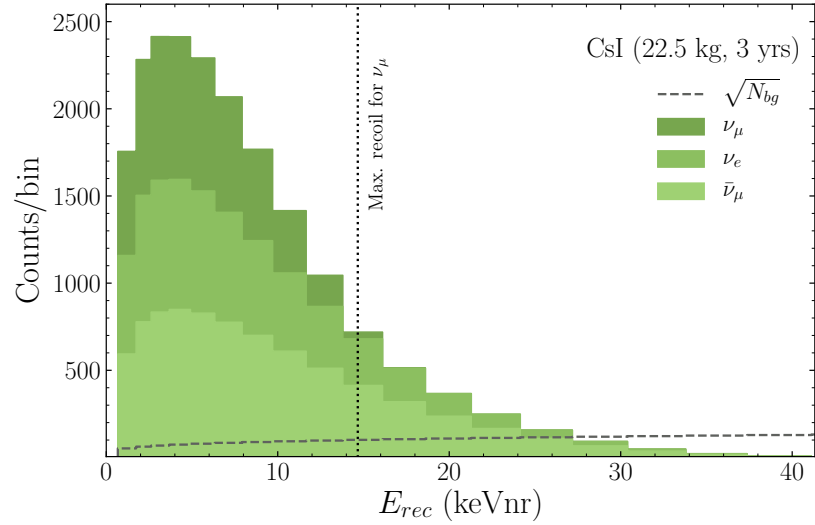


Figure 7.18: Expected event rates per bin in nuclear recoil energy, for the CsI detector. The contributions from the scattering of the different beam components are shown separately by the shaded histograms, as indicated by the legend. For comparison, the square root of the number of background events in each bin is also shown by the dashed histogram lines. The vertical dotted line indicates the maximum recoil energy allowed by a neutrino with energy $E_\nu = 29.8$ MeV, that is, the energy of the monochromatic prompt ν_μ flux.

detectors among the possibilities listed in Tab. 7.3, a more convenient option is available in the case of the gas TPC, since the detector can operate not only with xenon but with other noble gases as well (Ne, He, or Ar for instance). As illustration of this possibility, we show Fig. 7.19 the expected sensitivity regions in this plane using the gas TPC detector. In this case we show three different results: (i) the expected regions obtained using Xe as the target nucleus; (ii) the expected regions using Ar instead; and (iii) the results obtained using a combined run, where the detector uses Xe during the first half of the data taking period and Ar during the other half. From the figure we see how the combination of runs with the two selected nuclei leads to a substantially improved sensitivity.

7.4 Summary and conclusions

NSI-NC have the potential of spoiling the sensitivity of LBL accelerator experiments to leptonic CP violation. Furthermore, some of the degeneracies they introduce are exact at the probability level and thus impossible to lift with oscillation data. The sort of models leading to viable NSI makes them very difficult to constraint with other experiments, as they usually involve light particles and thus precise measurements at low momentum transfers are needed.

Fortunately, in the last years coherent neutrino-nucleus elastic scattering has been reliably detected. In this process, neutrinos interact coherently with an entire atomic nucleus, boosting the cross section and exchanging very little momentum with the detector. This way, NSI can be bounded with complementary scattering experiments not subject to the oscillation degeneracies.

In this chapter, we have comprehensively analysed the data from the COHERENT experiment. We have assessed the sensitivity of the results to the modelling of the background, nuclear

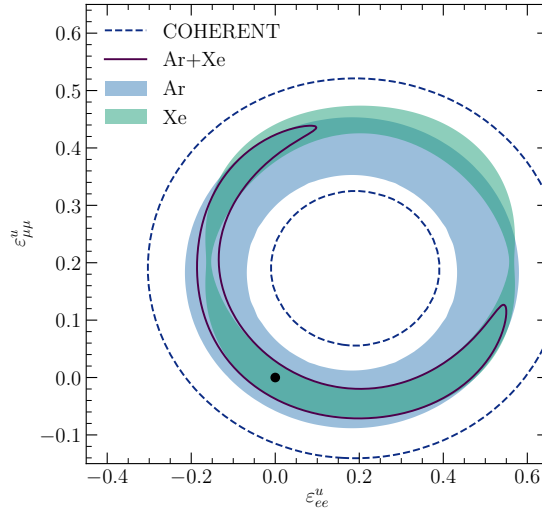


Figure 7.19: Expected allowed regions in the $(\epsilon_{ee}^u, \epsilon_{\mu\mu}^u)$ plane at the 90% C.L. for 2 d.o.f, for the gas TPC detector operating with two different nuclei (separate runs, each of them for 3 years), as well as for a configuration where the detector is filled with each of the two gases during half of the total data taking period (1.5 years running with ^{132}Xe , 1.5 years with ^{40}Ar). In all cases, the simulated data has been generated for the SM and the results are then fitted assuming NSI. For simplicity, the values for the rest of NSI parameters not shown in this figure have been set to zero.

form factor, and detector energy response. Some of these are poorly understood and directly affect the obtained bounds on NSI. Therefore, it is essential that these aspects are experimentally explored in detail.

We have also combined the COHERENT data with the bounds on NSI coming from neutrino oscillations. We have obtained bounds on the individual diagonal NSI, impossible to detect with oscillations, and we have excluded the LMA-D solution for a wide range of NSI models. Regarding CP violation, COHERENT significantly improves the robustness of LBL accelerator results. Without it, the determination of δ_{CP} (and also the mass ordering and θ_{23} octant) gets worsened once NSI are introduced. These NSI, within bounds from neutrino oscillation experiments, are disfavoured by COHERENT data.

This complementarity between coherent neutrino-nucleus elastic scattering and LBL accelerator experiments should be maintained in the future to ensure the success of the DUNE and Hyper-Kamiokande experiments. To that respect, we have explored the potential of the ESS, that will accumulate data one order of magnitude faster than COHERENT. On top of that, the possibility of using different detector materials will enhance the sensitivity to a variety of NSI models. We have seen that within few years of running, tight constraints on NSI can be placed. This way, coherent neutrino-nucleus elastic scattering could pave the way for a clean and robust measurement of leptonic CP violation in next generation experiments.

Chapter 8

Conclusions

Ĝemu kaj ploru, sed ĝis fino laboru.

— Ludwik Lejzer Zamenhof

We are living exciting times for neutrino physics. What started as an undetectable particle has turned itself into a precision tool to explore the next underlying theory of Nature. What started as oddball anomalies have turned themselves into a window to subtle differences among matter and antimatter. In this context, at the beginning of this thesis a statistical hint started to show up, pointing towards large CP violation in the leptonic sector.

If confirmed, this hint would imply that leptonic CP violation, as measured by the Jarlskog invariant in Eq. (2.89), can be about three orders of magnitude larger than quark CP violation. That is, it would be the strongest experimentally measured source of CP violation. Neutrino flavour transitions would provide us not only with our first laboratory evidence of BSM physics, but also with a new approach to understand the matter-antimatter asymmetry.

Nevertheless, CP violation induced by neutrino masses and mixings is a three-flavour effect, where all the mixing parameters are relevant. Because of that, it has to be explored from a global perspective, taking into account all experimental data relevant for neutrino flavour transitions. This has been the approach followed in Chapter 4, where a global fit to neutrino oscillation data in the three-neutrino framework has been presented.

We have first presented the results as of fall 2016, which correspond to the first original results obtained in this thesis. Quantitatively the determination of the two mass differences, three mixing angles and the relevant CP violating phase obtained under the assumption that their log-likelihood follows a χ^2 distribution is listed in Tab. 4.1, and the corresponding leptonic mixing matrix is given in Eq. (4.1). We have found that the maximum allowed CP violation in the leptonic sector parametrised by the Jarlskog determinant is $J_{\text{CP}}^{\text{max}} = 0.0329 \pm 0.0007$ ($^{+0.0021}_{-0.0024}$) at 1σ (3σ).

We have studied in detail how the sensitivity to the least-determined parameters θ_{23} , δ_{CP} and the mass ordering depends on the proper combination of the different data samples (Sec. 4.1.2). Furthermore we have quantified deviations from the Gaussian approximation in the evaluation of the confidence intervals for θ_{23} and δ_{CP} by performing a Monte Carlo study of the LBL accelerator and reactor results (Sec. 4.1.3).

As a result, we have found that the interpretation of the data from accelerator LBL experiments in the framework of three neutrino mixing requires using information from the reactor experiments, in particular about the mixing angle θ_{13} . But since reactor data also constrain

$|\Delta m_{3\ell}^2|$, the resulting confidence level of presently low confidence effects (in particular the non-maximality of θ_{23} and the mass ordering) is affected by the inclusion of this information in the combination. In addition, we also conclude that the present sensitivity to δ_{CP} is almost entirely driven by T2K. We find that, for the favoured regions in parameter space, the Gaussian limit is a very good approximation to quantify this sensitivity.

Afterwards, we have examined the evolution of the significance for CP violation as the NO ν A and T2K experiments released data. The results from the final global combination are shown in Figs. 4.18 and 4.19. As a result of the interplay between $\bar{\nu}_\mu$ disappearance, ν_e appearance and $\bar{\nu}_e$ appearance data, the unknowns start to clarify. There is no longer a strong degeneracy in the θ_{23} octant, normal mass ordering is currently favoured by the data, and there is a hint for $\delta_{\text{CP}} \sim \frac{3\pi}{2}$, i.e., maximal CP violation. $\delta_{\text{CP}} \sim \frac{\pi}{2}$ is disfavoured with $\sim 4\sigma$, but CP conservation is still allowed within $\sim 1.5\sigma$. For normal mass ordering, the NO ν A sensitivity is rather poor and the signal is mostly driven by T2K. Although NO ν A and T2K show a slight disagreement in the $\bar{\nu}_e$ appearance channel responsible for determining these unknowns (see Fig. 4.17a), the results are consistent within 1σ – 1.5σ .

However, the T2K hint does not come from directly measuring CP violation, but from a large $\nu_\mu \rightarrow \nu_e$ appearance signal. If interpreted in the three massive neutrino paradigm, this signal can only be accommodated by assuming large CP violation. Nevertheless, three light neutrinos is just the first effect from BSM physics that one expects. Other effects, parametrised by dimension-6 operators in the Lagrangian, could also be present and contribute to the observed signal at T2K.

Because of that, in Chapter 5 we have explored the possible new physics entering neutrino flavour transitions. Some of them can be constrained with electroweak precision observables, but others involve a two-neutrino vertex and are harder to bound. These include what are usually referred to as NSI-NC, that modify neutrino coherent scattering with the traversed matter. If they are mediated by rather light particles, bounds from scattering experiments can be naturally avoided, and they can only be constrained with neutrino flavour transitions. Furthermore, NSI introduce new sources of CP violation that do not require three-flavour effects and could be thus enhanced at accelerator LBL experiments. At the same time, NSI also introduce an exact degeneracy at the oscillation probability level, leading to what is known as the LMA-D solution where the mass ordering and the octant of θ_{12} are flipped and the CP phase is modified as $\delta_{\text{CP}} \rightarrow \pi - \delta_{\text{CP}}$. This could reduce the sensitivity to CP violation.

In Chapter 6, these models confront experimental data. Due to the large parameter space and variety of experiments involved, we first assess the sensitivity of neutrino oscillation experiments to CP conserving NSI. In particular we have considered NSI with an arbitrary ratio of couplings to up and down quarks and a lepton-flavour structure independent of the quark type. We have included in our fit all the solar, atmospheric, reactor and accelerator data commonly used for the standard three neutrino oscillation analysis, with the only exception of T2K and NO ν A appearance data whose recent hints in favor of CP violation are not easily accommodated within the CP-conserving approximation assumed in this fit. We have found that individual experiments allow very large NSI, particularly when they are adjusted to be suppressed for the particular matter composition traversed by the neutrino beam (see Figs. 6.2 and 6.5). Consequently, the bounds on the oscillation parameters get weakened (see Fig. 6.6). However, different experiments are sensitive to different matter profiles, energy ranges and oscillation channels. When combining all data, we find that the oscillation parameters are robustly determined (except slightly for θ_{12} , see Fig. 6.6) and that $\mathcal{O}(1)$ NSI are disfavoured (see Fig. 6.7). Having observed neutrino oscillations in a large variety of environments is crucial for this. We have also recast the results of our analysis in terms of the effective NSI parameters which describe the generalised matter potential in the Earth, Fig. 6.8, and are therefore the relevant quantities for the study of present and future atmospheric and LBL experiments.

Due to the robustness that the variety of experimental data provides, it is possible to move on and perform a global fit to all neutrino flavour transition data assuming that the most general CP-violating NSI are present. This is also done in Chapter 6 (see Figs. 6.9 to 6.12). We have concluded that the confidence level for the preference for a CKM-like CP phase close to $3\pi/2$ in T2K, which is the one that drives the preference in the global analysis, remains valid even when including all other phases in the extended scenario. The reason for this is that T2K has a relatively short baseline, the effects of the traversed matter are small, and so NSI strong enough to significantly affect it would have been detected by other experiments more sensitive to matter effects. Nevertheless, the $\text{NO}\nu\text{A}$ baseline is larger, and NSI within experimental bounds can significantly affect the interpretation of its data. Since the information on δ_{CP} is dominated by T2K, the global result ignoring the LMA-D solution is robust.

On the contrary, the preference for normal mass ordering in LBL experiments is totally lost when including NSI as large as allowed by the global analysis because of the intrinsic degeneracy in the Hamiltonian mentioned above, which implies the existence of an equally good fit to LBL results with inverted mass ordering and reversed octant of θ_{12} and $\delta_{\text{CP}} \rightarrow \pi - \delta_{\text{CP}}$ (so in this solution the favored δ_{CP} is also close to $3\pi/2$). In the global analysis the only relevant breaking of this degeneracy comes from the composition dependence of the matter potential in the Sun which disfavors the associated LMA-D with confidence level below 2σ . Finally, we have also studied the effect of NSI in the status of the non-maximality and octant determination for θ_{23} and find that for both orderings, for both LIGHT and DARK sectors, maximal $\theta_{23} = \pi/4$ is still disfavoured in the global fit at $\sim 1.5\sigma$.

These results are particularly worrisome in the context of future experiments. The Deep Underground Neutrino Experiment, for instance, is expected to determine CP violation with a very large statistical significance. This experiment is dominated by matter effects, and so it is potentially affected by the same sensitivity loss as $\text{NO}\nu\text{A}$. The advent of more neutrino oscillation experiments will not alleviate the situation, as part of the sensitivity loss comes from the generalised mass ordering degeneracy, exact for neutrino oscillations.

The only hope for lifting this degeneracy is bounding NSI with non-oscillation experiments. Traditional neutrino scattering experiments have large momentum transfers, and so bounds from them could be evaded if the mediator inducing NSI is light. Fortunately, in the last years the COHERENT experiment has measured coherent neutrino-nucleus elastic scattering. In this process, a neutrino interacts coherently with an entire atomic nucleus, exchanging a very small momentum that allows to probe light mediator-induced NSI. In Chapter 7, we develop a comprehensive analysis of data from the COHERENT experiment in the framework of NSI-NC. That analysis is combined with the measurements from neutrino flavour transitions described in Chapter 6.

We have quantified the dependence of our results for COHERENT with respect to the choice of detector Quenching Factor, nuclear form factor, and the treatment of the backgrounds. We find that the implementation of the steady-state background has a strong impact on the results of the analysis of COHERENT due to a slight background excess present in the data samples provided by the collaboration. Once this effect has been accounted for in the modelling of the expected backgrounds, the choice of Quenching Factor and nuclear form factor has a minor impact on the results obtained from the fit. We find that the inclusion of COHERENT to the CP-conserving analysis of oscillation data disfavors the LMA-D degeneracy for a wide range of NSI models (see Fig. 7.10).

We have also included COHERENT data in the CP-violating NSI analysis (see Figs. 7.12 to 7.15). Regarding the T2K results, COHERENT improves the constraints on large NSI moduli that could slightly spoil T2K, and so the fit gets even more robust. This is so in the global combination as well. For $\text{NO}\nu\text{A}$, including COHERENT has a marginal effect. In other words,

the NSI required to spoil the $\text{NO}\nu\text{A}$ results are not yet within the reach of COHERENT.

This programme of complementing LBL accelerator experiments with coherent neutrino-nucleus elastic scattering measurements should be further pursued in the near future to have better bounds when the future LBL accelerator experiments start taking data. COHERENT, though, is still limited by statistical uncertainties, as seen in Fig. 7.4; and by performing measurements with a single target nucleus. This limits its sensitivity to different NSI models, and reduces its efficiency in rejecting the LMA-D solution.

Luckily, one can perform high-statistics coherent neutrino-nucleus elastic scattering measurements provided by the upcoming European Spallation Source (ESS) sited in Lund, Sweden. The ESS will combine the world's most powerful superconducting proton linac with an advanced hydrogen moderator, generating the most intense neutron beams for multi-disciplinary science (see Fig. 7.16) and, as a byproduct, an intense and well-understood neutrino beam from pion decay at rest. The operating principle of the facility is the same as for the Spallation Neutron Source (SNS), whose neutrinos COHERENT detects. However, the ESS will provide an order of magnitude increase in neutrino flux with respect to the SNS due to a higher proton energy and luminosity. In addition, as it is still under construction there is potential space for modern detectors with various target nuclei. Its prospects for bounding NSI are also explored in Chapter 7. Particularly interesting is the possibility of performing measurements with gas TPC detectors, where the target nucleus can be changed without interrupting the experiment operation significantly. We have seen that within few years of running, tight constraints on NSI can be placed. This way, coherent neutrino-nucleus elastic scattering could pave the way for a clean and robust measurement of leptonic CP violation in next generation experiments.

In summary, this thesis started by rigorously quantifying the global significance of the hint for leptonic CP violation. After checking its robustness against the statistical assumptions, we have moved on to explore its sensitivity to physical assumptions. Being an indirect hint driven by an event excess, in principle it could depend on the framework in which it is interpreted. Nevertheless, thanks to the vast amount of neutrino flavour transition data recorded across three decades, the data interpretation of CP violation induced by mixing among three light neutrinos is found to be quite robust. Flavour transition data can be complemented with neutrino-nucleus coherent elastic scattering measurements, which should allow for a clean and robust measurement of leptonic CP violation in present and next generation experiments.

The study of neutrino physics started with a brave proposal by Pauli of an almost undetectable particle. The combination of theoretical and experimental courage led to colossal detectors that undoubtedly determined that neutrinos have mass, thus providing a clear sign of BSM physics. Currently, precision experiments are determining the last aspects of leptonic flavour mixing. In their way, they have found a robust hint for leptonic CP violation, guiding us towards a better understanding of Nature and the origin of the matter in the Universe. The bright future of this field, based on firm foundations as explored in this thesis, and the surprises it might reveal are something still beyond our comprehension.

Acknowledgements

Al mirar dentro de sí y al mundo
que lo que a todos les quitaste sola
que le rodea
te puedan a ti sola quitar todos
Cervantes ve que España,
y él,
y Don Quijote,
están de vuelta
de una gran cruzada . . .

— Blas de Otero

Capturing in a few paragraphs all the people that have contributed, in one way or another, to the long journey that finishes writing a PhD thesis is far from easy. It is definitely an incomplete and unfair list. But I will do my best to reflect what I feel while writing this chapter in the middle of a quarantine due to a worldwide pandemic.

No puedo sino comenzar agradeciendo a mi familia. Ellos son los únicos causantes de lo que me ha traído hasta aquí. Comenzando por mis abuelos, los que he conocido y los que no, que me han intentado transmitir el valor del esfuerzo, el trabajo duro, la humildad y los principios morales. Gracias Pilar, Teodoro, Julita, Esteban y Eulalia.

Por supuesto, mis padres juegan un papel esencial. Por haberme querido como nadie; por haberme apoyado en todas las decisiones, las fáciles y las difíciles; por haberme aconsejado pese a mi cabezonería innata; y por haberme facilitado que estudiase una carrera, un máster y un doctorado. Por aguantarme en los malos momentos, por bajarme los humos en los buenos. Por transmitirme un estilo de vida y el verdadero significado de la felicidad. Y, ante todo, gracias por contagiarme la pasión por la ciencia y el conocimiento, por el trabajo bien hecho y por la verdadera comprensión de los fenómenos naturales. Esta tesis y esta carrera es sobre todo vuestra, Maite y Esteban.

Siguiendo un orden cronológico, gracias, Juan Luis. Gracias. Pedro. Eskerrik asko, Julen. Fuisteis los mejores maestros, reales y virtuales, que pude tener. Un profesor normal se habría limitado a transmitir fórmulas. Vosotros transmitisteis ciencia, conocimiento, y pasión.

Mil gracias también a ti, Aarón. Por mantener una estrecha amistad desde hace ya casi 10 años. Por haber seguido ahí pese a los cambios y altibajos que ambos hemos tenido en nuestras vidas. Por aportar otra visión de ver las cosas, por restar seriedad a aquello que no la merece. Por tus consejos, por tu ayuda. Por esas noches de farmacias. *Annon allen.*

Y gracias también, Isa, por seguir ahí después de tanto tiempo. Porque nos conocemos desde hace más de 9 años, porque ambos hemos evolucionado muchísimo en todo este tiempo, pero porque cada vez que nos vemos parece que nada ha cambiado entre nosotros. Gracias por aportar una visión de la vida con los pies en la tierra pero sumamente humanista y literaria. Sin ti no

sería ni por asomo quien soy.

El proceso que termina con esta tesis comenzó allá por otoño de 2011 en una pequeña facultad de Ciencia y Tecnología cerca de Bilbao. Todo lo que escriba sobre las personas que más me acompañaron durante los años que pasé allí es poco. Gracias, Iker, Iñigo y Jorge. Por todo lo que compartimos durante aquellos años, y por todo lo que seguimos compartiendo pese a la distancia. Por ayudarme con las decisiones, por apoyarme en ellas, por hacer lo imposible para que todo salga bien. Sois los mejores compañeros de viaje. Refflotar Zimatek y todo lo que conllevó es una de las experiencias que guardo con mayor cariño. Es bien sabido, aunque la razón no está del todo clara, que algo que empezó con la pereza de un profesor de química no puede terminar mal. Gracias por ser unas personas tan definidas positivas.

Sería necesariamente incompleto nombrar a toda la gente, tanto compañeros como profesores o hasta miembros de Decanato o compañeros de teatro, con los que compartí aquellos años. Baste decir que sin la pasión por la Física, la Ciencia y la Vida que desarrollé gracias a ellos jamás habría continuado por la senda que finalmente seguí.

And this path went on in the best possible way. Thank you, Gunar, for introducing me to fundamental physics research (and thanks, Iñigo, for introducing us!). Your view of physics as a fundamentally experimental science has had a profound impact on my way of approaching research. Your thoughts about life have shaped the kind of researcher I am now. The opportunities you offered without even knowing me were invaluable. I had amazing research experiences those undergrad summers, and without them none of my motivation would be present. Along the same line, thank you Elke, Stephen, Carmen, Grant, Jasone and Dima. Thank you for trusting a naive undergraduate student, for patiently teaching him, for making him feel like at home far from it, and for selflessly encouraging and supporting him.

Aquesta aventura va seguir amb un petit salt al built. Gràcies a la gent que vaig conèixer al arribar a Barcelona, el canvi va ser molt més fàcil. Gràcies, Alba, per presentar-me'ls. Gràcies, Gemma i Sergi (i després Popep), per fer-me sentir com a casa. Trobaré molt a faltar l'ambient del Popiso. Gràcies, Marcs, Adrià, Albas, Elis, Fran, Irene, Isma, Joan . . . per ser la meva família aquí. Gemma, et vaig prometre que unes línies serien només per tu. Has alegrat els meus últims 5 anys. M'has escoltat com ningú, m'has estimat com una germana, m'has fet riure com la millor amiga. Et trobaré molt a faltar.

Part of my family during those early days were you, Clara, Armun, Giorgio, Elis, Víctor, Javi. I had an amazing time learning with you. Gracias en particular a Clara, porque a tu lado crecí enormemente, porque me diste muchos momentos inolvidables. Siempre es un placer defender los fueros a tu lado.

Gran parte de la culpa de que esta tesis exista es alguien que me ha acompañado, en la cercanía y en la distancia, durante los últimos cinco años. Gracias, Concha, por todo tu esfuerzo, entusiasmo y paciencia. Por transmitirme la pasión por la investigación en fenomenología de física de partículas. Por estar siempre ahí, dedicándome tu valioso tiempo y tu vasto conocimiento. Por mostrarme la satisfacción del trabajo bien hecho, la metodología rigurosa, la ética en el trabajo, y el análisis crítico necesario en toda ciencia. Gracias también por darme libertad, hacerme la vida fácil, y empujarme hacia la independencia. Espero haber adoptado al menos una pequeña parte de tus grandes cualidades investigadoras.

During my PhD years, I also had the chance of meeting and working with many different people. Thank you, Thomas and Michele, for your support and patience sharing your knowledge; thank you Joachim for being such a great source of ideas, enthusiasm, and opportunities. Gracias Jordi, gracias Jacobo, por aportar una visión fresca y diferente de la física. Es un placer trabajar con vosotros. Cada vez que hablamos sobre física me recordáis por qué trabajo en esto. Cada vez que hablamos sobre otros temas me demostráis lo completos que sois como personas. I would also like to thank for their warm hospitality all the local people that have made my life way easier

during my trips. I have really enjoyed discovering the support from the physics community.

Thank you also to all the PhD students I met. Nuno, it was a real pleasure sharing an office, conferences, and many discussions with you. You are a person with which I could talk about anything, and I had tons of fun discussing everything from physics to Catalan politics. Alisa, Ivan, Pere, Mona, Alvaro . . . you were great colleagues and friends. The ñam ñam group, thank you for all the fun we have at lunch time. One of the worst things of working from home during the quarantine has been missing that break. Dankon eĉ al la samideanoj kiuj mi konis dum ĉi tiu jaro kaj duono. Precipe al Xosé por via instruado, kaj al la aliaj en Barcelono aŭ en la tuta mondo. La ideoj de internacia frateco, de aparteni al la sama movado, kuraĝigis min por malfermi al la mondo.

Y no puedo terminar sin agradecerte también a ti, Irene. Por tu manera de entender la vida. Por tus consejos, tu apoyo, tu comprensión, tus sonrisas y tu infinito cariño. Gracias.

List of Figures

2.1	Some neutrino flavour oscillation probabilities. The results have been obtained using Ecuación (2.61) under the assumption of 3 light neutrinos and the values for the oscillation parameters in Ref. [111].	21
3.1	Convention for the numbering of mass eigenstates and possible orderings (NO in left, IO in right). The colours indicate the amount of mixing between mass and flavour eigenstates.	29
3.2	Nuclear reactions in the Sun that produce neutrinos. The top row corresponds to the pp cycle, and the bottom row to the CNO cycle. Above each reaction, the name with which the neutrinos produced there are denoted is indicated. Adapted from Refs. [138, 139].	30
3.3	Solar neutrino spectrum. Above each line, the reaction in which neutrinos are generated is indicated (see Figura 3.2). Extracted from Ref. [140]. The theoretical computations and uncertainties on flux normalisations are given in Refs. [136, 137]. Monochromatic fluxes, corresponding to electron capture processes, are given in units of $\text{cm}^{-2} \text{s}^{-1}$	31
3.4	$\nu_\mu + \nu_\tau$ flux vs ν_e flux, as measured by the SNO neutral current (purple), charged current (red), and elastic scattering (green) data. The region between the dashed lines corresponds to the prediction in Ref. [141] assuming neutrino flavour oscillations. The contours correspond to the joint confidence regions. Also shown in grey is the Super-Kamiokande measurement [142]. The hypothesis of no flavour transitions ($\phi_{\mu\tau} = 0$) is clearly excluded. Figure from Ref. [15].	32
3.5	Allowed regions of Δm^2 and $\sin^2 \theta$ that best describe solar data. The red regions correspond to the KamLAND reactor experiment, to be discussed later. Figure courtesy of M. C. Gonzalez-García and M. Maltoni.	33
3.6	Solar ν_e survival probability as a function of the neutrino energy, as well as some experimental data. Brx means Borexino and KL KamLAND. Earth matter effects, which induce a small day-night asymmetry, are also included. The transition between the vacuum-dominated regime, at lower energies and with $P_{ee} > \frac{1}{2}$; and the MSW-dominated regime, at higher energies and with $P_{ee} < \frac{1}{2}$, is clearly visible. Extracted from Ref. [143].	34
3.7	Atmospheric neutrino flux at the Super-Kamiokande site, averaged over all directions and over one year. Extracted from Ref. [144].	35

3.8	Super-Kamiokande neutrino events as a function of the zenith angle. The blue (red) lines shown the expectations without (with) $\nu_\mu \rightarrow \nu_\tau$ neutrino oscillations. The data points show a clear preference for ν_μ disappearance. The events are classified as “Sub-GeV” (“Multi-GeV”) if their deposited energy was < 1.33 GeV (> 1.33 GeV). The third column corresponds to up-going muons, generated by neutrino interactions with the surrounding rock, and classified as “UpStop” or “UpThrough” depending on whether the muons stopped inside the detector or not, respectively. The latter are generated by much more energetic neutrinos. Figure from Ref. [72].	37
3.9	Allowed regions of $ \Delta m^2 $ and $\sin^2 \theta$ that best describe atmospheric data at 90% CL, 95% CL, 99% CL and 3σ . Figure courtesy of M. C. Gonzalez-García and M. Maltoni.	38
3.10	Reactor $\bar{\nu}_e$ spectrum, as measured by the Daya Bay collaboration [150].	38
3.11	Ratio between the observed number of $\bar{\nu}_e$ events and the expectation without oscillations, as a function of $L_0/E_{\bar{\nu}_e}$. L_0 is the flux-weighted average distance to nuclear reactors, and $E_{\bar{\nu}_e}$ the antineutrino energy. The blue line corresponds to the expectation from oscillations. Figure from Ref. [34].	39
3.12	Energy spectra of events at the RENO and Daya Bay far detectors. The lower panels show the ratio among observed and predicted number of events, as well as the prediction from neutrino oscillations. The energy is given in terms of the prompt event energy $\simeq E_{\bar{\nu}_e} - 0.78$ MeV, with $E_{\bar{\nu}_e}$ the antineutrino energy.	40
3.13	Allowed region of $ \Delta m^2 $ and $\sin^2 \theta$ at 95% CL for each relevant medium baseline reactor experiment. Figure courtesy of M. C. Gonzalez-García and M. Maltoni.	41
3.14	Neutrino energy (left) and flux (left) as a function of the parent pion energy at different angles θ with respect to the parent beam. Placing the neutrino detector off-axis ($\theta \neq 0$) significantly reduces the neutrino energy spread for a non-monochromatic parent beam. The neutrino flux is also reduced, though.	42
3.15	Muon neutrino flux at the T2K experiment. OA refers to the off-axis angle θ . Extracted from Ref. [159].	42
3.16	Energy spectra of events at the K2K and MINOS detectors, along with the expectations, in solid and dark respectively. For K2K, the dashed line is the expected spectrum without oscillations <i>normalised to the observed number of events</i> . For MINOS, the clear line shows the expected number of events without oscillations.	43
3.17	Allowed regions, in colour, of $ \Delta m^2 $ and $\tan^2 \theta$ that best describe K2K (left) and MINOS (right) data at 90% CL, 95% CL, 99% CL and 3σ . For comparison, the corresponding regions from atmospheric neutrino data are also shown in lines at the same CL. Figure from Ref. [100].	44
3.18	T2K results as of January 2019. The ν_e appearance results are separated as CCQE or CC1 π depending on whether the final state contains no visible pions or a single visible pion. Extracted from Ref. [96].	45
3.19	NO ν A results as of June 2019. The appearance events are classified in three bins from lowest to highest purity: “Peripheral”, “Low PID”, and “High PID”. Extracted from Ref. [97].	46

- 4.1 Global 3ν oscillation analysis. Each panel shows the two-dimensional projection of the allowed six-dimensional region after marginalization with respect to the undisplayed parameters. The different contours correspond to 1σ , 90%, 2σ , 99%, 3σ CL (2 dof). The normalization of reactor fluxes is left free and data from short baseline reactor experiments are included as explained in the text. Note that as atmospheric mass-squared splitting we use Δm_{31}^2 for NO and Δm_{32}^2 for IO. The regions in the four lower panels are obtained from $\Delta\chi^2$ minimised with respect to the mass ordering. 52
- 4.2 Global 3ν oscillation analysis. The red (blue) curves correspond to Normal (Inverted) Ordering. The normalization of reactor fluxes is left free and data from short baseline reactor experiments are included. Note that as atmospheric mass-squared splitting we use Δm_{31}^2 for NO and Δm_{32}^2 for IO. 53
- 4.3 Dependence of the global $\Delta\chi^2$ function on the Jarlskog invariant. The red (blue) curves are for NO (IO). 55
- 4.4 Leptonic unitarity triangle for the first and third columns of the mixing matrix. After scaling and rotating the triangle so that two of its vertices always coincide with $(0,0)$ and $(1,0)$ we plot the 1σ , 90%, 2σ , 99%, 3σ CL (2 dof) allowed regions of the third vertex. Note that in the construction of the triangle the unitarity of the U^{lep} matrix is always explicitly imposed. The regions for both orderings are defined with respect to the common global minimum which is in NO. 56
- 4.5 Left: Allowed parameter regions (at 1σ , 90%, 2σ , 99% and 3σ CL for 2 dof) from the combined analysis of solar data for GS98 model (full regions with best fit marked by black star) and AGSS09 model (dashed void contours with best fit marked by a white dot), and for the analysis of KamLAND data (solid green contours with best fit marked by a green star) for fixed $\theta_{13} = 8.5^\circ$. Right: $\Delta\chi^2$ dependence on Δm_{21}^2 for the same three analyses after marginalizing over θ_{12} . . . 57
- 4.6 Determination of $\Delta m_{3\ell}^2$ at 1σ and 2σ (2 dof), where $\ell = 1$ for NO (upper panels) and $\ell = 2$ for IO (lower panels). The left panels show regions in the $(\theta_{23}, \Delta m_{3\ell}^2)$ plane using both appearance and disappearance data from MINOS (green line), T2K (red lines), NO ν A (light blue lines), as well as IceCube/DeepCore (orange lines) and the combination of them (colored regions). In these panels the constraint on θ_{13} from the global fit (which is dominated by the reactor data) is imposed as a Gaussian bias. The right panels show regions in the $(\theta_{13}, \Delta m_{3\ell}^2)$ plane using only Daya-Bay (black lines), reactor data without Daya-Bay (violet lines), and their combination (colored regions). In all panels solar and KamLAND data are included to constrain Δm_{21}^2 and θ_{12} . Contours are defined with respect to the global minimum of the two orderings. 58
- 4.7 $\Delta m_{3\ell}^2$ determination from LBL accelerator experiments, reactor experiments and their combination. Left (right) panels are for IO (NO). The upper panels show the 1-dim $\Delta\chi^2$ from LBL accelerator experiments after constraining *only* θ_{13} from reactor experiments (this is, marginalizing Eq. (4.3) with respect to θ_{23} and δ_{CP}). For each experiment $\Delta\chi^2$ is defined with respect to the global minimum of the two orderings. The lower panels show the corresponding determination when the full information of LBL and reactor experiments is used in the combination (this is, marginalizing Eq. (4.4) with respect to θ_{23} and δ_{CP}). 60

- 4.8 θ_{23} determination from LBL, reactor and their combination. Left (right) panels are for IO (NO). The upper panels show the 1-dim $\Delta\chi^2$ from LBL experiments after constraining *only* θ_{13} from reactor experiments (this is, marginalizing Eq. (4.3) with respect to $\Delta m_{3\ell}^2$ and δ_{CP}). For each experiment $\Delta\chi^2$ is defined with respect to the global minimum of the two orderings. The lower panels show the corresponding determination when the full information of LBL accelerator and reactor experiments is used in the combination (this is, marginalizing Eq. (4.4) with respect to $\Delta m_{3\ell}^2$ and δ_{CP}). 61
- 4.9 δ_{CP} determination from LBL, reactor and their combination. Left (right) panels are for IO (NO). The upper panels show the 1-dim $\Delta\chi^2$ from LBL experiments after constraining *only* θ_{13} from reactor experiments (this is, marginalizing Eq. (4.3) with respect to $\Delta m_{3\ell}^2$ and θ_{23}). For each experiment $\Delta\chi^2$ is defined with respect to the global minimum of the two orderings. The lower panels show the corresponding determination when the full information of LBL accelerator and reactor experiments is used in the combination (this is, marginalizing Eq. (4.4) with respect to $\Delta m_{3\ell}^2$ and θ_{23}). 62
- 4.10 Impact of our re-analysis of Super-Kamiokande atmospheric neutrino data [195] (70 bins in energy and zenith angle) on the determination of $\sin^2\theta_{23}$, δ_{CP} , and the mass ordering. The impact on all other parameters is negligible. 64
- 4.11 Allowed regions from the global data at 1σ , 90%, 2σ , 99% and 3σ CL (2 dof). We show projections onto different planes with δ_{CP} on the vertical axis after minimizing with respect to all undisplayed parameters. The lower (upper) panels correspond to IO (NO). Contour regions are derived with respect to the global minimum which occurs for NO and is indicated by a star. The local minimum for IO is shown by a black dot. 67
- 4.12 68%, 95% and 99% confidence levels (broken curves) for the test statistics (4.6) along with its value (solid curves) for the combination of T2K, NO ν A, MINOS and reactor data. The value of $\sin^2\theta_{23}$ given in each panel corresponds to the assumed true value chosen to generate the pseudo-experiments and for all panels we take $\Delta m_{3\ell, \text{true}}^2 = -2.53 \times 10^{-3} \text{ eV}^2$ for IO and $+2.54 \times 10^{-3} \text{ eV}^2$ for NO. The solid horizontal lines represent the 68%, 95% and 99% CL predictions from Wilks' theorem. 69
- 4.13 68%, 95% and 99% confidence levels (broken curves) for the test statistics (4.7) along with its value (solid curves) for the combination of T2K, NO ν A, MINOS and reactor data. The value of δ_{CP} above each plot corresponds to the assumed true value chosen to generate the pseudo-experiments and for all panels we take $\Delta m_{3\ell, \text{true}}^2 = -2.53 \times 10^{-3} \text{ eV}^2$ for IO and $+2.54 \times 10^{-3} \text{ eV}^2$ for NO. The solid horizontal lines represent the 68%, 95% and 99% CL predictions from Wilks' theorem. 71
- 4.14 δ_{CP} determination as of November 2017. Left (right) panels are for IO (NO). The upper panels constrain only θ_{13} from reactor experiments, whereas the lower panels include the full information from them: see Figura 4.9 and its description in the text for the difference among both procedures. 76
- 4.15 Updated NO ν A results on δ_{CP} and global combination as of January 2018. . . . 77
- 4.16 Updated NO ν A and T2K $\bar{\nu}_e$ appearance results and global combination projection on δ_{CP} as of November 2018. 79
- 4.17 Updated NO ν A and T2K $\bar{\nu}_e$ appearance results and global combination projection on δ_{CP} as of July 2019. 80

- 4.18 Global 3ν oscillation analysis. Each panel shows the two-dimensional projection of the allowed six-dimensional region after minimization with respect to the undisplayed parameters. The regions in the four lower panels are obtained from $\Delta\chi^2$ minimised with respect to the mass ordering. The different contours correspond to 1σ , 90%, 2σ , 99%, 3σ CL (2 dof). Coloured regions (black contour curves) are without (with) adding the Super-Kamiokande atmospheric results, provided as a $\Delta\chi^2$ table by the collaboration. Note that as atmospheric mass-squared splitting we use Δm_{31}^2 for NO and Δm_{32}^2 for IO. 81
- 4.19 Global 3ν oscillation analysis. We show $\Delta\chi^2$ profiles minimised with respect to all undisplayed parameters. The red (blue) curves correspond to Normal (Inverted) Ordering. Solid (dashed) curves are without (with) adding the Super-Kamiokande atmospheric results, provided as a $\Delta\chi^2$ table by the collaboration. Note that as atmospheric mass-squared splitting we use Δm_{31}^2 for NO and Δm_{32}^2 for IO. . . . 82
- 6.1 Two-dimensional projections of the 1σ , 90%, 2σ , 99% and 3σ CL (2 dof) allowed regions from the analysis of solar and KamLAND data in the presence of non-standard matter potential for the oscillation parameters $(\theta_{12}, \Delta m_{21}^2)$ after marginalizing over the NSI parameters and for θ_{13} fixed to $\sin^2\theta_{13} = 0.022$. The best-fit point is marked with a star. The results are shown for fixed values of the NSI quark coupling parameter η . For comparison the corresponding allowed regions for the analysis in terms of 3ν oscillations without NSI are shown as black void contours. Note that, as a consequence of the periodicity of η , the regions in the first ($\eta = -90^\circ$) and last ($\eta = +90^\circ$) panels are identical. 98
- 6.2 Two-dimensional projections of the 1σ , 90%, 2σ , 99% and 3σ CL (2 dof) allowed regions from the analysis of solar and KamLAND data in the presence of non-standard matter potential for the matter potential parameters $(\varepsilon_D, \varepsilon_N)$, for $\sin^2\theta_{13} = 0.022$ and after marginalizing over the oscillation parameters. The best-fit point is marked with a star. The results are shown for fixed values of the NSI quark coupling parameter η . The panels with a scale factor “[$\times N$]” in their lower-left corner have been “zoomed-out” by such factor with respect to the standard axis ranges, hence the grey square drawn in each panel always corresponds to $\max(|\varepsilon_D|, |\varepsilon_N|) = 2$ and has the same size in all the panels. For illustration we also show as shaded green areas the 90% and 3σ CL allowed regions from the analysis of the atmospheric and LBL data. Note that, as a consequence of the periodicity of η , the regions in the first ($\eta = -90^\circ$) and last ($\eta = +90^\circ$) panels are identical up to an overall sign flip. 99
- 6.3 90% and 3σ CL (1 dof) allowed ranges from the analysis of solar and KamLAND data in the presence of NSI, for the four relevant parameters (the matter potential parameters ε_D and ε_N as well as the oscillation parameters Δm_{21}^2 and $\sin^2\theta_{12}$) as a function of the NSI quark coupling parameter η , for $\sin^2\theta_{13} = 0.022$. In each panel the three undisplayed parameters have been marginalised. 101
- 6.4 Left: $\chi_{\text{LMA}}^2(\eta) - \chi_{\text{no-NSI}}^2$ (full lines) and $\chi_{\text{LMA-D}}^2(\eta) - \chi_{\text{no-NSI}}^2$ (dashed lines) for the analysis of different data combinations (as labeled in the figure) as a function of the NSI quark coupling parameter η . Right: $\chi_{\text{LMA-D}}^2(\eta) - \chi_{\text{LMA}}^2(\eta)$ as a function of η . See text for details. 102

- 6.5 Two-dimensional projections of the allowed regions onto the matter potential parameters ε_{\oplus} , φ_{12} , and φ_{13} after marginalization with respect to the undisplayed parameters. The large green regions correspond to the analysis of atmospheric, LBL-CPC, and medium baseline reactor data at 90% and 3σ CL. For comparison we show in yellow the corresponding results when omitting IceCube and reactor data. The solid coloured regions show the 1σ , 90%, 2σ , 99% and 3σ CL allowed regions once solar and KamLAND data are included. The best-fit point is marked with a star. 104
- 6.6 Two-dimensional projections of the allowed regions onto different vacuum parameters after marginalizing over the matter potential parameters (including η) and the undisplayed oscillation parameters. The solid coloured regions correspond to the global analysis of all oscillation data, and show the 1σ , 90%, 2σ , 99% and 3σ CL allowed regions; the best-fit point is marked with a star. The black void regions correspond to the analysis with the standard matter potential (i.e., without NSI) and its best-fit point is marked with an empty dot. For comparison, in the left panel we show in red the 90% and 3σ allowed regions including only solar and KamLAND results, while in the right panels we show in green the 90% and 3σ allowed regions excluding solar and KamLAND data, and in yellow the corresponding ones excluding also IceCube and reactor data. 106
- 6.7 90%, and 3σ CL (1 dof) allowed ranges for the NSI couplings from the global oscillation analysis in the presence of non-standard matter potential as a function of the NSI quark coupling parameter η . In each panel the undisplayed parameters have been marginalised. On the left panels the oscillation parameters have been marginalised within the LMA region while the right panels corresponds to LMA-D solutions. The ranges are defined with respect to the minimum for each η 109
- 6.8 Dependence of the $\Delta\chi^2$ function on the effective NSI parameters relevant for matter effects in LBL experiments with arbitrary values of η , from the global analysis of solar, atmospheric, LBL-CPC and reactor data. The upper (lower) panels correspond to solutions within the LMA (LMA-D) subset of parameter space. 110
- 6.9 Global analysis of solar, atmospheric, reactor and accelerator oscillation experiments, in the LIGHT side of the parameter space and for Normal Ordering of the neutrino states. The panels show the two-dimensional projections of the allowed parameter space after marginalization with respect to the undisplayed parameters. The different contours correspond to the allowed regions at 1σ , 2σ and 3σ for 2 degrees of freedom. Note that as atmospheric mass-squared splitting we use $\Delta m_{3\ell}^2 = \Delta m_{31}^2$ for NO. Also shown are the one-dimensional projections as a function of each parameter. For comparison we show as dotted lines the corresponding one-dimensional dependence for the same analysis assuming only standard 3ν oscillation (i.e., setting all the NSI parameters to zero). 115
- 6.10 Same as Fig. 6.10 but for DARK-IO solution. In this case $\Delta m_{3\ell}^2 = \Delta m_{32}^2 < 0$ and we plot its absolute value. The regions and one-dimensional projections are defined with respect to the *local* minimum in this sector of the parameter space. 116
- 6.11 $\Delta\chi_{\text{GLOB}}^2$ as a function of δ_{CP} after marginalizing over all the undisplayed parameters, for different combination of experiments. We include SOLAR + KamLAND + ATM + MBL-REA + MINOS to which we add T2K (left), NO ν A (center) and T2K + NO ν A (right). The different curves are obtained by marginalizing within different regions of the parameter space, as detailed in the legend. See text for details. 117

6.12	$\Delta\chi_{\text{GLOB}}^2$ as a function of $\sin^2\theta_{23}$ after marginalizing over all other parameters for the GLOBAL combination of oscillation experiments. The different curves correspond to marginalization within the different regions of the parameter space, as detailed in the legend. See text for details.	119
7.1	Schematic representation of coherent neutrino-nucleus elastic scattering. Here, Q is the momentum transfer, and T the recoil energy of the hit nucleus.	123
7.2	Neutrino flux spectra expected from π^+ decay at rest, in arbitrary units (a.u.), as a function of the neutrino energy in MeV. The three components of the flux are shown separately as indicated by the legend. The distributions have been normalised to one.	124
7.3	QF parametrizations used in our analysis of the COHERENT data. The left panel shows the curve provided in Ref. [307] (solid curve), while the right panel shows the corresponding result obtained for our fit to the calibration data of the Duke (TUNL) group [295], provided as part of the data release [300]. In both panels, the constant QF used in Ref. [295] is also shown for comparison. The three parametrizations are shown with a shaded band to indicate the values allowed at the 1σ CL in each case. For illustration, the vertical shaded area indicates approximately the range of nuclear recoil energies that enters the signal region used in the fit (the exact range varies with the nuisance parameters, and the exact QF parametrization used).	127
7.4	Residual events per bin obtained after subtracting C and AC data for the beam-ON sample, after being projected onto the PE (left panels) and time (right panels) axes and using the same cuts in PE and time as those applied to Fig. 3 in Ref. [295]. The observed data points are indicated with statistical error bars, as in Ref. [295]. In the upper panels the shaded histograms show the predicted event rates in the SM using the QF and nuclear form factor from Ref. [300]. In the middle panels they correspond to the predictions with the QF from the Chicago group (QF-C) in Ref. [307] and the nuclear form factor (FF) from Ref. [302, 303]. The lower panels have been obtained with the same form factor, but changing the QF to match the Duke (TUNL) measurements in Ref. [295] (QF-D). In all panels the prompt neutron background prediction is also shown for completeness. All the event histograms shown in this figure correspond to the SM prediction.	129
7.5	Total AC counts per bin, compared to the results of the exponential fit employed in Ref. [300] and described in Sec. 7.1.2 used to model the steady-state background. No cuts on the observed number of PE have been applied to this figure.	130
7.6	Total events per bin in the beam-ON C sample, after being projected onto the time (left) and PE (right) and imposing the cuts $5 < \text{PE} \leq 30$ and $t < 6 \mu\text{s}$. The observed data points are indicated with statistical error bars as in Fig. 7.4. The dark histograms show the expected background events for the steady-state contribution only. The upper panels have been obtained assuming that the time dependence of the background follows an exponential model, as in Ref. [300], while the lower panels have been obtained using our model (which follows the time dependence of the AC events, see text for details). The light histograms show the predicted total number of events, after adding all signal and background contributions. To ease the comparison among different panels, in this figure the signal has been computed in all cases using the same form factor and QF as in the data release [300]. All histograms shown correspond to the SM predicted event rates.	131

- 7.7 Comparison of our χ^2 for the COHERENT timing and energy data as a function of the number of signal CE ν NS events under the same assumptions on the background, systematics and expected time and energy dependence of signal, compared to that provided by COHERENT in figure S13 of Ref. [295]. For comparison, the vertical lines indicate the predicted event rates in the SM (with no systematic uncertainties), for different choices of QF and form factor used: dashed red corresponds to the prediction provided in the data release of 173 events [300], while solid green indicates our prediction using the QF from Ref. [307] (left panel in Fig. 7.3) and nuclear form factor of [302, 303]. 134
- 7.8 2σ allowed regions for the flavour-dependent weak charges for a variety of fits to COHERENT data as labeled in the figure. In all cases shown in the left panel, the QF, nuclear form factor and background assumptions are those employed in the data release [300]. On the right panel we show the dependence on the steady background modelling, nuclear form factor, and QF. The vertical lines indicate the SM value $Q_e^2 = Q_\mu^2 = 1353.5$. The coloured dots and the red cross mark the position of the best-fit for the various cases. 135
- 7.9 2σ allowed regions for the flavour-diagonal NSI coefficients $\varepsilon_{\alpha\beta}^{\text{coh}}$ (assuming zero non-diagonal couplings) for a variety of fits to COHERENT data as labelled in the figure. In all cases shown in the left panel, the QF, nuclear form factor and background assumptions are those employed in the data release [300]. On the right panel we show the dependence on the assumptions for steady background modelling, nuclear form factor, and QF. For simplicity, in this figure we set all off-diagonal NSI parameters to zero, but it should be kept in mind that the results of our global analysis presented in Sec. 7.2.1 have been obtained allowing all operators simultaneously in the fit. 137
- 7.10 Left: $\chi_{\text{LMA}}^2(\eta) - \chi_{\text{no-NSI}}^2$ (full lines) and $\chi_{\text{LMA-D}}^2(\eta) - \chi_{\text{no-NSI}}^2$ (dashed lines) for the analysis of different data combinations (as labeled in the figure) as a function of the NSI quark coupling parameter η . Right: $\chi_{\text{dark}}^2 - \chi_{\text{light}}^2 \equiv \chi_{\text{LMA-D}}^2(\eta) - \chi_{\text{LMA}}^2(\eta)$ as a function of η . See text for details. 140
- 7.11 Dependence of the $\Delta\chi_{\text{global}}^2$ function on the NSI couplings with up quarks (upper row), down quark (central row) and, protons (lower row) for the global analysis of oscillation and COHERENT data. In each panel χ_{global}^2 is marginalised with respect to the other five NSI couplings not shown and with respect to the oscillation parameters for the LMA (solid) and LMA-D (dashed) solutions. The different curves correspond to the different variants of the COHERENT analysis implemented in this chapter: total rate (black), t+E Data Release (red), t+E with QF-C (blue), and t+E with QF-D (brown); see text for details. 142
- 7.12 Global analysis of solar, atmospheric, reactor and accelerator oscillation experiments plus COHERENT, in the LIGHT side of the parameter space and for Normal Ordering of the neutrino states. The panels show the two-dimensional projections of the allowed parameter space after marginalization with respect to the undisplayed parameters. The different contours correspond to the allowed regions at 1σ , 2σ and 3σ for 2 degrees of freedom. Note that as atmospheric mass-squared splitting we use $\Delta m_{3\ell}^2 = \Delta m_{31}^2$ for NO. Also shown are the one-dimensional projections as a function of each parameter. For comparison we show as dotted lines the corresponding one-dimensional dependence for the same analysis assuming only standard 3ν oscillation (i.e., setting all the NSI parameters to zero). 145

- 7.13 Same as Fig. 6.10 but for DARK-IO solution. In this case $\Delta m_{3\ell}^2 = \Delta m_{32}^2 < 0$ and we plot its absolute value. The regions and one-dimensional projections are defined with respect to the *local* minimum in this sector of the parameter space. 146
- 7.14 $\Delta\chi^2$ as a function of δ_{CP} after marginalizing over all the undisplayed parameters, for different combination of experiments. We include SOLAR + KamLAND + ATM + MBL-REA + MINOS + COHERENT to which we add T2K (left), NO ν A (center) and T2K + NO ν A (right). The different curves are obtained by marginalizing within different regions of the parameter space, as detailed in the legend. See Figura 6.11 and the text around it for details. 147
- 7.15 $\Delta\chi^2$ as a function of $\sin^2\theta_{23}$ after marginalizing over all other parameters for the global combination of oscillation experiments + COHERENT. The different curves correspond to marginalization within the different regions of the parameter space, as detailed in the legend. See Figura 6.12 and the text around it for details. 147
- 7.16 (Source: ESS) Neutron production from existing and planned spallation sources. The nominal SNS power is 1 MW at proton energy 1 GeV, with a plan to reach 2 MW by 2026. The ESS power will be 5 MW at 2 GeV circa 2023, with the ability to further upgrade. Differences in the duration of the protons-on-target (POT) pulse are visible in the figure. The ESS will generate an increase in neutron brightness by a factor 30-100 with respect to previous spallation sources, and an order of magnitude larger neutrino yield than the SNS. 149
- 7.17 Expected allowed regions in the $(\epsilon_{ee}^u, \epsilon_{\mu\mu}^u)$ plane at the 90% confidence level (C.L.) for two degrees of freedom (d.o.f.) after three years of running. The different regions correspond to the expected results for the different detectors listed in Table 7.3, as indicated by the legend. In all cases, the simulated data has been generated for the SM (that is, setting all the operator coefficients to zero), and the results are then fitted assuming NSI. For simplicity, the rest of the NSI parameters not shown in the figure have been assumed to be zero. For comparison, the dashed lines show the allowed regions at 90% CL in this plane, as obtained in Ref. [249] from an analysis of current data from the COHERENT experiment [295], see text for details. 150
- 7.18 Expected event rates per bin in nuclear recoil energy, for the CsI detector. The contributions from the scattering of the different beam components are shown separately by the shaded histograms, as indicated by the legend. For comparison, the square root of the number of background events in each bin is also shown by the dashed histogram lines. The vertical dotted line indicates the maximum recoil energy allowed by a neutrino with energy $E_\nu = 29.8$ MeV, that is, the energy of the monochromatic prompt ν_μ flux. 152
- 7.19 Expected allowed regions in the $(\epsilon_{ee}^u, \epsilon_{\mu\mu}^u)$ plane at the 90% C.L. for 2 d.o.f, for the gas TPC detector operating with two different nuclei (separate runs, each of them for 3 years), as well as for a configuration where the detector is filled with each of the two gases during half of the total data taking period (1.5 years running with ^{132}Xe , 1.5 years with ^{40}Ar). In all cases, the simulated data has been generated for the SM and the results are then fitted assuming NSI. For simplicity, the values for the rest of NSI parameters not shown in this figure have been set to zero. . . 153

List of Tables

2.1	Multiplets and irreducible representations in which SM fermions fall. For the $SU(3)$ and $SU(2)$ groups, 1, 2 and 3 denote the singlet, doublet and triplet representations. For $U(1)$, a subindex Y , known as the hypercharge, indicates that the fermion f transforms as $f \rightarrow e^{iY\theta} f$, where θ is a real number. The different fermions are also known as <i>flavours</i>	10
3.1	Value of $\Delta\chi^2_\lambda$ corresponding to a given confidence level (CL) for different degrees of freedom (d.o.f.) of the underlying χ^2 distribution.	48
4.1	Three-flavour oscillation parameters from our fit to global data after the NOW 2016 and ICHEP-2016 conferences. The numbers in the 1st (2nd) column are obtained assuming NO (IO), i.e., relative to the respective local minimum, whereas in the 3rd column we minimise also with respect to the ordering. Note that $\Delta m^2_{3\ell} \equiv \Delta m^2_{31} > 0$ for NO and $\Delta m^2_{3\ell} \equiv \Delta m^2_{32} < 0$ for IO.	54
4.2	Three-flavour oscillation parameters from our fit to global data, including also our re-analysis of SK1–4 (4581 days) atmospheric data. The numbers in the 1st (2nd) column are obtained assuming NO (IO), i.e., relative to the respective local minimum, whereas in the 3rd column we minimise also with respect to the ordering. The omitted parameters are identical to Tab. 4.1.	64
4.3	Confidence level with which CP conservation ($\delta_{\text{CP}} = 0, 180^\circ$) is rejected (third column) and 90% and 95% confidence intervals for δ_{CP} (fourth and fifth column) for different sets of true values of the parameters and in the Gaussian approximation. Confidence intervals for δ_{CP} as well as the CL for CP conservation are defined for both orderings with respect to the global minimum (which happens for NO).	70
4.4	CL for the rejection of maximal θ_{23} mixing (third column), and 90% and 95% CL intervals for $\sin^2 \theta_{23}$ for different sets of true parameter values and in the Gaussian approximation (last row).	71
4.5	CL for the rejection of various combinations of mass ordering and θ_{23} octant with respect to the global best fit (which happens for NO and 1st octant). We quote the CL of the local minima for each ordering/octant combination, assuming three example values for the true value of δ_{CP} as well as for the Gaussian approximation (last row).	72

4.6	Expected and observed number of ν_e and $\bar{\nu}_e$ events in T2K, as of late 2016, for different values of δ_{CP} . The results are shown for NO, which increases the amount of ν_e events and decreases the amount of $\bar{\nu}_e$ events as the data indicates. The other mixing parameters are set to $\Delta m_{21}^2 = 7.53 \times 10^{-5} \text{ eV}^2$, $\sin^2 2\theta_{12} = 0.846$, $\sin^2 2\theta_{13} = 0.085$, $\Delta m_{32}^2 = 2.509 \times 10^{-3} \text{ eV}^2$ and $\sin^2 2\theta_{23} = 0.528$. Table adapted from Ref. [204].	74
4.7	Expected and observed number of ν_e and $\bar{\nu}_e$ events in T2K, as of late 2017, for different values of δ_{CP} . The results are shown for NO, which increases the amount of ν_e events and decreases the amount of $\bar{\nu}_e$ events as the data indicates. ν_e (CC1 π) refers to the channel where an electron and a single pion are detected in the final state. The other mixing parameters are set to $\Delta m_{21}^2 = 7.53 \times 10^{-5} \text{ eV}^2$, $\sin^2 \theta_{12} = 0.304$, $\sin^2 \theta_{13} = 0.0219$, $\Delta m_{32}^2 = 2.509 \times 10^{-3} \text{ eV}^2$ and $\sin^2 2\theta_{23} = 0.528$. Table adapted from Ref. [200].	75
6.1	2σ allowed ranges for the NSI couplings $\varepsilon_{\alpha\beta}^u$, $\varepsilon_{\alpha\beta}^d$ and $\varepsilon_{\alpha\beta}^p$ as obtained from the global analysis of oscillation data. The results are obtained after marginalizing over oscillation and the other matter potential parameters either within the LMA only and within both LMA and LMA-D subspaces respectively (this second case is denoted as LMA \oplus LMA-D).	108
7.1	Systematic uncertainties considered in the fit on acceptance efficiency parameters (Eq. (7.12)), normalisation of the signal and background contributions, and the QF. The steady-state normalisation uncertainty includes the statistical error of the sample (AC data). The quoted uncertainties on the QF also includes the error on the light yield (0.14%), which is however subdominant. For details on the QF parametrization, see Sec. 7.1.2.	133
7.2	2σ allowed ranges for the NSI couplings $\varepsilon_{\alpha\beta}^u$, $\varepsilon_{\alpha\beta}^d$ and $\varepsilon_{\alpha\beta}^p$ as obtained from the global analysis of oscillation plus COHERENT data. See text for details.	143
7.3	Summary of detector properties for CE ν NS at the ESS. We show the target nuclei and mass of different detectors, the steady-state background, the minimum detectable nuclear recoil energy E_{th} , the relative energy resolution $\Delta E/E$ at E_{th} , the maximum detectable nuclear recoil energy E_{max} , and the amount of CE ν NS events per year above threshold for a detector at 20 m from the source. Backgrounds listed do not include a 4×10^{-2} reduction by the pulsed character of the ESS beam. The background for bubble chambers is integrated above nucleation threshold (in counts per kg and day), and only the total event rate is used in the simulations. Other backgrounds are given in counts per keV, kg and day (ckkd). We conservatively adopt the background at E_{th} , which is typically maximal, for all higher energies. The relative energy resolution is assumed to depend on the nuclear recoil energy as $\propto \sqrt{E}$	149
7.4	Main properties of the nuclei for the different target nuclei considered in this section. The different columns indicate the isotope considered, together with the number of protons and neutrons, the ratio between them r , and the value of the nuclear mass in atomic mass units (a.m.u.). For the detectors using CsI and C ₃ F ₈ we take the weighted average between the two elements in the molecule.	151

References

- [1] I. Esteban, M. C. Gonzalez-Garcia, M. Maltoni, I. Martinez-Soler, and T. Schwetz, “Updated fit to three neutrino mixing: exploring the accelerator-reactor complementarity”, *JHEP* **01** (2017) 087, [arXiv:1611.01514 \[hep-ph\]](#).
- [2] I. Esteban, M. C. Gonzalez-Garcia, M. Maltoni, I. Martinez-Soler, and J. Salvado, “Updated Constraints on Non-Standard Interactions from Global Analysis of Oscillation Data”, *JHEP* **08** (2018) 180, [arXiv:1805.04530 \[hep-ph\]](#).
- [3] I. Esteban, M. C. Gonzalez-Garcia, A. Hernandez-Cabezudo, M. Maltoni, and T. Schwetz, “Global analysis of three-flavour neutrino oscillations: synergies and tensions in the determination of θ_{23} , δ_{CP} , and the mass ordering”, *JHEP* **01** (2019) 106, [arXiv:1811.05487 \[hep-ph\]](#).
- [4] I. Esteban, M. C. Gonzalez-Garcia, and M. Maltoni, “On the Determination of Leptonic CP Violation and Neutrino Mass Ordering in Presence of Non-Standard Interactions: Present Status”, *JHEP* **06** (2019) 055, [arXiv:1905.05203 \[hep-ph\]](#).
- [5] P. Coloma, I. Esteban, M. C. Gonzalez-Garcia, and M. Maltoni, “Improved global fit to Non-Standard neutrino Interactions using COHERENT energy and timing data”, *JHEP* **02** (2020) 023, [arXiv:1911.09109 \[hep-ph\]](#).
- [6] D. Baxter *et al.*, “Coherent Elastic Neutrino-Nucleus Scattering at the European Spallation Source”, *JHEP* **02** (2020) 123, [arXiv:1911.00762 \[physics.ins-det\]](#).
- [7] W. Pauli, “Pauli letter collection: letter to Lise Meitner.” Typed copy, Dec., 1930. <http://cds.cern.ch/record/83282>.
- [8] H. Bethe and R. Peierls, “The ‘neutrino’”, *Nature* **133** (1934) 532.
- [9] C. L. Cowan, F. Reines, F. B. Harrison, H. W. Kruse, and A. D. McGuire, “Detection of the free neutrino: A Confirmation”, *Science* **124** (1956) 103–104.
- [10] KATRIN Collaboration, M. Aker *et al.*, “An improved upper limit on the neutrino mass from a direct kinematic method by KATRIN”, *Phys. Rev. Lett.* **123** no. 22, (2019) 221802, [arXiv:1909.06048 \[hep-ex\]](#).
- [11] G. Danby, J. M. Gaillard, K. A. Goulianos, L. M. Lederman, N. B. Mistry, M. Schwartz, and J. Steinberger, “Observation of High-Energy Neutrino Reactions and the Existence of Two Kinds of Neutrinos”, *Phys. Rev. Lett.* **9** (1962) 36–44.
- [12] SNO Collaboration, Q. R. Ahmad *et al.*, “Direct evidence for neutrino flavor transformation from neutral current interactions in the Sudbury Neutrino Observatory”, *Phys. Rev. Lett.* **89** (2002) 011301, [arXiv:nucl-ex/0204008 \[nucl-ex\]](#).

- [13] SNO Collaboration, Q. R. Ahmad *et al.*, “Measurement of day and night neutrino energy spectra at SNO and constraints on neutrino mixing parameters”, *Phys. Rev. Lett.* **89** (2002) 011302, [arXiv:nucl-ex/0204009](#) [nucl-ex].
- [14] SNO Collaboration, S. N. Ahmed *et al.*, “Measurement of the total active B-8 solar neutrino flux at the Sudbury Neutrino Observatory with enhanced neutral current sensitivity”, *Phys. Rev. Lett.* **92** (2004) 181301, [arXiv:nucl-ex/0309004](#) [nucl-ex].
- [15] SNO Collaboration, B. Aharmim *et al.*, “Electron energy spectra, fluxes, and day-night asymmetries of B-8 solar neutrinos from measurements with NaCl dissolved in the heavy-water detector at the Sudbury Neutrino Observatory”, *Phys. Rev.* **C72** (2005) 055502, [arXiv:nucl-ex/0502021](#) [nucl-ex].
- [16] R. Becker-Szendy *et al.*, “The Electron-neutrino and muon-neutrino content of the atmospheric flux”, *Phys. Rev.* **D46** (1992) 3720–3724.
- [17] Kamiokande Collaboration, Y. Fukuda *et al.*, “Atmospheric muon-neutrino / electron-neutrino ratio in the multiGeV energy range”, *Phys. Lett.* **B335** (1994) 237–245.
- [18] Super-Kamiokande Collaboration, Y. Fukuda *et al.*, “Evidence for oscillation of atmospheric neutrinos”, *Phys. Rev. Lett.* **81** (1998) 1562–1567, [arXiv:hep-ex/9807003](#) [hep-ex].
- [19] A. G. Cohen and A. De Rujula, “Scars on the Cosmic Background Radiation?”, *Astrophys. J. Lett.* **496** no. 2, (Apr, 1998) L63–L65, [arXiv:astro-ph/9709132](#) [astro-ph].
- [20] W. H. Kinney, E. W. Kolb, and M. S. Turner, “Ribbons on the CBR sky: A Powerful test of a baryon symmetric universe”, *Phys. Rev. Lett.* **79** (1997) 2620–2623, [arXiv:astro-ph/9704070](#) [astro-ph].
- [21] A. D. Sakharov, “Violation of CP Invariance, C asymmetry, and baryon asymmetry of the universe”, *Pisma Zh. Eksp. Teor. Fiz.* **5** (1967) 32–35. [JETP Lett.5,24(1967); Sov. Phys. Usp.34,no.5,392(1991); Usp. Fiz. Nauk161,no.5,61(1991)].
- [22] J. Lesgourgues, G. Mangano, G. Miele, and S. Pastor, *Neutrino Cosmology*. Cambridge University Press, 2013.
- [23] B. T. Cleveland, T. Daily, R. Davis, Jr., J. R. Distel, K. Lande, C. K. Lee, P. S. Wildenhain, and J. Ullman, “Measurement of the solar electron neutrino flux with the Homestake chlorine detector”, *Astrophys. J.* **496** (1998) 505–526.
- [24] SAGE Collaboration, J. N. Abdurashitov *et al.*, “Solar neutrino flux measurements by the Soviet-American Gallium Experiment (SAGE) for half the 22 year solar cycle”, *J. Exp. Theor. Phys.* **95** (2002) 181–193, [arXiv:astro-ph/0204245](#) [astro-ph]. [Zh. Eksp. Teor. Fiz.122,211(2002)].
- [25] GALLEX Collaboration, W. Hampel *et al.*, “GALLEX solar neutrino observations: Results for GALLEX IV”, *Phys. Lett.* **B447** (1999) 127–133.
- [26] GNO Collaboration, M. Altmann *et al.*, “Complete results for five years of GNO solar neutrino observations”, *Phys. Lett.* **B616** (2005) 174–190, [arXiv:hep-ex/0504037](#) [hep-ex].
- [27] Kamiokande-II Collaboration, K. S. Hirata *et al.*, “Real time, directional measurement of B-8 solar neutrinos in the Kamiokande-II detector”, *Phys. Rev.* **D44** (1991) 2241. [Erratum: Phys. Rev.D45,2170(1992)].

- [28] Super-Kamiokande Collaboration, J. Hosaka *et al.*, “Solar neutrino measurements in Super-Kamiokande-I”, *Phys. Rev.* **D73** (2006) 112001, [arXiv:hep-ex/0508053](#) [[hep-ex](#)].
- [29] SNO Collaboration, B. Aharmim *et al.*, “Combined Analysis of all Three Phases of Solar Neutrino Data from the Sudbury Neutrino Observatory”, *Phys. Rev.* **C88** (2013) 025501, [arXiv:1109.0763](#) [[nucl-ex](#)].
- [30] KamLAND Collaboration, A. Gando *et al.*, “ ^7Be Solar Neutrino Measurement with KamLAND”, *Phys. Rev.* **C92** no. 5, (2015) 055808, [arXiv:1405.6190](#) [[hep-ex](#)].
- [31] G. Bellini *et al.*, “Precision measurement of the ^7Be solar neutrino interaction rate in Borexino”, *Phys. Rev. Lett.* **107** (2011) 141302, [arXiv:1104.1816](#) [[hep-ex](#)].
- [32] MACRO Collaboration, M. Ambrosio *et al.*, “Matter effects in upward going muons and sterile neutrino oscillations”, *Phys. Lett.* **B517** (2001) 59–66, [arXiv:hep-ex/0106049](#) [[hep-ex](#)].
- [33] Soudan 2 Collaboration, M. C. Sanchez *et al.*, “Measurement of the L/E distributions of atmospheric neutrinos in Soudan 2 and their interpretation as neutrino oscillations”, *Phys. Rev.* **D68** (2003) 113004, [arXiv:hep-ex/0307069](#) [[hep-ex](#)].
- [34] KamLAND Collaboration, S. Abe *et al.*, “Precision Measurement of Neutrino Oscillation Parameters with KamLAND”, *Phys. Rev. Lett.* **100** (2008) 221803, [arXiv:0801.4589](#) [[hep-ex](#)].
- [35] K2K Collaboration, S. H. Ahn *et al.*, “Detection of accelerator produced neutrinos at a distance of 250-km”, *Phys. Lett.* **B511** (2001) 178–184, [arXiv:hep-ex/0103001](#) [[hep-ex](#)].
- [36] MINOS Collaboration, P. Adamson *et al.*, “Measurement of Neutrino and Antineutrino Oscillations Using Beam and Atmospheric Data in MINOS”, *Phys. Rev. Lett.* **110** no. 25, (2013) 251801, [arXiv:1304.6335](#) [[hep-ex](#)].
- [37] Double Chooz Collaboration, H. de Kerret *et al.*, “First Double Chooz θ_{13} Measurement via Total Neutron Capture Detection”, [arXiv:1901.09445](#) [[hep-ex](#)].
- [38] Daya Bay Collaboration, D. Adey *et al.*, “Measurement of the Electron Antineutrino Oscillation with 1958 Days of Operation at Daya Bay”, *Phys. Rev. Lett.* **121** no. 24, (2018) 241805, [arXiv:1809.02261](#) [[hep-ex](#)].
- [39] RENO Collaboration, G. Bak *et al.*, “Measurement of Reactor Antineutrino Oscillation Amplitude and Frequency at RENO”, *Phys. Rev. Lett.* **121** no. 20, (2018) 201801, [arXiv:1806.00248](#) [[hep-ex](#)].
- [40] NOvA Collaboration, D. S. Ayres *et al.*, “NOvA: Proposal to Build a 30 Kiloton Off-Axis Detector to Study $\nu_\mu \rightarrow \nu_e$ Oscillations in the NuMI Beamline”, [arXiv:hep-ex/0503053](#) [[hep-ex](#)].
- [41] T2K Collaboration, K. Abe *et al.*, “The T2K Experiment”, *Nucl. Instrum. Meth.* **A659** (2011) 106–135, [arXiv:1106.1238](#) [[physics.ins-det](#)].
- [42] DUNE Collaboration, R. Acciarri *et al.*, “Long-Baseline Neutrino Facility (LBNF) and Deep Underground Neutrino Experiment (DUNE)”, [arXiv:1601.02984](#) [[physics.ins-det](#)].

- [43] Hyper-Kamiokande Proto-Collaboration Collaboration, K. Abe *et al.*, “Physics potential of a long-baseline neutrino oscillation experiment using a J-PARC neutrino beam and Hyper-Kamiokande”, *PTEP* **2015** (2015) 053C02, [arXiv:1502.05199](https://arxiv.org/abs/1502.05199) [hep-ex].
- [44] I. Esteban, M. Gonzalez-Garcia, A. Hernandez-Cabezudo, M. Maltoni, I. Martinez-Soler, and T. Schwetz, “NuFit 3.1 (2017)”. <http://www.nu-fit.org>.
- [45] I. Esteban, M. Gonzalez-Garcia, A. Hernandez-Cabezudo, M. Maltoni, I. Martinez-Soler, and T. Schwetz, “NuFit 3.2 (2018)”. <http://www.nu-fit.org>.
- [46] I. Esteban, M. Gonzalez-Garcia, A. Hernandez-Cabezudo, M. Maltoni, and T. Schwetz, “NuFit 4.1 (2019)”. <http://www.nu-fit.org>.
- [47] COHERENT Collaboration, D. Akimov *et al.*, “The COHERENT Experiment at the Spallation Neutron Source”, [arXiv:1509.08702](https://arxiv.org/abs/1509.08702) [physics.ins-det].
- [48] J. Dalton, *A new system of chemical philosophy*. R. Bickerstaff, London, 1808.
- [49] H. Geiger, E. Marsden, and E. Rutherford, “On a diffuse reflection of the α -particles”, *Proc. R. Soc. Lond. A* **82** (1909) 495–500.
- [50] H. Geiger and E. Rutherford, “The scattering of α -particles by matter”, *Proc. R. Soc. Lond. A* **83** (1910) 492–504.
- [51] E. Rutherford, “The scattering of alpha and beta particles by matter and the structure of the atom”, *Phil. Mag. Ser.6* **21** (1911) 669–688.
- [52] S. L. Glashow, “Partial Symmetries of Weak Interactions”, *Nucl. Phys.* **22** (1961) 579–588.
- [53] S. Weinberg, “A Model of Leptons”, *Phys. Rev. Lett.* **19** (1967) 1264–1266.
- [54] A. Salam, “Elementary Particle Theory. Relativistic Groups and Analyticity. Proceedings of the eighth Nobel Symposium”, *Science* **168** no. 3936, (1970) 1196–1197.
- [55] H. Fritzsch, M. Gell-Mann, and H. Leutwyler, “Advantages of the Color Octet Gluon Picture”, *Phys. Lett.* **47B** (1973) 365–368.
- [56] D. J. Gross and F. Wilczek, “Asymptotically Free Gauge Theories - I”, *Phys. Rev.* **D8** (1973) 3633–3652.
- [57] S. Weinberg, “Nonabelian Gauge Theories of the Strong Interactions”, *Phys. Rev. Lett.* **31** (1973) 494–497.
- [58] P. W. Higgs, “Broken Symmetries and the Masses of Gauge Bosons”, *Phys. Rev. Lett.* **13** (1964) 508–509. [,160(1964)].
- [59] F. Englert and R. Brout, “Broken Symmetry and the Mass of Gauge Vector Mesons”, *Phys. Rev. Lett.* **13** (1964) 321–323. [,157(1964)].
- [60] G. S. Guralnik, C. R. Hagen, and T. W. B. Kibble, “Global Conservation Laws and Massless Particles”, *Phys. Rev. Lett.* **13** (1964) 585–587. [,162(1964)].
- [61] CMS Collaboration, S. Chatrchyan *et al.*, “Observation of a New Boson at a Mass of 125 GeV with the CMS Experiment at the LHC”, *Phys. Lett.* **B716** (2012) 30–61, [arXiv:1207.7235](https://arxiv.org/abs/1207.7235) [hep-ex].

- [62] ATLAS Collaboration, G. Aad *et al.*, “Observation of a new particle in the search for the Standard Model Higgs boson with the ATLAS detector at the LHC”, *Phys. Lett.* **B716** (2012) 1–29, [arXiv:1207.7214 \[hep-ex\]](#).
- [63] S. Weinberg, “General Theory of Broken Local Symmetries”, *Phys. Rev.* **D7** (1973) 1068–1082.
- [64] N. Cabibbo, “Unitary Symmetry and Leptonic Decays”, *Phys. Rev. Lett.* **10** (1963) 531–533. [[648\(1963\)](#)].
- [65] M. Kobayashi and T. Maskawa, “CP Violation in the Renormalizable Theory of Weak Interaction”, *Prog. Theor. Phys.* **49** (1973) 652–657.
- [66] J. Bernabeu, G. C. Branco, and M. Gronau, “CP Restrictions on Quark Mass Matrices”, *Phys. Lett.* **169B** (1986) 243–247.
- [67] M. Gronau, A. Kfir, and R. Loewy, “Basis Independent Tests of CP Violation in Fermion Mass Matrices”, *Phys. Rev. Lett.* **56** (1986) 1538.
- [68] C. Jarlskog, “A Basis Independent Formulation of the Connection Between Quark Mass Matrices, CP Violation and Experiment”, *Z. Phys.* **C29** (1985) 491–497.
- [69] C. Jarlskog, “Commutator of the Quark Mass Matrices in the Standard Electroweak Model and a Measure of Maximal CP Violation”, *Phys. Rev. Lett.* **55** (1985) 1039.
- [70] R. S. Chivukula and H. Georgi, “Composite Technicolor Standard Model”, *Phys. Lett.* **B188** (1987) 99–104.
- [71] G. D’Ambrosio, G. F. Giudice, G. Isidori, and A. Strumia, “Minimal flavor violation: An Effective field theory approach”, *Nucl. Phys.* **B645** (2002) 155–187, [arXiv:hep-ph/0207036 \[hep-ph\]](#).
- [72] Particle Data Group Collaboration, M. Tanabashi *et al.*, “Review of Particle Physics”, *Phys. Rev.* **D98** no. 3, (2018) 030001. 2019 update.
- [73] E. Noether, “Invariant Variation Problems”, *Gott. Nachr.* **1918** (1918) 235–257, [arXiv:physics/0503066 \[physics\]](#). [[Transp. Theory Statist. Phys.1,186\(1971\)](#)].
- [74] W. A. Fowler, “Completion of the Proton-Proton Reaction Chain and the Possibility of Energetic Neutrino Emission by Hot Stars”, *Astrophys. J.* **127** (1958) 551–556.
- [75] A. G. W. Cameron, “Nuclear astrophysics”, *Ann. Rev. Nucl. Part. Sci.* **8** (1958) 299–326.
- [76] J. N. Bahcall, W. A. Fowler, I. Iben, Jr., and R. L. Sears, “Solar neutrino flux”, *Astrophys. J.* **137** (1963) 344–346.
- [77] R. Davis, Jr., D. S. Harmer, and K. C. Hoffman, “Search for neutrinos from the sun”, *Phys. Rev. Lett.* **20** (1968) 1205–1209.
- [78] Kamiokande Collaboration, Y. Fukuda *et al.*, “Solar neutrino data covering solar cycle 22”, *Phys. Rev. Lett.* **77** (1996) 1683–1686.
- [79] Super-Kamiokande Collaboration, M. B. Smy *et al.*, “Precise measurement of the solar neutrino day / night and seasonal variation in Super-Kamiokande-1”, *Phys. Rev.* **D69** (2004) 011104, [arXiv:hep-ex/0309011 \[hep-ex\]](#).

- [80] SNO Collaboration, Q. R. Ahmad *et al.*, “Measurement of the rate of $\nu_e + d \rightarrow p + p + e^-$ interactions produced by 8B solar neutrinos at the Sudbury Neutrino Observatory”, *Phys. Rev. Lett.* **87** (2001) 071301, [arXiv:nuc1-ex/0106015](#) [nuc1-ex].
- [81] F. Kaether, W. Hampel, G. Heusser, J. Kiko, and T. Kirsten, “Reanalysis of the GALLEX solar neutrino flux and source experiments”, *Phys. Lett.* **B685** (2010) 47–54, [arXiv:1001.2731](#) [hep-ex].
- [82] SAGE Collaboration, J. N. Abdurashitov *et al.*, “Measurement of the solar neutrino capture rate with gallium metal. III: Results for the 2002–2007 data-taking period”, *Phys. Rev.* **C80** (2009) 015807, [arXiv:0901.2200](#) [nuc1-ex].
- [83] Super-Kamiokande Collaboration, J. P. Cravens *et al.*, “Solar neutrino measurements in Super-Kamiokande-II”, *Phys. Rev.* **D78** (2008) 032002, [arXiv:0803.4312](#) [hep-ex].
- [84] Super-Kamiokande Collaboration, K. Abe *et al.*, “Solar neutrino results in Super-Kamiokande-III”, *Phys. Rev.* **D83** (2011) 052010, [arXiv:1010.0118](#) [hep-ex].
- [85] Y. Nakano, *8B solar neutrino spectrum measurement using Super-Kamiokande IV*. PhD thesis, U. Tokyo (main), 2016. http://www-sk.icrr.u-tokyo.ac.jp/sk/_pdf/articles/2016/doc_thesis_naknao.pdf.
- [86] M. Ikeda, “Solar neutrino measurements with Super-Kamiokande.” Talk given at the *XXVIII International Conference on Neutrino Physics and Astrophysics*, Heidelberg, Germany, June 4–9, 2018.
- [87] Borexino Collaboration, G. Bellini *et al.*, “Measurement of the solar 8B neutrino rate with a liquid scintillator target and 3 MeV energy threshold in the Borexino detector”, *Phys. Rev.* **D82** (2010) 033006, [arXiv:0808.2868](#) [astro-ph].
- [88] BOREXINO Collaboration, G. Bellini *et al.*, “Neutrinos from the primary proton–proton fusion process in the Sun”, *Nature* **512** no. 7515, (2014) 383–386.
- [89] IceCube Collaboration, M. G. Aartsen *et al.*, “Determining neutrino oscillation parameters from atmospheric muon neutrino disappearance with three years of IceCube DeepCore data”, *Phys. Rev.* **D91** no. 7, (2015) 072004, [arXiv:1410.7227](#) [hep-ex].
- [90] Super-Kamiokande Collaboration, K. Abe *et al.*, “Atmospheric neutrino oscillation analysis with external constraints in Super-Kamiokande I-IV”, *Phys. Rev.* **D97** no. 7, (2018) 072001, [arXiv:1710.09126](#) [hep-ex].
- [91] KamLAND Collaboration, A. Gando *et al.*, “Reactor On-Off Antineutrino Measurement with KamLAND”, *Phys. Rev.* **D88** no. 3, (2013) 033001, [arXiv:1303.4667](#) [hep-ex].
- [92] Daya Bay Collaboration, F. P. An *et al.*, “Improved Measurement of the Reactor Antineutrino Flux and Spectrum at Daya Bay”, *Chin. Phys.* **C41** no. 1, (2017) 013002, [arXiv:1607.05378](#) [hep-ex].
- [93] A. Cabrera Serra, “Double Chooz Improved Multi-Detector Measurements.” Talk given at the *CERN EP colloquium*, CERN, Switzerland, September 20, 2016.
- [94] MINOS Collaboration, P. Adamson *et al.*, “Electron neutrino and antineutrino appearance in the full MINOS data sample”, *Phys. Rev. Lett.* **110** no. 17, (2013) 171801, [arXiv:1301.4581](#) [hep-ex].

- [95] A. Izmaylov, “T2K Neutrino Experiment. Recent Results and Plans.” Talk given at the *Flavour Physics Conference*, Quy Nhon, Vietnam, August 13–19, 2017.
- [96] M. Friend, “Updated Results from the T2K Experiment with 3.13×10^{21} Protons on Target.” KEK seminar, January 10, 2019.
- [97] NOvA Collaboration, M. A. Acero *et al.*, “First Measurement of Neutrino Oscillation Parameters using Neutrinos and Antineutrinos by NOvA”, *Phys. Rev. Lett.* **123** no. 15, (2019) 151803, [arXiv:1906.04907 \[hep-ex\]](#).
- [98] S. Weinberg, “Baryon and Lepton Nonconserving Processes”, *Phys. Rev. Lett.* **43** (1979) 1566–1570.
- [99] M. C. Gonzalez-Garcia and Y. Nir, “Neutrino Masses and Mixing: Evidence and Implications”, *Rev. Mod. Phys.* **75** (2003) 345–402, [arXiv:hep-ph/0202058 \[hep-ph\]](#).
- [100] M. C. Gonzalez-Garcia and M. Maltoni, “Phenomenology with Massive Neutrinos”, *Phys. Rept.* **460** (2008) 1–129, [arXiv:0704.1800 \[hep-ph\]](#).
- [101] B. A. Kniehl and A. Pilaftsis, “Mixing renormalization in Majorana neutrino theories”, *Nucl. Phys.* **B474** (1996) 286–308, [arXiv:hep-ph/9601390 \[hep-ph\]](#).
- [102] P. Ramond, “The Family Group in Grand Unified Theories”, in *International Symposium on Fundamentals of Quantum Theory and Quantum Field Theory Palm Coast, Florida, February 25-March 2, 1979*, pp. 265–280. 1979. [arXiv:hep-ph/9809459 \[hep-ph\]](#).
- [103] M. Gell-Mann, P. Ramond, and R. Slansky, “Complex Spinors and Unified Theories”, *Conf. Proc.* **C790927** (1979) 315–321, [arXiv:1306.4669 \[hep-th\]](#).
- [104] T. Yanagida, “Horizontal gauge symmetry and masses of neutrinos”, *Conf. Proc.* **C7902131** (1979) 95–99.
- [105] R. N. Mohapatra and G. Senjanovic, “Neutrino Mass and Spontaneous Parity Nonconservation”, *Phys. Rev. Lett.* **44** (1980) 912. [[231\(1979\)](#)].
- [106] B. Pontecorvo, “Neutrino Experiments and the Problem of Conservation of Leptonic Charge”, *Sov. Phys. JETP* **26** (1968) 984–988. [[Zh. Eksp. Teor. Fiz.53,1717\(1967\)](#)].
- [107] Z. Maki, M. Nakagawa, and S. Sakata, “Remarks on the unified model of elementary particles”, *Prog. Theor. Phys.* **28** (1962) 870–880. [[34\(1962\)](#)].
- [108] P. Coloma and T. Schwetz, “Generalized mass ordering degeneracy in neutrino oscillation experiments”, *Phys. Rev.* **D94** no. 5, (2016) 055005, [arXiv:1604.05772 \[hep-ph\]](#). [Erratum: *Phys. Rev.*D95,no.7,079903(2017)].
- [109] E. K. Akhmedov and A. Yu. Smirnov, “Paradoxes of neutrino oscillations”, *Phys. Atom. Nucl.* **72** (2009) 1363–1381, [arXiv:0905.1903 \[hep-ph\]](#).
- [110] A. G. Cohen, S. L. Glashow, and Z. Ligeti, “Disentangling Neutrino Oscillations”, *Phys. Lett.* **B678** (2009) 191–196, [arXiv:0810.4602 \[hep-ph\]](#).
- [111] I. Esteban, M. C. Gonzalez-Garcia, A. Hernandez-Cabezudo, M. Maltoni, and T. Schwetz, “Global analysis of three-flavour neutrino oscillations: synergies and tensions in the determination of θ_{23} , δ_{CP} , and the mass ordering”, *JHEP* **01** (2019) 106, [arXiv:1811.05487 \[hep-ph\]](#). NuFIT 4.1 (2019), [www.nu-fit.org](#).

- [112] A. Halprin, “Neutrino Oscillations in Nonuniform Matter”, *Phys. Rev.* **D34** (1986) 3462–3466.
- [113] A. J. Baltz and J. Weneser, “Matter Oscillations: Neutrino Transformation in the Sun and Regeneration in the Earth”, *Phys. Rev.* **D37** (1988) 3364.
- [114] P. D. Mannheim, “Derivation of the Formalism for Neutrino Matter Oscillations From the Neutrino Relativistic Field Equations”, *Phys. Rev.* **D37** (1988) 1935.
- [115] C. W. Kim and A. Pevsner, *Neutrinos in physics and astrophysics*, vol. 8. Harwood Academic Press, 1993.
- [116] L. Wolfenstein, “Neutrino Oscillations in Matter”, *Phys. Rev.* **D17** (1978) 2369–2374. [,294(1977)].
- [117] S. P. Mikheyev and A. Yu. Smirnov, “Resonance Amplification of Oscillations in Matter and Spectroscopy of Solar Neutrinos”, *Sov. J. Nucl. Phys.* **42** (1985) 913–917. [Yad. Fiz.42,1441(1985); ,305(1986)].
- [118] M. C. Gonzalez-Garcia and M. Maltoni, “Atmospheric neutrino oscillations and new physics”, *Phys. Rev.* **D70** (2004) 033010, [arXiv:hep-ph/0404085](#) [hep-ph].
- [119] V. D. Barger, J. G. Learned, S. Pakvasa, and T. J. Weiler, “Neutrino decay as an explanation of atmospheric neutrino observations”, *Phys. Rev. Lett.* **82** (1999) 2640–2643, [arXiv:astro-ph/9810121](#) [astro-ph].
- [120] E. Lisi, A. Marrone, and D. Montanino, “Probing possible decoherence effects in atmospheric neutrino oscillations”, *Phys. Rev. Lett.* **85** (2000) 1166–1169, [arXiv:hep-ph/0002053](#) [hep-ph].
- [121] S. R. Coleman and S. L. Glashow, “Cosmic ray and neutrino tests of special relativity”, *Phys. Lett.* **B405** (1997) 249–252, [arXiv:hep-ph/9703240](#) [hep-ph].
- [122] S. L. Glashow, A. Halprin, P. I. Krastev, C. N. Leung, and J. T. Pantaleone, “Comments on neutrino tests of special relativity”, *Phys. Rev.* **D56** (1997) 2433–2434, [arXiv:hep-ph/9703454](#) [hep-ph]. [,966(1997)].
- [123] M. C. Gonzalez-Garcia and M. Maltoni, “Status of Oscillation plus Decay of Atmospheric and Long-Baseline Neutrinos”, *Phys. Lett.* **B663** (2008) 405–409, [arXiv:0802.3699](#) [hep-ph].
- [124] T. A. Mueller *et al.*, “Improved Predictions of Reactor Antineutrino Spectra”, *Phys. Rev.* **C83** (2011) 054615, [arXiv:1101.2663](#) [hep-ex].
- [125] P. Huber, “On the determination of anti-neutrino spectra from nuclear reactors”, *Phys. Rev.* **C84** (2011) 024617, [arXiv:1106.0687](#) [hep-ph]. [Erratum: *Phys. Rev.* **C85**,029901(2012)].
- [126] G. Mention, M. Fechner, T. Lasserre, T. A. Mueller, D. Lhuillier, M. Cribier, and A. Letourneau, “The Reactor Antineutrino Anomaly”, *Phys. Rev.* **D83** (2011) 073006, [arXiv:1101.2755](#) [hep-ex].
- [127] A. C. Hayes, J. L. Friar, G. T. Garvey, G. Jungman, and G. Jonkmans, “Systematic Uncertainties in the Analysis of the Reactor Neutrino Anomaly”, *Phys. Rev. Lett.* **112** (2014) 202501, [arXiv:1309.4146](#) [nucl-th].

- [128] D.-L. Fang and B. A. Brown, “Effect of first forbidden decays on the shape of neutrino spectra”, *Phys. Rev.* **C91** no. 2, (2015) 025503, [arXiv:1502.02246](#) [nucl-th]. [Erratum: *Phys. Rev.* **C93**,no.4,049903(2016)].
- [129] A. C. Hayes and P. Vogel, “Reactor Neutrino Spectra”, *Ann. Rev. Nucl. Part. Sci.* **66** (2016) 219–244, [arXiv:1605.02047](#) [hep-ph].
- [130] M. A. Acero, C. Giunti, and M. Laveder, “Limits on $\nu(e)$ and anti- $\nu(e)$ disappearance from Gallium and reactor experiments”, *Phys. Rev.* **D78** (2008) 073009, [arXiv:0711.4222](#) [hep-ph].
- [131] C. Giunti and M. Laveder, “Statistical Significance of the Gallium Anomaly”, *Phys. Rev.* **C83** (2011) 065504, [arXiv:1006.3244](#) [hep-ph].
- [132] LSND Collaboration, A. Aguilar-Arevalo *et al.*, “Evidence for neutrino oscillations from the observation of anti-neutrino(electron) appearance in a anti-neutrino(muon) beam”, *Phys. Rev.* **D64** (2001) 112007, [arXiv:hep-ex/0104049](#) [hep-ex].
- [133] MiniBooNE Collaboration, A. A. Aguilar-Arevalo *et al.*, “Significant Excess of ElectronLike Events in the MiniBooNE Short-Baseline Neutrino Experiment”, *Phys. Rev. Lett.* **121** no. 22, (2018) 221801, [arXiv:1805.12028](#) [hep-ex].
- [134] M. Dentler, A. Hernandez-Cabezudo, J. Kopp, P. A. N. Machado, M. Maltoni, I. Martinez-Soler, and T. Schwetz, “Updated Global Analysis of Neutrino Oscillations in the Presence of eV-Scale Sterile Neutrinos”, *JHEP* **08** (2018) 010, [arXiv:1803.10661](#) [hep-ph].
- [135] S. Böser, C. Buck, C. Giunti, J. Lesgourgues, L. Ludhova, S. Mertens, A. Schukraft, and M. Wurm, “Status of Light Sterile Neutrino Searches”, [arXiv:1906.01739](#) [hep-ex].
- [136] A. M. Serenelli, W. C. Haxton, and C. Pena-Garay, “Solar models with accretion. I. Application to the solar abundance problem”, *Astrophys. J.* **743** (2011) 24, [arXiv:1104.1639](#) [astro-ph.SR].
- [137] F. L. Villante, “ecCNO Solar Neutrinos: A Challenge for Gigantic Ultra-Pure Liquid Scintillator Detectors”, *Phys. Lett.* **B742** (2015) 279–284, [arXiv:1410.2796](#) [hep-ph].
- [138] Wikimedia Commons, “Fusion in the Sun.” https://commons.wikimedia.org/w/index.php?title=File:Fusion_in_the_Sun.svg&oldid=345769195, 2019. [Online; accessed 14-February-2020].
- [139] Wikimedia Commons, User:Borb, “CNO Cycle.” https://commons.wikimedia.org/w/index.php?title=File:CNO_Cycle.svg&oldid=272861408, 2017. [Online; accessed 14-February-2020].
- [140] A. Serenelli, “Alive and well: a short review about standard solar models”, *Eur. Phys. J.* **A52** no. 4, (2016) 78, [arXiv:1601.07179](#) [astro-ph.SR].
- [141] J. N. Bahcall, A. M. Serenelli, and S. Basu, “New solar opacities, abundances, helioseismology, and neutrino fluxes”, *Astrophys. J.* **621** (2005) L85–L88, [arXiv:astro-ph/0412440](#) [astro-ph].
- [142] Super-Kamiokande Collaboration, S. Fukuda *et al.*, “Determination of solar neutrino oscillation parameters using 1496 days of Super-Kamiokande I data”, *Phys. Lett.* **B539** (2002) 179–187, [arXiv:hep-ex/0205075](#) [hep-ex].

- [143] M. Maltoni and A. Yu. Smirnov, “Solar neutrinos and neutrino physics”, *Eur. Phys. J.* **A52** no. 4, (2016) 87, [arXiv:1507.05287 \[hep-ph\]](#).
- [144] M. Honda, M. Sajjad Athar, T. Kajita, K. Kasahara, and S. Midorikawa, “Atmospheric neutrino flux calculation using the NRLMSISE-00 atmospheric model”, *Phys. Rev.* **D92** no. 2, (2015) 023004, [arXiv:1502.03916 \[astro-ph.HE\]](#).
- [145] C. V. Achar *et al.*, “Detection of muons produced by cosmic ray neutrinos deep underground”, *Phys. Lett.* **18** (1965) 196–199.
- [146] F. Reines, M. F. Crouch, T. L. Jenkins, W. R. Kropp, H. S. Gurr, G. R. Smith, J. P. F. Sellschop, and B. Meyer, “Evidence for high-energy cosmic ray neutrino interactions”, *Phys. Rev. Lett.* **15** (1965) 429–433.
- [147] D. Casper *et al.*, “Measurement of atmospheric neutrino composition with IMB-3”, *Phys. Rev. Lett.* **66** (1991) 2561–2564.
- [148] Frejus Collaboration, K. Daum *et al.*, “Determination of the atmospheric neutrino spectra with the Frejus detector”, *Z. Phys.* **C66** (1995) 417–428.
- [149] NUSEX Collaboration, M. Aglietta *et al.*, “Experimental study of atmospheric neutrino flux in the NUSEX experiment”, *Europhys. Lett.* **8** (1989) 611–614.
- [150] Daya Bay Collaboration, F. P. An *et al.*, “Measurement of the Reactor Antineutrino Flux and Spectrum at Daya Bay”, *Phys. Rev. Lett.* **116** no. 6, (2016) 061801, [arXiv:1508.04233 \[hep-ex\]](#). [Erratum: *Phys. Rev. Lett.* 118, no. 9, 099902 (2017)].
- [151] CHOOZ Collaboration, M. Apollonio *et al.*, “Search for neutrino oscillations on a long baseline at the CHOOZ nuclear power station”, *Eur. Phys. J.* **C27** (2003) 331–374, [arXiv:hep-ex/0301017 \[hep-ex\]](#).
- [152] F. Boehm *et al.*, “Final results from the Palo Verde neutrino oscillation experiment”, *Phys. Rev.* **D64** (2001) 112001, [arXiv:hep-ex/0107009 \[hep-ex\]](#).
- [153] F. J. Hasert *et al.*, “Search for Elastic ν_μ Electron Scattering”, *Phys. Lett.* **46B** (1973) 121–124. [,5.11(1973); ,5.11(1973)].
- [154] T. Eichten *et al.*, “Measurement of the Neutrino - Nucleon Anti-neutrino - Nucleon Total Cross-sections”, *Phys. Lett.* **46B** (1973) 274–280.
- [155] A. C. Benvenuti *et al.*, “Observation of New Particle Production by High-Energy Neutrinos and anti-neutrinos”, *Phys. Rev. Lett.* **34** (1975) 419.
- [156] B. Pontecorvo, “Electron and Muon Neutrinos”, *Sov. Phys. JETP* **10** (1960) 1236–1240. [*Zh. Eksp. Teor. Fiz.* 37,1751(1959)].
- [157] M. Schwartz, “Feasibility of using high-energy neutrinos to study the weak interactions”, *Phys. Rev. Lett.* **4** (1960) 306–307.
- [158] U. Dore, P. Loverre, and L. Ludovici, “History of accelerator neutrino beams”, *Eur. Phys. J.* **H44** no. 4-5, (2019) 271–305, [arXiv:1805.01373 \[physics.acc-ph\]](#).
- [159] T2K Collaboration, K. Abe *et al.*, “T2K neutrino flux prediction”, *Phys. Rev.* **D87** no. 1, (2013) 012001, [arXiv:1211.0469 \[hep-ex\]](#). [Addendum: *Phys. Rev.* D87, no. 1, 019902 (2013)].

- [160] K2K Collaboration, E. Aliu *et al.*, “Evidence for muon neutrino oscillation in an accelerator-based experiment”, *Phys. Rev. Lett.* **94** (2005) 081802, [arXiv:hep-ex/0411038](#) [hep-ex].
- [161] MINOS Collaboration, D. G. Michael *et al.*, “Observation of muon neutrino disappearance with the MINOS detectors and the NuMI neutrino beam”, *Phys. Rev. Lett.* **97** (2006) 191801, [arXiv:hep-ex/0607088](#) [hep-ex].
- [162] S. S. Wilks, “The Large-Sample Distribution of the Likelihood Ratio for Testing Composite Hypotheses”, *Annals Math. Statist.* **9** no. 1, (1938) 60–62.
- [163] Y. Nakano, *⁸B solar neutrino spectrum measurement using Super-Kamiokande IV*. PhD thesis, Tokyo U., 2016-02. http://www-sk.icrr.u-tokyo.ac.jp/sk/_pdf/articles/2016/doc_thesis_naknao.pdf.
- [164] Y. Nakano, “Solar neutrino results from Super-Kamiokande.” Talk given at the *38th International Conference on High Energy Physics*, Chicago, USA, August 3–10, 2016.
- [165] K. Iwamoto, “Recent Results from T2K and Future Prospects.” Talk given at the *38th International Conference on High Energy Physics*, Chicago, USA, August 3–10, 2016.
- [166] A. Cervera, “Latest Results from Neutrino Oscillation Experiments.” Talk given at the SUSY 2016 Conference, Melbourne, Australia, July 3–8, 2016.
- [167] P. Vahle, “New results from NOvA.” Talk given at the *XXVII International Conference on Neutrino Physics and Astrophysics*, London, UK, July 4–9, 2016.
- [168] KamLAND Collaboration, A. Gando *et al.*, “Constraints on θ_{13} from A Three-Flavor Oscillation Analysis of Reactor Antineutrinos at KamLAND”, *Phys. Rev.* **D83** (2011) 052002, [arXiv:1009.4771](#) [hep-ex].
- [169] CHOOZ Collaboration, M. Apollonio *et al.*, “Limits on Neutrino Oscillations from the CHOOZ Experiment”, *Phys. Lett.* **B466** (1999) 415–430, [arXiv:hep-ex/9907037](#).
- [170] Palo Verde Collaboration, A. Piepke, “Final results from the Palo Verde neutrino oscillation experiment”, *Prog. Part. Nucl. Phys.* **48** (2002) 113–121.
- [171] M. Ishitsuka, “New results of Double Chooz.” Talk given at the Conference *Rencontres de Moriond EW 2016*, La Thuile, Italy, March 12–19, 2016.
- [172] Z. Yu, “Recent Results from the Daya Bay Experiment.” Talk given at the *XXVII International Conference on Neutrino Physics and Astrophysics*, London, UK, July 4–9, 2016.
- [173] S.-H. Seo, “New Results from RENO.” Talk given at the *XXVI International Conference on Neutrino Physics and Astrophysics*, Boston, USA, June 2–7, 2014.
- [174] J. Kopp, P. A. N. Machado, M. Maltoni, and T. Schwetz, “Sterile Neutrino Oscillations: The Global Picture”, *JHEP* **1305** (2013) 050, [arXiv:1303.3011](#) [hep-ph].
- [175] H. Kwon, F. Boehm, A. Hahn, H. Henrikson, J. Vuilleumier, *et al.*, “Search for neutrino oscillations at a fission reactor”, *Phys.Rev.* **D24** (1981) 1097–1111.
- [176] CALTECH-SIN-TUM Collaboration, G. Zacek *et al.*, “Neutrino Oscillation Experiments at the Gosgen Nuclear Power Reactor”, *Phys.Rev.* **D34** (1986) 2621–2636.
- [177] G. Vidyakin, V. Vyrodov, I. Gurevich, Y. Kozlov, V. Martemyanov, *et al.*, “Detection of anti-neutrinos in the flux from two reactors”, *Sov.Phys.JETP* **66** (1987) 243–247.

- [178] G. Vidyakin, V. Vyrodov, Y. Kozlov, A. Martemyanov, V. Martemyanov, *et al.*, “Limitations on the characteristics of neutrino oscillations”, *JETP Lett.* **59** (1994) 390–393.
- [179] A. Afonin, S. Ketov, V. Kopeikin, L. Mikaelyan, M. Skorokhvatov, *et al.*, “A study of the reaction $\bar{\nu}_e + p \rightarrow e^+ + n$ on a nuclear reactor”, *Sov.Phys.JETP* **67** (1988) 213–221.
- [180] A. Kuvshinnikov, L. Mikaelyan, S. Nikolaev, M. Skorokhvatov, and A. Etenko, “Measuring the $\bar{\nu}_e + p \rightarrow n + e^+$ cross-section and beta decay axial constant in a new experiment at Rovno NPP reactor. (In Russian)”, *JETP Lett.* **54** (1991) 253–257.
- [181] Y. Declais, J. Favier, A. Metref, H. Pessard, B. Achkar, *et al.*, “Search for neutrino oscillations at 15-meters, 40-meters, and 95-meters from a nuclear power reactor at Bugey”, *Nucl.Phys.* **B434** (1995) 503–534.
- [182] Y. Declais, H. de Kerret, B. Lefievre, M. Obolensky, A. Etenko, *et al.*, “Study of reactor anti-neutrino interaction with proton at Bugey nuclear power plant”, *Phys.Lett.* **B338** (1994) 383–389.
- [183] Z. D. Greenwood *et al.*, “Results of a two position reactor neutrino oscillation experiment”, *Phys. Rev.* **D53** (1996) 6054–6064.
- [184] NuFIT webpage, <http://www.nu-fit.org>.
- [185] M. C. Gonzalez-Garcia, M. Maltoni, and T. Schwetz, “Updated fit to three neutrino mixing: status of leptonic CP violation”, *JHEP* **11** (2014) 052, [arXiv:1409.5439](https://arxiv.org/abs/1409.5439) [hep-ph].
- [186] M. Gonzalez-Garcia, M. Maltoni, J. Salvado, and T. Schwetz, “Global fit to three neutrino mixing: critical look at present precision”, *JHEP* **1212** (2012) 123, [arXiv:1209.3023](https://arxiv.org/abs/1209.3023) [hep-ph].
- [187] T. Schwetz, “What is the probability that theta(13) and CP violation will be discovered in future neutrino oscillation experiments?”, *Phys. Lett.* **B648** (2007) 54–59, [arXiv:hep-ph/0612223](https://arxiv.org/abs/hep-ph/0612223) [hep-ph].
- [188] M. Blennow, P. Coloma, and E. Fernandez-Martinez, “Reassessing the sensitivity to leptonic CP violation”, *JHEP* **03** (2015) 005, [arXiv:1407.3274](https://arxiv.org/abs/1407.3274) [hep-ph].
- [189] M. C. Gonzalez-Garcia and C. Pena-Garay, “Three neutrino mixing after the first results from K2K and KamLAND”, *Phys. Rev.* **D68** (2003) 093003, [arXiv:hep-ph/0306001](https://arxiv.org/abs/hep-ph/0306001) [hep-ph].
- [190] Particle Data Group Collaboration, C. Patrignani *et al.*, “Review of Particle Physics”, *Chin. Phys.* **C40** no. 10, (2016) 100001.
- [191] J. Bergstrom, M. C. Gonzalez-Garcia, M. Maltoni, C. Pena-Garay, A. M. Serenelli, and N. Song, “Updated determination of the solar neutrino fluxes from solar neutrino data”, *JHEP* **03** (2016) 132, [arXiv:1601.00972](https://arxiv.org/abs/1601.00972) [hep-ph].
- [192] N. Vinyoles, A. M. Serenelli, F. L. Villante, S. Basu, J. Bergström, M. C. Gonzalez-Garcia, M. Maltoni, C. Peña-Garay, and N. Song, “A new Generation of Standard Solar Models”, *Astrophys. J.* **835** no. 2, (2017) 202, [arXiv:1611.09867](https://arxiv.org/abs/1611.09867) [astro-ph.SR].
- [193] T. J. C. Bezerra, H. Furuta, and F. Suekane, “Measurement of Effective Δm_{31}^2 using Baseline Differences of Daya Bay, RENO and Double Chooz Reactor Neutrino Experiments”, [arXiv:1206.6017](https://arxiv.org/abs/1206.6017) [hep-ex].

- [194] H. Seo *et al.*, “Spectral Measurement of the Electron Antineutrino Oscillation Amplitude and Frequency using 500 Live Days of RENO Data”, [arXiv:1610.04326 \[hep-ex\]](#).
- [195] Super-Kamiokande Collaboration, R. Wendell, “Atmospheric Results from Super-Kamiokande”, *AIP Conf. Proc.* **1666** (2015) 100001, [arXiv:1412.5234 \[hep-ex\]](#).
- [196] J. Kameda, “Recent results from Super-Kamiokande on atmospheric neutrinos and next project: Hyper-Kamiokande.” Talk given at the *XII Rencontres de Vietnam: NuFact 2016*, Qui Nhon, Vietnam, August 21–27, 2016.
- [197] K. P. Lee, “Study of the neutrino mass hierarchy with the atmospheric neutrino data observed in Super-Kamiokande.” Ph.D. thesis, The University of Tokyo, 2012.
- [198] J. Elevant and T. Schwetz, “On the determination of the leptonic CP phase”, *JHEP* **09** (2015) 016, [arXiv:1506.07685 \[hep-ph\]](#).
- [199] M. Blennow, P. Coloma, P. Huber, and T. Schwetz, “Quantifying the sensitivity of oscillation experiments to the neutrino mass ordering”, *JHEP* **03** (2014) 028, [arXiv:1311.1822 \[hep-ph\]](#).
- [200] T2K Collaboration, K. Abe *et al.*, “Search for CP Violation in Neutrino and Antineutrino Oscillations by the T2K Experiment with 2.2×10^{21} Protons on Target”, *Phys. Rev. Lett.* **121** no. 17, (2018) 171802, [arXiv:1807.07891 \[hep-ex\]](#).
- [201] A. Cervera, A. Donini, M. B. Gavela, J. J. Gomez Cadenas, P. Hernandez, O. Mena, and S. Rigolin, “Golden measurements at a neutrino factory”, *Nucl. Phys.* **B579** (2000) 17–55, [arXiv:hep-ph/0002108 \[hep-ph\]](#). [Erratum: *Nucl. Phys.*B593,731(2001)].
- [202] M. Freund, “Analytic approximations for three neutrino oscillation parameters and probabilities in matter”, *Phys. Rev.* **D64** (2001) 053003, [arXiv:hep-ph/0103300 \[hep-ph\]](#).
- [203] E. K. Akhmedov, R. Johansson, M. Lindner, T. Ohlsson, and T. Schwetz, “Series expansions for three flavor neutrino oscillation probabilities in matter”, *JHEP* **04** (2004) 078, [arXiv:hep-ph/0402175 \[hep-ph\]](#).
- [204] T2K Collaboration, K. Abe *et al.*, “Combined Analysis of Neutrino and Antineutrino Oscillations at T2K”, *Phys. Rev. Lett.* **118** no. 15, (2017) 151801, [arXiv:1701.00432 \[hep-ex\]](#).
- [205] NOvA Collaboration, M. A. Acero *et al.*, “New constraints on oscillation parameters from ν_e appearance and ν_μ disappearance in the NOvA experiment”, *Phys. Rev.* **D98** (2018) 032012, [arXiv:1806.00096 \[hep-ex\]](#).
- [206] M. Wascko, “T2K Status, Results, and Plans.” Talk given at the *XXVIII International Conference on Neutrino Physics and Astrophysics*, Heidelberg, Germany, June 4–9, 2018.
- [207] M. Sanchez, “NOvA Results and Prospects.” Talk given at the *XXVIII International Conference on Neutrino Physics and Astrophysics*, Heidelberg, Germany, June 4–9, 2018.
- [208] J. Hewes, “Neutrino Oscillation Results from NOvA.” Talk given at *NuPhys2019: Prospects in Neutrino Physics*, London, UK, December 16–18, 2019.
- [209] DUNE Collaboration, S. Jones *et al.*, “Deep Underground Neutrino Experiment (DUNE), Far Detector Technical Design Report, Volume 1 Introduction to DUNE”, [arXiv:2002.02967 \[physics.ins-det\]](#).

- [210] DUNE Collaboration, S. Jones *et al.*, “Deep Underground Neutrino Experiment (DUNE), Far Detector Technical Design Report, Volume II DUNE Physics”, [arXiv:2002.03005](#) [[hep-ex](#)].
- [211] DUNE Collaboration, S. Jones *et al.*, “Deep Underground Neutrino Experiment (DUNE), Far Detector Technical Design Report, Volume III DUNE Far Detector Technical Coordination”, [arXiv:2002.03008](#) [[physics.ins-det](#)].
- [212] DUNE Collaboration, S. Jones *et al.*, “Deep Underground Neutrino Experiment (DUNE), Far Detector Technical Design Report, Volume IV Far Detector Single-phase Technology”, [arXiv:2002.03010](#) [[physics.ins-det](#)].
- [213] Hyper-Kamiokande Collaboration, K. Abe *et al.*, “Hyper-Kamiokande Design Report”, [arXiv:1805.04163](#) [[physics.ins-det](#)].
- [214] A. Broncano, M. B. Gavela, and E. E. Jenkins, “The Effective Lagrangian for the seesaw model of neutrino mass and leptogenesis”, *Phys. Lett.* **B552** (2003) 177–184, [arXiv:hep-ph/0210271](#) [[hep-ph](#)]. [Erratum: *Phys. Lett.*B636,332(2006)].
- [215] A. Broncano, M. B. Gavela, and E. E. Jenkins, “Neutrino physics in the seesaw model”, *Nucl. Phys.* **B672** (2003) 163–198, [arXiv:hep-ph/0307058](#) [[hep-ph](#)].
- [216] A. Abada, C. Biggio, F. Bonnet, M. B. Gavela, and T. Hambye, “Low energy effects of neutrino masses”, *JHEP* **12** (2007) 061, [arXiv:0707.4058](#) [[hep-ph](#)].
- [217] E. Fernandez-Martinez, J. Hernandez-Garcia, and J. Lopez-Pavon, “Global constraints on heavy neutrino mixing”, *JHEP* **08** (2016) 033, [arXiv:1605.08774](#) [[hep-ph](#)].
- [218] M. Blennow, P. Coloma, E. Fernandez-Martinez, J. Hernandez-Garcia, and J. Lopez-Pavon, “Non-Unitarity, sterile neutrinos, and Non-Standard neutrino Interactions”, *JHEP* **04** (2017) 153, [arXiv:1609.08637](#) [[hep-ph](#)].
- [219] J. W. F. Valle, “Resonant Oscillations of Massless Neutrinos in Matter”, *Phys. Lett.* **B199** (1987) 432–436.
- [220] M. M. Guzzo, A. Masiero, and S. T. Petcov, “On the MSW effect with massless neutrinos and no mixing in the vacuum”, *Phys. Lett.* **B260** (1991) 154–160. [[369\(1991\)](#)].
- [221] T. Ohlsson, “Status of non-standard neutrino interactions”, *Rept. Prog. Phys.* **76** (2013) 044201, [arXiv:1209.2710](#) [[hep-ph](#)].
- [222] O. G. Miranda and H. Nunokawa, “Non standard neutrino interactions: current status and future prospects”, *New J. Phys.* **17** no. 9, (2015) 095002, [arXiv:1505.06254](#) [[hep-ph](#)].
- [223] M. B. Gavela, D. Hernandez, T. Ota, and W. Winter, “Large gauge invariant non-standard neutrino interactions”, *Phys. Rev.* **D79** (2009) 013007, [arXiv:0809.3451](#) [[hep-ph](#)].
- [224] S. Davidson, C. Pena-Garay, N. Rius, and A. Santamaria, “Present and future bounds on nonstandard neutrino interactions”, *JHEP* **03** (2003) 011, [arXiv:hep-ph/0302093](#) [[hep-ph](#)].
- [225] C. Biggio, M. Blennow, and E. Fernandez-Martinez, “General bounds on non-standard neutrino interactions”, *JHEP* **08** (2009) 090, [arXiv:0907.0097](#) [[hep-ph](#)].

- [226] C. Biggio, M. Blennow, and E. Fernandez-Martinez, “Loop bounds on non-standard neutrino interactions”, *JHEP* **03** (2009) 139, [arXiv:0902.0607](#) [hep-ph].
- [227] M. C. Gonzalez-Garcia, M. Maltoni, and J. Salvado, “Testing matter effects in propagation of atmospheric and long-baseline neutrinos”, *JHEP* **05** (2011) 075, [arXiv:1103.4365](#) [hep-ph].
- [228] M. C. Gonzalez-Garcia and M. Maltoni, “Determination of matter potential from global analysis of neutrino oscillation data”, *JHEP* **09** (2013) 152, [arXiv:1307.3092](#) [hep-ph].
- [229] S. Antusch, J. P. Baumann, and E. Fernandez-Martinez, “Non-Standard Neutrino Interactions with Matter from Physics Beyond the Standard Model”, *Nucl. Phys.* **B810** (2009) 369–388, [arXiv:0807.1003](#) [hep-ph].
- [230] Y. Farzan, “A model for large non-standard interactions of neutrinos leading to the LMA-Dark solution”, *Phys. Lett.* **B748** (2015) 311–315, [arXiv:1505.06906](#) [hep-ph].
- [231] Y. Farzan and I. M. Shoemaker, “Lepton Flavor Violating Non-Standard Interactions via Light Mediators”, *JHEP* **07** (2016) 033, [arXiv:1512.09147](#) [hep-ph].
- [232] K. S. Babu, A. Friedland, P. A. N. Machado, and I. Mocioiu, “Flavor Gauge Models Below the Fermi Scale”, [arXiv:1705.01822](#) [hep-ph].
- [233] Y. Farzan and M. Tortola, “Neutrino oscillations and Non-Standard Interactions”, *Front.in Phys.* **6** (2018) 10, [arXiv:1710.09360](#) [hep-ph].
- [234] P. B. Denton, Y. Farzan, and I. M. Shoemaker, “A Plan to Rule out Large Non-Standard Neutrino Interactions After COHERENT Data”, [arXiv:1804.03660](#) [hep-ph].
- [235] J. Heeck, M. Lindner, W. Rodejohann, and S. Vogl, “Non-Standard Neutrino Interactions and Neutral Gauge Bosons”, *SciPost Phys.* **6** no. 3, (2019) 038, [arXiv:1812.04067](#) [hep-ph].
- [236] CHARM Collaboration, J. Dorenbosch *et al.*, “Experimental Verification of the Universality of ν_e and ν_μ Coupling to the Neutral Weak Current”, *Phys. Lett.* **B180** (1986) 303–307.
- [237] NuTeV Collaboration, G. P. Zeller *et al.*, “A Precise determination of electroweak parameters in neutrino nucleon scattering”, *Phys. Rev. Lett.* **88** (2002) 091802, [arXiv:hep-ex/0110059](#) [hep-ex]. [Erratum: *Phys. Rev. Lett.* 90,239902(2003)].
- [238] G. Branco, M. Rebelo, and J. Silva-Marcos, “Degenerate and quasidegenerate majorana neutrinos”, *Phys.Rev.Lett.* **82** (1999) 683–686, [arXiv:hep-ph/9810328](#).
- [239] C. Jarlskog, “Flavor projection operators and applications to CP violation with any number of families”, *Phys.Rev.D* **36** (1987) 2128.
- [240] P. Bakhti and Y. Farzan, “Shedding light on LMA-Dark solar neutrino solution by medium baseline reactor experiments: JUNO and RENO-50”, *JHEP* **07** (2014) 064, [arXiv:1403.0744](#) [hep-ph].
- [241] O. G. Miranda, M. A. Tortola, and J. W. F. Valle, “Are solar neutrino oscillations robust?”, *JHEP* **10** (2006) 008, [arXiv:hep-ph/0406280](#) [hep-ph].
- [242] A. de Gouvea, A. Friedland, and H. Murayama, “The Dark side of the solar neutrino parameter space”, *Phys. Lett.* **B490** (2000) 125–130, [arXiv:hep-ph/0002064](#) [hep-ph].

- [243] A. M. Dziewonski and D. L. Anderson, “Preliminary reference earth model”, *Phys. Earth Planet. Interiors* **25** (1981) 297–356.
- [244] A. Friedland, C. Lunardini, and M. Maltoni, “Atmospheric neutrinos as probes of neutrino-matter interactions”, *Phys. Rev.* **D70** (2004) 111301, [arXiv:hep-ph/0408264](https://arxiv.org/abs/hep-ph/0408264) [hep-ph].
- [245] H. Nunokawa, S. J. Parke, and R. Zukanovich Funchal, “Another possible way to determine the neutrino mass hierarchy”, *Phys. Rev.* **D72** (2005) 013009, [arXiv:hep-ph/0503283](https://arxiv.org/abs/hep-ph/0503283) [hep-ph].
- [246] T.-K. Kuo and J. T. Pantaleone, “The Solar Neutrino Problem and Three Neutrino Oscillations”, *Phys. Rev. Lett.* **57** (1986) 1805–1808.
- [247] M. M. Guzzo, H. Nunokawa, P. C. de Holanda, and O. L. G. Peres, “On the massless ‘just-so’ solution to the solar neutrino problem”, *Phys. Rev.* **D64** (2001) 097301, [arXiv:hep-ph/0012089](https://arxiv.org/abs/hep-ph/0012089) [hep-ph].
- [248] P. Coloma, P. B. Denton, M. C. Gonzalez-Garcia, M. Maltoni, and T. Schwetz, “Cur-tailing the Dark Side in Non-Standard Neutrino Interactions”, *JHEP* **04** (2017) 116, [arXiv:1701.04828](https://arxiv.org/abs/1701.04828) [hep-ph].
- [249] P. Coloma, M. C. Gonzalez-Garcia, M. Maltoni, and T. Schwetz, “COHERENT En-lightenment of the Neutrino Dark Side”, *Phys. Rev.* **D96** no. 11, (2017) 115007, [arXiv:1708.02899](https://arxiv.org/abs/1708.02899) [hep-ph].
- [250] IceCube Collaboration, J. P. Yañez *et al.*, “IceCube Oscillations: 3 years muon neutrino disappearance data.”. http://icecube.wisc.edu/science/data/nu_osc.
- [251] B. J. P. Jones, *Sterile neutrinos in cold climates*. PhD thesis, Massachusetts Institute of Technology, 2015. available from <http://hdl.handle.net/1721.1/101327>.
- [252] C. A. Argüelles, *New Physics with Atmospheric Neutrinos*. PhD thesis, University of Wisconsin, Madison, 2015. available from <https://docushare.icecube.wisc.edu/dsweb/Get/Document-75669/thesis.pdf>.
- [253] IceCube Collaboration, M. G. Aartsen *et al.*, “Searches for Sterile Neutrinos with the IceCube Detector”, *Phys. Rev. Lett.* **117** no. 7, (2016) 071801, [arXiv:1605.01990](https://arxiv.org/abs/1605.01990) [hep-ex].
- [254] A. Radovic, “Latest oscillation results from NOvA.”. Joint Experimental-Theoretical Physics Seminar, Fermilab, USA, January 12, 2018.
- [255] N. Graf, “Search for Flavor Changing Non-standard Interactions with the MINOS+ Experiment”, [arXiv:1511.00204](https://arxiv.org/abs/1511.00204) [hep-ex].
- [256] M. Dentler, A. Hernández-Cabezudo, J. Kopp, M. Maltoni, and T. Schwetz, “Sterile neu-trinos or flux uncertainties? — Status of the reactor anti-neutrino anomaly”, *JHEP* **11** (2017) 099, [arXiv:1709.04294](https://arxiv.org/abs/1709.04294) [hep-ph].
- [257] Daya Bay Collaboration, F. P. An *et al.*, “Measurement of electron antineutrino oscillation based on 1230 days of operation of the Daya Bay experiment”, *Phys. Rev.* **D95** no. 7, (2017) 072006, [arXiv:1610.04802](https://arxiv.org/abs/1610.04802) [hep-ex].
- [258] H. Seo, “New Results from RENO.”. Talk given at the *EPS Conference on High Energy Physics*, Venice, Italy, July 5–12, 2017.

- [259] M. C. Gonzalez-Garcia, M. Maltoni, I. Martinez-Soler, and N. Song, “Non-standard neutrino interactions in the Earth and the flavor of astrophysical neutrinos”, *Astropart. Phys.* **84** (2016) 15–22, [arXiv:1605.08055 \[hep-ph\]](#).
- [260] A. Friedland and C. Lunardini, “A Test of tau neutrino interactions with atmospheric neutrinos and K2K”, *Phys.Rev.* **D72** (2005) 053009, [arXiv:hep-ph/0506143 \[hep-ph\]](#).
- [261] A. Esmaili and A. Yu. Smirnov, “Probing Non-Standard Interaction of Neutrinos with IceCube and DeepCore”, *JHEP* **06** (2013) 026, [arXiv:1304.1042 \[hep-ph\]](#).
- [262] J. Salvado, O. Mena, S. Palomares-Ruiz, and N. Rius, “Non-standard interactions with high-energy atmospheric neutrinos at IceCube”, *JHEP* **01** (2017) 141, [arXiv:1609.03450 \[hep-ph\]](#).
- [263] J. Kopp, M. Lindner, T. Ota, and J. Sato, “Non-standard neutrino interactions in reactor and superbeam experiments”, *Phys. Rev.* **D77** (2008) 013007, [arXiv:0708.0152 \[hep-ph\]](#).
- [264] ISS Physics Working Group Collaboration, A. Bandyopadhyay, “Physics at a future Neutrino Factory and super-beam facility”, *Rept. Prog. Phys.* **72** (2009) 106201, [arXiv:0710.4947 \[hep-ph\]](#).
- [265] A. M. Gago, H. Minakata, H. Nunokawa, S. Uchinami, and R. Zukanovich Funchal, “Resolving CP Violation by Standard and Nonstandard Interactions and Parameter Degeneracy in Neutrino Oscillations”, *JHEP* **01** (2010) 049, [arXiv:0904.3360 \[hep-ph\]](#).
- [266] P. Coloma, A. Donini, J. Lopez-Pavon, and H. Minakata, “Non-Standard Interactions at a Neutrino Factory: Correlations and CP violation”, *JHEP* **08** (2011) 036, [arXiv:1105.5936 \[hep-ph\]](#).
- [267] P. Coloma, “Non-Standard Interactions in propagation at the Deep Underground Neutrino Experiment”, *JHEP* **03** (2016) 016, [arXiv:1511.06357 \[hep-ph\]](#).
- [268] M. Masud, A. Chatterjee, and P. Mehta, “Probing CP violation signal at DUNE in presence of non-standard neutrino interactions”, *J. Phys.* **G43** no. 9, (2016) 095005, [arXiv:1510.08261 \[hep-ph\]](#).
- [269] A. de Gouvêa and K. J. Kelly, “Non-standard Neutrino Interactions at DUNE”, *Nucl. Phys.* **B908** (2016) 318–335, [arXiv:1511.05562 \[hep-ph\]](#).
- [270] J. Liao, D. Marfatia, and K. Whisnant, “Degeneracies in long-baseline neutrino experiments from nonstandard interactions”, *Phys. Rev.* **D93** no. 9, (2016) 093016, [arXiv:1601.00927 \[hep-ph\]](#).
- [271] K. Huitu, T. J. Kärkkäinen, J. Maalampi, and S. Vihonen, “Constraining the nonstandard interaction parameters in long baseline neutrino experiments”, *Phys. Rev.* **D93** no. 5, (2016) 053016, [arXiv:1601.07730 \[hep-ph\]](#).
- [272] P. Bakhti and Y. Farzan, “CP-Violation and Non-Standard Interactions at the MOMENT”, *JHEP* **07** (2016) 109, [arXiv:1602.07099 \[hep-ph\]](#).
- [273] M. Masud and P. Mehta, “Nonstandard interactions spoiling the CP violation sensitivity at DUNE and other long baseline experiments”, *Phys. Rev.* **D94** (2016) 013014, [arXiv:1603.01380 \[hep-ph\]](#).

- [274] S. C and R. Mohanta, “Impact of lepton flavor universality violation on CP-violation sensitivity of long-baseline neutrino oscillation experiments”, *Eur. Phys. J.* **C77** no. 1, (2017) 32, [arXiv:1701.00327 \[hep-ph\]](#).
- [275] A. Rashed and A. Datta, “Determination of mass hierarchy with $\nu_\mu \rightarrow \nu_\tau$ appearance and the effect of nonstandard interactions”, *Int. J. Mod. Phys.* **A32** no. 11, (2017) 1750060, [arXiv:1603.09031 \[hep-ph\]](#).
- [276] M. Masud and P. Mehta, “Nonstandard interactions and resolving the ordering of neutrino masses at DUNE and other long baseline experiments”, *Phys. Rev.* **D94** no. 5, (2016) 053007, [arXiv:1606.05662 \[hep-ph\]](#).
- [277] M. Blennow, S. Choubey, T. Ohlsson, D. Pramanik, and S. K. Raut, “A combined study of source, detector and matter non-standard neutrino interactions at DUNE”, *JHEP* **08** (2016) 090, [arXiv:1606.08851 \[hep-ph\]](#).
- [278] S.-F. Ge and A. Yu. Smirnov, “Non-standard interactions and the CP phase measurements in neutrino oscillations at low energies”, *JHEP* **10** (2016) 138, [arXiv:1607.08513 \[hep-ph\]](#).
- [279] D. V. Forero and W.-C. Huang, “Sizable NSI from the $SU(2)_L$ Scalar Doublet-Singlet Mixing and the Implications in Dune”, [arXiv:1608.04719 \[hep-ph\]](#).
- [280] S. Fukasawa, M. Ghosh, and O. Yasuda, “Sensitivity of the T2HKK experiment to nonstandard interactions”, *Phys. Rev.* **D95** no. 5, (2017) 055005, [arXiv:1611.06141 \[hep-ph\]](#).
- [281] J. Liao, D. Marfatia, and K. Whisnant, “Nonstandard neutrino interactions at DUNE, T2HK and T2HKK”, *JHEP* **01** (2017) 071, [arXiv:1612.01443 \[hep-ph\]](#).
- [282] K. N. Deepthi, S. Goswami, and N. Nath, “Can nonstandard interactions jeopardize the hierarchy sensitivity of DUNE?”, *Phys. Rev.* **D96** no. 7, (2017) 075023, [arXiv:1612.00784 \[hep-ph\]](#).
- [283] K. N. Deepthi, S. Goswami, and N. Nath, “Challenges posed by non-standard neutrino interactions in the determination of δ_{CP} at DUNE”, *Nucl. Phys.* **B936** (2018) 91–105, [arXiv:1711.04840 \[hep-ph\]](#).
- [284] D. Meloni, “On the systematic uncertainties in DUNE and their role in New Physics studies”, *JHEP* **08** (2018) 028, [arXiv:1805.01747 \[hep-ph\]](#).
- [285] L. J. Flores, E. A. Garcés, and O. G. Miranda, “Exploring NSI degeneracies in long-baseline experiments”, *Phys. Rev.* **D98** no. 3, (2018) 035030, [arXiv:1806.07951 \[hep-ph\]](#).
- [286] S. Verma and S. Bhardwaj, “Non-standard interactions and parameter degeneracies in DUNE and T2HKK”, [arXiv:1808.04263 \[hep-ph\]](#).
- [287] A. Chatterjee, F. Kamiya, C. A. Moura, and J. Yu, “Impact of Matter Density Profile Shape on Non-Standard Interactions at DUNE”, [arXiv:1809.09313 \[hep-ph\]](#).
- [288] M. Masud, S. Roy, and P. Mehta, “Correlations and degeneracies among the NSI parameters with tunable beams at DUNE”, [arXiv:1812.10290 \[hep-ph\]](#).
- [289] D. V. Forero and P. Huber, “Hints for leptonic CP violation or New Physics?”, *Phys. Rev. Lett.* **117** no. 3, (2016) 031801, [arXiv:1601.03736 \[hep-ph\]](#).

- [290] J. Liao, D. Marfatia, and K. Whisnant, “Nonmaximal neutrino mixing at NOvA from nonstandard interactions”, [arXiv:1609.01786](#) [[hep-ph](#)].
- [291] F. Feroz and M. P. Hobson, “Multimodal nested sampling: an efficient and robust alternative to MCMC methods for astronomical data analysis”, *Mon. Not. Roy. Astron. Soc.* **384** (2008) 449, [arXiv:0704.3704](#) [[astro-ph](#)].
- [292] F. Feroz, M. P. Hobson, and M. Bridges, “MultiNest: an efficient and robust Bayesian inference tool for cosmology and particle physics”, *Mon. Not. Roy. Astron. Soc.* **398** (2009) 1601–1614, [arXiv:0809.3437](#) [[astro-ph](#)].
- [293] F. Feroz, M. P. Hobson, E. Cameron, and A. N. Pettitt, “Importance Nested Sampling and the MultiNest Algorithm”, [arXiv:1306.2144](#) [[astro-ph.IM](#)].
- [294] M. Galassi *et al.*, *GNU Scientific Library Reference Manual*. Network Theory Ltd., 3 ed., 2009. <https://www.gnu.org/software/gsl/doc/html/>. Edited by Brian Gough.
- [295] COHERENT Collaboration, D. Akimov *et al.*, “Observation of Coherent Elastic Neutrino-Nucleus Scattering”, *Science* **357** no. 6356, (2017) 1123–1126, [arXiv:1708.01294](#) [[nucl-ex](#)].
- [296] D. Z. Freedman, “Coherent Neutrino Nucleus Scattering as a Probe of the Weak Neutral Current”, *Phys. Rev.* **D9** (1974) 1389–1392.
- [297] S. Klein and J. Nystrand, “Exclusive vector meson production in relativistic heavy ion collisions”, *Phys. Rev.* **C60** (1999) 014903, [arXiv:hep-ph/9902259](#) [[hep-ph](#)].
- [298] R. H. Helm, “Inelastic and Elastic Scattering of 187-Mev Electrons from Selected Even-Even Nuclei”, *Phys. Rev.* **104** (1956) 1466–1475.
- [299] J. D. Lewin and P. F. Smith, “Review of mathematics, numerical factors, and corrections for dark matter experiments based on elastic nuclear recoil”, *Astropart. Phys.* **6** (1996) 87–112.
- [300] COHERENT Collaboration, D. Akimov *et al.*, “COHERENT Collaboration data release from the first observation of coherent elastic neutrino-nucleus scattering”, [arXiv:1804.09459](#) [[nucl-ex](#)].
- [301] G. Fricke, C. Bernhardt, K. Heilig, L. A. Schaller, L. Schellenberg, E. B. Shera, and C. W. de Jager, “Nuclear Ground State Charge Radii from Electromagnetic Interactions”, *Atom. Data Nucl. Data Tabl.* **60** (1995) 177–285.
- [302] J. Menendez, “Private communication.”.
- [303] P. Klos, J. Menéndez, D. Gazit, and A. Schwenk, “Large-scale nuclear structure calculations for spin-dependent WIMP scattering with chiral effective field theory currents”, *Phys. Rev.* **D88** no. 8, (2013) 083516, [arXiv:1304.7684](#) [[nucl-th](#)]. [Erratum: *Phys. Rev.* **D89**,no.2,029901(2014)].
- [304] M. Hoferichter, P. Klos, J. Menéndez, and A. Schwenk, “Analysis strategies for general spin-independent WIMP-nucleus scattering”, *Phys. Rev.* **D94** no. 6, (2016) 063505, [arXiv:1605.08043](#) [[hep-ph](#)].

-
- [305] M. Hoferichter, P. Klos, J. Menéndez, and A. Schwenk, “Nuclear structure factors for general spin-independent WIMP-nucleus scattering”, *Phys. Rev.* **D99** no. 5, (2019) 055031, [arXiv:1812.05617 \[hep-ph\]](#).
- [306] J. Barranco, O. G. Miranda, and T. I. Rashba, “Probing New Physics with Coherent Neutrino Scattering Off Nuclei”, *JHEP* **12** (2005) 021, [arXiv:hep-ph/0508299 \[hep-ph\]](#).
- [307] J. I. Collar, A. R. L. Kavner, and C. M. Lewis, “Response of CsI[Na] to Nuclear Recoils: Impact on Coherent Elastic Neutrino-Nucleus Scattering (CE ν NS)”, *Phys. Rev.* **D100** no. 3, (2019) 033003, [arXiv:1907.04828 \[nucl-ex\]](#).
- [308] P. Barbeau, “Private communication.”.
- [309] J. B. Birks, “Scintillations from Organic Crystals: Specific Fluorescence and Relative Response to Different Radiations”, *Proc. Phys. Soc.* **A64** (1951) 874–877.
- [310] J. Ziegler, “The Stopping and Range of Ions in Matter.” <http://www.srim.org>.
- [311] C. Giunti, “General COHERENT Constraints on Neutrino Non-Standard Interactions”, [arXiv:1909.00466 \[hep-ph\]](#).
- [312] M. Cadeddu, F. Dordei, C. Giunti, Y. F. Li, and Y. Y. Zhang, “Neutrino, Electroweak and Nuclear Physics from COHERENT Elastic Neutrino-Nucleus Scattering with a New Quenching Factor”, *Phys. Rev.* **D101** no. 3, (2020) 033004, [arXiv:1908.06045 \[hep-ph\]](#).